

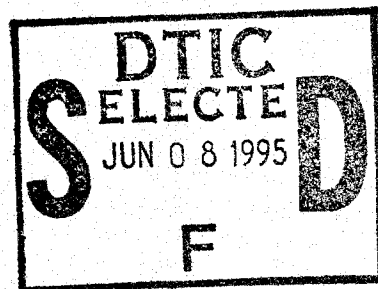
# UNCLASSIFIED

<b>AD NUMBER</b>
ADB199453
<b>NEW LIMITATION CHANGE</b>
<b>TO</b> Approved for public release, distribution unlimited
<b>FROM</b> Distribution authorized to DoD and DoD contractors only; Software Documentation; Apr 95. Other requests shall be referred to Chief of Naval Research, 800 N. Quincy St., Arlington, VA 22217-5660.
<b>AUTHORITY</b>
ONR ltr., 19 Feb 97

THIS PAGE IS UNCLASSIFIED

Distribution authorized to Department of Defense and DoD contractors only; Software Documentation. Date of Determination: April 1995. Other requests shall be referred to the Chief of Naval Research, 800 North Quincy Street, Arlington, VA 22217-5660

# APL-UW High-Frequency Ocean Environmental Acoustic Models Handbook



DESTRUCTION NOTICE: — For classified documents follow the procedures in DoD 5220.22-M, Industrial Security Manual, Section II-19 or DoD 5200.1-R, Information Security Program Regulation, Chapter IX. For unclassified, limited documents, destroy by any method that will prevent disclosure of contents or reconstruction of the document.

Technical Report  
**APL-UW TR 9407**  
**AEAS 9501**  
October 1994

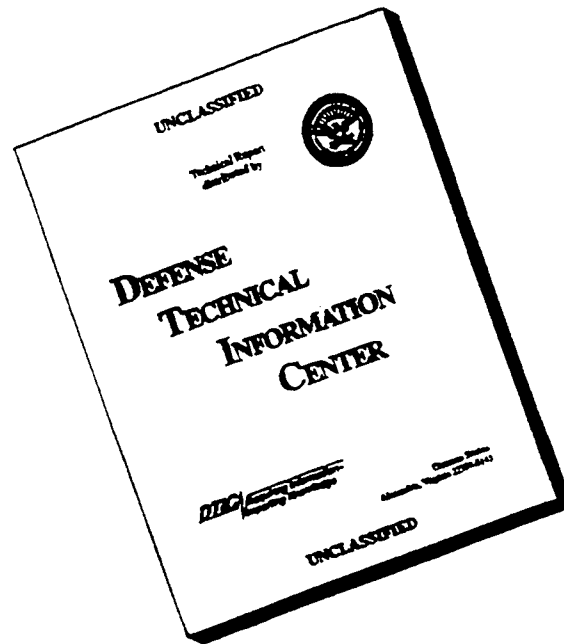
~~Original contains color~~  
plates: All DTIC reproductions will be in black and white.

DTIC QUALITY INSPECTED 3

tract N00039-91-C-0072

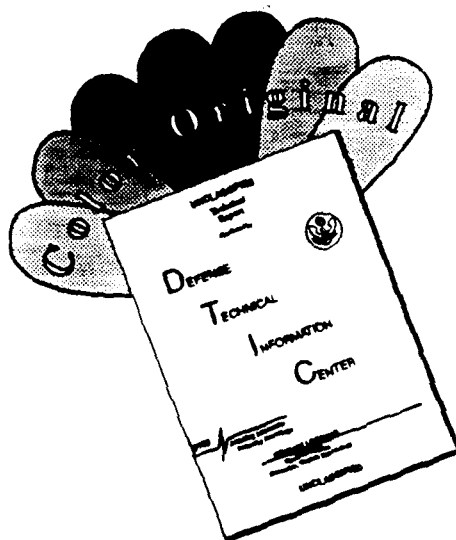
19950605 090

# DISCLAIMER NOTICE



**THIS DOCUMENT IS BEST  
QUALITY AVAILABLE. THE  
COPY FURNISHED TO DTIC  
CONTAINED A SIGNIFICANT  
NUMBER OF PAGES WHICH DO  
NOT REPRODUCE LEGIBLY.**

# DISCLAIMER NOTICE



THIS DOCUMENT IS BEST QUALITY AVAILABLE. THE COPY FURNISHED TO DTIC CONTAINED A SIGNIFICANT NUMBER OF COLOR PAGES WHICH DO NOT REPRODUCE LEGIBLY ON BLACK AND WHITE MICROFICHE.



# APL-UW High-Frequency Ocean Environmental Acoustic Models Handbook

Accession For	
NTIS	CRA&I <input type="checkbox"/>
DTIC	TAB <input checked="" type="checkbox"/>
Unannounced <input type="checkbox"/>	
Justification .....	
By .....	
Distribution/ .....	
Availability Codes	
Dist	Avail and/or Special
D-16	

DESTRUCTION NOTICE: — For classified documents follow the procedures in DoD 5220.22-M, Industrial Security Manual, Section II-19 or DoD 5200.1-R, Information Security Program Regulation, Chapter IX. For unclassified, limited documents, destroy by any method that will prevent disclosure of contents or reconstruction of the document.

Technical Report  
**APL-UW TR 9407**  
**AEAS 9501**  
October 1994



**Applied Physics Laboratory University of Washington**  
1013 NE 40th Street Seattle, Washington 98105-6698

Contract N00039-91-C-0072

### *ACKNOWLEDGMENTS*

This report was sponsored by the Advanced Environmental Acoustic Support Program of the Office of Naval Research, Code 322TE, with technical management by Barry Blumenthal. Funding was provided through the APL-UW omnibus contract with the Space and Naval Warfare System Command, N00039-91-C-0072.

## ABSTRACT

This report updates several high-frequency acoustic models used in simulations and system design by Navy torpedo and mine countermeasure programs. The models presented augment and supersede those given previously in APL-UW technical note 7-79 (August 1979) and its successors, APL-UW technical reports 8407 and 8907. The report addresses the interaction of high-frequency acoustic energy with the ocean's volume, surface, bottom, and ice. It also addresses ambient noise generated by physical processes at the ocean surface and by biological organisms. The results are given in a form that can be exploited in simulations. The relevant fundamental experimental and theoretical research by APL and others upon which these models are based is available in the references.

## TABLE OF CONTENTS

	<i>Page</i>
INTRODUCTION .....	1
A. BACKGROUND AND HISTORY .....	1
B. GUIDE FOR QUICK ENGINEERING ASSESSMENT CALCULATIONS.....	2
C. IMPLEMENTATION SOFTWARE .....	6
 <b>I. VOLUME</b>	
A. SPEED OF SOUND IN SEAWATER .....	I-1
1. Chen-Millero-Li Equation.....	I-1
2. MacKenzie Equation .....	I-2
3. Characteristics.....	I-3
4. Comparisons.....	I-3
B. ABSORPTION COEFFICIENT .....	I-5
C. BACKSCATTERING.....	I-12
1. Introduction .....	I-12
2. Deep Open Ocean .....	I-14
3. Shallow Waters .....	I-17
4. Ice-Covered Regions .....	I-21
5. Spectral Spreading.....	I-21
References .....	I-23
 <b>II. SURFACE</b>	
Introduction.....	II-1
A. WIND SPEED AND SEA STATE.....	II-2
B. BACKSCATTER .....	II-5
1. Scattering from Bubbles.....	II-6
2. Scattering from Sea Surface Roughness .....	II-7
a. Scattering from small-scale roughness .....	II-7
b. Scattering from facets.....	II-8
c. Interpolation between the $\sigma_{sc}$ and $\sigma_f$ cross sections.....	II-9
3. Total Surface Backscattering Strength $\sigma_r + \sigma_b$ .....	II-10
4. Model/Data Comparisons.....	II-10

5. Model Implementation Notes and Model Accuracy .....	II-15
a. Implementation.....	II-15
b. Accuracy.....	II-15
6. Spectral Spread .....	II-16
C. FORWARD LOSS .....	II-19
1. Introduction .....	II-19
2. Preliminary Discussion.....	II-19
3. Effective Reflection Loss for Forward Scattering in Reverberation Simulations .....	II-20
4. Absorption Due to Near-Surface Bubbles .....	II-21
a. Depth-dependent formulation of the <i>SBL</i> model .....	II-24
b. Recommended version based on a linear sound speed profile .....	II-25
5. Model Usage Notes and Accuracy .....	II-26
a. Model usage notes.....	II-26
b. Model accuracy .....	II-27
6. Coherent Reflection Loss .....	II-28
7. Time-Dependent Intensity and Frequency Coherence in Forward Scattering .....	II-29
a. Time-dependent intensity .....	II-29
b. Frequency coherence .....	II-32
8. Frequency Spreading.....	II-33
9. Statistics.....	II-33
D. AMBIENT NOISE.....	II-34
1. Ambient Noise Multipath Expressions.....	II-34
2. Simplified Expressions for Isovelocity, Deep Water Conditions .....	II-39
3. Surface Radiation Pattern (N).....	II-40
4. Noise Level at the Air/Sea Interface at Normal Incidence (A), Wind Effects .....	II-40
5. Noise Level at the Air/Sea Interface at Normal Incidence (A), Combined Wind and Rain Effects.....	II-42
6. Summary.....	II-45
References .....	II-48

**III. BIOLOGICAL HIGH-FREQUENCY AMBIENT NOISE**

A. BACKGROUND .....	III-1
B. GENERALIZED FREQUENCY DISTRIBUTION .....	III-1
C. GENERALIZED MARINE MAMMAL AMBIENT NOISE .....	III-2
D. GENERALIZED SNAPPING SHRIMP LEVELS .....	III-3
E. OTHER INVERTEBRATE NOISE SOURCES .....	III-8
References .....	III-10
Bibliography .....	III-10

**IV. BOTTOM**

Introduction .....	IV-1
A. MODEL INPUT PARAMETERS .....	IV-2
1. Comments on Geoacoustic Modeling .....	IV-3
2. Definition of Model Input Parameters .....	IV-4
3. Table for Model Parameters in Terms of Sediment Name .....	IV-5
4. Model Input Parameters Using Grain Size .....	IV-7
5. Model Input Parameters Using Geoacoustic Data .....	IV-11
6. Refinement of Input Parameters Using Backscattering Data .....	IV-13
7. Use of Bottom Roughness Data .....	IV-14
8. Limits on Model Parameters .....	IV-17
B. FORWARD LOSS .....	IV-18
1. Statement of the Forward Loss Model .....	IV-18
2. Model Accuracy .....	IV-19
3. Numerical Considerations .....	IV-21
C. BACKSCATTER .....	IV-21
1. Introduction .....	IV-21
2. Equations for Bottom Backscattering Strength .....	IV-22
a. Roughness scattering cross section, $\sigma_r(\theta)$ .....	IV-26
<i>Kirchhoff Approximation</i> .....	IV-27
<i>Composite Roughness Approximation</i> .....	IV-28
<i>Large-Roughness Scattering Cross Section</i> .....	IV-31
<i>Interpolation Between Approximations</i> .....	IV-32
b. Sediment volume scattering cross section, $\sigma_v(\theta)$ .....	IV-33
3. Model Accuracy .....	IV-35
4. Numerical Considerations .....	IV-36

D. BISTATIC SCATTERING .....	IV-37
1. Model Inputs.....	IV-38
2. Equations for Bottom Bistatic Scattering Strength .....	IV-43
a. Definition of geometric parameters .....	IV-44
b. Roughness scattering cross section.....	IV-45
<i>Kirchhoff Approximation</i> .....	IV-45
<i>Perturbation Approximation</i> .....	IV-46
<i>Interpolation Between Approximations</i> .....	IV-47
c. Sediment volume scattering cross section .....	IV-47
3. Model Accuracy .....	IV-48
4. Numerical Considerations .....	IV-49
References .....	IV-50
 V. ARCTIC	
Introduction.....	V-1
A. SOUND SPEED AND ATTENUATION .....	V-2
1. Vertical Sound Speed as a Function of Salinity and Temperature ...	V-2
2. Average Longitudinal Sound Speed as a Function of Thickness and Air/Ice Interface Temperature .....	V-4
3. Attenuation as a Function of Temperature .....	V-6
B. SCATTERING AND FORWARD ENERGY LOSS FROM UNRIDGED ICE .....	V-6
1. Forward Scattering.....	V-6
a. Energy loss.....	V-6
b. Scattering coefficient .....	V-8
c. Time-dependent intensity after forward scattering.....	V-9
2. Near Normal Incidence .....	V-10
a. Unridged ice amplitude "reflection" coefficient .....	V-10
b. Scattering from an ice block .....	V-11
3. Low Angle Backscatter .....	V-12
C. ICE KEELS .....	V-15
1. Formation of Ridges .....	V-15
2. Ridge Structure .....	V-15
3. Keel Statistics.....	V-16

D. ICE KEEL REFLECTIONS.....	V-18
1. Point-Like Nature.....	V-18
2. Reflector Density .....	V-18
3. Response Pattern.....	V-20
4. Frequency Dependence .....	V-20
5. Modeling of Ice Keels .....	V-22
References .....	V-26



## *Introduction*

## A. BACKGROUND AND HISTORY

This report is a revision of APL-UW TR 8907 and provides an up-to-date record of the environmental acoustic models used in simulation studies at the Applied Physics Laboratory, University of Washington. The report addresses the interaction of sound with the ocean's volume, surface, bottom, and ice and discusses ambient noise generated by processes at the ocean surface and by biological organisms.

The document is divided into five sections:

*Volume* (sound speed, attenuation, backscattering),

*Surface* (sea state, backscatter, forward loss, ambient noise),

*Biological Ambient Noise* (general frequency distributions, noise levels of snapping shrimp, other invertebrate noise sources),

*Bottom* (model inputs, forward loss, backscatter, bistatic scatter),

*Arctic* (sound speed and attenuation [in ice], scattering and energy loss from unridged ice, ice keels, ice keel reflections).

As an aid to the users of previous versions of this document, a synopsis of changes found in each section is given below.

**Volume:** The order of preference for sound-speed models has changed. Arguments for the order are given; however, several models are still listed as possibilities, and the final decision is left to the user. The backscatter model gives more detailed regional recommendations.

**Surface:** The backscatter model has undergone significant revision, including notational changes. The general form now consists of two terms:  $\sigma_b$ , or the scattering due to bubbles, and  $\sigma_r$ , or the scattering due to interface roughness. Both of these terms are estimated by submodels which have also been revised. The forward loss model has been revised to include a wind-speed dependent threshold for wave breaking and

subsequent production of bubbles, and different wind-speed and frequency dependencies. This model assumes isovelocity conditions in the upper 10 m of water. An alternate version is also available for general sound-speed profiles and accommodates ray vertexing near the surface. Minor changes have been made in the model for the time spread in forward scattering. There have been changes in the coefficients in the ambient noise model that depend on wind speed and rain rate. The model assumes the same form as the previous version, however, and therefore can be easily adapted.

**Biological Ambient Noise:** This is a completely new section. Its primary emphasis is on the distribution, levels, and spectra of ambient noise caused by snapping shrimp. This ambient noise source can dominate all others in some shallow water environments.

**Bottom:** The forward loss and backscattering models are unchanged. The bistatic model is new; however, many of the parameters used to drive the model are the same as those for the forward loss and backscattering models. The bistatic model is capable of treating all scattering geometries, including forward and backscattering. Thus, if desired, the user can replace the forward loss and backscattering models by this one bistatic scattering model. It is important to note that the results obtained using the bistatic model in the forward and backward directions are consistent with the forward loss and backscattering models.

**Arctic:** New equations are given for sound speed and attenuation in ice. A forward scattering model is given that uses the same high-frequency approximation used in the "Surface" section. This allows calculation of the pulse elongation seen when an acoustic signal is forward scattered off nonridged ice.

## **B. GUIDE FOR QUICK ENGINEERING ASSESSMENT CALCULATIONS**

This guide is intended to allow quick access to equations useful in preliminary assessment calculations so that the engineer/scientist can perform overview calculations (e.g., the sonar equation) without undue delay. In this guide, the reader is directed, by page number,

to specific equations and figures that can be used in such calculations. Some users may find it useful to compile the appropriate pages in a quick reference document.

## **1. Volume**

### Speed of Sound in Water

Use the Mackenzie equation on page I-3.

### Absorption Coefficient in Water

Use Table 2 beginning on page I-8. This table is for zero depth. It can be used to 100-m depth with negligible error. It gives attenuation values at temperatures and salinities most often seen in the ocean.

### Backscattering

#### Deep Ocean

Use values given in the first two paragraphs on page I-16.

#### Shallow Water (less than 200 m deep)

Use values as described on page I-19 in the first paragraph and in the following paragraphs that continue on page I-21.

#### Ice Covered Regions

Use value given on page I-21.

## **2. Surface**

### Backscattering

For frequencies between 15 and 35 kHz, Figure 2a on page II-11 gives useful backscattering strengths as a function of angle for wind speeds from 3 to 15 m/s. Likewise, Figure 2b (page II-11) can be used to determine backscattering from 50 to 70 kHz. As indicated by Figure 1 on page II-5, over 80% of oceanic winds fall within this 3 to 15 m/s wind-speed window. For other conditions, Eqs. 1-16 on pages II-5 to II-10 must be used.

### Spectral Spread in Backscattering

Use Figure 9 on page II-18 to estimate the normalized spread (Eq. 19 on page II-16) as a function of rms wave height. Wave height is related to wind speed by Eq. 22 on page II-17. Figure 9 is for a grazing angle of  $60^\circ$  and an up/down wave direction. For other conditions, use Eqs. 19–24 on pages II-16 and II-17.

### Forward Loss

Use Eq. 27 on page II-20 along with the definition of SBL(dB) in Eq. 28 on page II-21 to calculate forward loss as a function of wind speed and grazing angle.

### Time Dependence of Forward Scattered Energy

This is for cases where the pulse elongation seen in the forward scattered signal is important (in addition to the forward loss). Use Eqs. 40–42 on pages II-29 and II-30. Compare results with Figure 14 on page II-32.

### Frequency Spreading Associated with Forward Scattering

Use Eq. 43a on page II-33.

### Ambient Noise in Isovelocity Deep Water— Without Rain

Use curves of Figure 17a on page II-43 that are associated with Eq. 53. That figure shows the pressure received at an omnidirectional hydrophone as a function of frequency for sea states 0 to 6. Use Table 2 on page II-4 to relate wind speed to sea state.

### Ambient Noise in Isovelocity Deep Water — With Rain

Use Figure 18a on page II-46 to bound ambient noise levels for sea states between 0 and 5 and rain rates from 0 to 10 mm/hour.

### Ambient Noise in Shallow Water

Unfortunately, simple Wenz-type curves do not suffice to obtain useful estimates in this case. The equations of the Ambient Noise section will have to be coded in detail.

### 3. Biological Ambient Noise

Snapping shrimp are the principal source of biological ambient noise. Use text on page III-7 to determine their associated noise spectrum level. Table I on page III-2 gives signal characteristics of some significant sources of high frequency biological ambient noise (other than snapping shrimp).

### 4. Bottom

#### Forward Loss vs Grazing Angle

Use Figure 1 on page IV-19. Sediment descriptors on the figure come from Table 2 on page IV-6. The bulk grain size given in Table 2 is defined in Eq. 1 on page IV-7.

#### Backscattering Strength vs Grazing Angle

Use Table 3 on pages IV-23 to IV-25. Sediment descriptors given in Table 3 come from Table 2 on page IV-6. The bulk grain size given in Table 2 is defined in Eq. 1 on page IV-7.

### 5. Arctic

#### Sound Speed in Ice

Use Eqs. 1 and 2 on pages V-2 and V-3.

#### Attenuation in Ice

Use Eq. 4 on page V-6.

#### Forward Loss—Away from Normal Incidence

Use Figure 3 and the text on page V-7.

#### Forward Loss - Near Normal Incidence

Use Figure 5 on page V-11.

### Time Dependence of Forward Scattered Energy

This is for cases where the pulse elongation seen in the forward scattered signal is important (in addition to the forward loss). Use Eqs. 6 and 7 on page V-9. Refer to Eqs. 40–42 on pages II-29 and II-30 for parameter definitions.

### Low Angle Backscatter from Unridged Ice

Use Figure 7 and Eq. 10 on page V-14.

### Average Target Strength of Ice Keels

Use Figure 11 on page V-22.

## **C. IMPLEMENTATION SOFTWARE**

### **1. Introduction**

Listed below are models from APL-UW TR 9407 that were selected for implementation in FORTRAN. Each model is implemented in a separate subroutine that is suitable for inclusion into a larger simulation. For each model, a test driver that has two functions is provided. The main function provides the user with the capability of making test runs and examining the model results. The secondary function, in many cases, provides a table suitable for inclusion in a Generic Sonar Model (GSM) input file. The test drivers may also provide a starting point for development of software to support other simulations. Names of test drivers and outputs are provided below.

The software conforms to commonly accepted software engineering standards such as those described in *Software Engineering* by Roger Pressman, McGraw-Hill, 1987. Complete descriptions of software functions are provided in the subfunctions that implement the acoustic models. Input arguments are checked to assure they are within acceptable intervals. Where possible, the subroutines key variable names to the names used in the text of APL-UW TR 9407 and link FORTRAN expressions with equations in the report's text. This is intended to ease cross referencing between the text and the software.

The first argument in most functions is a logical variable, debug. If debug is true, volumes of intermediate variables will be printed for debugging purposes and will allow the

user to determine the origin of model characteristics. In the drivers, test inputs for each model are listed, along with the results of the model computation. This will allow the user to compare results of his or her computations with ours to identify compiler and machine-dependent problems.

Department of Defense (DoD) agencies and DoD contractors can receive further information regarding this software by contacting Chris Eggen (206-543-9804) or Kevin Williams (206-543-3949) at APL-UW, or by contacting the APL front desk (206-543-1300) to page either Kevin or Chris. Alternatively, email may be sent to *chris@apl.washington.edu* or *williams@apl.washington.edu*. A distribution of the software will be made after obtaining verification of requester's status (preferably via a DoD contract number, if requester is not a DoD agency) and a sponsor request. Requester must provide APL-UW with a blank copy of the preferred means of data transfer. We are equipped to send data on a SUN cartridge tape, a 9-track tape, or an 8-mm tape. Agencies that are not DoD or DoD contractors should coordinate requests for information and software through the Chief of Naval Research, Code 322TE, Ballston Tower One, 800 North Quincy Street, Arlington, VA 22217-5660.

## 2. Software Descriptions

A description of software is provided for each model encoded. The function implementing the model in this report is named and a description is provided, if necessary. This is followed by specifications of the arguments, the returned quantity, and the subfunctions (if any) used by the main model function. Finally, the test driver supplied to run the model function is described.

### Sound Speed

Function: ssp94.f

Arguments:	depth	= depth (m)
	temp	= temperature (degrees C)
	sal	= salinity (ppt)

Returns: Sound speed in m/s



Subfunctions: None

Driver: sspat94.f

Operation: Reads input file of depth, temperature, and salinity and computes sound speed and attenuation vs depth. Alternatively, reads input file of depth and sound speed, inverts sound speed to obtain temperature and salinity, and computes attenuation vs depth. Output files are suitable for inclusion into GSM input files.

Inputs:

line 1	Name of input file
line 2	Name of output sound speed file
line 3	Name of output attenuation file
line 4	Frequency (kHz), pH
line 5	Temperature units in input file
line 6	Depth and sound speed units in input file
line 7	Depth and sound speed units desired in output file

Other subroutines used by the driver:

fit	Fits a regression line to loss (dB) vs grazing angle
gsmtab	Writes a table to a file in standard GSM format

### Attenuation

Function: attn94.f

Arguments:

freq	= signal frequency (kHz)
ph	= ph measure of acid-base (0–14)
depth	= depth (m)
temp	= temperature (degrees C)
sal	= salinity (ppt)
sonspd	= sound speed (m/s) (inverted to obtain temperature and salinity if these are 0)

Returns: Attenuation in dB/km

Subfunctions: None

Driver:       sspat94.f

This program serves as a driver for both sound speed and attenuation. See description of driver for sound speed.

### Surface Reflection Loss

There are three separate functions implementing this model.

Function: sbl94.f

This function implements the most direct form of the model, the equations of which are derived assuming all loss is due to an attenuating layer of bubbles and isovelocity propagation.

Arguments:   debug   = logical flag set to true if debug printouts desired  
              thetad   = grazing angle (degrees)  
              ws       = wind speed (m/s)  
              freq     = signal frequency (kHz)

Returns:      Surface reflection power loss

Subfunctions: None

Driver 1: tsloss.f

Operation: Computes surface reflection loss vs grazing angle at 0.1 degree intervals below 1 degree and at 1.0 degree intervals between 1 and 90 degrees, and converts to dB. It then examines the results and retains only sufficient vectors in the final matrix to support linear interpolation. It outputs the matrix in a table suitable for GSM

Inputs:      line 1   Wind speed in m/s and frequency in kHz  
              line 2   Name of output file

Other subroutines used by driver:

              fit       Fits a regression line to loss (dB) vs grazing angle  
              gsmtab   Writes a table to a file in standard GSM format

Driver 2:     tslos2.f

Operation:   Computes surface reflection loss vs wind speed from 0 m/s to 15 m/s

at 0.15 m/s intervals for a fixed grazing angle. Outputs the results in an ascii file

Inputs:     line 1    Wind speed in m/s and grazing angle in degrees  
          line 2    Name of output file

Function: batn94.f

This function computes bubble attenuation in the 10 m below the surface for a simulation that can use such information to predict loss for rays that intersect or come close to the surface. For an isovelocity sound speed profile, rays transiting such a bubble attenuation layer and hitting the surface at a grazing angle of  $\theta$  would suffer a loss equal to that computed by the sbl94.f

Arguments:  debug   = logical flag set to true if debug printouts desired  
          depth    = depth below surface (m)  
          ws       = wind speed (m/s)  
          freq     = signal frequency (kHz)

Returns:    Attenuation (dB/m)

Subfunctions: None

Driver:     tbatn.f

Operation:  Computes bubble attenuation vs depth for the 10 m below the surface at 0.5 m intervals. Outputs table vs depth in table suitable for GSM

Inputs:     line 1    Wind speed in m/s and frequency in kHz  
          line 2    Name of output file

Other subroutines used by driver:

          gsmstab   Writes a table to a file in standard GSM format

Function: sbl94i.f

This function computes the loss for a ray transiting the bubble attenuation layer and either vertexing or reflecting off the surface. It performs an integration of loss over the ray path assuming a piecewise linear sound speed profile in the upper 10 m of the water column. For a ray intersecting the surface, the results

can be interpreted as a surface reflection loss. For an isovelocity sound speed profile, the results will be the same as the loss computed by sbl94.f

Arguments: debug = logical flag set to true if debug printouts desired  
 depths = reference depth (m)  
 elevs = elevation angle at reference depth (degrees)  
 ws = wind speed (m/s)  
 freq = signal frequency (kHz)

Returns: loss for ray transiting layer within 10 m of surface (dB)

Subfunctions:

Internal: integrnd Integrand for depth integral

erf Error function

External: dqags, dqagse, dqpsrt, dqk21, dqelg, xerror, xerrwv, xerprt,  
 xerabt, xerctl, xgetua, xersav, fdump, j4save, s88fmt, d1mach,  
 i1mach: Performs double precision numerical integration

Driver 1: tslosi.f

Operation: Computes surface reflection loss vs grazing angle for a given sound speed profile by calling sbl94i with depths = 0 and elevs = grazing angle. As for sbl94, it does this at 0.1 degree intervals below 1 degree and at 1.0 degree intervals between 1 and 90 degrees, and converts to dB. It then examines the results and retains only sufficient vectors in the final matrix to support linear interpolation. It outputs the matrix in a table suitable for GSM

Inputs: line 1 Wind speed in m/s and frequency in kHz  
 line 2 Name of file containing sound speed profile (m m/s)  
 line 3 Name of output file

Other subroutines used by driver:

fit Fits a regression line to loss (dB) vs grazing angle  
 gsmtab Writes a table to a file in standard GSM format

Driver 2:      tslosj.f

Operation:    Computes the loss for rays transiting the bubble attenuation layer and either vertexing or reflecting off the surface using the algorithm in sbl94i.f. Gets information defining series of rays from the user and for each ray, writes the loss to standard output and to an ascii file

Inputs:       line 1       Wind speed in m/s and grazing angle in degrees  
                  line 2       Name of file containing sound speed profile (m/s)  
                  line 3       Name of output file  
                  line 4-end    Reference depth (m) and elevation at reference depth (degrees)

#### Surface Scattering Strength

Function: srfs94.f

Arguments:    debug    = logical flag set to true if debug printouts desired  
                  thetad    = grazing angle (degrees)  
                  ws        = wind speed (m/s)  
                  freq     = signal frequency (kHz)  
                  ierr     = equals error code (if nonzero)

Returns:       Surface scattering strength in dB

Subfunctions:

Internal:      fcet94       Computes the scattering cross-section due to the large-scale wave facets  
                  sscr94       Computes scattering cross-section due to small-scale roughness according to composite roughness theory  
                  dB15\_of\_fc    Computes the angle at which facet scattering falls to 15 dB below the maximum at  $\theta = 90^\circ$   
                  bubl94       Computes the scattering cross-section due to bubbles according to resonant bubble scattering theory  
                  sb194       Called to compute attenuation of energy by the bubble field on rays contributing to roughness scattering

Driver: tsscat.f

Operation: Computes surface scattering strength vs grazing angle at one degree intervals and writes it in table suitable for GSM

Inputs:     line 1    Wind speed in m/s  
             line 2    Frequency in kHz  
             line 3    Name of output file

Other subroutines used by driver:

     gsmstab   Writes a table to a file in standard GSM format

### Bottom Reflection Loss

Function: blos94.f

Arguments: debug   = logical flag set to true if debug printouts desired  
             thetad   = grazing angle (degrees)  
             rho       = density ratio at bottom interface (dimensionless)  
             nu        = sound speed ratio at bottom interface (dimensionless)  
             delta     = loss parameter of bottom (dimensionless)

Returns:     Bottom reflection power loss

Subfunctions: None

Driver:       tbscat.f

Operation: Develops physical bottom parameters from several types of bottom inputs. Computes bottom reflection power loss vs grazing angle at 5.0 degree intervals and converts to dB. Increases resolution if reflection loss changes by more than 0.5 dB between angles. Computes bottom scattering strength vs grazing angle at 1.0 degree intervals. Outputs both sets of results in single file as tables suitable for input to GSM

Inputs:     line 1    Method of bottom characterization  
             line 2    For method 1, six bottom parameters  
                          For method 2, bottom type from APL-UW TR 9407  
                          For method 3, bulk grain size  
                          For method 4, porosity of the upper few centimeters of the  
                          bottom

For method 5, six bottom parameters that are known; then  
 next card includes miscellaneous information about the  
 bottom to compute parameters that are not known

For method 6, bulk mass ratio, bulk sound speed ratio, or  
 bulk porosity (i.e., values below the top few centimeters  
 of the bottom) where known

Next line Frequency (kHz) and sound speed in water at bottom (m/s)

Next line Name of output file

Other subroutines used by driver:

bnam2des	Returns six bottom parameters for a given bottom type
gsiz2des	Returns six bottom parameters for a given bulk grain size
por2des	Returns six bottom parameters for a given porosity
rho2gsiz	Returns bulk grain size for a given mass ratio
nu2gsiz	Returns bulk grain size for a given sound speed ratio
des2des	Inputs six bottom parameters and returns zeros if not valid
alph2delt	Returns loss parameter from attenuation in the surficial sediment and from density ratio.
meas2relp	Returns the relief bottom descriptors from measured 1-dimensional bottom characteristics
bulk2gsiz	Returns bulk grain size from bulk mass ratio, bulk sound speed ratio, or bulk porosity
rquadr	Returns real roots for a quadratic polynomial with real coefficients
rcubic	Returns real roots for a cubic polynomial with real coefficients
gsmtab	Writes a table to a file in standard GSM format

Bottom Backscattering Strength

Function: btms94.f

Arguments: debug = logical flag set to true if debug printouts desired  
 thetad = grazing angle (degrees)  
 freq = signal frequency (kHz)  
 cs = sound speed in water at bottom (m/s)  
 rho = density ratio at bottom interface (dimensionless)  
 nu = sound speed ratio at bottom interface (dimensionless)  
 delta = loss parameter of bottom (dimensionless)  
 w2 = spectral strength ( $\text{cm}^4$ )  
 gamma = spectral exponent (dimensionless)  
 sigma2 = volume parameter (dimensionless)  
 ierr = equals error code (if nonzero)

Returns: Bottom backscattering strength in dB

Subfunctions:

Internal: gammaf Computes the gamma function  
 erf Computes the error function  
 sigmpr Computes the bottom backscattering cross-section in the  
 small roughness perturbation approximation  
 sigmpv Computes sediment volume backscattering cross-section

External: None

Driver: tbscat.f

This program serves as the driver for both bottom reflection loss and bottom scattering strength. See the description of driver for bottom reflection loss.

Bottom Bistatic Scattering Strength

Function: bibs94.f

Arguments: debug = logical flag set to true if debug printouts desired  
 thetai = incident grazing angle (degrees)  
 thetas = scattered grazing angle (degrees)



phis = scattered out-of-plane angle (degrees)  
 freq = signal frequency (kHz)  
 cs = sound speed in water at bottom (m/s)  
 rho = density ratio at bottom interface (dimensionless)  
 nu = sound speed ratio at bottom interface (dimensionless)  
 delta = loss parameter of bottom (dimensionless)  
 w2 = spectral strength ( $\text{cm}^4$ )  
 gamma = spectral exponent (dimensionless)  
 w3 = sediment inhomogeneity spectral strength ( $\text{cm}^3$ )  
 gamma3 = sediment inhomogeneity spectrum exponent  
 (dimensionless)  
 mu = ratio of normalized compressibility to density fluctuations  
 (dimensionless)

Returns: Bottom bistatic scattering strength in dB

Subfunctions:

Internal:    gammaf    Computes the gamma functions  
              smbfrl    Simple model for bottom forward reflection loss

External:    None

Driver:      tbbset.f

Operation:    Develops physical bottom parameters from several types of bottom inputs. Computes bottom bistatic scattering strength for a given incident grazing angle vs a predefined set of scattered grazing out-of-plane angles. Outputs results on standard output and in an ascii file.

Inputs: line 1    Frequency (kHz) and sound speed in water at bottom (m/s)  
          line 2    Method of bottom characterization  
          line 3    For method 1, eight bottom parameters  
                      For method 2, bottom type from APL-UW TR 9407  
                      For method 3, bulk grain size  
                      For method 4, porosity of the upper few centimeters of the  
                                  bottom

For method 5, eight bottom parameters that are known.

Then next card includes miscellaneous information about the bottom to compute those that are not known.

For method 6, bulk mass ratio, bulk sound speed ratio, or bulk porosity (i.e., values below the top few centimeters of the bottom) where known

Next line Single or first, last, and increment in incident grazing angles (degrees)

Next line Single or first, last, and increment in scattered grazing angles (degrees)

Next line Single or first, last, and increment in scattered out-of-plane angles (degrees)

Next line Name of output file

Other subroutines used by driver:

bnam2des	Returns six bottom parameters for a given bottom type
gsiz2des	Returns six bottom parameters for a given bulk grain size
por2des	Returns six bottom parameters for a given porosity
rho2gsiz	Returns bulk grain size for a given mass ratio
nu2gsiz	Returns bulk grain size for a given sound speed ratio
des2des	Inputs six bottom parameters and returns zeros if not valid
alph2delt	Returns loss parameter from attenuation in the surficial sediments and from density ratio.
meas2relp	Returns the relief bottom descriptors from measured 1-dimensional bottom characteristics
bulk2gsiz	Returns bulk grain size from bulk mass ratio, bulk sound speed ratio, or bulk porosity
mon2bist	Returns three bistatic volume parameters given the six monostatic bottom descriptors

rquadr	Returns real roots for a quadratic polynomial with real coefficients
rcubic	Returns real roots for a cubic polynomial with real coefficients
gsmtab	Writes a table to a file in standard GSM format

# **I. Volume**

## A. SPEED OF SOUND IN SEAWATER

The speed of sound in seawater can be measured directly with a velocimeter, but high precision is possible only if sophisticated velocimeters, rather than expendable velocimeters, are used. Therefore, sound speed is customarily calculated using temperature, salinity, and pressure (T,S,P) data from a conductivity-temperature-depth (CTD) cast together with an equation for sound speed. This technique is an accurate and economical means of determining a sound-speed profile.

There are many equations for calculating sound speed from temperature, salinity, and pressure measurements.<sup>1-10</sup> APL-UW recommends the Chen-Millero-Li equation<sup>6,10,11</sup> because it is the most accurate and because it is valid over the broadest range of environmental conditions. A simpler but less accurate equation is Mackenzie's nine-term equation.<sup>7</sup>

### 1. Chen-Millero-Li Equation

APL-UW recommends the Chen-Millero-Li equation<sup>6,10,11</sup> (shown on the following page) because the uncertainty in this equation is  $\pm 0.05$  m/s and because it is valid for temperatures from 0 to 40°C, salinities from 0 to 40‰ (‰ = ppt), and pressures from 0 to 1000 bars. Sound-speed equations are accurate only over the specified range of temperature, salinity, and pressure from which they were derived and should not be relied upon outside this range. The original Chen-Millero equation was recently modified to correct for pressure-dependent biases of 0.6 m/s.<sup>9,10,12</sup> See Table 1 for conversion factors.

*Table 1. Pressure conversions.*

1 kg/cm <sup>2</sup>	=	0.980665	bar
1 lb/in. <sup>2</sup>	=	0.0689476	bar
1 atm	=	1.01325	bar

**Chen-Millero-Li Equation, Refs. 6, 10, and 11****C<sub>tsp</sub>** : Sound speed (m/s)**T** : Temperature (°C),  $0 \leq T \leq 40$ **S** : Salinity (‰),  $0 \leq S \leq 40$ **P** : Pressure (bars),  $0 \leq P \leq 1000$ **C<sub>w</sub> (T,P)** : Represents the sound speed of pure water, Ref. 11**C<sub>c</sub> (T,P)** : Represents the correction to the original equation, Ref. 10
$$\left. \begin{array}{l} A(T,P) S \\ B(T,P) S^{3/2} \\ D(P) S^2 \end{array} \right\} : \text{Salinity-related terms, Ref. 6}$$
**C<sub>tsp</sub>** = 1745.0954 for **P** = 1000 bars, **T** = 40°C, **S** = 40‰

$$C_{tsp} = C_w(T,P) - C_c(T,P) + A(T,P) S + B(T,P) S^{3/2} + D(P) S^2$$

$$\begin{aligned} C_w(T,P) = & 1402.388 + 5.03711 T - 5.80852 \times 10^{-2} T^2 + 3.3420 \times 10^{-4} T^3 - 1.4780 \times 10^{-6} T^4 + 3.1464 \times 10^{-9} T^5 \\ & + (0.153563 + 6.8982 \times 10^{-4} T - 8.1788 \times 10^{-6} T^2 + 1.3621 \times 10^{-7} T^3 - 6.1185 \times 10^{-10} T^4) P \\ & + (3.1260 \times 10^{-5} - 1.7107 \times 10^{-6} T + 2.5974 \times 10^{-8} T^2 - 2.5335 \times 10^{-10} T^3 + 1.0405 \times 10^{-12} T^4) P^2 \\ & + (-9.7729 \times 10^{-9} + 3.8504 \times 10^{-10} T - 2.3643 \times 10^{-12} T^2) P^3 \end{aligned}$$

$$\begin{aligned} C_c(T,P) = & (0.0029 - 2.19 \times 10^{-4} T + 1.4 \times 10^{-5} T^2) P \\ & + (-4.76 \times 10^{-6} + 3.47 \times 10^{-7} T - 2.59 \times 10^{-8} T^2) P^2 \\ & + 2.68 \times 10^{-9} P^3 \end{aligned}$$

$$\begin{aligned} A(T,P) = & 1.389 - 1.262 \times 10^{-2} T + 7.164 \times 10^{-5} T^2 + 2.006 \times 10^{-6} T^3 - 3.21 \times 10^{-8} T^4 \\ & + (9.4742 \times 10^{-5} - 1.2580 \times 10^{-5} T - 6.4885 \times 10^{-8} T^2 + 1.0507 \times 10^{-8} T^3 - 2.0122 \times 10^{-10} T^4) P \\ & + (-3.9064 \times 10^{-7} + 9.1041 \times 10^{-9} T - 1.6002 \times 10^{-10} T^2 + 7.988 \times 10^{-12} T^3) P^2 \\ & + (1.100 \times 10^{-10} + 6.649 \times 10^{-12} T - 3.389 \times 10^{-13} T^2) P^3 \end{aligned}$$

$$B(T,P) = -1.922 \times 10^{-2} - 4.42 \times 10^{-5} T + (7.3637 \times 10^{-5} + 1.7945 \times 10^{-7} T) P$$

$$D(P) = 1.727 \times 10^{-3} - 7.9836 \times 10^{-6} P$$

**2. Mackenzie Equation**

Mackenzie's equation<sup>7</sup> is simpler but less accurate than the Chen-Millero-Li equation. This equation is a function of temperature, salinity, and depth (instead of pressure). The Mackenzie equation is valid for a range of temperatures from -2 to 30°C, salinities from 30 to 40‰, and depths to 8000 m. Within this more limited range of temperature, salinity, and

depth, the uncertainty of this equation is  $\pm 0.07$  m/s, while the difference between the Mackenzie and Chen-Millero-Li equations is  $\pm 0.5$  m/s over the *entire* validity range of the Chen-Millero-Li equation. Pressure can be converted to depth by the approximation  $P \times 0.99 \approx D$ , where  $P$  is pressure in decibars (10 dbars = 1 bar) and  $D$  is depth in meters. Using this approximation in the Mackenzie equation yields a sound-speed estimate that agrees with the Chen-Millero-Li equation (over its entire range) to within  $\pm 0.5$  m/s. (See Table 1 for conversion factors).

#### Mackenzie Equation, Ref.7

$C_{tsd}$  : Sound speed (m/s)

$T$  : Temperature ( $^{\circ}\text{C}$ ),  $-2 \leq T \leq 30$

$S$  : Salinity ( $\text{‰}$ ),  $30 \leq S \leq 40$

$D$  : Depth (meters),  $0 \leq D \leq 8000$

$$C_{tsd} = 1448.96 + 4.591 T - 5.304 \times 10^{-2} T^2 + 2.374 \times 10^{-4} T^3 \\ + 1.340 (S-35) + 1.630 \times 10^{-2} D + 1.675 \times 10^{-7} D^2 \\ - 1.025 \times 10^{-2} T(S-35) - 7.139 \times 10^{-13} TD^3$$

### 3. Characteristics

Sound speed increases with increasing temperature, salinity, or pressure. Figure 1 shows an example of corresponding temperature, salinity, and sound-speed profiles from the Sargasso Sea. In general, an increase in temperature of  $1^{\circ}\text{C}$  at  $10^{\circ}\text{C}$  increases the sound speed by 3.6 m/s, and an increase in salinity of  $1\text{‰}$  increases the sound speed by 1.3 m/s.

### 4. Comparisons

Although 99.95% of the world's oceans have temperatures that range from  $-2$  to  $30^{\circ}\text{C}$ , salinities from 33 to  $37\text{‰}$ , and pressures from 0 to  $\approx 1000$  bars,<sup>13</sup> recent tactical interest in littoral environments requires accurate estimates of sound speed in low-salinity conditions, such as those occurring near river outlets. The Chen-Millero-Li equation, with a range that extends to pure water, addresses the low-salinity regime. On the other hand, some regions of tactical interest may require accurate estimates of sound speed in high-temperature/high-salinity conditions. Unfortunately, none of the current sound-speed equations are reliable at

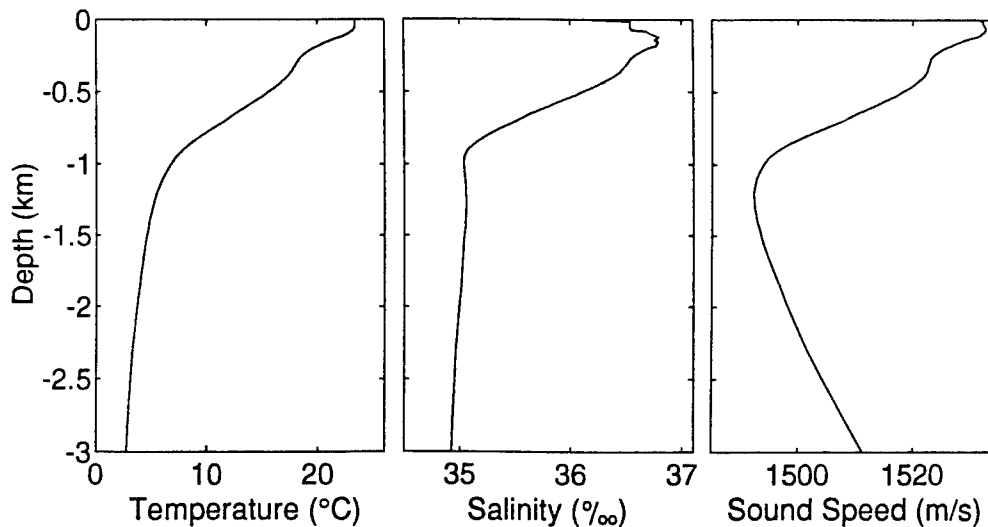


Figure 1. Corresponding temperature, salinity, and sound speed profiles from a CTD cast obtained in the Sargasso Sea. Sound speed increases toward the surface because of increasing temperature and toward the bottom because of increasing pressure.

temperatures greater than  $40^{\circ}\text{C}$  or salinities greater than  $40\text{‰}$ . Although rare, such conditions do occur, e.g., in portions of the Persian Gulf and the Mediterranean Sea, and, therefore, sound-speed equations may be inadequate in these regions.

Two equations in common use by the Navy are the Wilson equation<sup>1</sup> and the more recent Del Grosso equation<sup>5</sup>, also known as NRLII. The Chen-Millero-Li equation is superior to both these equations. The Del Grosso equation agrees with the Chen-Millero-Li equation to within  $0.15\text{ m/s}$  over the (T,S,P) range of the original Del Grosso and Mader measurements<sup>14</sup> (temperatures from  $0$  to  $15^{\circ}\text{C}$ , salinities from  $33$  to  $38\text{‰}$ , and pressures from  $0$  to  $\approx 1000$  bars), but, despite original claims,<sup>5</sup> it is grossly in error for salinities less than about  $30\text{‰}$  (see Figure 2).

While the 1960 Wilson sound-speed equation is still in common use, researchers have demonstrated several problems with this equation. First, there are a number of inconsistencies in the data set used to derive the Wilson equation, some of which were caused by non-uniform pressure dependence.<sup>4,11,12</sup> Second, the Wilson equation has an overall bias on the order of  $0.5\text{ m/s}$ <sup>4,11</sup> and a pressure-dependent bias on the order of  $0.6\text{ m/s}$ .<sup>10,12</sup> For these reasons APL-UW does not recommend the Wilson equation, although for many applications the errors are inconsequential.



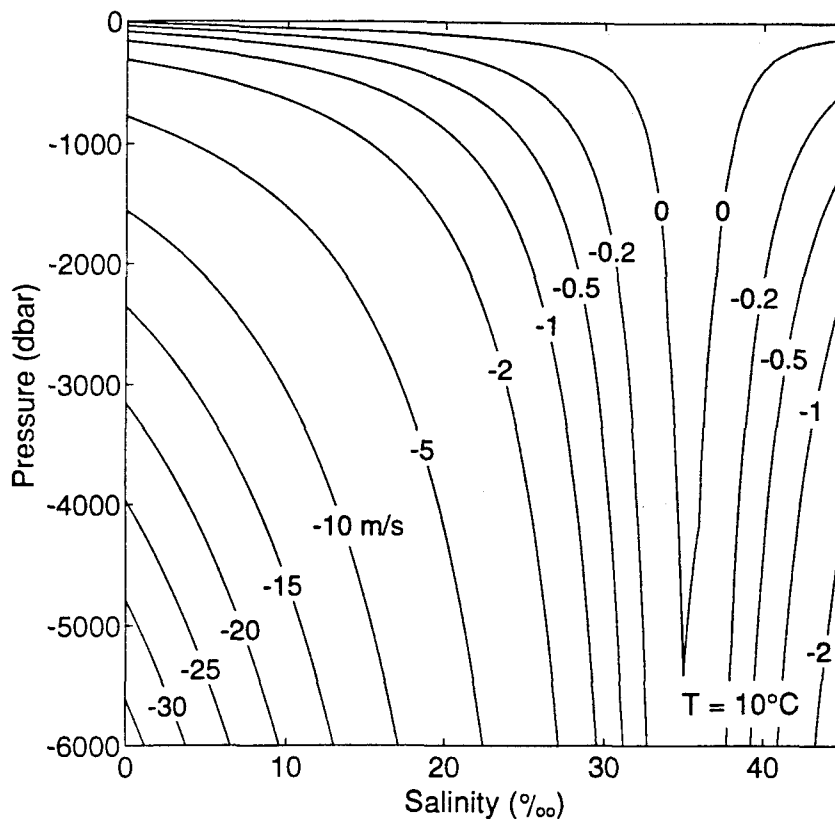


Figure 2. The difference between the Chen-Millero-Li equation and the Del Grosso equation for 10°C temperature. Del Grosso's equation is not valid for low-salinity seawater under pressure. An accurate interpretation of this figure requires consideration of (T,S,P) values that actually occur in oceans (see Ref. 2). Sound speed has not been accurately measured above a salinity of about 40‰. Contour units are meters/second. Modified from Ref. 12.

## B. ABSORPTION COEFFICIENT

The sound absorption coefficient,  $\alpha$ , is computed using the Francois-Garrison equation<sup>15</sup> shown in Figure 3, in which the absorption coefficient is computed as the sum of three contributions: boric acid, magnesium sulfate, and pure water. The absorption encountered in a particular area may vary by  $\pm 10\%$  from the given equation, and such bounds should be used when evaluating acoustic system performance.

The form of the Francois-Garrison equation uses relaxation theory and has been verified by laboratory measurements (e.g., Ref. 16). The constants for the equation, however,

## TOTAL SOUND ABSORPTION IN SEAWATER

$$\text{Total Absorption} = \text{Boric Acid Contrib.} + \text{MgSO}_4 \text{ Contrib.} + \text{Pure Water Contrib.}$$

$$\alpha = \frac{A_1 P_1 f_1^2}{f^2 + f_1^2} + \frac{A_2 P_2 f_2^2}{f^2 + f_2^2} + A_3 P_3 f^2 \quad \text{dB km}^{-1}$$

for frequency  $f$  in kilohertz.

## Boric Acid Contribution

$$A_1 = \frac{8.86}{c} \times 10^{(0.78 \text{ pH} - 5)} \quad \text{dB km}^{-1} \text{ kHz}^{-1}$$

$$P_1 = 1$$

$$f_1 = 2.8 (S/35)^{0.5} 10^{(4 - 1245/\theta)} \quad \text{kHz},$$

where  $c$  is the sound speed (m/s), given approximately by

$$c = 1412 + 3.21 T + 1.19 S + 0.0167 D,$$

$T$  is the temperature ( $^{\circ}\text{C}$ ),  $\theta = 273 + T$ ,  $S$  is the salinity (‰), and  $D$  is the depth (m).

 MgSO<sub>4</sub> Contribution

$$A_2 = 21.44 \frac{S}{c} (1 + 0.025 T) \quad \text{dB km}^{-1} \text{ kHz}^{-1}$$

$$P_2 = 1 - 1.37 \times 10^{-4} D + 6.2 \times 10^{-9} D^2$$

$$f_2 = \frac{8.17 \times 10^{(8 - 1990/\theta)}}{1 + 0.0018 (S - 35)} \quad \text{kHz}$$

## Pure Water Contribution

For  $T \leq 20^{\circ}\text{C}$ ,

$$A_3 = 4.937 \times 10^{-4} - 2.59 \times 10^{-5} T + 9.11 \times 10^{-7} T^2 - 1.50 \times 10^{-8} T^3 \quad \text{dB km}^{-1} \text{ kHz}^{-2}.$$

For  $T > 20^{\circ}\text{C}$ ,

$$A_3 = 3.964 \times 10^{-4} - 1.146 \times 10^{-5} T + 1.45 \times 10^{-7} T^2 - 6.5 \times 10^{-10} T^3 \quad \text{dB km}^{-1} \text{ kHz}^{-2}.$$

$$P_3 = 1 - 3.83 \times 10^{-5} D + 4.9 \times 10^{-10} D^2.$$

Figure 3. Francois-Garrison equation for sound absorption in seawater.<sup>15</sup>

were selected to fit numerous and widely distributed oceanic measurements made by APL-UW and others.

The boric acid contribution to the equation was determined from reported measurements in several oceans with salinities of 34–41‰, temperatures of  $-2^{\circ}$  to  $22^{\circ}\text{C}$ , and depths to 1500 m. The contribution may not be accurate below 200 Hz because of scattering and bottom leakage losses. Above 20 kHz the boric acid contribution becomes insignificant.

The magnesium sulfate contribution was determined from field measurements for salinities of 30–35‰, temperatures of 2 to  $22^{\circ}\text{C}$ , and depths to 3500 m. The contribution has been verified for frequencies up to 600 kHz.

The pure water contribution produces over 90% of the total absorption at frequencies above 600 kHz. It was determined from laboratory measurements at temperatures from  $0$ – $30^{\circ}\text{C}$  and for pressures equivalent to depths to 10,000 m.

Table 2 provides absorption coefficient values (from Figure 3) for temperatures and salinities most often encountered, for zero depth, and for a typical near-surface ocean pH of 8. For depths less than 100 m, the table can be used with negligible error. For waters with extreme pH values (i.e.,  $<7.7$  or  $>8.2$ ), using the table will produce appreciable discrepancies below 10 kHz and discrepancies as high as 40% below 1 kHz. (See Refs. 17 and 18 for the variation of pH with depth and geographic location.) Figure 4 gives guidelines for ocean pH values estimated at the depth of the SOFAR channel axis. Lovett<sup>17</sup> took pH values from atlases edited by Gorshkov,<sup>18</sup> corrected for pressure, interpolated to the SOFAR axis depth, and displayed contours of the boric acid absorption term ( $A$ ), using

$$A = 0.0237 \times 10^{(0.83\text{pH} - 6.0)} \quad (1)$$

Here we have used Eq. 1 to back out the pressure-corrected pH values for the contours originally shown by Lovett.

The temperature dependence is illustrated in Figure 5 for several frequencies and for typical ocean conditions ( $S = 35\text{‰}$ ,  $D = 100$  m). For other conditions, Table 2 or the equations in Figure 3 should be used.

Table 2. Absorption in seawater according to the Francois-Garrison equation (dB/km).<sup>15</sup> The upper value for each frequency is for  $S = 30\text{‰}$  and the lower for  $S = 35\text{‰}$ . Depth = 0 and pH = 8.

Freq. (kHz)	Temperature (°C)															
	-1.8	1.5	-1	0	2	4	6	8	10	12	14	16	18	20	25	30
0.4	0.021	0.021	0.020	0.020	0.019	0.018	0.017	0.016	0.015	0.014	0.013	0.013	0.012	0.011	0.010	0.008
0.4	0.020	0.020	0.020	0.019	0.018	0.017	0.016	0.015	0.015	0.014	0.013	0.012	0.011	0.011	0.009	0.008
0.6	0.036	0.036	0.036	0.035	0.034	0.033	0.032	0.031	0.030	0.028	0.027	0.026	0.025	0.023	0.020	0.018
0.6	0.036	0.036	0.036	0.035	0.034	0.033	0.032	0.030	0.029	0.028	0.026	0.025	0.024	0.022	0.019	0.017
0.8	0.050	0.050	0.049	0.049	0.049	0.048	0.047	0.046	0.045	0.044	0.042	0.041	0.039	0.038	0.033	0.030
0.8	0.051	0.051	0.051	0.051	0.050	0.049	0.048	0.046	0.045	0.043	0.042	0.040	0.038	0.036	0.032	0.028
1	0.061	0.061	0.061	0.061	0.061	0.061	0.061	0.060	0.059	0.058	0.057	0.056	0.054	0.052	0.048	0.043
1	0.064	0.064	0.064	0.064	0.064	0.063	0.062	0.061	0.060	0.059	0.057	0.055	0.054	0.052	0.047	0.042
2	0.111	0.111	0.111	0.111	0.112	0.112	0.113	0.114	0.114	0.115	0.116	0.117	0.117	0.117	0.116	0.113
2	0.122	0.122	0.122	0.122	0.122	0.122	0.122	0.122	0.123	0.123	0.123	0.123	0.123	0.122	0.119	0.115
4	0.256	0.254	0.252	0.248	0.240	0.233	0.227	0.223	0.219	0.216	0.214	0.212	0.212	0.211	0.213	0.215
4	0.291	0.290	0.287	0.282	0.272	0.264	0.256	0.250	0.245	0.241	0.237	0.235	0.233	0.232	0.231	0.231
6	0.485	0.481	0.475	0.463	0.440	0.420	0.401	0.384	0.369	0.356	0.345	0.335	0.327	0.321	0.309	0.304
6	0.558	0.553	0.546	0.532	0.505	0.481	0.459	0.438	0.420	0.405	0.391	0.379	0.368	0.360	0.344	0.335
8	0.794	0.788	0.777	0.755	0.714	0.675	0.638	0.605	0.575	0.547	0.522	0.500	0.481	0.464	0.430	0.409
8	0.918	0.910	0.897	0.872	0.824	0.778	0.735	0.696	0.660	0.627	0.597	0.571	0.547	0.526	0.485	0.457
10	1.18	1.17	1.15	1.12	1.06	0.995	0.938	0.884	0.835	0.789	0.747	0.709	0.675	0.644	0.581	0.536
10	1.36	1.35	1.33	1.29	1.22	1.15	1.08	1.02	0.963	0.909	0.859	0.815	0.774	0.737	0.661	0.606
12	1.62	1.61	1.59	1.55	1.46	1.38	1.30	1.22	1.15	1.08	1.02	0.962	0.910	0.863	0.764	0.689
12	1.88	1.86	1.84	1.79	1.69	1.59	1.50	1.41	1.33	1.25	1.18	1.11	1.05	0.992	0.874	0.784
14	2.12	2.10	2.08	2.03	1.92	1.82	1.71	1.61	1.51	1.42	1.34	1.26	1.19	1.12	0.978	0.867
14	2.45	2.43	2.41	2.35	2.23	2.10	1.98	1.86	1.75	1.65	1.55	1.45	1.37	1.29	1.12	0.992
16	2.65	2.64	2.61	2.55	2.43	2.30	2.17	2.05	1.93	1.81	1.70	1.60	1.50	1.41	1.22	1.07
16	3.07	3.05	3.02	2.96	2.82	2.67	2.52	2.37	2.23	2.10	1.97	1.85	1.74	1.63	1.41	1.23
18	3.22	3.20	3.18	3.12	2.98	2.84	2.69	2.53	2.39	2.24	2.11	1.98	1.86	1.74	1.50	1.30
18	3.73	3.71	3.68	3.61	3.46	3.29	3.11	2.94	2.77	2.60	2.44	2.29	2.15	2.02	1.73	1.50
20	3.81	3.79	3.76	3.70	3.57	3.41	3.24	3.06	2.89	2.72	2.55	2.40	2.25	2.11	1.81	1.56
20	4.40	4.39	4.36	4.29	4.13	3.95	3.75	3.55	3.35	3.15	2.96	2.78	2.61	2.44	2.09	1.80
22	4.41	4.39	4.37	4.31	4.18	4.01	3.83	3.62	3.43	3.23	3.04	2.85	2.68	2.57	2.15	1.84
22	5.09	5.09	5.06	5.00	4.83	4.65	4.43	4.21	3.98	3.75	3.53	3.31	3.11	2.91	2.48	2.13
24	5.00	5.00	4.98	4.93	4.80	4.64	4.45	4.22	4.01	3.78	3.56	3.35	3.14	2.94	2.51	2.15
24	5.79	5.78	5.76	5.70	5.56	5.37	5.14	4.91	4.65	4.39	4.13	3.88	3.65	3.41	2.91	2.49
26	5.61	5.60	5.59	5.56	5.45	5.28	5.09	4.86	4.61	4.37	4.12	3.87	3.64	3.42	2.91	2.49
26	6.47	6.47	6.46	6.42	6.29	6.12	5.89	5.64	5.36	5.07	4.79	4.51	4.23	3.97	3.38	2.88

Table 2, cont.

Freq. (kHz)	Temperature (°C)															
	-1.8	1.5	-1	0	2	4	6	8	10	12	14	16	18	20	25	30
28	6.19	6.20	6.20	6.19	6.09	5.94	5.75	5.51	5.25	4.98	4.71	4.43	4.18	3.92	3.34	2.85
28	7.15	7.15	7.15	7.13	7.04	6.89	6.66	6.40	6.10	5.78	5.47	5.16	4.85	4.55	3.87	3.30
30	6.78	6.79	6.80	6.81	6.75	6.62	6.43	6.19	5.92	5.63	5.33	5.03	4.74	4.45	3.80	3.24
30	7.81	7.82	7.84	7.85	7.80	7.66	7.45	7.18	6.87	6.53	6.19	5.84	5.50	5.17	4.40	3.75
40	9.45	9.50	9.59	9.74	9.94	10.0	9.95	9.78	9.52	9.19	8.81	8.40	7.97	7.53	6.48	5.53
40	10.8	10.9	11.0	11.2	11.4	11.5	11.5	11.3	11.0	10.7	10.2	9.75	9.25	8.75	7.52	6.42
50	11.7	11.8	12.0	12.3	12.8	13.2	13.4	13.4	13.3	13.1	12.7	12.3	11.8	11.2	9.77	8.39
50	13.3	13.4	13.6	14.0	14.7	15.1	15.4	15.5	15.4	15.1	14.7	14.2	13.6	13.0	11.3	9.74
60	13.6	13.7	13.9	14.4	15.3	16.0	16.5	16.9	17.1	17.0	16.8	16.4	15.9	15.3	13.6	11.8
60	15.4	15.6	15.8	16.4	17.4	18.3	19.0	19.5	19.7	19.6	19.4	19.0	18.4	17.7	15.7	13.7
70	15.2	15.4	15.7	16.3	17.4	18.5	19.4	20.1	20.6	20.8	20.8	20.6	20.2	19.6	17.7	15.6
70	17.2	17.4	17.7	18.4	19.8	21.1	22.2	23.1	23.7	24.0	24.0	23.8	23.4	22.7	20.6	18.1
80	16.7	16.9	17.3	17.9	19.3	20.6	21.9	23.0	23.8	24.4	24.7	24.8	24.5	24.1	22.2	19.8
80	18.8	19.0	19.4	20.2	21.9	23.5	25.0	26.3	27.3	28.1	28.5	28.6	28.4	27.9	25.8	23.0
90	18.2	18.4	18.7	19.5	21.0	22.6	24.1	25.5	26.8	27.7	28.4	28.8	28.8	28.6	26.9	24.3
90	20.3	20.6	21.0	21.9	23.7	25.6	27.4	29.2	30.6	31.8	32.7	33.2	33.3	33.0	31.2	28.2
100	19.6	19.8	20.2	21.0	22.6	24.4	26.1	27.9	29.4	30.8	31.9	32.6	33.0	33.0	31.7	29.1
100	21.8	22.1	22.5	23.4	25.4	27.5	29.7	31.7	33.6	35.3	36.6	37.5	38.0	38.1	36.7	33.7
120	22.6	22.8	23.1	23.9	25.7	27.6	29.8	32.0	34.2	36.2	38.0	39.6	40.7	41.4	41.3	39.1
120	24.8	25.1	25.5	26.5	28.6	31.0	33.6	36.2	38.8	41.3	43.5	45.3	46.7	47.6	47.7	45.2
140	25.8	25.9	26.3	27.0	28.7	30.8	33.1	35.6	38.2	40.9	43.4	45.6	47.6	49.1	50.7	49.4
140	28.1	28.3	28.7	29.6	31.8	34.3	37.1	40.1	43.2	46.4	49.4	52.1	54.5	56.3	58.4	57.1
160	29.3	29.4	29.7	30.3	31.9	33.9	36.3	39.0	41.9	45.0	48.1	51.0	53.7	56.0	59.6	59.7
160	31.6	31.8	32.2	33.0	35.0	37.5	40.4	43.7	47.2	50.9	54.5	58.0	61.3	64.0	68.5	68.8
180	33.1	33.2	33.4	33.9	35.3	37.2	39.5	42.3	45.4	48.8	52.3	55.8	59.2	62.2	67.9	69.7
180	35.5	35.6	35.9	36.6	38.4	40.8	43.7	47.1	50.9	54.9	59.1	63.3	67.3	70.9	77.8	80.2
200	37.4	37.4	37.5	37.8	38.9	40.6	42.9	45.6	48.8	52.4	56.3	60.2	64.1	67.8	75.5	79.3
200	39.8	39.9	40.1	40.6	42.1	44.3	47.2	50.6	54.4	58.7	63.3	68.0	72.7	77.1	86.4	91.1
250	49.8	49.7	49.5	49.2	49.4	50.3	52.0	54.5	57.6	61.3	65.6	70.2	75.1	80.1	92.1	101
250	52.2	52.1	52.0	52.0	52.6	54.1	56.4	59.6	63.4	68.0	73.1	78.7	84.5	90.4	105	116
300	64.9	64.5	63.9	63.0	61.8	61.7	62.6	64.4	76.2	70.7	75.0	79.8	85.2	90.9	106	120
300	67.3	67.0	66.5	65.8	65.1	65.6	67.1	69.6	73.1	77.5	82.7	88.6	95.1	102	120	137

Table 2, cont.

Freq. (kHz)	Temperature (°C)															
	-1.8	1.5	-1	0	2	4	6	8	10	12	14	16	18	20	25	30
350	82.6	81.9	80.9	79.1	76.5	75.1	74.9	75.9	77.9	81.0	85.0	89.8	95.3	101	119	136
350	85.0	84.4	83.5	81.9	79.8	79.0	79.4	81.1	84.0	87.9	92.9	98.8	105	113	133	154
400	103	102	100	97.7	93.3	90.4	88.9	88.8	90.0	92.4	95.9	100	106	112	130	151
400	105	105	103	100	96.6	94.3	93.4	94.1	96.1	99.4	104	110	116	124	146	170
450	126	125	123	119	112	108	105	103	104	105	108	112	117	123	142	164
450	129	127	125	122	116	112	109	109	110	112	116	121	128	135	158	185
500	152	150	147	142	133	127	122	119	118	119	121	124	129	135	154	177
500	154	153	150	145	137	131	127	125	125	126	129	134	140	147	170	198
600	212	209	205	197	183	171	163	157	153	151	151	153	156	160	178	203
600	214	212	207	199	186	175	167	162	159	158	160	162	167	173	195	225
700	282	279	272	261	240	224	211	201	194	189	187	186	187	190	205	229
700	285	281	275	264	244	228	215	206	200	196	195	196	198	203	222	252
800	364	359	350	335	307	284	266	251	240	232	227	224	223	224	235	257
800	366	361	353	338	311	288	271	257	247	240	235	234	234	236	252	280
900	456	450	439	419	383	353	329	309	293	281	273	267	263	262	269	288
900	459	452	442	422	386	357	333	314	299	289	281	277	275	274	286	311
1000	560	551	538	513	468	430	398	373	352	336	324	315	308	304	306	321
1000	562	554	540	515	471	434	403	378	359	344	332	325	319	316	323	344

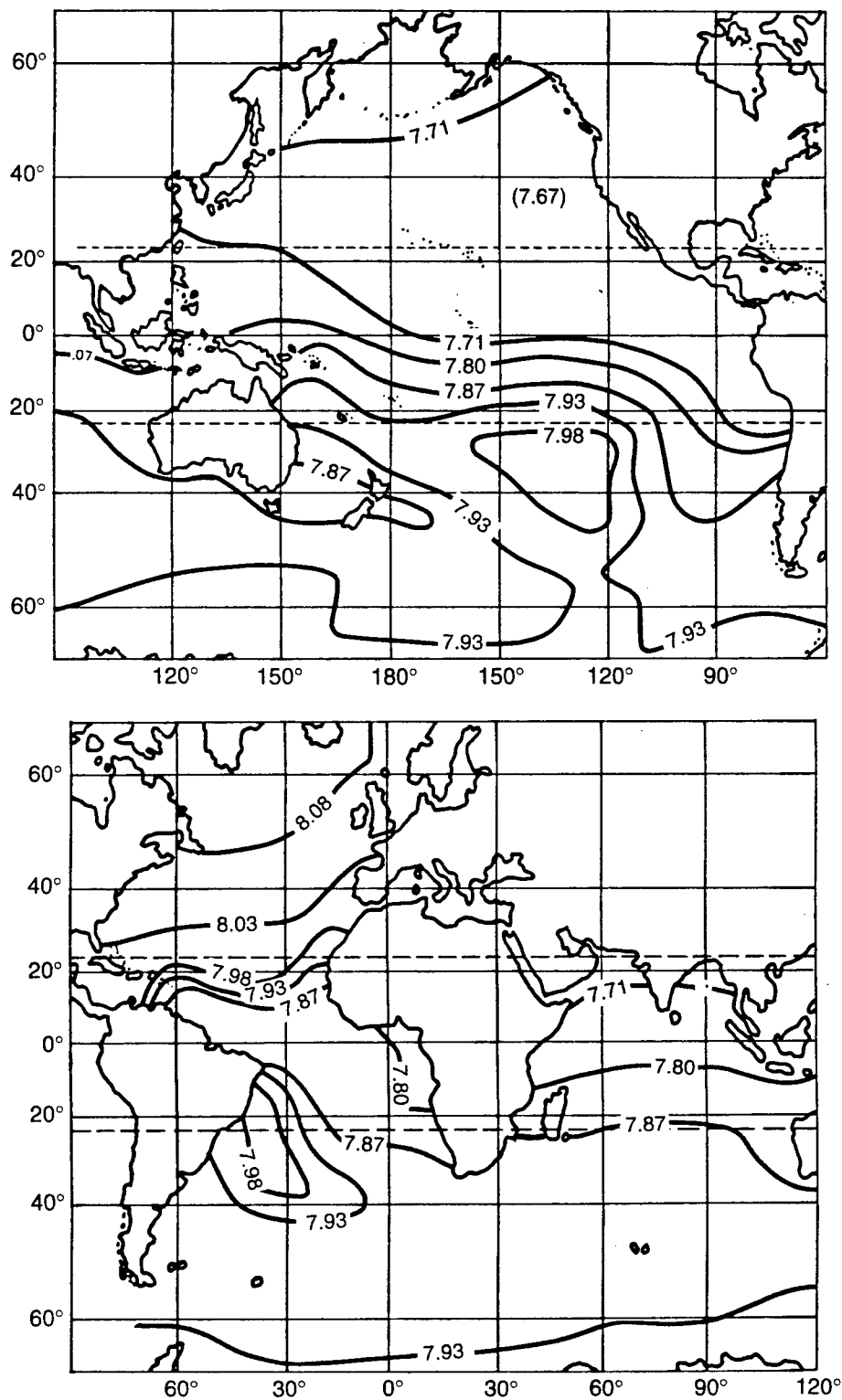


Figure 4. Geographic variation in pH (using contours given by Lovett<sup>17</sup>).

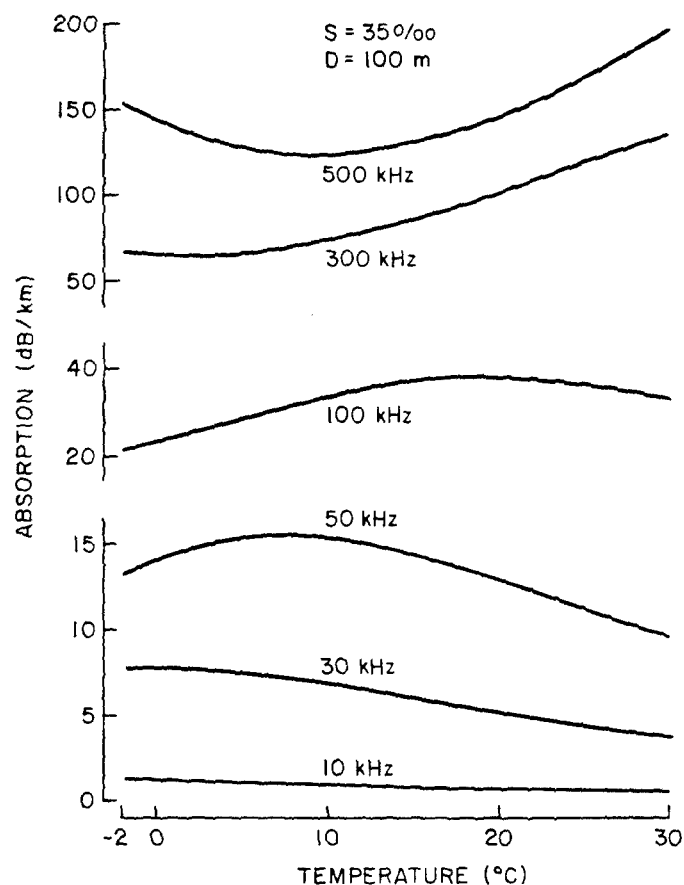


Figure 5. Temperature dependence of the logarithmic absorption coefficient  $\alpha$ .

## C. BACKSCATTERING

### 1. Introduction

The energy backscattered from the ocean volume is determined primarily by the marine biota in the water column, although important contributions may also be made by temperature inhomogeneities, bubbles, and particulate matter. In the frequency range defined as "high" (10–60 kHz), the backscatter through the water column is dominated by smaller fish, both with and without resonant gas-filled swim bladders, and dense aggregations of zooplankton. Volume backscatter is highly variable throughout the ocean, and there are significant changes both in backscatter intensity and in depth distribution with changes in geographical location, depth, season, frequency, and time of day. Prediction of these



changes is complicated by environmental factors that play a major role in the spatial distribution and migration of fish and zooplankton; these factors include nutrient availability, light level, temperature distribution, and bottom topography. All these factors create conditions that attract biota to an area, but also influence the role predation will play in controlling the abundance and distribution of fish.

Because of the extensive dimensions of the ocean and our limited facilities to sample it, our ability to predict volume backscatter in a particular region is limited, and all predictions have a high variance associated with them. An extensive database and the acoustic survey data supporting it (termed a databank) have been compiled by the U.S. Naval Oceanographic Office (NAVOCEANO) as part of the Oceanographic and Atmospheric Master Library (OAML). The database covers a frequency range of 2–50 kHz, four seasons, and day and night conditions for most of the northern hemisphere, including the Arctic. The data that support this database are based on extensive surveys at frequencies between 25 and 50 kHz in many important areas; these surveys were conducted by both NAVOCEANO and marine research institutes of various nations. Because acoustic backscatter is highly variable over space and time, operational measurements are always preferred. In their absence, we recommend that, where available, the volume scattering data in the databank be used for volume scattering predictions.

In the absence of data from a particular area of interest, we recommend using the OAML database with the following caveat. Except for areas where there are data to support the OAML volume scattering database, the predictions offered are uncertain. This is particularly true in shallow areas near continental shelves, especially areas of high upwelling or of major fishing activity. As an alternative in these areas, we suggest the following regional abstractions, based in part on a review of worldwide mesopelagic fish abundance,<sup>19</sup> mesopelagics being the main volume backscatterers in deep ocean areas, and in part on a review of worldwide fisheries catch and fish stock abundance data,<sup>20</sup> primarily for shallow coastal areas.

Significant advances are currently being made in explicitly linking fish and zooplankton spatial distributions, both horizontally and vertically, to environmental factors that can

be measured more regularly and synoptically than the backscatter itself. However, it is premature to include this information in this report because the regional extent of this work is so limited.

Japanese researchers<sup>21,22</sup> have successfully correlated pelagic fish production to sea surface temperature in the North Central Pacific Ocean. Swartzman et al.<sup>23</sup> found that the horizontal distribution of Alaska pollock in the Bering Sea during summer was strongly influenced by bottom depths and ocean fronts along the continental shelf break, while vertical distribution also depended on the thermocline depth. Marchal et al.<sup>24</sup> found that the depth of the scattering layer off the coast of West Africa at night was directly proportional to the thermocline depth, with mesopelagics that migrated to the surface staying above the thermocline. These studies suggest the eventual successful use of satellite and other remotely sensed environmental data as a supplement to acoustic surveys for predicting acoustic volume scattering.

## **2. Deep Open Ocean**

Table 3 summarizes the volume backscattering in various regions of the Atlantic, Pacific, Indian, and Arctic oceans (see Figure 6 for map). For each region, Table 3 gives a column scattering strength (CSS) or its estimated range. In this document, CSS is defined as the decibel equivalent to the backscattering cross section per unit volume integrated through the water column, which itself is dimensionless. Also provided are commonly observed scattering layers and additional comments on volume backscatter in a region, where relevant. In open ocean areas and some coastal regions (e.g., the Arabian Sea), backscatter is dominated by mesopelagic fish in the Myctophidae and Gonostomatidae families. These fish tend to aggregate in dense layers, often deep in the water column. The mesopelagic aggregates in intertropical and tropical waters can be distinguished from those in temperate waters.<sup>25</sup> The first group consists of mostly active swimmers that undergo diel (day to night) vertical migration; the second group is more passive and does not undergo diel migration. The lack of diel migration of the deep scattering layer(s) in temperate waters has been observed frequently in acoustic surveys.<sup>26,27</sup>

Table 3. Volume backscatter regions of the world's oceans. Map ID numbers refer to regions of similar backscattering shown in Figure 6. Geographically split regions (e.g., 1a and 1b) are combined.

Map ID	Region	Column Scattering Strength (dB range)	Scattering Layers	Comments
1	North and South Atlantic (> 45°N and > 45°S)	(-43, -45) dB	0-100 m day and night	
2	Central and Equatorial Atlantic (< 45°N and < 45°S)	(-47, -50) dB	300-700 m day 0-100 m night	Lower backscatter nearer equator
3	Coastal North and South Atlantic	(-43, -47) dB	0-50 m	Higher dB range in upwelling and mixing areas, e.g., Namibian and N. African upwelling, George's bank
3'		(-37, -40) dB	0-100 m day and night	
4	West Mediterranean	(-40, -45) dB	0-50 m; 375-1000 m day 0-100 m; 400-500 m night	
5	East Mediterranean	-50 dB	as in W. Med.	Higher backscatter within 200 m isobath
6	Mid-Pacific Ocean	(-46, -50) dB	450-700 m day 0-50 m night	Higher backscatter nearer equator
7	North Pacific	(-44, -45) dB	200 or 400-600 m day. 0-50 m or 200 m and 800-1000 m night.	
8	Pacific temperate coastal	-45 dB	110-400 m day and night	
9	Pacific coastal upwelling	-38 dB	0-100 m; 400-700 m day and night	
10	Pacific southeast Asia rim	-44 dB	0-200 m night 500-800 m day and night	
11	Pacific subantarctic	(-44, -45) dB	400-600 m day and night	
12	Indian Ocean north rim	(-37, -40) dB	0-50 m night 100-200 m; 250-300 m day	World's highest mesopelagic fish production
13	Indian Ocean south rim	-44 dB	150-350 m day 0-100 m night	
14	Central Indian Ocean	-54 dB	150-350 m day 0-100 m night	

If the operating area is uncertain or a more generic input is desired, we suggest using a nighttime profile with a strong scattering layer from the surface to 300-m depth and a background level that is 13 dB less. For a daytime profile assume a deep scattering layer between 300 and 600 m and a background level that is 13 dB less. The volume scattering strength within the scattering layer can be assumed to depend on the level of production in the region. Suggested values (for 10–60 kHz) are:

Dense marine life (upwelling and mixing areas shown in Figure 7):

$$S_v = -66 \text{ dB re m}^{-1}$$

Intermediate marine life (most other temperate coastal areas):

$$S_v = -74 \text{ dB re m}^{-1}$$

Sparse marine life (nonupwelling and mixing tropic areas):

$$S_v = -81 \text{ dB re m}^{-1}.$$

An index of marine production, based on the Coastal Zone Color Scanner satellite images for primary production, is given in Figure 7.

From the information provided in Table 3, we can calculate other parameters of interest, including the volume scattering strength in the scattering layer (in decibels/meter) and the cumulative scattering strength through the scattering layer (in decibels). To do this, we must assume a relationship between the volume scattering strength of the scattering layer and the scattering strength of the background volume. In the computations below, we assume a background level 13 dB below the scattering layer level. Given the water column volume scattering strength, CSS, the scattering layer volume scattering strength,  $S_v$ , is given by

$$S_v = \text{CSS} - 10 \log \left[ 10^{-1.3} (D - d_v) + d_v \right], \quad (2)$$

where  $D$  is the water column depth in meters and  $d_v$  is the thickness of the scattering layer in meters. All logarithms are to the base 10. Similarly, CSS can be calculated from  $S_v$ .

## World Backscatter Regions (Deep Water)

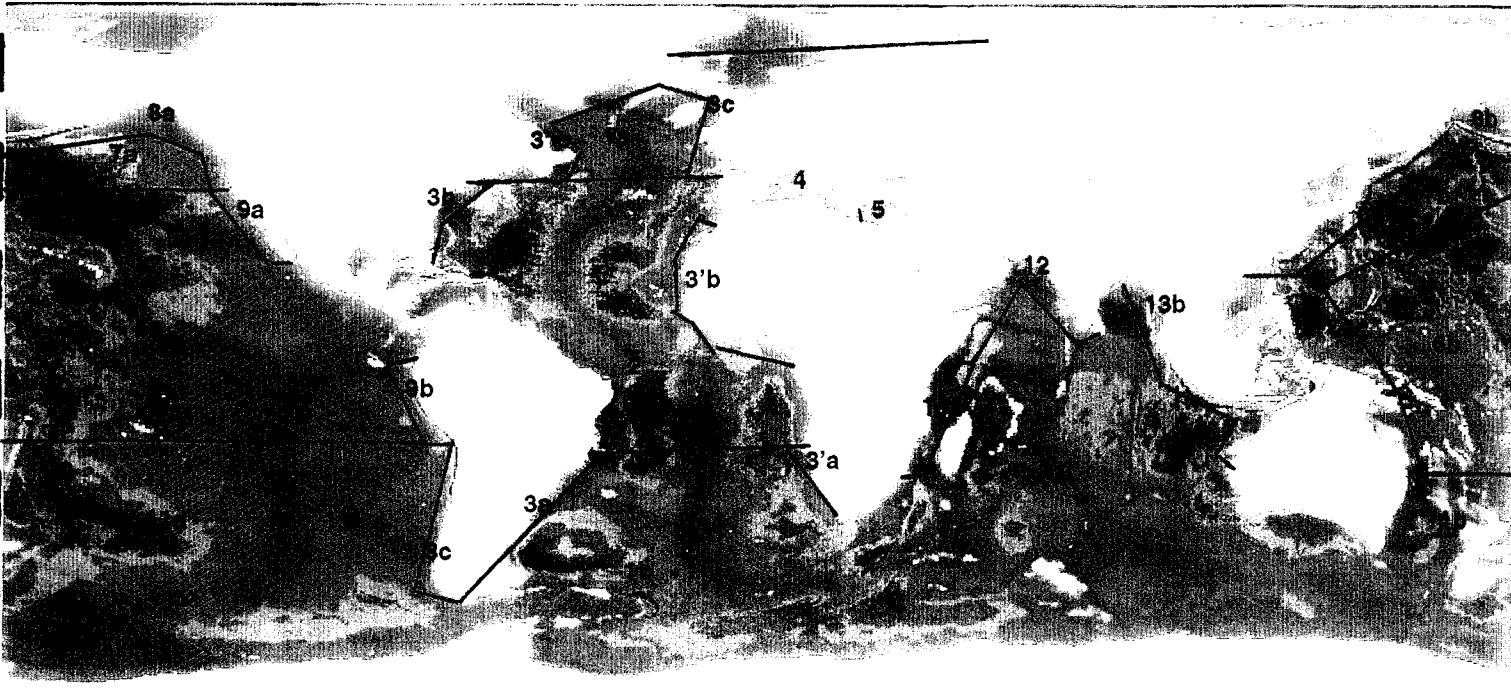


Figure 6. Deep-water backscattering regions in the Atlantic, Pacific, and Indian oceans. Numbered regions are defined in Table 3. Background map shows ocean bathymetry. Depth ranges from yellow (shallow) through green and blue to purple (very deep). When regions defined in Table 3 are not contiguous the separate parts are distinguished by a, b, or c.

### 3. Shallow Waters

Areas of high pelagic fish density exist along the continental shelves in many coastal regions, but the distribution of such areas is determined by the environment, depending frequently on wind-driven upwelling or other forms of nutrient mixing leading to high primary and secondary production. Fisheries exist in these coastal regions for many pelagic species, including sardine, anchovy, herring, pilchard, hake, menhaden, pollock, and cod. Volume backscattering in these regions can be high near the surface but is extremely variable owing to the schooling nature of these species. Also zooplankton abundance, especially euphausiids, may be high enough in highly productive shallow areas to significantly affect volume scattering.

### World Average Annual Primary Production

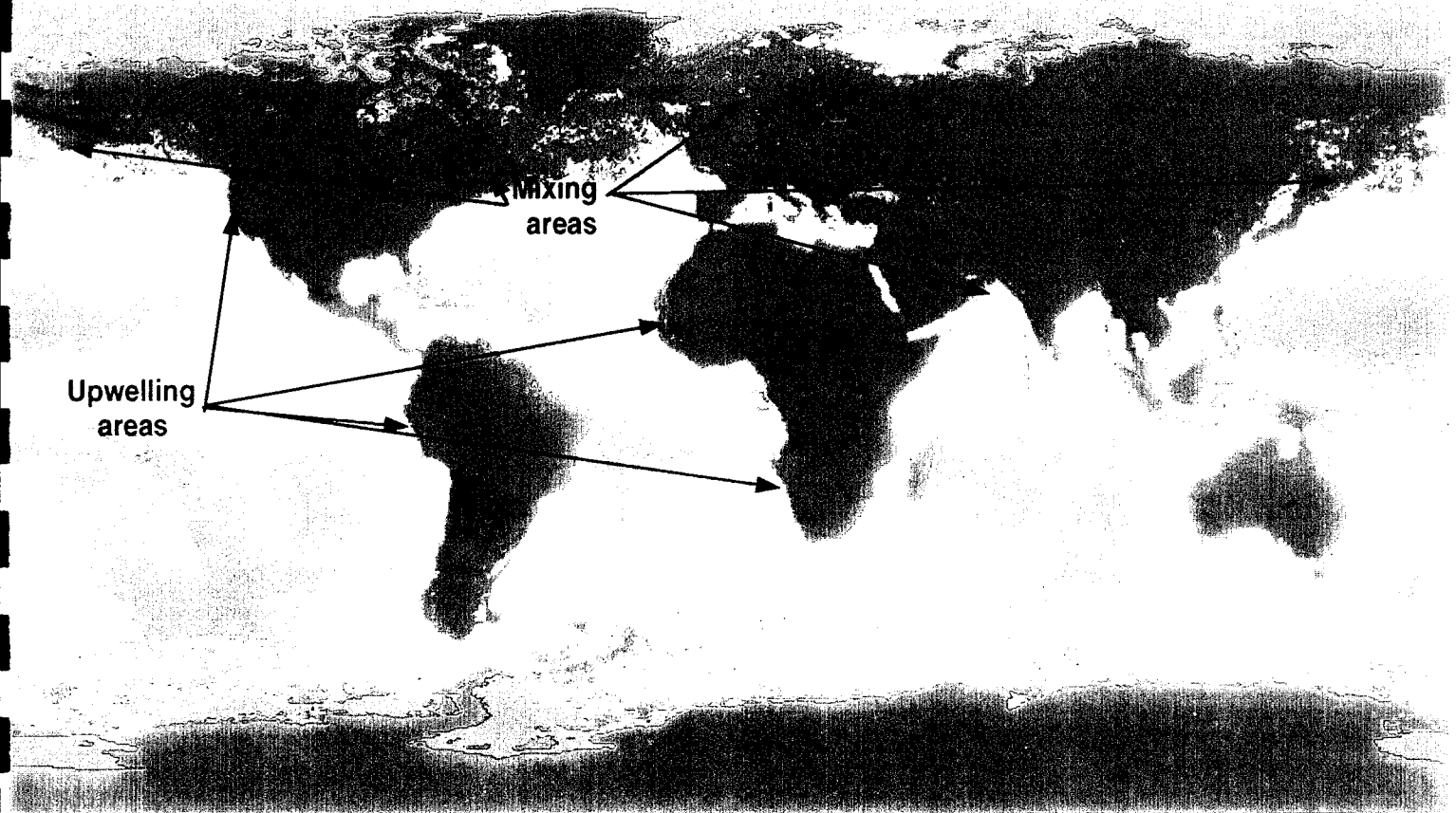


Figure 7. World annual average ocean primary productivity obtained from Coastal Zone Color Scanner satellite images. Major upwelling and front mixing areas are shown. Primary production ranges from orange (low) through yellow and green to blue (high).

In waters less than 200 m deep, volume scattering may be considered frequency independent (at frequencies between 10 and 60 kHz). Volume scattering, to a first approximation, can be assumed to be uniform in depth. The following rule of thumb can be applied:

Dense marine life (upwelling and mixing areas in Figure 7):

$$S_v = -62 \text{ dB re m}^{-1}$$

Intermediate marine life (most other temperate coastal areas):

$$S_v = -72 \text{ dB re m}^{-1}$$

Sparse marine life (nonupwelling and mixing tropics areas):

$$S_v = -85 \text{ dB re m}^{-1}.$$

As marine life becomes more dense, there is a tendency, especially during the spring in shallow temperate waters, to have a shallow scattering layer (0–20 m) composed largely of zooplankters, which will have a higher backscatter than given above for frequencies between 25 and 60 kHz.

#### 4. Ice-Covered Regions

The Arctic Ocean and adjacent waters are ice covered for most of the year. Measurements of volume scattering under the solid ice cap and in the marginal ice zone show nearly constant backscatter from 100–600 m.<sup>28,29</sup> Scattering at high frequencies (10–60 kHz) is more variable in the top 100 m, with no day to night variation. Frequency independence over the frequency range of interest is substantiated by available data. We suggest using an average level of  $-75 \text{ dB re m}^{-1}$ .

#### 5. Spectral Spreading

Volume-induced spectral spreading is determined by volume scatterers whose speed distribution in deep water is assumed to be Gaussian with a standard deviation of 0.13 m/s (0.25 knot). Data available in the literature have not been completely analyzed to substantiate this assumption, but it is reasonable for most conditions. Data taken on the shallow water Quinault acoustic test range,<sup>30</sup> however, show wider spectral widths because of scattering from bubbles and marine organisms near the surface that undergo orbital motion owing to large surface waves with long periods. Because these spectral widths are comparable to those for the surface backscatter, it is recommended that the spectral widths for volume scattering near the surface be calculated using the spectral widths appropriate for the surface backscatter (see Eq. 18 in Section II, this report) modified by a depth dependence equal to  $e^{-\kappa z}$ , where  $\kappa$  is the wave number corresponding to the peak of the surface-wave spectrum, and  $z$  is the depth. In particular, the equation for the half-power spectral width is

$$\Delta f_{3\text{dB}} = \begin{cases} 2.35 \left( \frac{0.13}{1.5} \right) f & U < 1 \text{ m/s} \\ \left\{ \left( \eta \cdot f \cdot e^{-Kz} \right)^5 + \left[ 2.35 \left( \frac{0.13}{1.5} \right) f \right]^5 \right\}^{1/5} & U \geq 1 \text{ m/s}, \end{cases} \quad (3)$$

where  $K = (0.88)^2 g U^{-2}$ ,  $\eta = \text{Eq. 20 of Section II}$ ,  $g$  is the gravitational constant ( $\text{m/s}^2$ ),  $U$  is the wind speed ( $\text{m/s}$ ),  $f$  is the frequency ( $\text{kHz}$ ), and  $z$  is depth below the surface ( $\text{m}$ ). Figure 8 shows results from Eq. 3 for  $f = 25 \text{ kHz}$ ,  $\phi$  (Eq. 23 of Section II)  $= 0$ , and several wind speeds.

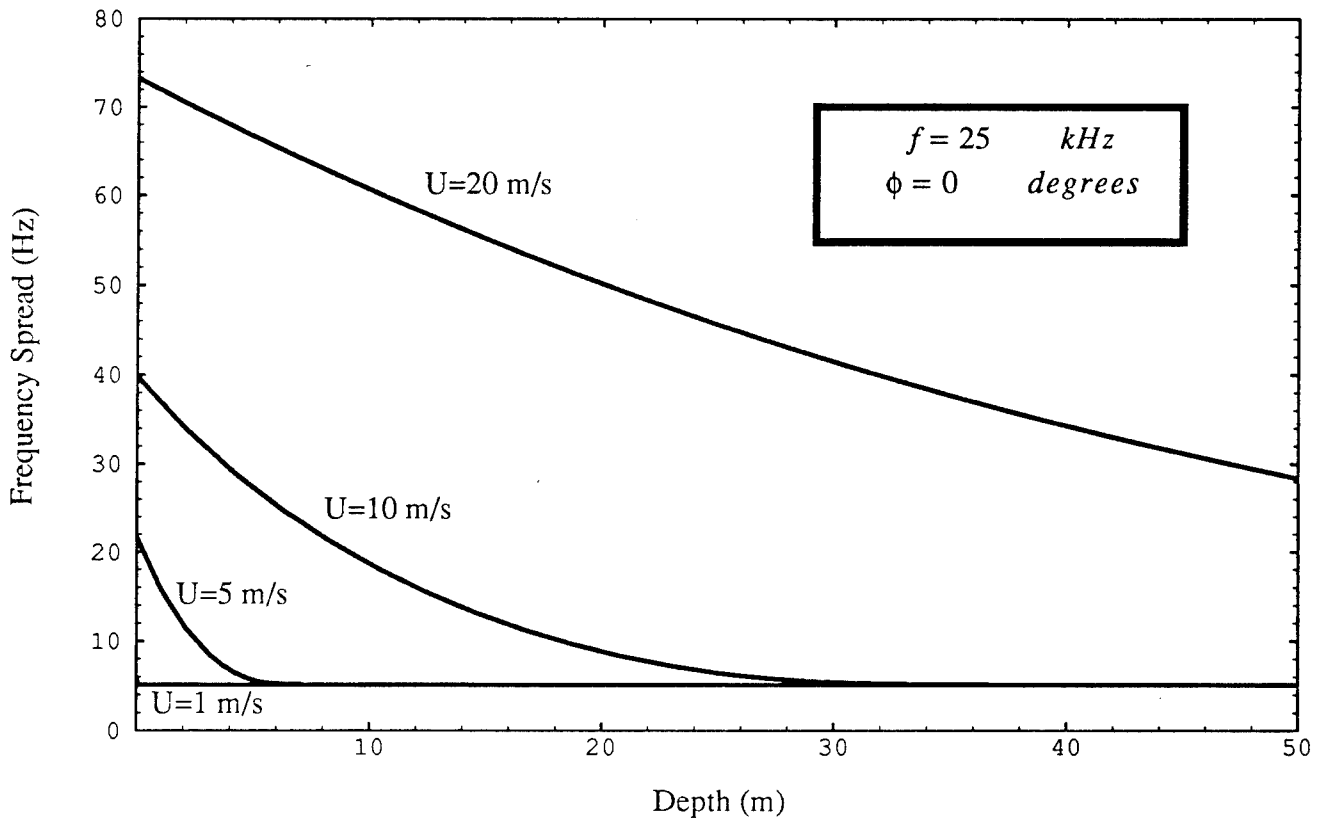


Figure 8. The half-power spectral width from Eq. 3 plotted for several wind speeds.



## REFERENCES — Section I

1. W. D. Wilson, "Equation for the speed of sound in seawater," *J. Acoust. Soc. Am.*, 32, 1357, (1960).
2. C. C. Leroy, "Development of simple equations for accurate and more realistic calculation of the speed of sound in seawater," *J. Acoust. Soc. Am.*, 46, 216–226, (1969).
3. H. W. Frye and J. D. Pugh, "New equation for the speed of sound in seawater," *J. Acoust. Soc. Am.*, 50, 384–386, (1971).
4. E. R. Anderson, "Sound speed in seawater as a function of realistic temperature - salinity - pressure domains," Ocean Science Department, Naval Undersea Research Development Center, NAVUSEARANDCENTP 243, 1971.
5. V. A. Del Grosso, "New equation for the speed of sound in natural waters (with comparisons to other equations)," *J. Acoust. Soc. Am.*, 56, 1084–1091, (1974).
6. C. Chen and F. J. Millero, "Speed of sound in seawater at high pressures," *J. Acoust. Soc. Am.*, 62, 1129–1135, (1977).
7. K. V. Mackenzie, "Discussion of sea water sound-speed determinations," *J. Acoust. Soc. Am.*, 70, 801–806, (1981).
8. J. L. Spiesberger and K. Metzger, "A new algorithm for sound speed in seawater," *J. Acoust. Soc. Am.*, 89, 2677–2688, (1991).
9. J. L. Spiesberger, "Is Del Grosso's sound-speed algorithm correct?" *J. Acoust. Soc. Am.*, 93, 2235–2237, (1993).
10. F. J. Millero and X. Li, "Comments on 'On equations for the speed of sound in seawater' [*J. Acoust. Soc. Am.* 93, 255–275 (1993)]," *J. Acoust. Soc. Am.*, 95, 2757–2759, (1994).
11. C. Chen and F. J. Millero, "Re-evaluation of Wilson's soundspeed measurements in pure water," *J. Acoust. Soc. Am.*, 60, 1270–1273, (1976).
12. B. D. Dushaw, P. F. Worcester, B. D. Cornuelle, and B. M. Howe, "On equations for the speed of sound in seawater," *J. Acoust. Soc. Am.*, 93, 255–275, (1993).
13. W. D. Wilson, "Speed of sound in seawater as a function of temperature, pressure, and salinity," *J. Acoust. Soc. Am.*, 32, 641–644, (1960).

14. V. A. Del Grosso, and C. W. Mader, "Speed of sound in sea water samples," *J. Acoust. Soc. Am.*, 52, 961-974, (1972).
15. R.E. Francois and G.R. Garrison, "Sound absorption based on ocean measurements. Part I: Pure water and magnesium sulfate contributions; Part II: Boric acid contribution and equation for total absorption," *J. Acoust. Soc. Am.*, 72, 896-907 and 1879-1890 (1982).
16. F.H. Fisher and V.P. Simmons, "Sound absorption in sea water," *J. Acoust. Soc. Am.*, 62, 558-56 (1977).
17. J.R. Lovett, "Geographic variation of low-frequency sound absorption in the Atlantic, Indian, and Pacific oceans," *J. Acoust. Soc. Am.* 67, 338-340 (1980).
18. S.G. Gorshkov (Ed.), *World Ocean Atlas, Atlantic and Indian Oceans*, Vol. 2, 234-235, and *World Ocean Atlas, Pacific Ocean*, Vol. 1, 234-235 (Pergamon, 1974).
19. J. Gjøsæter and K. Kawaguchi, "A review of the world resources of mesopelagic fish," FAO Fisheries Technical Paper #193, FAO, Rome, Italy, 1980, 151 pp.
20. FAO Yearbook Fishery Statistics: Catches and Landings, 7, Food and Agricultural Organization, Rome, Italy, 1992.
21. H. Tameishi and I. Yamanaka, "Application of NOAA AVHRR data for fisheries service," Japan Fisheries Information Service Center Technical Bulletin, 1990, 29 pp.
22. I. Yamanaka, S. Ito, K. Niwa, R. Tanabe, Y. Yabuta and S. Chikunu, "The fisheries forecasting system in Japan for coastal pelagic fish," FAO Fisheries Technical Paper 301, FAO, Rome, 1988, 72 pp.
23. G.L. Swartzman, W. Stuetzle, K. Kulman, and M. Powojowski, "Relating the distribution of pollock schools in the Bering Sea to environmental factors," *ICES J. Mar. Sci.*, 51, 481-492, (1994).
24. E. Marchal, F. Gerlotto, and B. Stequert, "On the relationship between scattering layer, thermal structure and tuna abundance in the Eastern Atlantic equatorial current system," *Oceanol. Acta*, 16(3), 261-272, (1993).
25. E.G. Barham, "Deep-sea fishes: Lethargy and vertical orientation," In *Proceedings of an International Symposium on Biological Sound-Scattering in the Ocean*, G.B. Farquhar, Rep. MC-005, Maury Center for Ocean Science, Washington, D.C., pp. 100-118, 1971.

26. G.L. Swartzman, R.T. Miyamoto, and J.S. Wigton, APP Volume Scattering Strength (VSS) Inputs for the Mediterranean Sea, Sargasso Sea, U.S. Pacific Coast, and Bering Sea (U), APL-UW TR 9020, September 1991. (Confidential)
27. G.L. Swartzman, R.T. Miyamoto, J.S. Wigton, and R.K. Kerr. APP Volume Scattering Strength (VSS) Inputs for the Gulf of Alaska, Barents Sea, Norwegian Sea, and North Sea, APL-UW TR 9212, November 1992. (Confidential)
28. G. Maris and G.J. O'Brien, ICEX 1-86 Arctic Volume Scatter Strength (U), NUSC TM-87-1103, June 1987. (Secret).
29. T. Wen, R.P. Stein, F.W. Karig, R.T. Miyamoto, and W.J. Felton, Environmental Measurements in the Beaufort Sea, Spring 1987, APL-UW 1-87. February 1988.
30. S.O. McConnell, Simulation and Analysis of Acoustic Measurements Made in 1983 at the Shallow Water Quinault Range (U), APL-UW TR 8909, April 1990. (Confidential)

## II. Surface

### *Introduction*

All models concerning ambient noise radiation and scattering from the sea surface, and scattering and attenuation from near-surface bubbles, are contained in this section. The models are applicable over the frequency interval 10–100 kHz, although we caution that much of the data used in model development and verification lies within a narrower frequency interval of 20–50 kHz. The exception to this is the ambient noise model which predicts wind- and rain-generated ambient noise over the frequency interval 1–100 kHz. (Shipping and other noise sources are not considered; for biological noise, see Section III.)

Most of the models in this section require frequency  $f$  in kilohertz and wind speed  $U$  in meters/second (measured at a height of 10 m) as model inputs; other model inputs will be introduced as necessary. Wind speed is used as a model input because it is the parameter most easily and reliably measured in operational and test areas, and it is the best known environmental correlate to sea surface conditions and near-surface bubble concentration.

Included within Section II.A is a discussion of sea state, which can be used as a single-parameter description of sea surface conditions combining both wind speed and wave height. This section is included primarily to distinguish the three sea state codes currently in use and to provide a conversion to wind speed and wave height when sea state is the only environmental descriptor available. (The sea state parameter is not used explicitly in any of the models given in this section.)

The effects of near-surface bubbles enter into nearly all of the models. At low to moderate grazing angles, surface backscatter is dominated by returns from the near-surface layer. At moderate to high angles, the bubble layer acts as an absorber. This absorption (or, more precisely, extinction) effect is the reason for the loss of acoustic energy. This loss is also an important element in the ambient noise model because noise generated at the air/sea interface must propagate through the bubble layer to reach the receiver (it is assumed that the receiver is below the bubble layer).

## A. WIND SPEED AND SEA STATE

The 10 m measurement height for wind speed is the standard reference height for wind speed measurements at sea. In general, wind speed measurements made at heights above 10 m will be greater than those made at 10 m, and measurements made at heights below 10 m will be less. The exact change in wind speed with measurement height depends on the stability of the air/sea interface, which is largely dependent on the air/sea temperature difference  $\Delta C$ . Knowing  $\Delta C$ , one may use tables given in Smith<sup>1</sup> to convert measurements made at heights other than 10 m to the standard reference height. Note that wind speed measurements taken at heights within the range 5–20 m differ from those taken at the standard 10 m by less than 10%.

A far more important source of error in wind speed estimates is the averaging period during which measurements were made. This period should be at least 20 min, but no greater than 1 hour, for wind speed to correlate with sea surface conditions<sup>2</sup> and near-surface bubble concentration. The averaging period should ideally be just prior to the time of the acoustic measurements. Wind speed measurements taken over very short averaging periods will introduce error into model predictions because such measurements will be unduly influenced by gusts or quiescent periods and therefore will be less correlated with sea surface conditions and bubble concentration.

The term sea state, with its long history in the field of naval oceanography, has become a useful code for describing the surface conditions of the open ocean and is widely used today. Unfortunately for scientific purposes, sea state is a loosely defined quantity at best, with several definitions available.<sup>3–7</sup> A brief description of three of the more commonly found definitions is given in Table 1. In addition to the problems associated with conflicting definitions, it is also apparent that these definitions are based on fully developed wind-driven seas and do not encompass the full range of surface conditions.

Three conditions can cause the general wind-speed/wave-height relationship to deviate significantly from that for the fully developed sea: limited fetch, limited

Table 1. Various sea state codes currently in use.

Sea State	USHO Code <sup>a</sup>		WMO Code <sup>b</sup>		Bunker Ramo Guide <sup>c</sup>	
	Wind Speed, kn	Significant Wave Height, ft	Wind Speed, kn	Significant Wave Height, ft	Wind Speed, kn	Significant Wave Height, ft
0	<1	0	<3	0	<sup>d</sup>	<sup>d</sup>
1	1-3	<1	4-6	0-1	1-4	0-2
2	4-6	1-3	7-10	1-2	4-10	2-3
3	7-10	3-5	11-16	2-4	7-15	3-4
4	11-27	5-8	17-21	4-8	14-27	4-8
5	28-40	8-12	22-27	8-13	27-40	8-12
6	41-47	12-20	28-47	13-20	40-48	12-20
7	48-55	20-40	48-55	20-30	48-55	20-40
8	56-63	>40	56-63	30-45	55-65	>40
9	>64	>40	>64	>45	<sup>d</sup>	<sup>d</sup>

<sup>a</sup>U.S. Hydrographic Office code<sup>4</sup><sup>b</sup>World Meteorological Organization<sup>7</sup><sup>c</sup>Bunker Ramo Guide<sup>6</sup><sup>d</sup>undefined

duration, and swell from distant sources. The first two generally result in wave heights considerably less than those for a fully developed sea, whereas the third usually produces larger wave heights for the same wind speed. All three can play a significant role in modifying the general surface conditions described by the sea state.

Of the three sea state codes presented in Table 1, the WMO code is the one recommended, for two reasons. First, it is the most widely used, both worldwide and in the United States. Second, this code conforms more closely to the Pierson-Moskowitz<sup>8</sup> relationship between wave height and wind speed for fully developed seas. Table 2 summarizes the specific wind speeds and wave heights to use in accordance with the WMO sea state code.

Wind speed is the key environmental correlate used as input for the acoustic models that predict surface backscattering strength, surface forward loss, and ambient noise level. The probability of encountering a given wind speed is plotted in Figure 1, which shows that 80% of oceanic winds typically range between ~3 and 11 m/s. The median

*Table 2. Recommended wind speeds and wave heights for WMO sea states.*

WMO Sea State	Wind Speed, <sup>a</sup>		Significant Wave Height, <sup>a</sup>		rms Wave Height,	
	kn	(m/s)	ft	(m)	ft	(m)
0	1.5	(0.8)	0.0	(0.0)	0.0	(0.0)
1	5.0	(2.6)	0.5	(0.15)	0.13	(0.04)
2	8.5	(4.4)	1.5	(0.46)	0.38	(0.12)
3	13.5	(6.9)	3.0	(0.91)	0.75	(0.23)
4	19.0	(9.8)	6.0	(1.8)	1.5	(0.46)
5	24.5	(12.6)	10.5	(3.2)	2.6	(0.79)
6	37.5	(19.3)	16.5	(5.0)	4.1	(1.25)
7	51.5	(26.5)	25.0	(7.6)	6.3	(1.9)
8	59.5	(30.6)	37.5	(11.4)	9.4	(2.9)
9	>64.0	(>32.9)	>45.0	(>13.7)	>11.3	(>3.4)

<sup>a</sup>Median values of wind speed and wave height have been used in lieu of the ranges shown in Table 1.



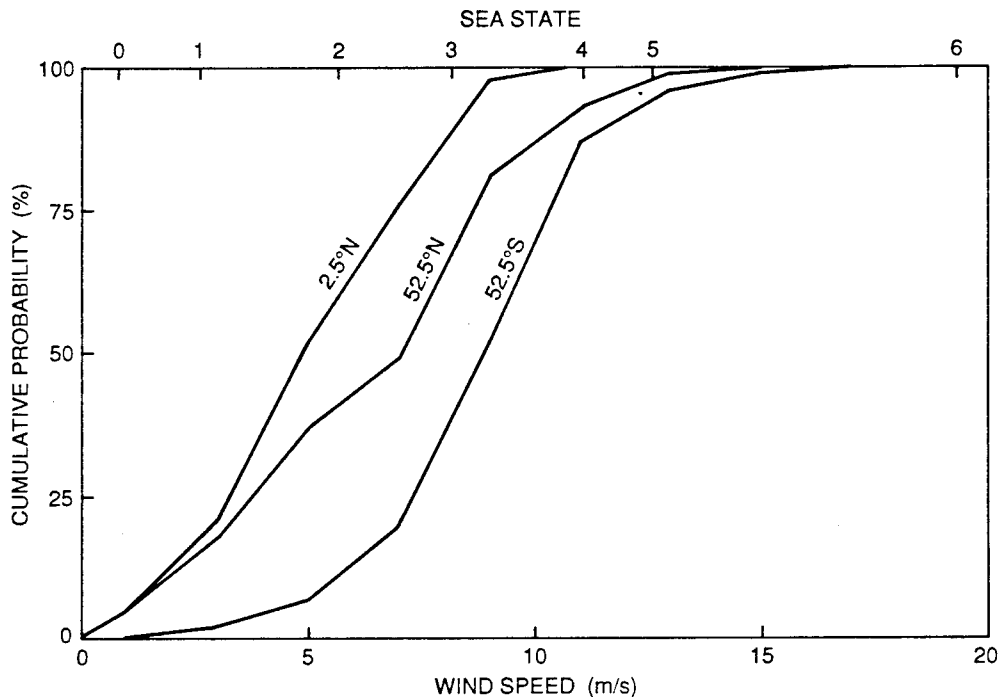


Figure 1. Examples of cumulative probability distribution of measured oceanic winds with corresponding sea states for these latitudes.<sup>9</sup> These data were obtained using the Seasat radar altimeter and averaged over the 3 months that Seasat was in operation (7 July to 10 October 1978).

wind speed for the three cases shown ranges from 5 m/s to 9 m/s; winds corresponding to sea state 0 or sea state 6 and beyond have a very low probability of occurrence. The figure shows representative cumulative probability curves; wind probability data for specific geographical locations and seasons can be found in marine climatic atlases.

## B. BACKSCATTER

Sufficient experimental and theoretical work has been done in the past few years to show that scattering from near-surface bubbles dominates at low to moderate grazing angles and that scattering from the air/sea interface dominates at high grazing angles. The resultant surface scattering strength (in decibels) is expressed as

$$S_s = 10 \log [\sigma_r(\theta) + \sigma_b(\theta)] \quad , \quad (1)$$

where

$\sigma_b$  = dimensionless backscattering cross section per unit solid angle per unit surface area due to volumetric bubble scattering

$\sigma_r$  = dimensionless backscattering cross section per unit solid angle per unit surface area due to sea surface roughness scattering.

The roughness contribution  $\sigma_r$  is divided into two components:

$\sigma_f$ , due to large-scale wave facets based on specular point theory

$\sigma_{sc}$ , due to small-scale roughness.

The term  $\sigma_b$  treats both scattering (reradiation) and absorption from bubbles in a consistent manner. The components in  $\sigma_r$  contain an additional factor that takes into account bubble extinction (reradiation plus absorption) because the acoustic signal must traverse the bubbly layer to reach the air/sea interface.

## 1. Scattering from Bubbles

Crowther,<sup>10</sup> and later McDaniel and Gorman,<sup>11</sup> developed the expression for the backscattering cross section of a horizontally homogeneous layer of near-surface bubbles. The expression, recently modified by McDaniel<sup>12</sup> to include coherent addition of two of the four paths involved, is

$$\sigma_b = \frac{\beta_v}{4\pi} \frac{\delta_r}{\delta} \left[ \frac{1 + 8\beta e^{-2\beta} - e^{-4\beta}}{2\beta} \right], \quad (2)$$

where

$$\beta = \beta_v / \sin\theta \quad (\theta = \text{grazing angle}) \quad (3)$$

and

$$\delta_r = \text{reradiation damping coefficient at resonance} = 0.0136 \quad (4)$$

The quantity  $\beta_v$  is related to the depth-integrated bubble density of resonant sized bubbles. It has been estimated as a function of wind speed  $U$  (in meters/second) and frequency  $f$  (in kilohertz) by inverting Eq. 2 to yield  $\beta_v$ , using the large backscattering database described in Ref. 15. The result is

$$\beta_v = 10^{(-5.2577 + 0.4701 U)(f/25)^{0.85}}, \quad U < 11 \text{ m/s} \quad (5)$$

$$\beta_v = \beta_v(U = 11 \text{ m/s})(U/11)^{3.5}, \quad U \geq 11 \text{ m/s}$$

The remaining variable is the total damping coefficient (reradiation plus thermal) at resonance  $\delta$ , which is a function of frequency:

$$\delta = 2.55 \times 10^{-2} f^{1/3} \quad (6)$$

Equation 6 is from McConnell and Dahl<sup>13</sup> and represents a fit to measurements by Devin.<sup>14</sup>

Note that the azimuthal scattering angle does not appear in Eq. 2; measurements to date have not shown the scattering cross section to depend on this angle. Also, at high bubble densities, Eq. 2 reduces to

$$\sigma_b = \frac{\sin \theta}{8\pi} \frac{\delta_r}{\delta} \quad (7)$$

and the scattering cross section becomes independent of bubble density (and wind speed). This saturation condition has been verified by several experiments.<sup>15-17</sup> The low bubble density limit when  $\beta \ll 1$  is also of interest, in which case  $\sigma_b$  becomes

$$\sigma_b = 1.5 \frac{\beta_v}{\pi} \frac{\delta_r}{\delta} \quad (8)$$

## 2. Scattering from Sea Surface Roughness

### a. Scattering from small-scale roughness

Like  $\sigma_b$ ,  $\sigma_{sc}$  is based on data but guided by theory, in this case composite roughness theory developed by McDaniel and Gorman<sup>11</sup> and McDaniel.<sup>18</sup> This theory is founded on Bragg scattering from surface ripples satisfying the condition  $L_R = \lambda/2\cos\theta$ , where

$L_R$  is the ripple wavelength and  $\lambda$  the acoustic wavelength. These ripples ride upon the large-scale waves, and their composite describes the surface roughness. The main effect of the large-scale waves is to modulate the local grazing angle  $\theta$ . The large-scale waves also shadow portions of the wave profile, but this effect on backscattering strength is restricted to angles less than  $5^\circ$  where bubble scattering is predominant.<sup>18</sup> As a result, the Rayleigh-Rice formulation for the scattering cross section can be applied, giving

$$\sigma_{sc} = A(U) \tan^4 \theta, \quad \theta \leq 85^\circ \quad (9)$$

$$\sigma_{sc} = 0, \quad \theta > 85^\circ$$

with an adjustable coefficient  $A$  fitted to data in the grazing angle interval  $30^\circ$ – $70^\circ$ . The interpolation formula described below will take care of the sharp transition at  $85^\circ$ .

The grazing angle dependence,  $\tan^4 \theta$  is supported by data reported by Monti et al.<sup>16</sup> and Waltzman and Thorsos.<sup>19</sup> These data (taken at 10–60 kHz) indicated no obvious trend with frequency. According to the Rayleigh-Rice formulation, this frequency independence is consistent with a  $\tan^4 \theta$  grazing angle dependence because the two dependencies are linked together by the shape of the wave-height power spectral density  $W(k)$ . The grazing angle and frequency dependencies imply that  $W(k) \sim k^{-4}$ , where  $k$  is the wavenumber for surface roughness. The wind speed dependence of  $\sigma_{sc}$  was found from acoustic data by Waltzman and Thorsos<sup>19</sup> and McConnell,<sup>20</sup> giving the coefficient  $A$  as a function of wind speed:

$$A(U) = 1.3 \times 10^{-5} U^2 \quad (10)$$

Note that since  $\sigma_{sc}$  is dimensionless,  $1.3 \times 10^{-5}$  must have implicit dimensions  $s^2/m^2$ .

#### b. Scattering from facets

The term  $\sigma_f$  in the expression for the surface scattering strength is applicable for the near-specular scattering that occurs at steep grazing angles. Like  $\sigma_b$  and  $\sigma_{sc}$ , the form of the equation for  $\sigma_f$  is guided by theory,<sup>21</sup> but the dependence on environmental conditions is found in the acoustic data. For very high grazing angles,  $\theta \geq 70^\circ$ , the theory reduces to the high-frequency limit of the Kirchhoff approximation and, assuming a Gaussian, isotropic distribution of surface slopes, the scattering cross section is

$$\sigma_f = \frac{\sec^4 \gamma}{4\pi s^2} \exp \left[ \frac{-\tan^2 \gamma}{s^2} \right] \quad (11)$$

where  $\gamma = 90 - \theta$  is the facet reflection angle and  $s^2$  is the mean square surface slope. The mean square surface slope is estimated using

$$s^2 = 4.6 \cdot 10^{-3} \log_e (2.1 U^2) \quad U \geq 1 \text{ m/s} \quad (12)$$

$$s^2 = 0.0034 \quad U < 1 \text{ m/s}$$

The origins of the submodel for  $s^2$  and its comparison with data are discussed in Section II.B.2.c. The physical basis for this theory is that the strongest returns near vertical incidence will come from properly oriented facets on the sea surface that specularly reflect energy back to the receiver.

### c. Interpolation between the $\sigma_{sc}$ and $\sigma_f$ cross sections

The surface roughness component  $\sigma_r$  to the total surface scattering strength is found by interpolating between  $\sigma_{sc}$  and  $\sigma_f$ , using the interpolation function<sup>22</sup>

$$f(x) = \frac{1}{1 + e^x} \quad (13)$$

and first computing  $\sigma_{r_1}$  such that

$$\sigma_{r_1}(\theta) = f(x)\sigma_f(\theta) + [1 - f(x)]\sigma_{sc}(\theta) \quad (14)$$

with the argument of the interpolation function defined as

$$x = 0.524(\theta_f - \theta) \quad (15)$$

where angles  $\theta$  and  $\theta_f$  are expressed in degrees. This transition occurs in the vicinity of  $\theta_f$ , defined as the angle at which  $\sigma_f$  is 15 dB below its peak value at  $\theta = 90^\circ$ . Finding  $\theta_f$  depends on the angular quantization (we use  $1^\circ$  in the sample plots given next). For an arbitrary quantization,  $\theta_f$  is defined as the *smallest* angle  $\theta$  that satisfies  $10 \log[\sigma_f(90^\circ)/\sigma_f(\theta)] \leq 15$  dB. The interpolation function provides for a smooth transition between the two cross sections, each of which is based on approximations valid only

within a certain range of grazing angles. Finally,  $\sigma_r$  is computed from  $\sigma_{r_1}$  by correcting for the extinction loss due to penetration through the near-surface bubble layer, giving

$$\sigma_r(\theta) = \sigma_{r_1}(\theta) 10^{-SBL(\theta)/10} \quad (16)$$

The equation for *SBL* (surface bubble loss) is given in the next section (Eq. 28).

### 3. Total Surface Backscattering Strength $\sigma_r + \sigma_b$

Model predictions of total surface backscattering strength as a function of grazing angle at frequencies of 25 kHz and 60 kHz and wind speeds between 3 and 15 m/s are shown in Figures 2a and 2b. The model is clearly much more sensitive to wind speed when it is less than about 8 m/s. The reason is that surface wave breaking shuts down within this lower wind speed range, and therefore the production of near-surface bubbles is much reduced.<sup>23</sup>

### 4. Model/Data Comparisons

Representative model/data comparisons are presented in this section. The data originate from three experiments representing both deep water and shallow water conditions: FLIP77,<sup>15</sup> a 1977 deep ocean experiment conducted off the California coast; NOREX85,<sup>16</sup> a 1985 shallow water experiment conducted 40 nm west of the German and Danish coastline in waters 30 m deep; SAXON-FPN,<sup>24</sup> a 1992 shallow water experiment conducted at the NOREX85 site.

Figures 3–5 compare model predictions with FLIP77 data. In Figures 3 and 4, the model inputs for wind speed are the measured wind speed  $\pm 1$  m/s. In Figure 3, for example, the measured wind speed is 4.5 m/s, and the model is run at 5.5 m/s (dashed line) and 3.5 m/s (solid line). In Figure 5, the wind speed is 12.8 m/s and wind speed changes of 1 m/s make little difference in the model's predictions. Agreement between the model and the data is quite satisfactory.

Figures 6–8 compare model predictions with data from the NOREX85 and SAXON-FPN shallow water data sets. In Figure 6, SAXON-FPN data taken at various

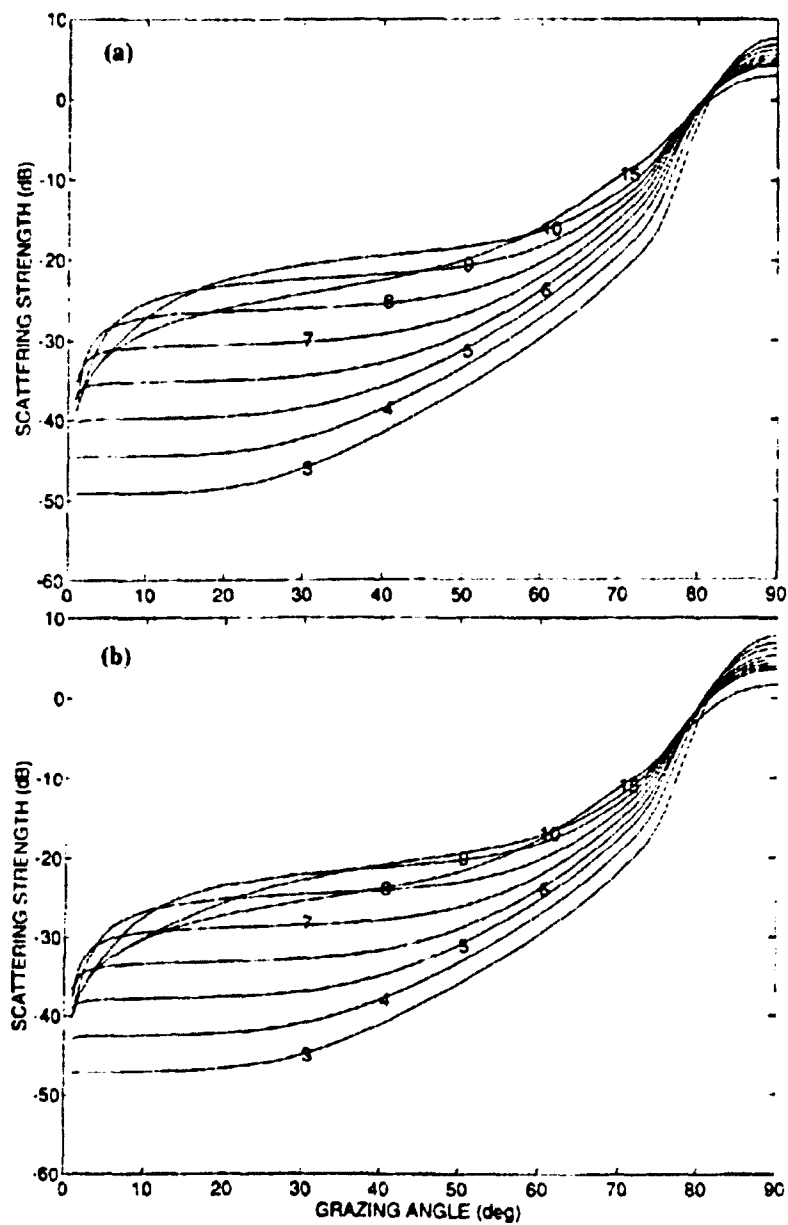


Figure 2. Grazing angle dependence of surface backscattering strength at (a) 25 kHz and (b) 60 kHz for wind speeds between 3 and 15 m/s; the number on each curve indicates the wind speed.

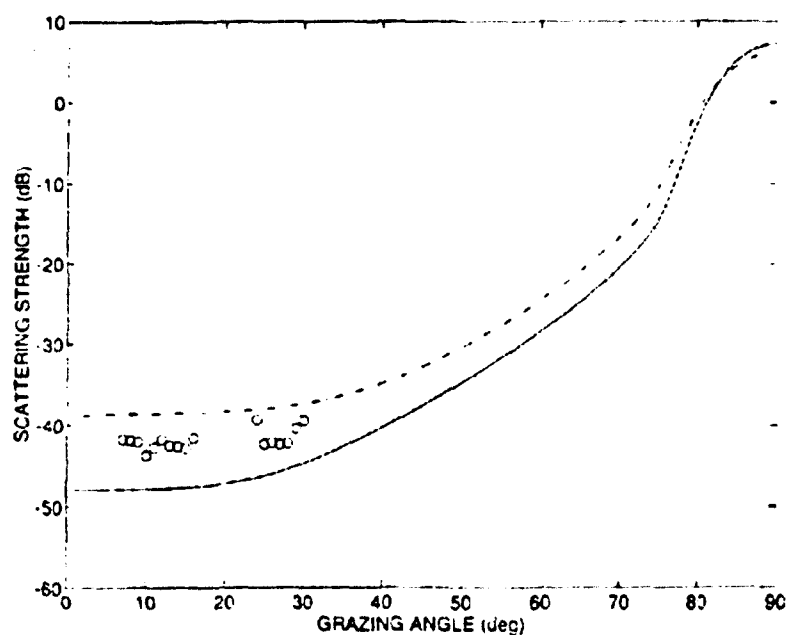


Figure 3. Comparison of backscattering model with data from FLIP77. Model inputs are  $f = 15$  kHz and  $U = 3.5$  m/s (solid line) and  $5.5$  m/s (dashed line), representing a  $\pm 1$  m/s spread about the measured wind speed of  $4.5$  m/s.

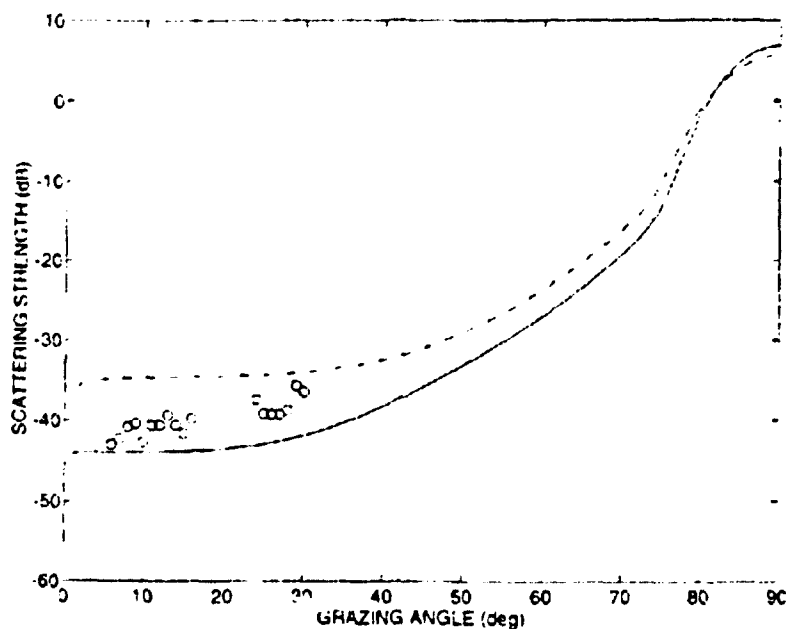


Figure 4. Comparison of backscattering model with data from FLIP77. Model inputs are  $f = 25$  kHz and  $U = 4.1$  m/s (solid line) and  $6.1$  m/s (dashed line), representing a  $\pm 1$  m/s spread about the measured wind speed of  $5.1$  m/s.



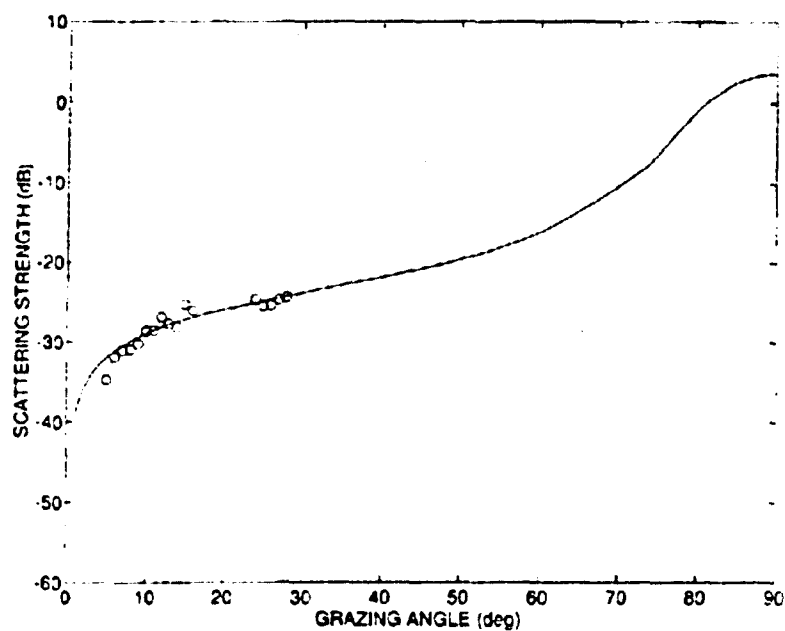


Figure 5. Comparison of backscattering model with data from FLIP77. Model inputs are  $f = 25$  kHz and  $U = 12.8$  m/s.

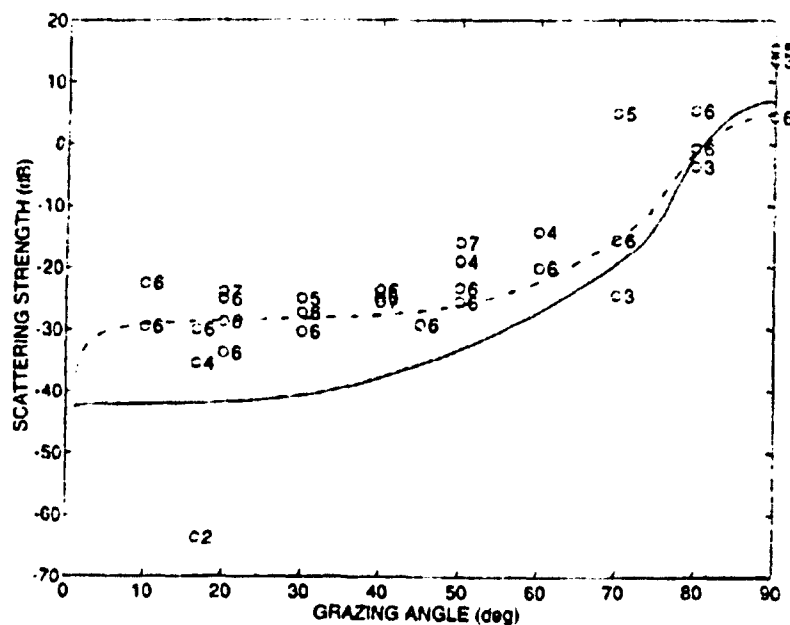


Figure 6. Comparison of backscattering model with data from SAXON FPN. Model inputs are  $f = 70$  kHz and  $U = 1$  m/s (dotted line), 4 m/s (solid line), and 7 m/s (dashed line). The number beside each data point is the wind speed.

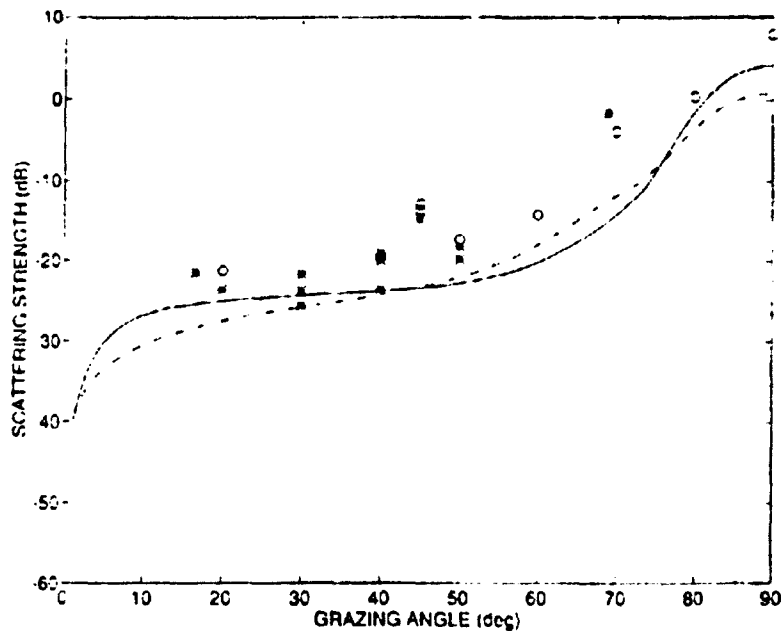


Figure 7. Comparison of backscattering model with data from SAXON FPN. Model inputs are  $f = 70 \text{ kHz}$  and  $U = 8 \text{ m/s}$  (solid line), and  $16 \text{ m/s}$  (dashed line). Circles represent data taken in the wind speed interval  $12 < U \leq 16 \text{ m/s}$ ; asterisks represent data taken in the wind speed interval  $8 < U \leq 12 \text{ m/s}$ .

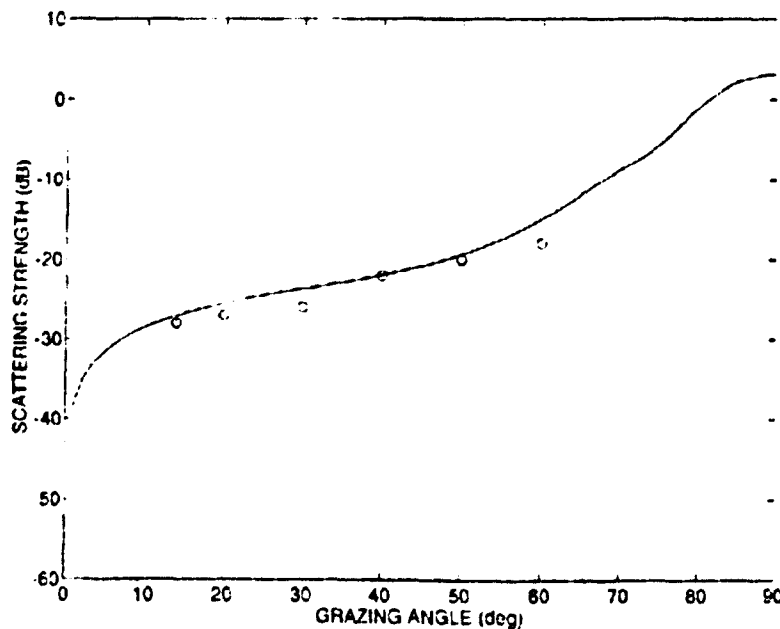


Figure 8. Comparison of backscattering model with data from NOREX85. Model inputs are  $f = 18 \text{ kHz}$  and  $U = 17 \text{ m/s}$ .

low wind speeds (noted in the figure) are compared with model predictions for  $U = 1$  m/s (dotted line), 4 m/s (solid line), and 7 m/s (dashed line). In Figure 7, wind speed data between 8 and 16 m/s, also taken during SAXON-FPN, are shown grouped together. The circles represent data taken at wind speeds of 12–16 m/s; asterisks represent the interval 8–12 m/s. The model results are for  $U = 8$  m/s (solid line) and  $U = 16$  m/s (dashed line); the results for the two wind speeds are distinguishable, but their difference is less than the overall spread of the data. Data from NOREX85 are shown in Figure 8.

## 5. Model Implementation Notes and Model Accuracy

### a. Implementation

- Additional care must be taken to compute the backscattering strength at grazing angles approaching  $0^\circ$  to avoid numerical problems. We recommend that the scattering strength values for grazing angles  $< 0.5^\circ$  be arbitrarily determined by linear extrapolation of the values at  $1^\circ$  and  $0.5^\circ$ .

### b. Accuracy

- For wind speeds greater than about 8 m/s, and at all grazing angles, a nominal estimate of model uncertainty is  $\pm 4$  dB; that is, most data will fall within this range of the model.
- For wind speeds less than about 8 m/s, model uncertainty necessarily increases because the precise threshold for wave breaking (and bubble production) may vary. Furthermore, in approximately half the data runs we examined that were taken in the wind speed range 4 to 8 m/s, scattering strength in the grazing angle range  $\theta = 5^\circ$ – $20^\circ$  decreased with  $\theta$  more strongly than what the model predicts. The reason for this remains unclear. However, within the wind speed range of 4 to 8 m/s, the air-sea interface is typically more sensitive to small changes in wind speed. Therefore, model predictions based on wind speed alone are more difficult. An

estimate of model uncertainty for wind speed less than 8 m/s is  $\pm 5$  dB. We recommend, however, that simulations be made using a  $\pm 1$  m/s wind speed spread about the actual measured wind speed. This provides the simulator with a realistic guide as to the range of expected reverberation levels.

- The model has been compared with data taken at frequencies between 12 and 70 kHz, and a frequency dependence in model accuracy has not been observed.

## 6. Spectral Spread

The power spectrum of a signal scattered from the sea surface at high frequencies has been found to have a Gaussian shape and a width principally dependent on wave height.<sup>15</sup> The spectrum is expressed simply as

$$P(f) = A e^{-(f-f_s)^2/2\sigma^2} \quad (17)$$

where  $A$  is the spectral amplitude (normalized to unity in this discussion),  $f_s$  is the spectral shift, and  $\sigma$  is the standard deviation, which is related to the half-power spectral width by

$$\Delta f_{3dB} = 2.35\sigma \quad (18)$$

The spectral shift for a free-swimming vehicle is usually negligible compared with that associated with the vehicle's velocity. For a fixed sonar (e.g., bottom-mounted) the shift is typically determined by the radial component of the tidal current. In the following discussion, expressions are given for the normalized spectral width

$$\eta = \frac{\Delta f_{3dB} \text{ (Hz)}}{f \text{ (kHz)}} \quad (19)$$

and the spectral shift is ignored.

The expression for  $\eta$  can be factored as follows:

$$\eta = 2.35 F_1(f) F_2(0, \theta) \sigma_h \quad (20)$$

where  $\sigma_h$  is associated with the orbital motion of the sea surface in the up/down wave direction. From the data given by McConnell et al.,<sup>15</sup> this is

$$\sigma_h = 0.894 h^{0.44} \quad (21)$$

where  $h$  is the rms wave height in meters. The rms wave height (in meters) can be estimated from wind speed (in meters/second), assuming a Pierson-Moskowitz<sup>8</sup> model for the sea surface giving

$$h = 5.33 \times 10^{-3} U^2 \quad (22)$$

Note that the commonly used significant wave height  $H_{1/3}$  is equal to 4 times  $h$ .

The combined orbital motion term has a marked dependence on azimuthal angle at low grazing angles. Both open ocean and fetch limited data have shown that the angular factor in Eq. 20 can be fitted by the expression

$$F_2(\phi, \theta) = \begin{cases} 1.0 - 0.0034 |\phi| \cos \theta & |\phi| \leq 90^\circ \\ 1.0 - 0.0034 | |\phi| - 180 | \cos \theta & 90^\circ < |\phi| \leq 180^\circ \end{cases} \quad (23)$$

The azimuthal angle  $\phi$  is defined as  $0^\circ$  in the up-wave heading (the direction of acoustic propagation is opposite to the wave front velocity vector),  $\pm 90^\circ$  in the cross-wave heading, and  $180^\circ$  in the down-wave heading.

The factor  $F_1(f)$  in the orbital motion term of Eq. 20 describes the variation of the spectral width with frequency. The normalized width decreases with increasing frequency as

$$F_1(f) = 1.0 - 0.0084(f - 25) \quad (24)$$

Figure 9 shows the final result for  $\eta$  in the up/down-wave direction for three selected frequencies and a grazing angle of  $60^\circ$ . The frequency dependence given by Eq. 24 is shown in this figure, as is the variation with wave height specified by Eq. 21.

The model is well supported by data for the grazing angle range  $0^\circ$ – $30^\circ$  and the frequency range 15–60 kHz. The spectral width data also agree well with radar data, particularly at C band (6.7 cm wavelength: see Valenzuela and Laing<sup>25</sup> and McConnell<sup>15,20</sup>).

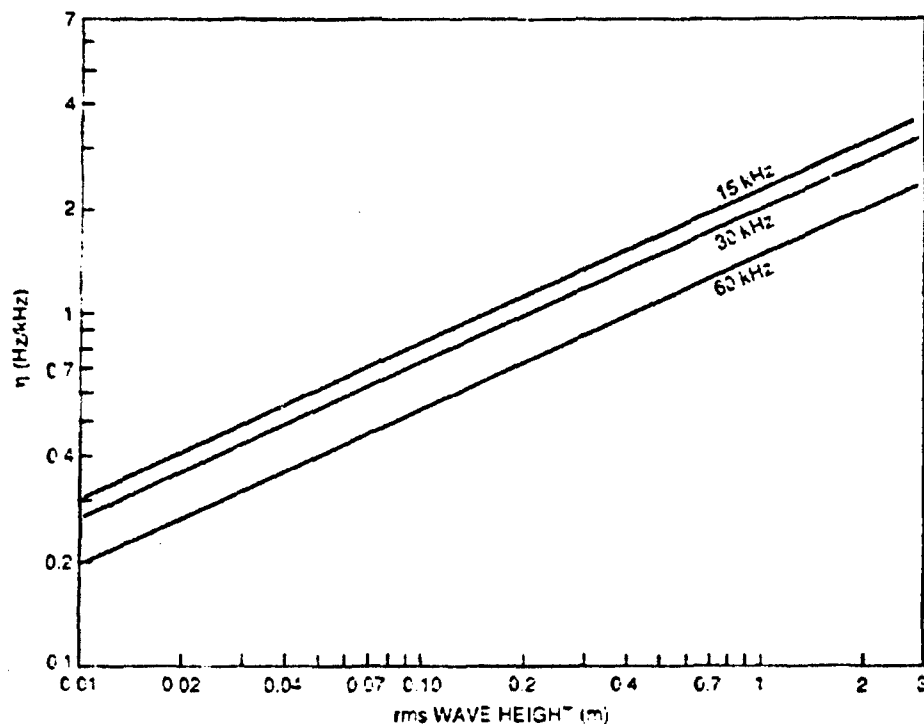


Figure 9. Wave height dependence of the normalized spectral width in the up/down wave direction at three frequencies.

The frequency dependence given by Eq. 24 between 60 kHz and 100 Hz is simply an extrapolation based on data taken in the 15–60 kHz range. No acoustic data were available at grazing angles beyond 60°; the suggested model is based on theoretical arguments and radar data. Finally, it is possible to have additional spectral spreading due to Doppler motion caused by the small-scale waves. This condition would exist only if backscattering were dominated by small-scale, or capillary, waves, as described by  $\sigma_{sc}$  (Eq. 9). The effect on total spectral spread is not significant, and data presented in Refs. 15, 20, and 25 are well described using Eq. 20 without an additional term associated with capillary waves.

## C. FORWARD LOSS

### 1. Introduction

Models for high-frequency surface forward scattering and reflection are briefly summarized here. Supporting discussion and additional references to the literature are given in Ref. 26. At high frequencies, incoherent scattering near the specular direction (forward scattering) almost always dominates over coherent reflection because of the large roughness of the sea surface. Therefore, modeling of forward scattering is important for predicting the reduction in level and time spreading of acoustic signals. The properties to be modeled include the scattered intensity, frequency spreading, and statistics.

For the high frequencies of interest here, the angular distribution of the scattered intensity can be estimated using a facet-reflection-type model.<sup>26,27</sup> Data in support of such a modeling approach are reported by McConnell<sup>28</sup> and by Dahl and McConnell.<sup>29</sup> If relatively wide vertical and horizontal beam widths are involved, a detailed scattering model describing the angular distribution of scattered intensity near the specular direction is not necessary to simulate typical propagation and reverberation conditions. In such cases, the single bounce, forward scattered signal can be adequately represented by an effective reflection loss. Invoking this approximation requires that vertical beam widths be  $\geq 20^\circ$  and horizontal beam widths be  $\geq 5^\circ$ . In the following we assume these beam pattern criteria are approximately satisfied.

### 2. Preliminary Discussion

The time-dependent received intensity after a surface bounce, excluding the direct path contribution, can be written as

$$I_{\text{received}}(t) = I_{\text{total}}(t) a_b \quad (25)$$

where

$I_{\text{total}}(t)$  = total intensity (coherent plus incoherent) following the surface interaction, neglecting absorption

TR 9407 II-19

$a_b$  = absorption factor due to bubbles.

The frequency spreading effects will be described later in Section II.C.8. The factor  $I_{\text{total}}(t)$  can be written (see Section II of Ref. 26)

$$I_{\text{total}}(t) = I_{\text{coh}}(t) + I_s(t) \quad , \quad (26)$$

where

$I_{\text{coh}}(t)$  = coherent (reflected) intensity

$I_s(t)$  = incoherent (scattered) intensity.

The coherent intensity shows no pulse elongation; the incoherent, or scattered, intensity does. Thus, in general, both  $I_{\text{coh}}(t)$  and  $I_s(t)$  contribute during the first part of the received signal with a duration equal to the transmitted pulse length, whereas subsequently only  $I_s(t)$  is present.

### 3. Effective Reflection Loss for Forward Scattering in Reverberation Simulations

In reverberation, or total backscattering, ray paths involving surface bounces contribute to the reverberation level, particularly in shallow water or surface ducts. These surface bounces involve surface forward scattering, possibly reflection, and absorption due to near-surface bubbles. In reverberation simulations involving a few bounces and using wide vertical beams, it should be a good approximation<sup>26</sup> to model the surface bounce as a reflection with the reflection loss given entirely by the "surface bubble loss" (SBL). Thus, the surface reflection loss  $RL$  is given by

$$RL \text{ (dB)} = SBL \text{ (dB)} = -10 \log_{10} a_b \quad , \quad (27)$$

where the surface bubble loss is given by Eq. 28.

In this approximation, no loss is associated with scattering from the air/sea interface, so in the absence of bubble attenuation this scattering is treated as a 0 dB reflection loss. This approximate treatment of surface scattering is justified when the beams are



sufficiently wide (Ref. 26, Section V.A) and when the pulse elongation due to forward scattering can be ignored. The latter condition is met when the elongation time  $L$  is small compared with the time scales over which the total reverberation changes (see Section II.C.6).

In general, the 0 dB loss model for surface scattering should be adequate for simulating volume and boundary reverberation involving wide beams and few surface bounces. However, in applications such as the simulation of target returns involving pulses with high temporal resolution, it may be necessary to account for the pulse elongation caused by the surface interaction (Ref. 26, Section V.C) and the concomitant reduction in peak amplitude.

If more than about three surface bounces contribute significantly to the reverberation or target return, then the loss owing to angular spreading in the vertical can become important. This loss arises because the cumulative angular spreading associated with rough interface interactions causes energy to arrive outside the main part of the receiver beam pattern or to be lost in the bottom above the critical angle. For surface ducting situations, angular spreading appears as an effective duct leakage because energy is directed into grazing angles greater than the critical ray angle for the duct. Unfortunately, very little information is available on the loss due to angular spreading in multiple bounces.

#### 4. Absorption Due to Near-Surface Bubbles

The absorption effect of bubbles near the surface can be described by a surface bubble loss, which is related to  $a_b$  via Eq. 27. A model for  $SBL$  is<sup>30</sup>

$$SBL \text{ (dB)} = \frac{1.26 \times 10^{-3}}{\sin \theta} U^{1.57} f^{0.85}, \quad U \geq 6 \text{ m/s} \quad (28a)$$

$$SBL \text{ (dB)} = SBL(U = 6 \text{ m/s}) e^{1.2(U-6)}, \quad U < 6 \text{ m/s} \quad (28b)$$

where  $U$  is wind speed measured 10 m above the sea surface,  $f$  is acoustic frequency in kilohertz, and  $\theta$  is the nominal grazing angle of the surface bounce path ( $\theta > 0^\circ$ ). The

model includes a wind speed threshold of 6 m/s to account for the threshold of breaking waves (also known as the Beaufort velocity) and subsequent production of bubbles.

Figures 10–12 show representative model/data comparisons for data collected between 20 and 40 kHz in the open ocean<sup>31</sup> off California and in coastal waters<sup>13</sup> off Whidbey Island in Puget Sound. Because the data were collected at different grazing angles, all data have been normalized to  $10^\circ$ . The model provides a reasonable representation of both open ocean and coastal data, with nearly all data points falling within  $\pm 3$  dB of the predicted curves.

Scattering from bubbles will prevent *SBL* from becoming arbitrarily large. A nominal limit for *SBL* is 30 dB, based on scattering from the underside of a uniform layer of near-surface bubbles. However, such a limiting value for *SBL* has not been observed in

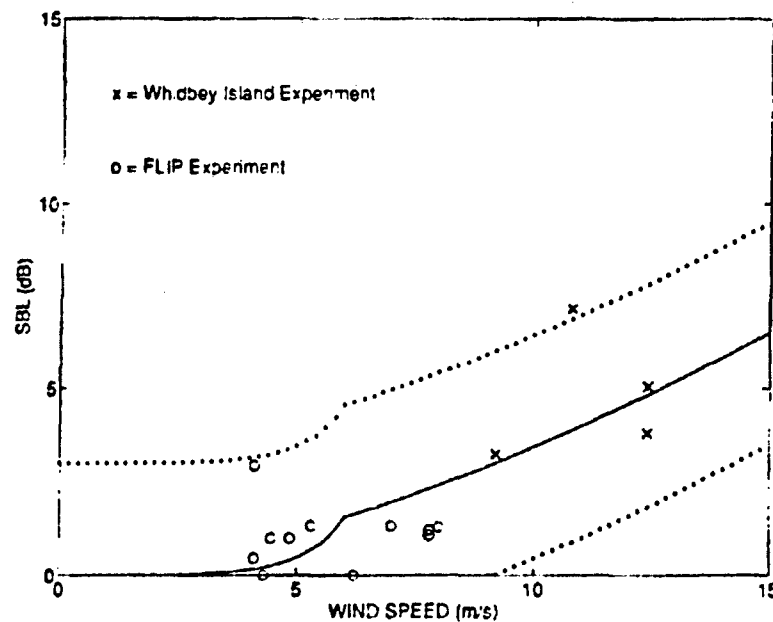


Figure 10. Comparison of SBL model predictions (solid line) with measured 20-kHz data from the FLIP and Whidbey Island experiments. Data from various grazing angles have been normalized to  $10^\circ$  grazing angle. Upper and lower dotted lines represent a  $\pm 3$  dB interval about the predicted curve.

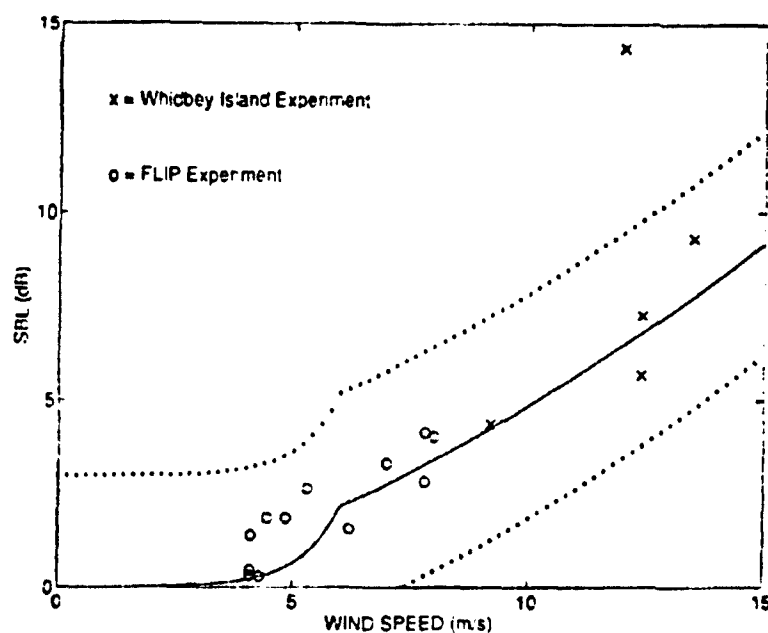


Figure 11. Comparison of SBL model predictions (solid line) with measured 30-kHz data from the FLIP and Whidbey Island experiments. Data from various grazing angles have been normalized to  $10^\circ$  grazing angle. Upper and lower dotted lines represent a  $\pm 3$  dB interval about the predicted curve.

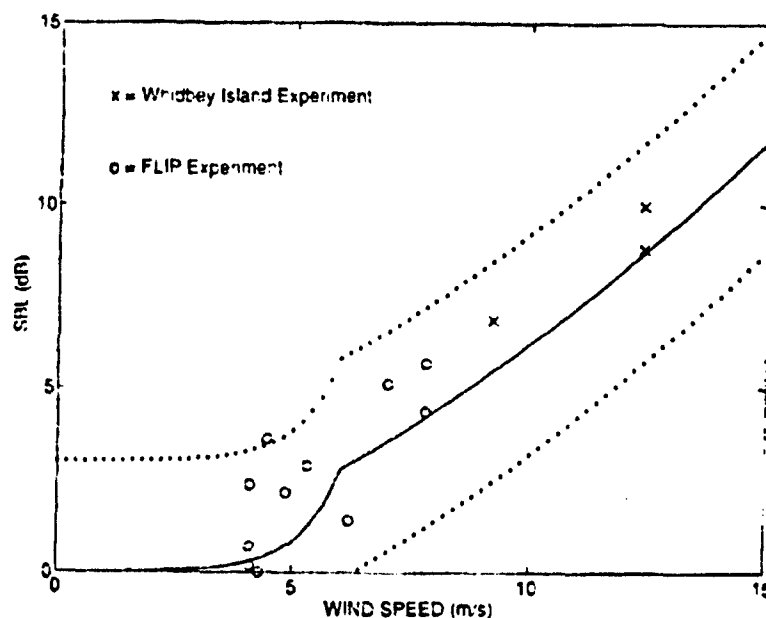


Figure 12. Comparison of SBL model predictions (solid line) with measured 40-kHz data from the FLIP and Whidbey Island experiments. Data from various grazing angles have been normalized to  $10^\circ$  grazing angle. Upper and lower dotted lines represent a  $\pm 3$  dB interval about the predicted curve.

data, because the patchiness of the bubble layer will nearly always admit some surface-scattered energy to pass. Thus we suggest a nominal upper limit of  $SBL_{\max}$  equal to 15 dB. This value is based on the  $SBL$  measurements reported by Thorsos,<sup>32</sup> McConnell and Dahl,<sup>13</sup> and Dahl.<sup>31</sup>

#### a. Depth-dependent formulation of the $SBL$ model

The formulation in Eq. 28 represents the two-way depth integrated bubble attenuation for a surface-reflecting ray under isovelocity conditions. Since isovelocity is assumed, however, the model cannot account for refraction effects, and in the case of ray vertexing ( $\theta \rightarrow 0$ ) the model becomes invalid. By ray vertexing, we mean the ray goes through a turning point at depth  $z_v$  because of refraction. This case is only important for estimating  $SBL$  if the ray vertexes within 10 m of the surface, i.e., if  $z_v$  is less than 10 m, because bubble attenuation will be extremely weak beyond this depth.

Below we provide an alternate depth-dependent formulation<sup>30</sup> of Eq. 28 that accommodates rays vertexing within 10 m of the surface. Two versions are given: the first (Eq. 29) applies to an arbitrary sound speed profile, and the second (Eq. 34) applies to a linearized sound speed profile. We recommend use of the Eq. 34 by linearizing the sound speed profile in the top 10 m of water.

The version that applies to an arbitrary sound speed profile is

$$SBL \text{ (dB)} = 2 \int_{z_v}^{10} \frac{\alpha(z)}{\sin[\theta(z)]} dz, \quad (29)$$

where  $\alpha(z)$  is the depth-dependent bubble attenuation coefficient,  $z_v$  is the vertexing depth of the ray, and  $\theta(z)$  is the local grazing angle at depth  $z$ , which is a function of the sound speed profile. The attenuation coefficient is

$$\alpha(z) = \alpha_0 e^{-z/L_B}, \quad (30)$$

where  $L_B$  (in meters) is the decay constant, or e-folding depth, for the exponential decay and

$$\alpha_0 = 0.63 \times 10^{-3} U^{1.57} f^{0.85} / L_B, \quad U \geq 6 \text{ m/s} \quad (31a)$$

$$= \alpha_0(U = 6 \text{ m/s}) e^{1.2(U-6)}, \quad U < 6 \text{ m/s} \quad (31b)$$

A simple model describing  $L_B$  vs wind speed (in meters/second) for bubbles within the resonant size range most relevant to torpedo frequencies is

$$L_B = 0.07 \times U \quad (32)$$

This equation, which describes measurements reported in Ref. 33, produces estimates of  $L_B$  that fall approximately between estimates derived from similar models reported in Refs. 34 and 35.

The attenuation coefficient  $\alpha(z)$  is integrated between a depth of 10 m and  $z_1$  and multiplied by 2 to estimate the two-way depth-integrated bubble attenuation, which is equivalent to *SBL*. For example, if the ray reflects from the sea surface,  $z_1$  equals 0; if the ray vertexes within 10 m of the sea surface, then  $z_1$  is the vertex depth. The user is cautioned that Eq. 29 has a singular point when  $\theta(z) \rightarrow 0$  which will cause numerical problems if not handled correctly.

#### b. Recommended version based on a linear sound speed profile

To estimate *SBL* for rays that vertex within 10 m of the sea surface, we recommend linearizing the sound speed profile in the upper 10 m such that it satisfies the form

$$c(z) = c_0 + gz \quad (33)$$

where  $c_0$  is the sound speed at the surface,  $g$  is the sound speed gradient in inverse seconds with  $g < 0$  representing downward refraction, and  $z$  is depth measured from the sea surface. The result is

$$SBL = 2\alpha_0 R_c e^{-z/L_s} \frac{1}{2} \sqrt{\frac{\pi}{k}} \Phi(\sqrt{k} \theta_{10}) \quad (34)$$

In Eq. 34,  $\Phi$  is the tabulated probability integral, or error function, and is defined as

$$\Phi(x) = \frac{2}{\sqrt{\pi}} \int_0^x e^{-t^2} dt . \quad (35)$$

The remaining variables in Eq. 34 are

- $R_c$  = the ray's radius of curvature, which is equal to  $c_v/|g|$
- $c_v$  = the sound speed at the vertex depth  $z_v$
- $\theta_{10}$  = local grazing angle (in radians) of the ray at 10 m depth
- $k$  =  $R_c/(2L_B)$ .

The argument  $\sqrt{k}\theta_{10}$  of  $\Phi$  will in many cases be  $\geq 2$ , making  $\Phi$  nearly unity, and it is sufficient to write

$$SBL \text{ (dB)} = 2\alpha_0 \sqrt{R_c L_B \pi/2} e^{-z_v/L_s} \quad (36)$$

as the surface bubble loss for a ray that has vertexed within  $z_v$  m of the sea surface.

## 5. Model Usage Notes and Accuracy

### a. Model usage notes

- The coefficients in the model are based on acoustic measurements made in the frequency range 20–50 kHz. The model is therefore a high-frequency model; as a broad guideline, the model's applicable frequency range is 10–100 kHz. We note that the *SBL* model has recently been shown to give results that are very consistent with results from a model developed at the Naval Undersea Warfare Center for ship sonar frequencies.<sup>36</sup>
- The effect of near-surface bubbles on the real part of the sound speed (known as the sound speed anomaly) is ignored, since within the model's applicable frequency range the main effect of bubbles is attenuation, equivalent to the imaginary part of sound speed.

- The model is based on measurements from a single surface bounce path. To compute *SBL* for propagation channels involving multiple surface (and bottom) interactions, the total *SBL* is the sum of the individual *SBL* values computed for each surface interaction. We caution that model performance for these conditions has not been evaluated.
- The model does not address geographical dependencies. We expect that, in general, littoral waters and more pristine oceanic waters will differ in terms of bubble properties. With few exceptions, however, bubble measurements reported in the literature show within-region variability that tends to obscure any between-region variability, e.g., cf. Refs. 13 and 33. This fact, taken together with the data shown in Figures 10–12 (showing both coastal and oceanic data), support use of a single model at the present time.
- Equation 28, rather than the alternate depth-dependent version in Eq. 29, should be used when *SBL* is used as a submodel for surface backscattering (Section II.B) and ambient noise (Section II.D).

#### **h. Model accuracy**

- The model's uncertainty in comparisons with the current *SBL* database is approximately  $\pm 3$  dB. As a predictive model, however, we assign more conservative error bounds of  $\pm 4$  dB.
- Ping-to-ping fluctuations in *SBL* will be approximately bounded by  $-3$  and  $+5$  dB about the predicted mean *SBL* value. These fluctuations are dominated by sea surface scintillation, or the phase randomization that occurs in forward scattering.
- The *SBL* model predicts the mean energy loss in surface bounce paths due to extinction from near-surface bubbles, where the energy, or time-integrated intensity, can be modeled with a 0 dB loss in the absence of bubbles. Model performance will be degraded in conditions under which the 0 dB loss case cannot be assumed. Some examples where this could occur are as follows:

- The model is used to simulate data gathered with narrow transmit and receive beam patterns (see Section II, Introduction). In this case, the measured *SBL* will be greater than the simulated *SBL* because the data undersample the angular distribution of the scattered intensity.
- The model is used to simulate the loss in the peak value of short-pulse data. A short pulse is defined as one with a duration time  $\tau$  much less than the characteristic pulse elongation time  $L$  for surface-scattered arrivals. For short pulses, the energy loss and the peak intensity loss no longer track each other. The total energy will be underestimated when based on estimates of peak intensity, resulting in data losses that are greater than the simulated losses. A rough guide is  $L < 4R$ , where  $L$  is in milliseconds and range  $R$  is in kilometers. A more precise model for  $L$  is given in the Section II.C.7.

## 6. Coherent Reflection Loss

The combined effect of coherent reflection and incoherent surface forward scattering can often be modeled for wide beams by using no loss; the effective reflection loss is then determined entirely by losses due to bubbles. In a particular model application, the coherent reflection loss (the loss due to the surface interaction and associated with the coherent part alone) in Eq. 26 may be of interest.

The coherent intensity can be described with a reflection coefficient<sup>26,27</sup>

$$R = e^{-\chi^2} , \quad (37)$$

where  $\chi$  is the surface roughness parameter given by

$$\chi = \frac{4\pi h \sin\theta}{\lambda} . \quad (38)$$

where

$h$  = rms surface wave height (m) (see Eq. 22)



$\lambda$  = acoustic wavelength (m)

$\theta$  = specular grazing angle.

The coherent intensity is significant only when the wind speed and corresponding wave height are low enough that  $\chi < 2$ . For these conditions, bubble losses can be neglected. The coherent reflection loss,  $RL$ , which is  $-10 \log_{10} R$ , is given by

$$RL_{\text{coh}} (\text{dB}) = 305 f^2 h^2 \sin^2 \theta \quad , \quad (39)$$

where  $f$  is in kilohertz,  $h$  is in meters, and a sound speed of 1500 m/s has been assumed.

At high acoustic frequencies, the coherent intensity is significant only when the sea surface is nearly calm; for typical ocean conditions,  $I_{\text{coh}}(t)$  is negligible compared with  $I_s(t)$ . We have included the expression for coherent reflection loss (Eq. 39) for completeness. Its accuracy is good except at very low grazing angles (see Ref. 26, Section IV).

## 7. Time-Dependent Intensity and Frequency Coherence in Forward Scattering

### a. Time-dependent intensity

The surface roughness will again be assumed to be large ( $\chi \geq 2$ ), since this limit covers most cases of practical interest at high frequencies. We can neglect  $I_{\text{coh}}(t)$ , so

$$I_{\text{total}}(t) \approx I_s(t) \quad .$$

Consider a single surface bounce and, again, wide beam patterns. The energy,  $\int I_s(t) dt$ , can be modeled with a 0 dB loss, but  $I_s(t)$  itself will exhibit pulse elongation. (Bubble attenuation must also be included (see Eqs. 25 and 27). It is assumed here that such attenuation does not change the form of the time dependence of the received intensity.) A characteristic elongation time,  $L$ , for  $I_s(t)$  can be estimated from (Ref. 26, Section V.C).

$$L = \frac{2r_1 r_2}{r_1 + r_2} \frac{s^2}{c} (1 - e^{-\theta^2 r_1}) \quad , \quad (40)$$

where

$r_1$  and  $r_2$  = incident and scattered slant ranges along the specular path (m)

$c$  = speed of sound (m/s)

$\theta$  = specular grazing angle

$s^2$  = (large-scale) mean square surface slope

$$\gamma_0 = \tan^{-1}(s).$$

The mean square surface slope  $s^2$  is estimated using

$$s^2 = 0.0046 \log_e(2.1U^2) \quad U \geq 1 \text{ m/s} \quad (41a)$$

$$s^2 = 0.0034 \quad U < 1 \quad (41b)$$

Equation 41 represents a logarithmic fit by Phillips<sup>38</sup> to the optical glitter measurements of Cox and Munk.<sup>39</sup> The glitter measurements were made from a slick-covered sea surface which effectively removed surface wavenumber components shorter than about 30 cm; hence they represent measurement of the "large-scale" sea surface slope.

Figure 13 shows the square root of Eq. 41, equal to large-scale slope  $s$ , compared with acoustic estimates of  $s$  made in open ocean conditions.<sup>40</sup> The estimates were derived by first measuring  $L$  and then inverting Eq. 40 to obtain an estimate of  $s$ . The model for  $L$  based on Eqs. 40 and 41 described the data in Figure 13 to within an average relative error of  $\pm 30\%$ . Note that the spread in the data is quite typical of sea surface slope measurements.

If we use the expression for  $L$  given by Eq. 40, the time dependence of the scattered intensity is

$$I_s(\tau) = \frac{I_0 A_0}{(r_1 + r_2)^2} \begin{cases} 0 & \tau \leq 0 \\ \Phi(\sqrt{\tau/L}) & 0 \leq \tau \leq \tau_0 \\ \Phi(\sqrt{\tau/L}) - \Phi[\sqrt{(\tau - \tau_0)/L}] & \tau \geq \tau_0 \end{cases} \quad (42)$$

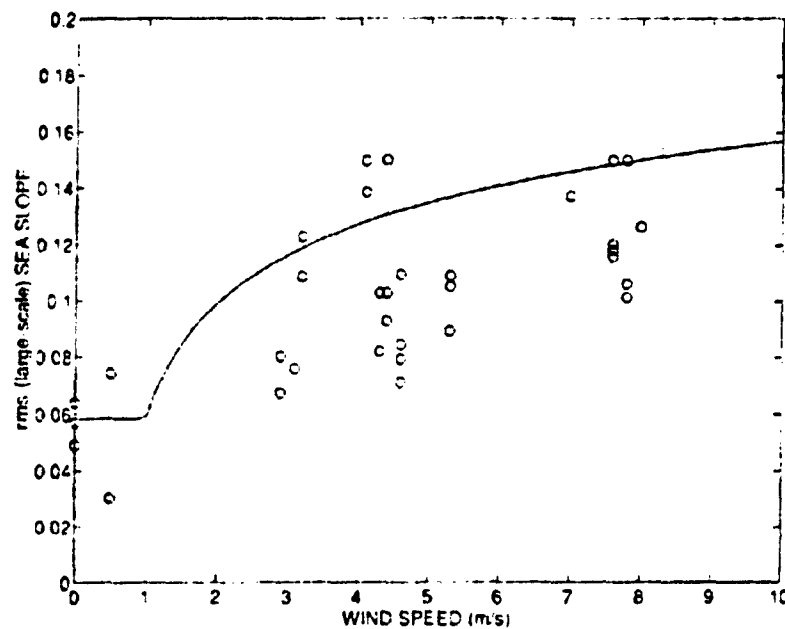


Figure 13. Model for rms sea slope  $s$  (equal to square root of Eq. 41a) vs estimates of  $s$  derived from measurements of  $L$  and inversion of Eq. 40.

where

$$\tau = t - t_s$$

$t_s$  = travel time for the specular ray path referenced to the time of transmit ( $t = 0$ )

$\tau_0$  = transmit pulse length (rectangular pulse)

$I_0$  = transmit pulse intensity

$A_0$  = unit area

and where  $\Phi(x)$  is the probability integral given in Eq. 35. Equation 42 provides the form for  $I_s(t)$  for a single surface interaction; the generalization to multiple bounces is given in Ref. 26, Section V.C. An illustration of the combined effect of increasing elongation time and increasing surface bubble loss is given in Figure 14, where the scattered intensity has been normalized by the multiplicative factor in Eq. 42, i.e.,  $I_0 A_0 / (r_1 + r_2)^2$ .

For very short pulses, it is clear from Eq. 42 and Figure 14 that the scattered intensity will not reach its final asymptotic (or peak) value. For modeling target returns, say a single highlight, this reduction in intensity may be important when using pulses with high time resolution; the associated loss can be estimated as  $10 \log \Phi(\sqrt{\tau_c/L})$ . Finally, it should be pointed out that this loss and the elongation time  $L$  depend on the assumption of an isovelocity ocean. Strong deviations from this assumption (e.g., a ray that is close to vertexing at the sea surface) will invalidate the formulation for  $I_s(\tau)$  given by Eq. 42.

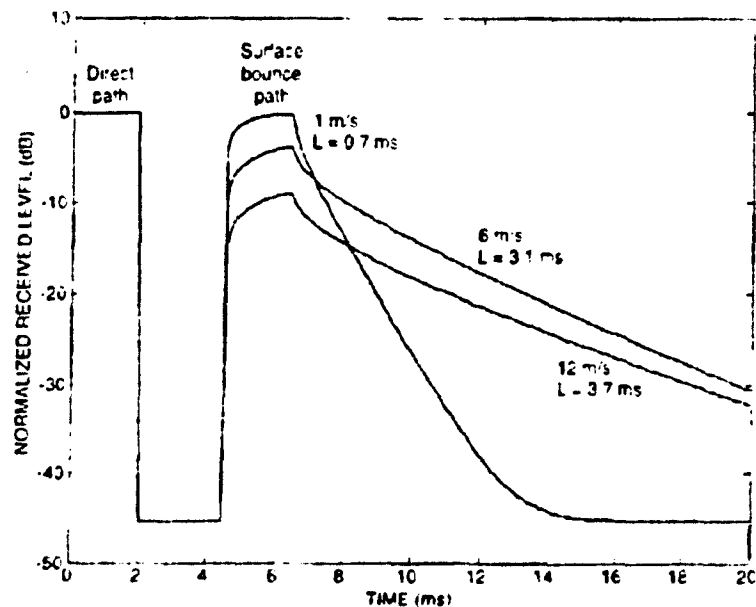


Figure 14. Model of the surface forward bounce signal illustrating the effects of time elongation of the transmitted pulse (2 ms pulse length) and surface bubble loss. Elongation times and wind speed are noted. The grazing angle is  $7.6^\circ$ , the frequency is 25 kHz, the source and receiver depths are both 50 m, and the range is 750 m. The noise level has been arbitrarily set at  $-15$  dB.

#### b. Frequency coherence

The inverse  $L^{-1}$  (in hertz) is a measure of the coherence bandwidth of the channel<sup>20</sup> and therefore important both in designing waveforms and in determining signal-processing strategies. Application of Eqs. 40 and 41 to estimate  $L^{-1}$  provides a means to

obtain realistic estimates of the coherence bandwidth for the channel as a function of both acquisition geometry and environment. When coherence bandwidth  $L^{-1}$  is estimated, the relative error translates to approximately +40% and -20%.

## 8. Frequency Spreading

For an incident high-frequency monochromatic wave, the forward-scattered signal can be approximated as a Gaussian spectral distribution about an unshifted center frequency when  $\chi > 1$  (Ref. 26, Section VII; Ref. 41). If we assume a Pierson-Moskowitz surface wave spectrum,<sup>8</sup> the 3 dB spectral width of the forward-scattered signal is given<sup>42</sup> by

$$\Delta f_{3dB} \text{ (Hz)} = 0.128 U f \sin \theta, \quad (43a)$$

with  $U$  in meters/second and  $f$  in kilohertz, or

$$\Delta f_{3dB} \text{ (Hz)} = 1.76 h^{-1/3} f \sin \theta, \quad (43b)$$

with  $h$  in meters (Eq. 22). At low grazing angles, the spectral spread of forward scatter is generally negligible, especially in comparison to spectral widths associated with the long pulse lengths typically used in practice (e.g., the spread is 3 Hz at a frequency of 20 kHz, an rms wave height of 1 m, and a grazing angle of 5°).

Measurements by Roderick<sup>41</sup> support Eq. 43, and its accuracy is considered satisfactory. Some differences can be expected when the surface wave spectrum deviates from the Pierson-Moskowitz spectral form.

## 9. Statistics

After a surface bounce, the amplitude statistics over an ensemble of pings are adequately described by the Rayleigh distribution<sup>26, 43-45</sup> whenever the roughness parameter  $\chi$  given by Eq. 38 exceeds 2. Deviations from the Rayleigh distribution have been observed in backscattering measurements involving small patch sizes. For example, data taken in Dahab Bay appear to deviate from the Rayleigh distribution for patch sizes

$<30 \text{ m}^2$ , although this deviation was not observed for open ocean measurements.<sup>46</sup> These observations should be viewed as a cautionary note for high-resolution systems that employ narrow beams. Given a Rayleigh distribution, the relative probability of obtaining a pressure amplitude (or envelope value),  $A$ , is given by

$$P(A) = \frac{A}{\langle p^2 \rangle} \exp(-A^2/2 \langle p^2 \rangle) \quad (44)$$

where  $p$  is the instantaneous pressure and the angle brackets denote the ensemble average at a given time in the ping cycle. The mean square instantaneous pressure is related to the mean square amplitude, or envelope value, by  $\langle p^2 \rangle = 1/2 \langle A^2 \rangle$ . The equivalent intensity distribution is

$$P(I) = \frac{1}{\langle I \rangle} \exp(-I/\langle I \rangle) \quad (45)$$

where  $I$  is proportional to  $A^2$ . The models in Sections II.C.3 and II.C.6 pertain to the mean  $\langle I \rangle$ .

For low roughness ( $\chi < 2$ ), a constant reflection coefficient plus a random scattered component has been modeled with the Rician distribution.<sup>45,47</sup> Since low roughness conditions seldom occur at high frequencies, and since the Rician distribution is more concentrated about the mean than the Rayleigh distribution, we recommend use of the Rayleigh distribution.

## D. AMBIENT NOISE

### 1. Ambient Noise Multipath Expressions

At frequencies above 1 kHz, the most ubiquitous source of ambient noise in the ocean arises from the action of wind on the water surface. Above 50 kHz, thermal noise may predominate when the levels of wind or other sources of surface-generated sound (e.g., precipitation and shipping) are very low. Of these other surface sources, only rain noise will be treated here. Biological sources of ambient noise, such as snapping shrimp, are examined in Section III.

The resultant ambient noise model, then, consists of two types of noise originating at the sea surface, namely wind and rain, plus thermal noise due to molecular agitation. The total noise level detected at the receiver is

$$P_r = P_s + P_T \quad , \quad (46)$$

where

$P_r$  = total received noise power spectral density ( $\mu\text{Pa}^2/\text{Hz}$ )

$P_s$  = surface noise power spectral density ( $\mu\text{Pa}^2/\text{Hz}$ )

$P_T$  = thermal noise power spectral density ( $\mu\text{Pa}^2/\text{Hz}$ ).

and the decibel equivalents are defined as

$$NSL = 10 \log P_r$$

$$NL_s = 10 \log P_s$$

$$NL_T = 10 \log P_T.$$

The thermal noise term is given by

$$NL_T = -15 + 20 \log f - DI - E \quad , \quad (47)$$

where  $f$  is frequency in kilohertz and  $DI$  and  $E$ , respectively, are the directivity index and efficiency in decibels.<sup>48</sup>

The surface-generated noise contribution is found by integrating over a uniform distribution of surface radiators, taking into account propagation from the surface to the receiver and the receiver beam pattern. To obtain realistic results in shallow water and at lower frequencies, the propagation model must include multipath contributions to the total noise level, particularly for sites having hard bottoms.

Two equivalent expressions have been developed for implementation on a computer to determine the noise level for directional receivers. The first expression is tailored to computer codes that calculate transmission loss as a function of horizontal range; i.e., the primary integration variable is range.

$$P_S = A \int_0^{R_{\max}} \left\{ \sum_{\text{paths}} \left[ \int_{-\pi}^{\pi} b_r(\theta_r, \phi) d\phi \right] NV(\theta_s) a(R) h(R) \right\} dR, \quad (48)$$

where

$A$  = scale factor (function of wind speed, rain rate, and frequency) or noise source level *at the air/sea interface* at vertical incidence ( $\mu\text{Pa}^2/\text{Hz/steradian}$ )

$N$  = surface radiation pattern including loss owing to a near-surface bubble layer

$a(R)$  = a term that accounts for propagation and interface (reflection) loss

$h(R)$  = "spreading" loss, from surface generator to receiver

$b_r(\theta_r, \phi)$  = receiver beam pattern (intensity ratio)

$R$  = horizontal range to surface generator

$R_{\max}$  = maximum range for integration over surface area

$\theta_s$  = surface grazing angle for ray between receiver and surface

$\theta_r$  = ray angle at the receiver (positive angles being above horizontal)

$\phi$  = azimuthal angle.

Multipaths are implicitly taken into account by summing over all relevant paths connecting the surface to the receiver at each range increment as shown in Figure 15a. To determine the number of requisite paths and  $R_{\max}$  for a given environment, several



trial runs are usually made in which these parameters are increased until  $P_S$  converges to a stable upper limit.

The second expression for  $P_S$ , illustrated in Figure 15b, is best suited to computer models that propagate a fan of ray tubes (indexed by elevation angle rather than horizontal range) emanating from the receiver. In this case, the integration is over elevation angle and is given by<sup>49</sup>

$$P_S = 2\pi A \int_{-\pi/2}^{\pi/2} H(\theta_r) B(\theta_r) d\theta_r, \quad (49)$$

where

$$B(\theta_r) = \frac{1}{2\pi} \int_{-\pi}^{\pi} b_r(\theta_r, \phi) d\phi \quad (50)$$

and

$$H(\theta_r) = N(\theta_s) \frac{\cos\theta_r}{\sin\theta_s} \sum_{k=0}^M 10^{-TL_k/10}, \quad (51)$$

where  $\theta_s$  is a function of  $\theta_r$ .

Equation 49 conveniently factors the noise into  $B(\theta_r)$ , a received noise beam pattern, and  $H(\theta_r)$ , a propagation term weighted by the surface radiation pattern,  $N(\theta_s)$ . The summation term in Eq. 51 represents the absorption loss along each ray (tube) plus the boundary bounce loss for each boundary interaction. The quantity  $M$  is the total number of boundary interactions required for  $H(\theta_r)$  to converge and is assumed to be determined automatically in computer implementation of Eqs. 49-51. For example, if two boundary bounces ( $M = 2$ ) are sufficient for  $H(\theta_r)$  to converge to 95% of the value that would be obtained for  $M = \infty$ , then the transmission loss for the path from radiator  $R$  shown in Figure 15b is

$$TL_2 = \alpha(s_1 + s_2 + s_3) + RL(\theta_p) + SBL(\theta_s). \quad (52)$$

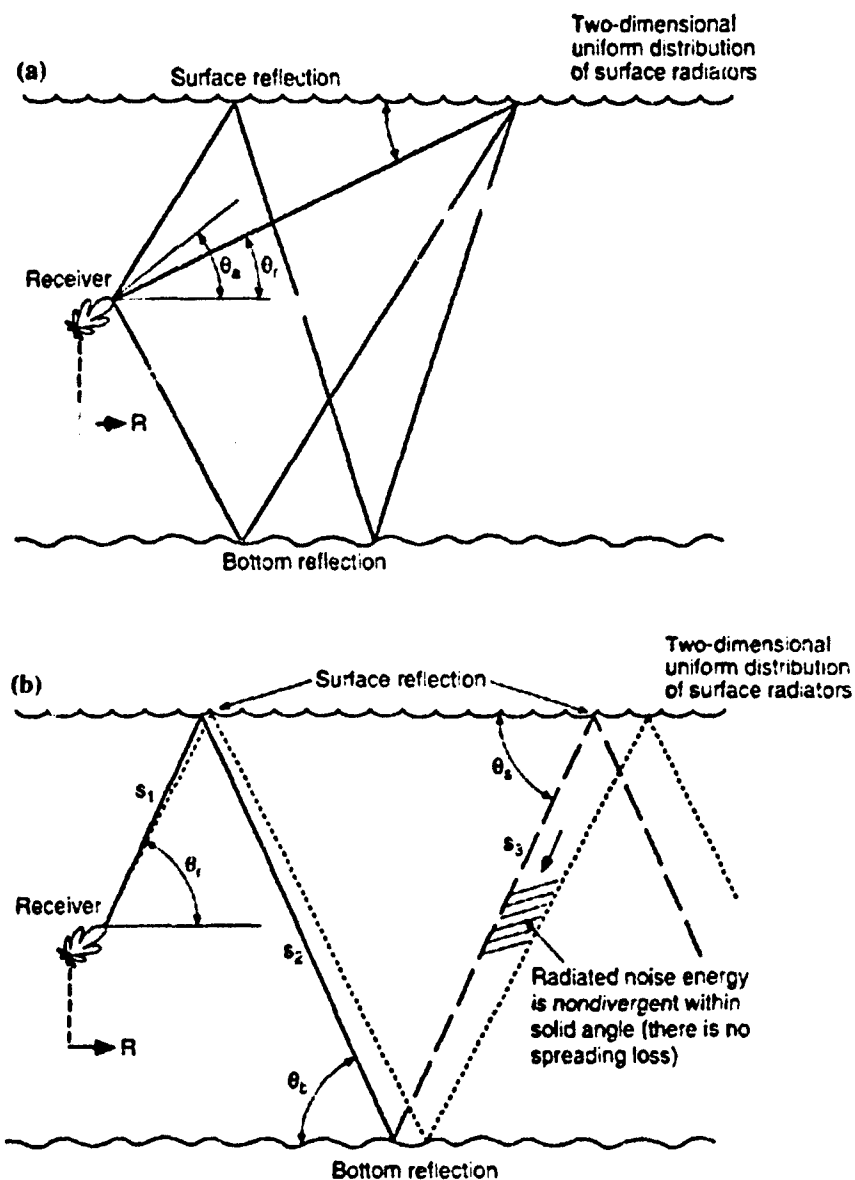


Figure 15. Diagrams illustrating two methods of calculating the surface-generated noise level for a hydrophone located at depth  $D$ , corresponding to Eqs. 48 and 49. The method shown in 15a uses range to index rays from the surface to the receiver; the method in 15b uses the received elevation angle.

where  $\theta_b$  is the bottom grazing angle and  $s_1$ ,  $s_2$ , and  $s_3$  are the lengths shown in Fig. 15b. Expressions for the absorption coefficient  $\alpha$ , bottom loss  $RL$ , and surface bubble loss  $SBL$  are given in Sections I, V, and II.C, respectively.

## 2. Simplified Expressions for Isovelocity, Deep Water Conditions

For isovelocity conditions and omnidirectional or highly directional hydrophones, Eqs. 48 and 49 can be simplified to provide analytical expressions useful under a wide range of conditions. An omnidirectional hydrophone is defined by  $b_r(\theta, \phi) = 1$ . Performing the double integration (using numbers given in Section D.3) in Eqs. 48 and 49 yields

$$P_S = 2\pi A E_3 (0.23\alpha D + \beta_v) \quad (53)$$

where  $D$  is the hydrophone depth in meters and  $\beta_v$  is the depth-integrated total extinction cross section for a near-surface bubble layer. (An expression for  $\beta_v$  in terms of the depth-integrated bubble density is given by Eq. 5.) The quantity  $E_3$  is the third-order exponential integral function and is defined as

$$E_3(x) = \int_1^\infty \frac{e^{-xt}}{t^3} dt \quad (54)$$

If both chemical absorption ( $\alpha$ ) and bubble absorption ( $\beta_v$ ) effects are negligible, Eq. 53 reduces to

$$P_S = \pi A \quad (55)$$

If, for example, the argument of  $E_3$  in Eq. 53 is less than 0.06, then the error in using Eq. 55 instead of Eq. 53 is less than 0.5 dB. Equations 53 and 55 are based on only direct path contributions to the noise and therefore do not include multipaths. Thus these expressions are most accurate for either the deep ocean or environments in which the bottom is quite soft and has an associated high bounce loss.

For narrow beams and relatively high grazing angles, the received noise level can be approximated by

$$P_S = A \sin \theta_a 10^{-[2\alpha r_a + SBL(\theta_a)]/20} \Delta \Omega, \quad (56)$$

where  $\theta_a$  is the beam axis elevation angle,  $r_a$  is the slant range to the surface for the beam axis ray, and  $\Delta \Omega$  is the equivalent solid angle of the receiver beam. This approximation relies on a small range of variation of  $\sin \theta 10^{-SBL(\theta)/20}$  over the beam pattern. Tests using this approximation compared with evaluations of Eq. 48 have shown that, for  $\theta_a > 25^\circ$  (where  $\theta_a$  is the elevation angle of the sonar; see Figure 15a) and  $\Delta \theta < 10^\circ$  (where  $\Delta \theta$  is the beamwidth in elevation angle), the results given by Eq. 56 are within 0.5 dB of those given by Eq. 48. This holds true even for nonisovelocity conditions and realistic sound speed profiles because at high grazing angles the effects of the sound speed profile are minimized.

### 3. Surface Radiation Pattern (N)

The primary environmental quantities of interest in Eqs. 48 and 49 are  $A$  and  $N(\theta_s)$ . Most studies of the surface radiation pattern  $N$  have shown good agreement with a dipole radiation pattern for ambient noise generated at the sea surface.<sup>50,50,51</sup> At higher wind speeds and frequencies, however, this radiation pattern is modified by a near-surface layer of bubbles through which the noise generated at the air/sea interface must propagate. The resultant effective noise radiation pattern below this bubble layer<sup>52</sup> is

$$N(\theta_s) = 10^{-SBL(\theta_s)/20} \sin^2 \theta_s, \quad (57)$$

where the surface bubble loss is given by Eqs. 28a and 28b. Since  $SBL$  is inversely proportional to  $\sin \theta_s$ , radiation at the lowest grazing angles is the most strongly affected by the presence of an absorptive bubble layer. Figure 16 shows that, as expected, the radiation pattern ( $N$ ) varies most rapidly with wind speed at the lowest grazing angles; the variation at vertical incidence is small even at the highest wind speeds shown.

### 4. Noise Level at the Air/Sea Interface at Normal Incidence (A), Wind Effects

Measurements of wind-generated noise have shown that wind speed is the main environmental parameter governing the noise scale factor  $A$ . When the sea surface

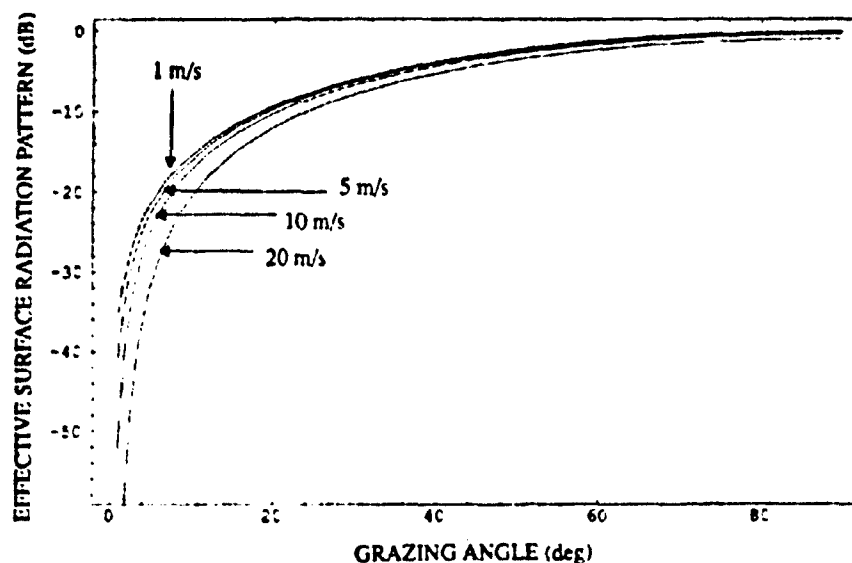


Figure 16. The effective surface radiation pattern showing the dipole pattern at low wind speeds, when near-surface bubble absorption is negligible, and the increasing attenuation of the noise level, especially at low grazing angles, as bubble absorption increases with wind speed ( $f = 20$  kHz).

becomes colder than the air above, however, the component of  $A$  due to wind ( $A_w$ ) also becomes a function of the air/sea temperature difference.<sup>53</sup> At a reference frequency of 20 kHz, this dependence on wind speed and air/sea temperature difference is expressed as

$$10 \log A_{w, 20} = \begin{cases} 20.5 + 22.4 \log U & \Delta T < 1^\circ\text{C} \quad U \geq 1 \text{ m/s} \\ 20.5 + 22.4 \log U - 0.26 (\Delta T - 1.0)^2 & \Delta T \geq 1^\circ\text{C} \quad U \geq 1 \text{ m/s} \end{cases} \quad (58)$$

where  $\Delta T = T_{\text{air}} - T_{\text{sea}}$  and  $U$  is the wind speed in meters per second at a 10 m reference height.<sup>20,52-54</sup> The temperature difference term is usually not important; typically it only becomes significant for coastal locales with offshore winds or for enclosed seas during the summertime.

The frequency dependence of the noise level at the sea surface is

$$10 \log A_w = 10 \log A_{w,20} + 20.7 - 15.9 \log f, \quad U \geq 1 \text{ m/s} \quad (59)$$

This is the noise source level *at the air/sea interface* (the effects of a near-surface bubble layer have been incorporated into the expression for the radiation pattern, Eq. 57).

The ambient noise levels predicted for an omnidirectional hydrophone in an iso-velocity, deep water situation can be compared to the Wenz curves through the use of either Eq. 55 (ignoring bubble effects) or Eq. 53 (which includes bubble effects through the inclusion of the depth-integrated total extinction cross section  $\beta_t$ ). The result of this comparison is shown in Figure 17a for frequencies from 1–100 kHz for several sea states. (The wind speeds in meters/second appropriate for each sea state were taken from Table 2 in Section II.A.) There are three notable features: (1) the effect of bubbles is predicted to be negligible at low sea states; (2) at sea state 0 (ss0), Eqs. 53 and 55 predict lower noise levels than the Wenz curves; (3) at sea states other than ss0, Eqs. 53 and 55 predict higher noise levels than the Wenz curves. These last two features can be examined relative to a set of data acquired by Farmer and Lemon<sup>52</sup> at 4.3 kHz for wind speeds of 0.5–25 m/s. Figure 17b shows those data along with the predictions of Wenz and Eq. 53, indicating that Eq. 53 is a better predictor for these data: i.e., the data show lower noise levels than the Wenz predictions at low wind speeds and higher noise levels at high wind speeds.

##### 5. Noise Level at the Air/Sea Interface at Normal Incidence (A), Combined Wind and Rain Effects

Recent measurements of rain noise in the open ocean have shown that the noise level depends on both rain rate and wind speed.<sup>54–57</sup> The scale factor at 20 kHz,  $A_{r,20}$ , is modeled simply by

$$10 \log A_{r,20} = b(U) + a(U) \log RR \quad RR \geq 10^{-2} \text{ mm/h} \quad (60)$$

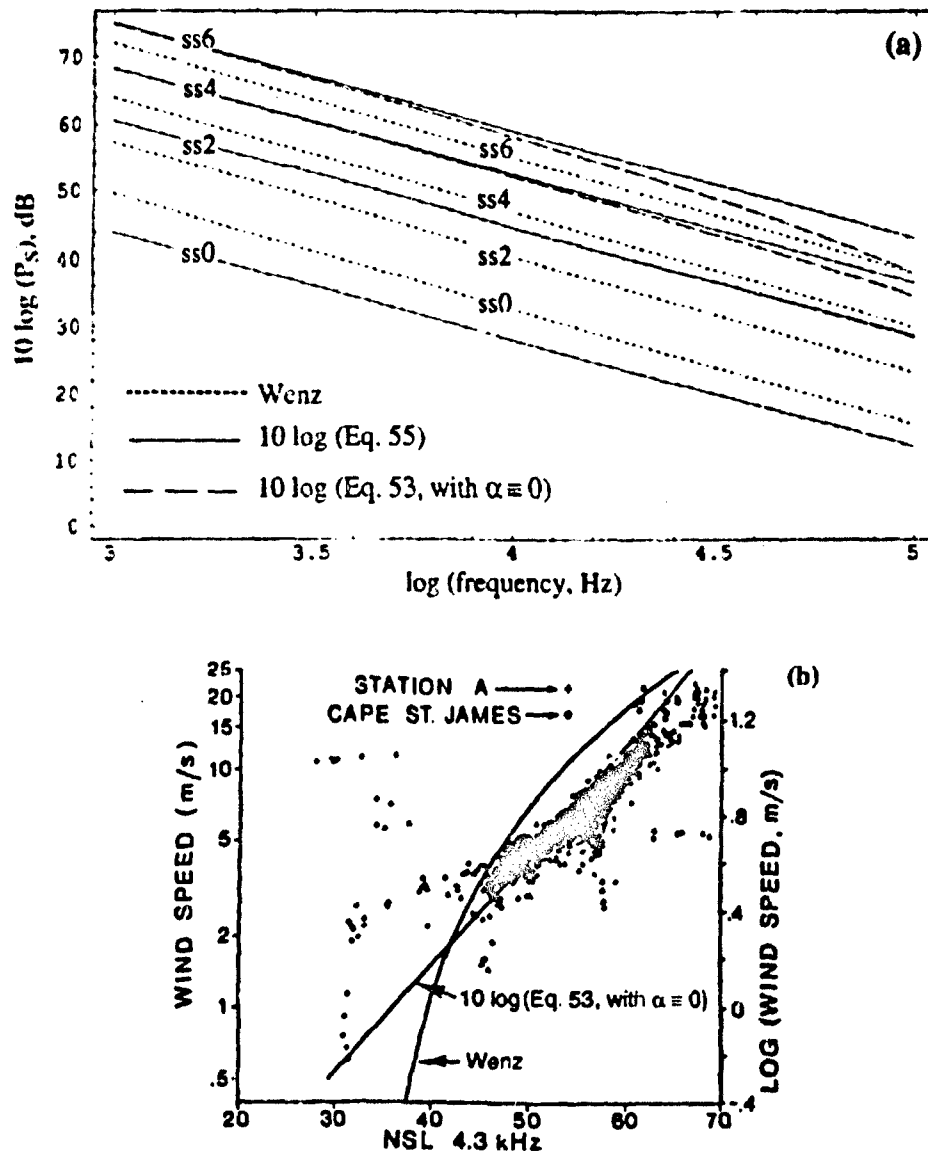


Figure 17. (a) Pressure received at an omnidirectional hydrophone calculated via the Wenz equation, via  $10 \log(\text{Eq. 55})$ , which does not include bubble effects, and via  $10 \log(\text{Eq. 53, with } \alpha \approx 0)$ , which does include bubble effects. (b) Wenz equation and  $10 \log(\text{Eq. 53, with } \alpha \approx 0)$  compared with data taken by Farmer and Lemon.<sup>52</sup>

where  $RR$  is the rain rate in millimeters/hour and the dependence on wind speed comes in through the coefficients  $a$  and  $b$ :

$$a = \begin{cases} 25.0, & U \leq 1.5, \\ 5.0 + 5.7(5.0 - U), & 1.5 < U < 5.0, \\ 5.0, & U \geq 5.0, \end{cases} \quad (61)$$

and

$$b = \begin{cases} 41.6, & U \leq 1.5, \\ 50.0 - 2.4(5.0 - U), & 1.5 < U < 5.0, \\ 50.0, & U \geq 5.0. \end{cases} \quad (62)$$

As with the wind noise spectrum, the model for the frequency spectrum of rain noise was obtained by making power law fits to measured spectra. To maintain simplicity in the modeled spectra, rain noise data taken at very low wind speeds ( $< 3$  m/s) and displaying highly peaked spectra are not used in the fitting procedure (Refs. 58 and 59 show examples of these highly peaked spectra measured in a lake). The resultant rain noise spectra are

$$10 \log A_r = \begin{cases} 10 \log A_{r,20} - 10.0 \log f, & 1 \leq f < 10, & RR \geq 10^{-2} \text{ mm/h}, \\ 10 \log A_{r,20} + 49.0 \log f - 59.0, & 10 \leq f < 16, & RR \geq 10^{-2} \text{ mm/h}, \\ 10 \log A_{r,20}, & 16 \leq f \leq 24, & RR \geq 10^{-2} \text{ mm/h}, \\ 10 \log A_{r,20} - 23.0 \log f + 31.7, & 24 < f \leq 100, & RR \geq 10^{-2} \text{ mm/h}. \end{cases} \quad (63)$$

As with the wind noise spectra, a reference frequency of 20 kHz was chosen. The principal difference between the recommended spectra given in Eq. 63 and the highly peaked spectra mentioned earlier occurs only in the vicinity of this plateau. The user is cautioned that data on rain rate are primarily for rain rates less than 10 mm/h. There are sparse data which indicate that for rain rates greater than 10 mm/h Eq. 63 may overpredict the noise level by at least several decibels. Therefore we recommend that 10 mm/h be used as the model input for  $RR > 10$  mm/h.

To find the scaling factor  $A$  when both wind and rain are present, simply add the two contributions as follows:

$$10 \log A = 10 \log(A_w + A_r) \quad (64)$$



From Eqs. 58 and 60, it can be seen that neither contribution goes to zero at zero wind speed or no rain. In accordance with available data, we set  $A_w = 0$  when  $U < 1$  m/s and  $A_r = 0$  when  $RR < 10^{-2}$  mm/h. Under these circumstances, either the hydrophone system's self-noise or thermal noise is the limiting noise; thermal noise tends to be dominant at higher frequencies (above ~30 kHz). The ambient noise levels predicted for an omnidirectional hydrophone in an isovelocity, deep water environment for various combinations of sea state (where the appropriate wind speed in meters/second for each sea state was determined from Table 2 in Section II.A) and rain rate are shown in Figure 18. A comparison between the predictions of the ambient noise model and one set of data from Ref. 55 is shown in Figure 18b.

## 6. Summary

We believe the model presented in Eq. 59 for wind-generated ambient noise is reasonably accurate, particularly for sea surface temperatures that are nearly the same as or warmer than the air above: in this case, the model is consistent with a large body of data extending back to WW II. The only significant deviation is when it is snowing or when the air temperature is below freezing or both<sup>54</sup> (in which case the noise level is consistently 5 dB less than that given by Eq. 59). The quantity with the greatest degree of uncertainty is the surface bubble loss effect (Eq. 57). As discussed in Section II.C, *SBL* displays a wide range of variability for a given wind speed.

The rain noise model, on the other hand, has much less data to support it. Also, it is based on the occurrence of "normal" rain, i.e., rain containing droplets greater than 2 mm in diameter. Reference 60 has shown that for "misty" rain the noise levels can be 30 dB higher than the model predictions for frequencies above 10 kHz. As an aid to the user, Figures 19a and 19b show the received noise field (Eq. 48 or 49) as a function of elevation angle for frequencies of 5, 15, and 40 kHz and a soft mud bottom. The bottom loss is large and increases with frequency, so that the effect of ambient noise energy being scattered off the bottom is minimal at 40 kHz (Figure 19c). Comparison of Figures 19b and 19d, which is the same as Figure 19b but for a hard bottom, indicates the significance of bottom type on the angular dependence of the ambient noise received.

Thermal noise at frequencies below 100 kHz is usually of little consequence and has received little experimental attention. Recent measurements, however, confirm the thermal noise model presented here for omnidirectional hydrophones.<sup>54</sup>

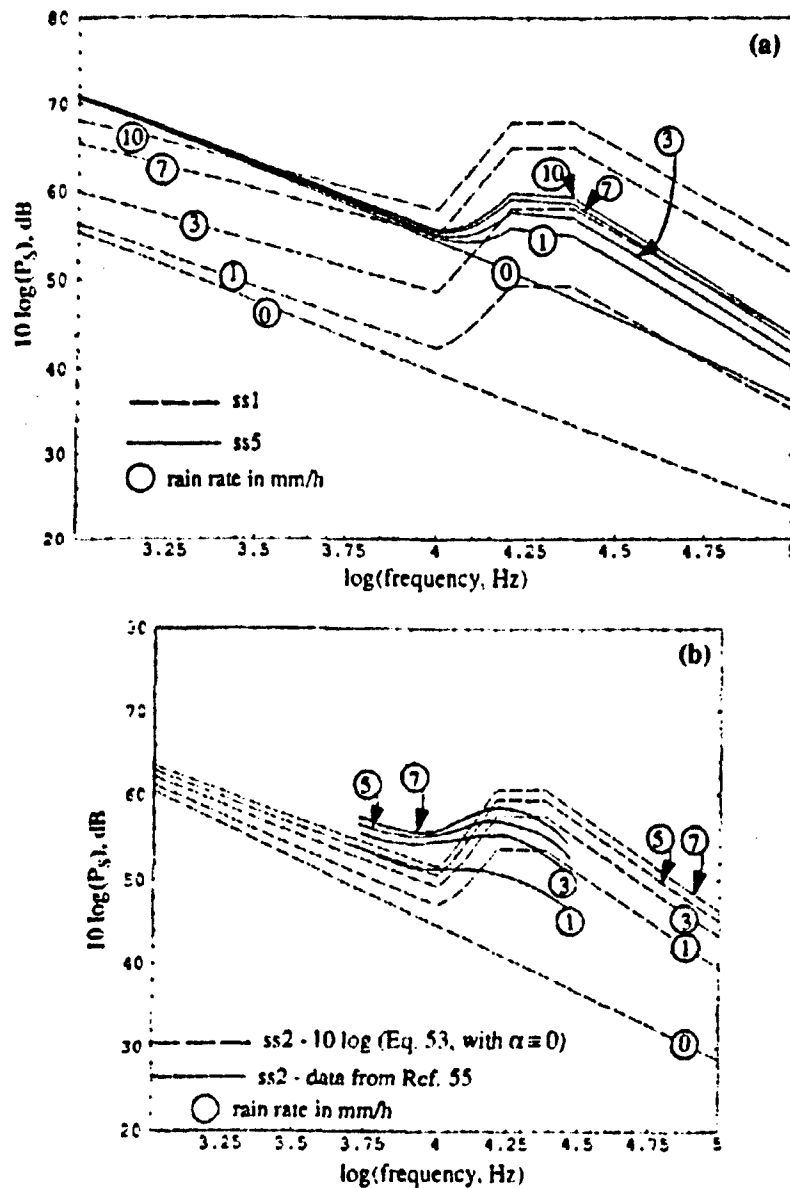


Figure 18. (a)  $10 \log$  (Eq. 53, with  $\alpha \approx 0$ ) plotted for five rain rates and two sea states. (b) Comparison between  $10 \log$  (Eq. 53, with  $\alpha \approx 0$ ) and some of the data from Ref. 55.

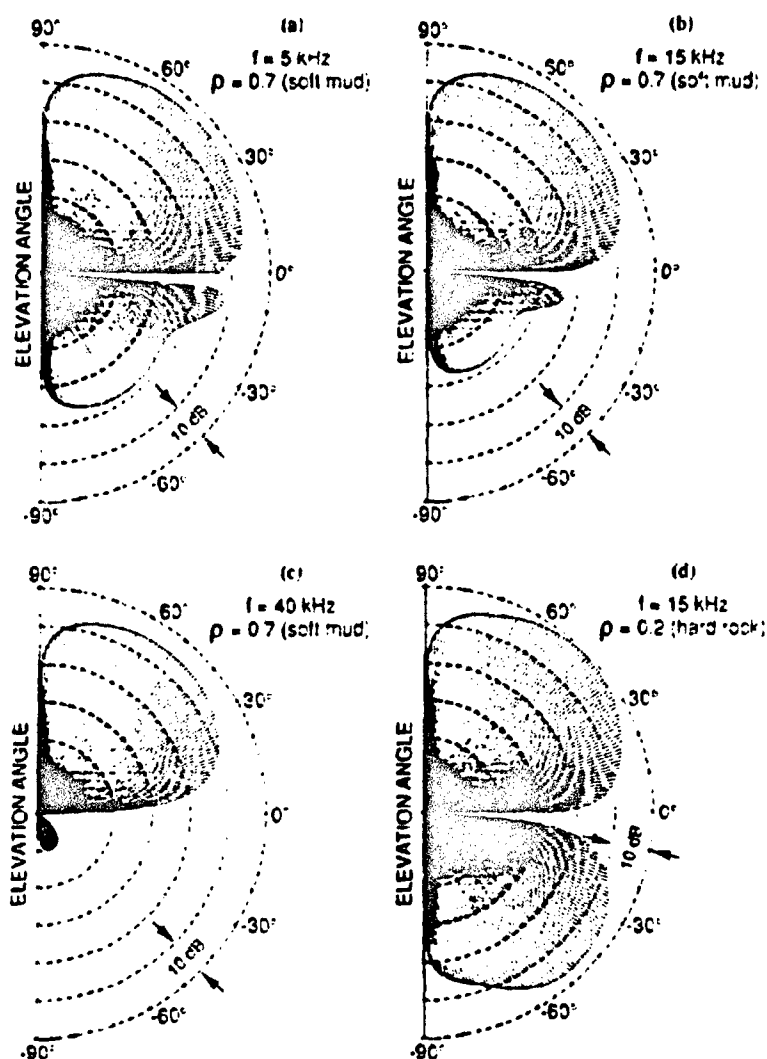


Figure 19. Polar diagrams of  $H(\theta)$  from Eq. 53, showing elevation angle dependence of the received noise field for a receiver at 120 m depth, a wind speed of 2.5 m/s, and a water depth of 400 m. (a)–(c) For a bottom of soft mud with a porosity of 0.7, both bottom loss and absorption increase rapidly as the frequency is increased from 5 kHz to 40 kHz; the effect is most evident for the down-looking angles. (d) For a hard rock or gravel bottom at 15 kHz, the levels for bottom-reflected energy are significantly higher.

TR 9407 II-47

ADB199453

## REFERENCES — Section II

1. S.D. Smith, "Coefficients for sea surface wind stress, heat flux, and wind profiles as a function of wind speed and temperature," *J. Geophys. Res.*, 93(C12), 15,467-15,472 (December 1988).
2. J.L. Hanson, Winds, waves, and bubbles at the air-sea boundary, *Johns Hopkins Technical Digest*, 14, 200-208 (1993).
3. N. Bowditch, *American Practical Navigator* (U.S. Government Printing Office, 1958), p. 1059.
4. R.H. Fairbridge, *The Encyclopedia of Oceanography* (Reinhold Publ. Co., New York, 1966).
5. E.L. Bialek (compiler), *Handbook of Oceanographic Tables* (SP-68) (U.S. Naval Oceanographic Office, Washington, D.C., 1966).
6. Bunker Ramo, "A Guide to Sea State, with a Listing of Visual and Tactile Clues" (source: Director of Marketing, Ocean Surveillance Systems, 31717 La Tienda Drive, Westlake Village, California 91361; undated), 1 p.
7. D.G. Groves and L.M. Hurt, *Ocean World Encyclopedia* (McGraw-Hill, New York, 1980).
8. W.J. Pierson, Jr., and L. Moskowitz, "A proposed spectral form for fully developed wind seas based on the similarity theory of S. A. Kitaigorodskii," *J. Geophys. Res.*, 69, 5181-5190 (1964).
9. D.B. Chelton, K.J. Hussey, and M.E. Parke, "Global satellite measurements of water vapour, wind speed and wave height," *Nature*, 294, 529-532 (1981).
10. P.A. Crowther, "Acoustical scattering from near-surface bubble layers," in *Cavitation and Inhomogeneities in Underwater Acoustics*, edited by W. Lauterborn (Springer-Verlag, New York, 1980), pp. 195-204.
11. S.T. McDaniel and A.D. Gorman, "Acoustic and radar sea-surface backscatter," *J. Geophys. Res.*, 87, 4127-4136 (1982).
12. S.T. McDaniel, "Sea surface reverberation: A review," *J. Acoust. Soc. Am.*, 94, 1905-1922 (1993).
13. S.O. McConnell and P.H. Dahl, "Vertical incidence backscatter and surface forward scattering loss from near-surface bubbles," *OCEANS '91*, 1, 434-441, 1991.

II-48 TR 9407

ADB199453

14. C. Devin, "Survey of thermal, radiation, and viscous damping of pulsating air bubbles in water," *J. Acoust. Soc. Am.*, 31, 1654-1667 (1959).
15. S.O. McConnell, J.G. Lilly, and G.R. Steiner, "Modeling of High-Frequency Surface Reverberation and Ambient Noise (U)," APL-UW 7821, Applied Physics Laboratory, University of Washington, November 1978. (Confidential)
16. J.M. Monti, P.D. Koenigs, B. Nützel, and H. Herwig, "The Influence of Surface Roughness and Bubbles on Sea Surface Acoustic Scattering," NUSC TR 7955, November 1987.
17. G.R. Garrison, S.R. Murphy, and D.S. Potter, "Measurements of backscattering of underwater sound from the sea surface," *J. Acoust. Soc. Am.*, 32, 104-111 (1960).
18. S.T. McDaniel, "Diffractive corrections to the high-frequency Kirchhoff approximation," *J. Acoust. Soc. Am.*, 79, 952-957 (1986).
19. R. Waltzman and E.I. Thorsos, "High Frequency Bistatic and Monostatic Surface Backscatter Measured in the Open Ocean," APL-UW 2-82, Applied Physics Laboratory, University of Washington, October 1982.
20. S.O. McConnell, "Remote sensing of the air-sea interface using microwave acoustics," in *Proceedings of OCEANS '83* (Marine Technology Society and IEEE, 1983), pp. 85-92.
21. D.E. Barrick, "Rough surface scattering based on specular point theory," *IEEE Trans. Antennas and Propagation*, AP-16, 449-454 (1968).
22. P.D. Mourad and D.R. Jackson, "High frequency sonar equation models for bottom backscatter and forward loss," *OCEANS '89*, Seattle, Washington, 1989.
23. E.C. Monahan, "Occurrence and evolution of acoustically relevant sub-surface bubble plumes and their associated, remotely monitorable, surface whitecaps," in *Natural Physical Sources of Underwater Sound*, 503-517, B.R. Kerman (ed.), Kluwer Academic, Boston, 1993.
24. B. Nützel, H. Herwig, and A. Schmidt, "Acoustic and microwave backscattering of the sea surface," *IEEE OCEANS 93*, Victoria, B.C., 1993.
25. G.R. Valenzuela and M.B. Laing, "Study of Doppler spectra of radar sea echo," *J. Geophys. Res.*, 75, 551-563 (1970).
26. E.I. Thorsos, "Surface Forward Scattering and Reflection," APL-UW 7-83, Applied Physics Laboratory, University of Washington, May 1984.

TR 9407 II-49

27. D.E. Funk and K.L. Williams, "A physically motivated simulation technique for high-frequency forward scattering derived using specular point theory," *J. Acoust. Soc. Am.*, 91(5), 2606-2614 (May 1992).
28. S.O. McConnell, "Surface Forward Reflection and Scattering, Surface Back-scattering, and Ambient Noise Measurements Made During GTV Adaptive Signal Processing Test (U)," APL-UW TM 5-83, Applied Physics Laboratory, University of Washington, 1983. (Confidential)
29. P.H. Dahl and S. O. McConnell, "Measurements of Acoustic Spatial Coherence in a Near-Shore Environment," APL-UW TR 9016, Applied Physics Laboratory, University of Washington, August 1990.
30. P.H. Dahl, "Revisions and Notes on a Model for Bubble Attenuation in Near-Surface Acoustic Propagation," APL-UW TR 9411, Applied Physics Laboratory, University of Washington, July 1994.
31. P.H. Dahl, "Bubble Attenuation Effects in High-Frequency Surface Forward Scattering Measurements from FLIP," APL-UW TR 9307, Applied Physics Laboratory, University of Washington, May 1993.
32. E.I. Thorsos, "High frequency surface forward scattering measurements," presented at the 108th meeting of the Acoustical Society of America, October 1984.
33. P.H. Dahl and A. T. Jessup, "On bubble clouds produced by breaking waves: An event analysis of ocean acoustic measurement," accepted by *J. Geophys. Res.*, August 1994.
34. P. A. Crowther, H. J. S. Griffiths, and A. Hansla, "Dependence of sea surface noise in narrow beams on windspeed and vertical angle," in *Natural Physical Sources of Underwater Sound*, pp. 31-44, B.R. Kerman, (ed.), Kluwer Academic Publishers, Boston, 1993.
35. M. V. Hall, "A comprehensive model of wind-generated bubbles in the ocean and predictions of the effects on sound propagation at frequencies up to 40 kHz," *J. Acoust. Soc. Am.*, 86, 1103-1117 (1989).
36. R.J. Christian, D.G. Browning, and D.G. Williams, "Revisions to an empirical surface loss model using a correction for pH-dependent attenuation," presented at the 127th Meeting of the Acoustical Society of America, Cambridge, Massachusetts, June 1994.
37. C. Eckart, "The scattering of sound from the sea surface," *J. Acoust. Soc. Am.*, 25, 566-570 (1953).

U-50 TR 9407

ADB199453

38. O.M. Phillips, *The Dynamics of the Upper Ocean*, Cambridge University Press, Cambridge, Massachusetts, 1977, pp. 177-179.
39. C.S. Cox and W.H. Munk, "Statistics of the sea surface derived from sun glitter," *J. Mar. Res.*, 13, 198-227 (1954).
40. P.H. Dahl and A. Al-Kurd, "Time Spread and Frequency Coherence in Acoustic Forward Scattering from the Sea Surface," APL-UW TR 9405, Applied Physics Laboratory, University of Washington, May 1994.
41. W.I. Roderick and W.G. Kanahis, "Scattering coefficients and Doppler spectra of specularly scattered sound from the sea surface," *J. Acoust. Soc. Am. Suppl. 1*, 69, S96 (1981).
42. R.L. Swarts and C.J. Eggen, "Simplified model of the spectral characterization of high-frequency surface scatter," *J. Acoust. Soc. Am.*, 59, 846-851 (1976).
43. M.J. Pollack, "Surface reflection of sound at 100 kc," *J. Acoust. Soc. Am.*, 30, 343-347 (1958).
44. D.C. Witmarch, "Underwater-acoustic-transmission measurements," *J. Acoust. Soc. Am.*, 35, 2014-2018 (1983).
45. E.P. Gulin and K.I. Malyshev, "Statistical characteristics of sound signals reflected from the undulating sea surface," *Sov. Phys. Acoust.*, 8, 228-234 (1963).
46. S.O. McConnell and J.G. Lilly, "Surface Reverberation and Ambient Noise Measured in the Open Ocean and Dabob Bay (U)," APL-UW 7727, Applied Physics Laboratory, University of Washington, 15 January 1978.
47. P. Beckmann and A. Spizzichino, *The Scattering of Electromagnetic Waves from Rough Surfaces* (Pergamon Press, Oxford, 1963).
48. R.J. Urick, *Principles of Underwater Sound* (McGraw-Hill, New York, 1975), p. 187.
49. J.G. Dworski and J.A. Mercer, "Ambient Noise and Its Impact on the QSAM System," APL-UW TM 1-86, Applied Physics Laboratory, University of Washington, 1986.
50. E.M. Arase and T. Arase, "Correlation of ambient sea noise," *J. Acoust. Soc. Am.*, 40, 205-210 (1966).

TR 9407 II-51

ADB199453

51. R.M. Hanson, "The effect of propagation conditions on wind-generated noise at real shallow water sites," in *Sea Surface Sound: Natural Mechanisms of Surface Generated Noise in the Ocean*, edited by B.R. Kerman (Kluwer Academic Publishers, Boston, 1988), pp. 281-294.
52. D.M. Farmer and D.D. Lemon, "The influence of bubbles on ambient noise at high wind speeds," *J. Phys. Oceanogr.*, **14**, 1762-1778 (1984).
53. P.C. Wille and D. Geyer, "Measurements on the origin of the wind-dependent ambient noise variability in shallow water," *J. Acoust. Soc. Am.*, **75**, 173-185 (1984).
54. S.O. McConnell, "Behm Canal Ambient Noise Measurements: Final Report," APL-UW TM 2-89, Applied Physics Laboratory, University of Washington, April 1989.
55. J.A. Scrimger, D.J. Evans, and W. Lee, "Underwater noise due to rain—Open ocean measurements," *J. Acoust. Soc. Am.*, **85**, 726-731 (1989).
56. S.O. McConnell, M.P. Schilt, and J.G. Dworski, "Ambient noise measurements from 100 Hz to 80 kHz in an Alaskan fjord," *J. Acoust. Soc. Am.*, **91**, 1990-2003 (1992).
57. J.A. Nystuen, "An explanation of the sound generated by light rain in the presence of wind," in *Natural Physical Sources of Underwater Sound*, 659-668, B.R. Kerman (ed.), Kluwer Academic, Boston, 1993.
58. J.A. Scrimger, D.J. Evans, G.A. McBean, D.M. Farmer, and B.R. Kerman, "Underwater noise due to rain, hail, and snow," *J. Acoust. Soc. Am.*, **81**, 79-86 (1987).
59. J.A. Nystuen and D.M. Farmer, "The sound generated by precipitation striking the ocean surface," in *Sea Surface Sound: Natural Mechanisms of Surface Generated Noise in the Ocean*, edited by B.R. Kerman (Kluwer Academic Publishers, Boston, 1988), pp. 485-500.
60. J.A. Nystuen, "Rainfall measurements using underwater ambient noise," *J. Acoust. Soc. Am.*, **79**, 972-982 (1986).



### **III. Biological High-Frequency Ambient Noise**

ADB199453

## A. BACKGROUND

Invertebrates, fish, and marine mammals have long been known to be ambient noise sources. Many of these organisms produce sound levels that are well in excess of those produced by purely physical phenomena (wind, wave activity, rain, etc.) and are often as intense as those produced by many electronic systems (e.g., >200 dB at 1 m re 1  $\mu$ Pa). In many cases, this noise may interfere with or otherwise disrupt our ability to utilize high-frequency acoustic signals for detecting objects or for determining environmental noise sources. Biological noise sources are of particular significance in shallow water. There is a need to develop a set of parameters that will allow estimation of the potential for, and/or the levels of, such interference.

A principal source of ambient noise is snapping shrimp, though other invertebrates can contribute as well. Marine mammals, especially porpoises and dolphins, are a highly variable and unpredictable source of ambient noise. Many species of fish are also known to produce persistent levels of ambient noise in many, especially tropical, environments. Some data exist on these sources of ambient noise production, but much of the data is probably dated and may be seriously deficient at frequencies above 20 kHz. Some sources will be more difficult to predict than others, especially the more migratory marine mammals. However, benthic or less migratory sources (e.g., fish) can be predictable if measurements are available to establish a pattern of distribution, frequency of occurrence, and other abundance-related information.

## B. GENERALIZED FREQUENCY DISTRIBUTION

Some generalization of these sources of biological ambient noise is possible:

- (1) Frequencies less than 5 kHz will be strongly influenced by fish distributions.
- (2) Impulse noise producing a steady background level is dominated by invertebrates and can be severe at frequencies of 10 to 20 kHz and higher.

TR 9407 III-1

- (3) Intermittent pulses or periods of high ambient noise dominated by echolocation and vocalization by marine mammals at frequencies greater than 20 kHz will be a significant factor in some localities and extremely difficult to predict.

A summary of some of these sources is given in Table 1.

*Table 1. Signal characteristics of some significant sources of high-frequency biological ambient noise.*

Organism	Frequency Range (kHz)	Frequency of Peak Energy (kHz)	Pressure Level (dB at 1 m re 1 $\mu$ Pa)
Spiny Lobster ( <i>Palinuris</i> spp.)	0.04-1.2	0.006-0.8 2.5-4.7	97
Harbor Porpoise	*	20-150	112
Common Dolphin	*	20-100	140
Snapping Shrimp	2-200	4-8	155
Beluga Whale	*	40, 80, 120	160-180
Sperm Whale	0.2-32	5-6	174-184
Killer Whale	0.1-30	14	178
Bottlenose Dolphin	15-130	100-130	>200

\*Unknown

### C. GENERALIZED MARINE MAMMAL AMBIENT NOISE

No method is available to predict the occurrence of marine mammals in any environment, although the distribution of some mammals is known for broad areas. The frequency spectra for some of the whales and porpoises listed in Table 1 are shown in Figure 1. If marine mammal activity coincides with operations at a particular locality, it may be necessary to suspend measurement efforts until these animals depart. Otherwise, there will be periods of high-level aperiodic interference (biological ambient noise)

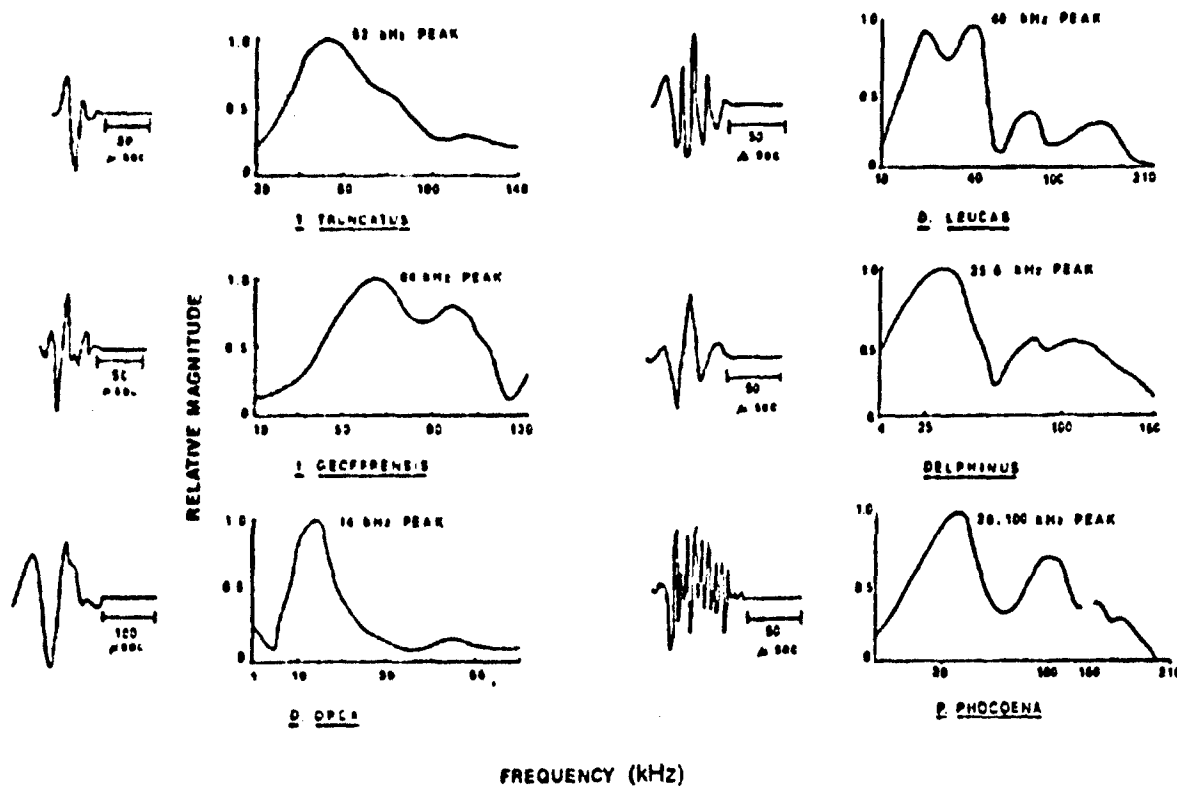


Figure 1. Time signature and spectral composition of sounds from selected whales and porpoises. (after Busnel and Fish<sup>1</sup>)

which will have to be accounted for or eliminated. Table 2 lists the species names of additional whales and porpoises that are known to produce such sounds; however, the exact spectral composition and levels of these sounds are unknown.

#### D. GENERALIZED SNAPPING SHRIMP LEVELS

The level of ambient noise produced by snapping shrimp will depend on three conditions: (1) the presence of suitable habitat, (2) the proximity of the listener to that habitat, and (3) the operating frequency. The general location of snapping shrimp is roughly bounded by 40°N to 40°S, approximately the boundary of the 11°C isotherm in winter (see Figure 2). In addition, water depths of less than 60 m within this general region are more likely to contain snapping shrimp populations. Shrimp populations will

TR 9407 III-3

Table 2. Other whale or dolphin species known to produce echolocation pulses.

Organism	Comments
<i>Cephalorhynchus</i> spp. (Heavy Sided Dolphin)	Coastal; southern hemisphere
<i>Grampus griseus</i> (Risso's Dolphin)	Oceanic; all oceans in temperate seas, including the Mediterranean.
<i>Globicephala melana</i> (Long-Finned Pilot Whale)	Oceanic but some coastal; most of North Atlantic and southern hemisphere.
<i>Kogia breviceps</i> (Pigmy Sperm Whale)	Frequently coastal; most of the temperate oceans.
<i>Kogia simus</i> (Dwarf Sperm Whale)	Similar to <i>K. breviceps</i> .
<i>Lagenorhynchus acutus</i> (Atlantic White-Sided Dolphin)	Continental shelf and shelf edge; North Atlantic.
<i>Lagenorhynchus albirostris</i> (White-Beaked Dolphin)	Continental shelf and shelf edge; North Atlantic
<i>Lagenorhynchus australis</i> (Peale's Dolphin)	Coastal and shelf; tip of South America
<i>Lagenorhynchus obscurus</i> (Dusky Dolphin)	Southern hemisphere
<i>Lagenorhynchus obliquidens</i> (Pacific White-Sided Dolphin)	Oceanic, but some coastal distribution.
<i>Phocoenoides dalli</i> (Dall's Porpoise)	Shelf slope but some coastal; North Pacific.
<i>Stenella coeruleoalba</i> (Striped Dolphin)	Oceanic; all N. Pacific, all N. Atlantic and Mediterranean.
<i>Stenella longirostris</i> (Spinner Dolphin)	Oceanic predominantly but some proximity to coastal waters.
<i>Stenella plagiodon</i> (Spotted Dolphin)	Oceanic; Atlantic south of Cape Cod and in Caribbean.
<i>Steno bredanensis</i> (Rough-Toothed Dolphin)	Coastal; eastern Japan, eastern and western Atlantic, occasional in central Atlantic.
<i>Tursiops aduncus</i> (Arabian Dolphin)	Indian Ocean and Red Sea subspecies of <i>T. truncatus</i>

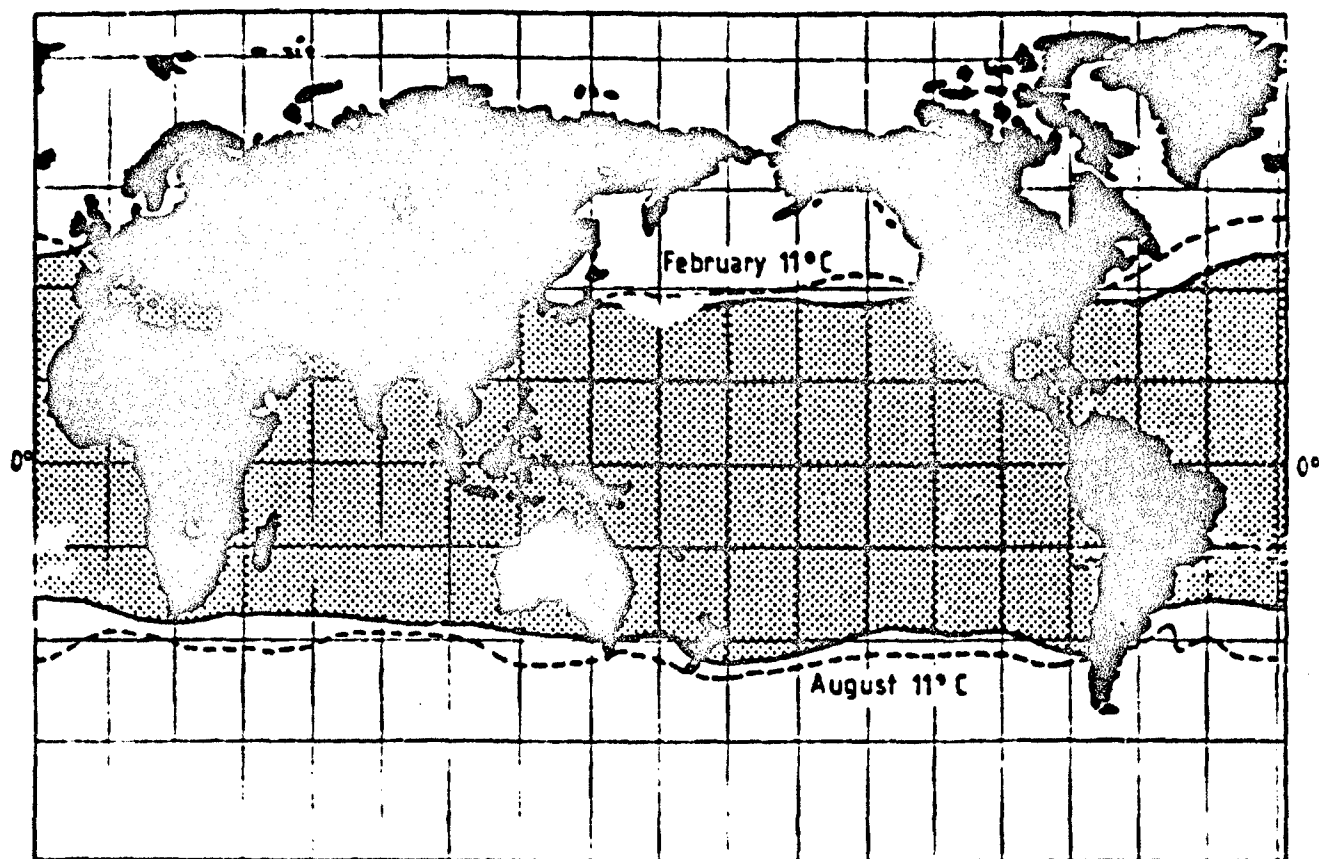


Figure 2. Worldwide distribution of snapping shrimp according to Johnson et al.<sup>2</sup> Snapping shrimp are found in the shaded area wherever the bottom depth is less than 60 m and the bottom sediment is suitable. (after Cato and Bell<sup>3</sup>).

be most abundant where there are numerous hiding places, as will be found on bottom sediments consisting of rough boulders, cobbles, or coral rubble. Shale or other loose rock structures are also favorable environments whereas sand or mud are not. Patches of suitable bottom types can be isolated or widely separated and may not be well documented on bottom sediment maps; in such cases, accurate survey data will be critical to identify the locations of possible snapping shrimp sites.

In close proximity to individual shrimp, the peak sound pressure level of an individual snap can be 140 to 160 dB re  $1 \mu\text{Pa}^2$ ; the noise spectral level is generally 60 to 80 dB (re  $1 \mu\text{Pa}^2/\text{Hz}$ ) (see Figure 3). The rate at which the spectral level decreases with

TR 9407 III-5

ADB199455

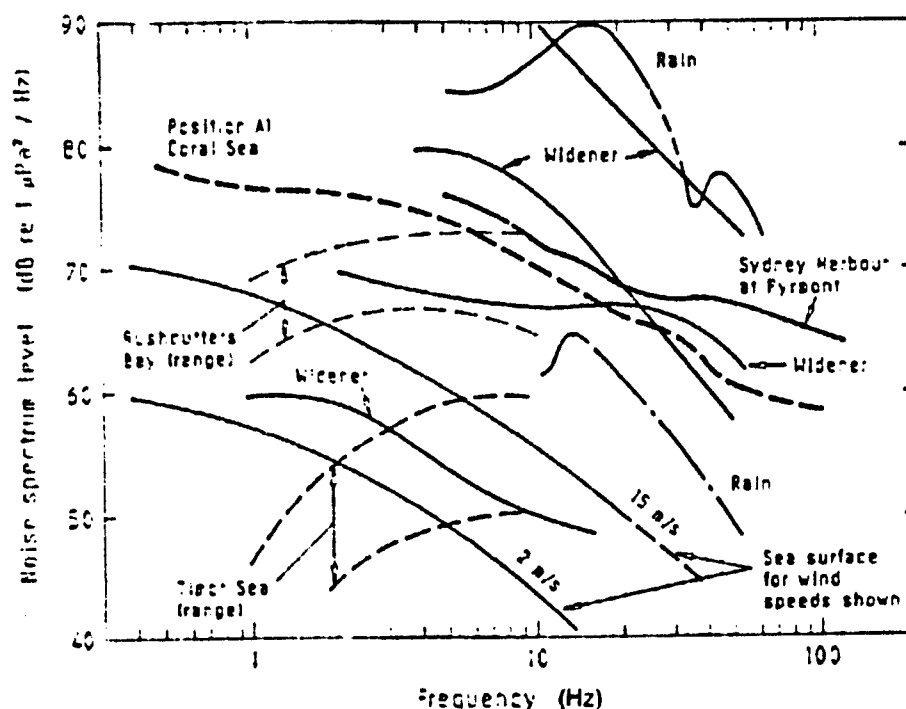


Figure 3. Comparison of time-averaged snapping shrimp noise spectra at different localities. The measurements labeled "Widener" were off Florida with a microphone resting on the bottom.<sup>4</sup> Spectra of surface-generated noise and rain noise are also shown. The precipitation rate was 1.2 mm/h for the lower curve and 260 mm/h for the upper curve. (after Cazo and Bell<sup>3</sup>)

distance from the center of a concentration of shrimp will depend on the frequency of operation (for an example of the one-way loss due to distance and attenuation at frequencies of 10–20 kHz, see Figure 4). Given the presence of snapping shrimp, then, in general, shrimp snaps will always be greater than wind-generated noise and approximately bounded by rain noise for frequencies between 10 and 200 kHz. There is no observed fluctuation by season for shrimp noise; however, there is a nighttime increase of up to 8 dB. This may reflect the activity of either the shrimp themselves or of other benthic animals, which then disturb the snapping shrimp.

The generalized falloff of noise spectral level with frequency is 0.13 dB/kHz from 5 kHz to 175 kHz, or approximately 20 dB from 25 kHz to 175 kHz (Figure 5). There is some direct evidence that shrimp snaps do not occur randomly but rather are frequently correlated with each other in bursts of pulses.

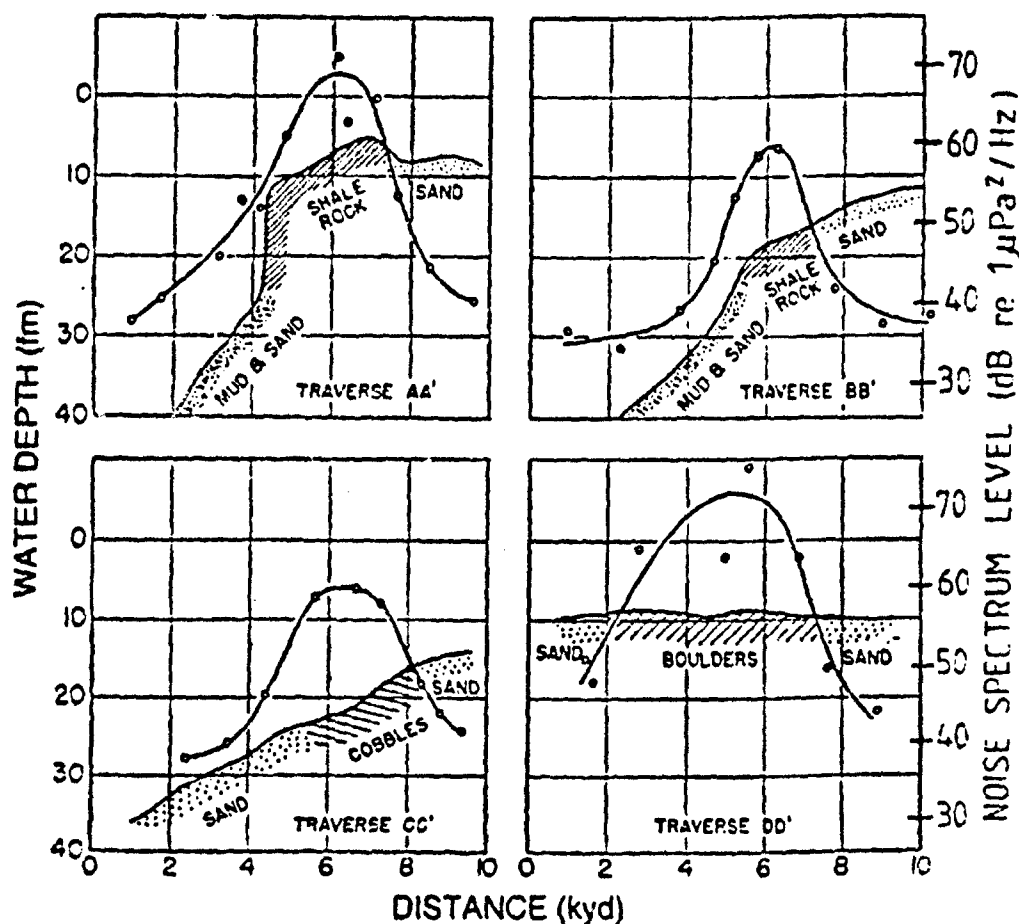


Figure 4. Variation of shrimp noise level off California during traverses over differing bottom sediments and depth. Levels shown use the average of 10, 15, and 20 kHz levels. (after Johnson et al.<sup>2</sup>, from Cato and Bell<sup>1</sup>)

If conditions are such that populations of snapping shrimp are potentially present, assume a level of 70 dB (for 5 kHz to 20 kHz) for the noise spectral level and make adjustments for frequency (for frequencies >20 kHz) and distance from the position of the shrimp concentration ( $0.13 \text{ dB/kHz}$  and  $20 \log \text{ range}$  plus  $2\alpha$  range, respectively). If it is nighttime, add 8 dB. The estimate will be approximate and will most likely be on the low side. Actual values of the noise spectral level may deviate from this estimate by more than 10 dB, but determining these values will require direct measurements in the environment of interest.



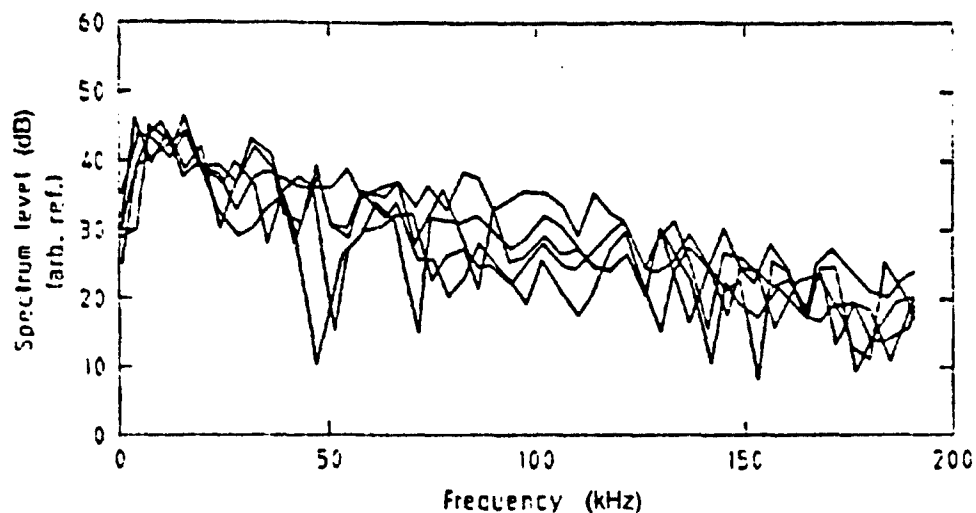


Figure 5. Overplot of multiple single shrimp snaps from Sydney Harbor showing the decline in spectral level with frequency. (after Cato and Bell<sup>3</sup>)

### E. OTHER INVERTEBRATE NOISE SOURCES

A number of other species of shrimp, crabs, sea urchins, and barnacles are known to produce clicks at various frequencies. These are itemized in Table 3. These sources of biological ambient noise are poorly studied, but may be of importance in some environments.

Table 3. Other invertebrates known to produce ambient noise.

Organism	Comments
Shrimp in the genera <i>Pontonia</i> , Typton, and <i>Coralliocaris</i>	Little is known about noise mechanisms and levels Little is known about noise mechanisms and levels
Various species of fiddler crabs, especially in the genus <i>Uca</i>	
The box crab <i>Calappa flammea</i>	Occurs in the Bahamas.
The black mussel <i>Mytilus edulis</i>	Produces pulse sounds at 1-4 kHz.
Some sea urchins: <i>Evechinus chloroticus</i> <i>Strongylocentrotus dröbachiensis</i> <i>Diadema setosum</i>	May produce sounds at 30 Hz - 5 kHz.
North Atlantic barnacles <i>Balanus eburneus</i> <i>Balanus balanoides</i>  <i>Balanus tintinnabulum</i> <i>Balanus perforatus</i>	Produces sounds similar to snapping shrimp Produces sounds similar to snapping shrimp; occurs in warm seas. Produces sharp clicks; oceanic, in warm seas Produces rhythmic rubbing sounds; occurs in the Mediterranean.

## REFERENCES — Section III

1. R.G. Busnel and J.F. Fish (editors), *Animal Sonar Systems* (Plenum Press, New York, 1979), 1135 pp.
2. M.W. Johnson, F.A. Everest, and R.W. Young. "The role of snapping shrimp (*Crangon and Synalpheus*) in the production of underwater noise in the sea," *Biol. Bull. Woods Hole*, 93(2), 122-138 (1947).
3. D.H. Cato and M.J. Bell. Ultrasonic Ambient Noise in Australian Shallow Water at Frequencies Up to 200 kHz. Technical Report MRI-TR-91\_23, Materials Research Laboratory, 1991. 28 pp.
4. M.W. Widener, "Ambient noise levels in selected shallow water off Miami, Florida," *J. Acoust. Soc. Am.*, 42, 904-905 (1967).

## BIBLIOGRAPHY — Section III

- Albers, V.M., 1965: *Underwater Acoustics Handbook—II* (Pennsylvania State University Press), 356 pp.
- Au, W.W.L., 1979: "Echolocation signals of the Atlantic bottlenose dolphin (*Tursiops truncatus*) in open waters," in *Animal Sonar Systems* edited by R.G. Busnel and J.F. Fish (Plenum Press, New York), pp. 251-290.
- Busnel, R.G. (editor), 1963: *Acoustic Behavior of Animals* (Elsevier, New York), 933 pp.
- Busnel, R.G. and J.F. Fish (editors), 1979: *Animal Sonar Systems* (Plenum Press, New York), 1135 pp.
- Cato, D.H., and M.J. Bell. 1991: Ultrasonic Ambient Noise in Australian Shallow Water at Frequencies Up to 200 kHz, Technical Report MRL-TR-91\_23, Materials Research Laboratory, 28 pp.
- Caldwell, D.K., J.H. Prescott, and M.C. Caldwell. 1960: "Production of pulsed sounds by the pigmy sperm whale *Kogia breviceps*," *Bull So. Calif. Acad. Sci.*, 65(4), 245-248.
- Diercks, J.K., 1979: "Signal characteristics for target localization and discrimination," in *Animal Sonar Systems*, R.G. Busnel and J.F. Fish (editors), Plenum Press, New York, 229-308.
- Ellis, R., 1980: *The Book of Whales*, Alfred Knopf, New York. 202 pp.

- Fish, M.P., and W.H. Mowbray, 1970: *Sounds of Western North Atlantic Fishes: A Reference File of Biological Underwater Sounds*, The Johns Hopkins Press, Baltimore.
- Hershkovitz, P., 1966: "Catalog of living whales," *Bull. Smithsonian Inst.*, 246, 1-259.
- Johnson, M.W., F.A. Everest, and R.W. Young, 1947: "The role of snapping shrimp (*Crango* and *Synalpheus*) in the production of underwater noise in the sea, *Biol. Bull. Woods Hole*, 93(2), 122-138.
- Johnson, M.W., 1948: "Sound as a tool in marine ecology. from data on biological noises and the deep scattering layer." *J. Marine Res.*, 7, 443-458.
- Knudsen, V.O., R.S. Alford, and J.W. Emling, 1948: "Underwater ambient noise," *J. Marine Res.*, 7, 410.
- MacGinitie, G.E., and N. MacGinitie, 1949: *Natural History of Marine Animals*, McGraw-Hill, New York, 473 pp.
- Martin, A.R. (editor), 1990: *The Illustrated Encyclopedia of Whales and Dolphins*, Portland House, New York, 192 pp.
- Nachtigal, P.E., 1979: Bibliography of echolocation papers on aquatic mammals published between 1966 and 1978," in *Animal Sonar Systems*, edited by R.G. Busnel and J.F. Fish, Plenum Press, New York, pp. 1029-1069.
- Tavolga, W.N. (editor), 1964: *Marine Bioacoustics*, Pergamon Press, New York.
- Urick, R.J., 1967: *Principles of Underwater Sound for Engineers*, McGraw-Hill, New York, 342 pp.
- Walker, R.A., 1963: "Some intense low frequency underwater sounds of wide geographic distribution, apparently of biological origin," *J. Acoust. Soc. Am.*, 35, 1816.
- Watkins, W.A., 1979: "Click sounds from animals at sea," in *Animal Sonar Systems*, R.G. Busnel and J.F. Fish (editors), Plenum Press, New York, pp. 291-297.
- Watkins, W.A., 1974: "Bandwidth limitations and analysis of cetacean sounds, with comments on delphinid sonar measurements and analysis," *J. Acoust. Soc. Am.*, 55, 849.
- Watson, L., 1981: *Sea Guide to Whales of the World*, E.P. Dutton, New York, 302 pp.
- Widener, M.W., 1967: "Ambient noise levels in selected shallow water off Miami, Florida," *J. Acoust. Soc. Am.*, 42, 904-905.
- Wenz, G.M., 1962: "Acoustic ambient noise in the ocean: spectra and sources," *J. Acoust. Soc. Am.*, 34, 1936.

TR 9407 III-11

Wood, F.G., and W.E. Evans., 1979: "Adaptiveness and ecology of echolocation in toothed whales," in *Animal Sonar Systems*, edited by R.G. Busnel and J.F. Fish, Plenum Press, New York, pp. 381-425.

III-12 TR 9407

ADB199453

#### **IV. Bottom**

ADB199453

### *Introduction*

This section contains the models for bottom forward loss, backscattering strength, and bistatic scattering strength applicable over the frequency interval 10–100 kHz. The forward loss and backscattering models are identical to those defined in the previous version of this document.<sup>1</sup> The bistatic model is new. The models employ a mixture of theory and data fitting and all use the same set of bottom parameters.

This section is divided into four parts: Section IV.A discusses the physics and model inputs, IV.B treats the forward loss model, and IV.C and IV.D treat the backscattering and bistatic scattering models.

For those who want to make quick estimates of forward loss or backscattering strength based on minimal knowledge of bottom type, we offer here a guide to relevant tables and curves:

#### **Bottom loss vs grazing angle**

Use curves of Figure 1 (page IV-19).

The loss is independent of frequency.

#### **Backscattering strength vs grazing angle**

Use curves of Figure 2 (page IV-26), which are computed for a frequency of 30 kHz.

More generally, consult Table 3 (page IV-23) and interpolate if necessary.

No similar plots or tables are available for the bistatic scattering model. To use the mathematical expressions that constitute the separate models, model input parameters must be determined. Section IV.A on model inputs provides the necessary information. Once model inputs are available, they can be inserted in the equations for forward loss (Section IV.B), backscattering strength (Section IV.C), or bistatic scattering strength (Section IV.D) without further reading. The text explains the models and indicates the accuracy that can be expected. The equations given for the three models are straightforward, analytic expressions; however, the forward loss model involves considerably fewer equations than the backscattering and bistatic models.

TR 9407 IV-1

It is important to understand a technical issue that arises in applying the models to scattering near the specular direction. The loss model treats the interface as perfectly flat and gives the energy loss for perfect, mirror-like reflection. The two scattering models, however, yield predictions for the angular spread of this energy due to interface roughness. If one integrates over this angular spread, the total energy will be approximately equal to the reflected energy predicted by the loss model. There is a danger of double counting if the scattering and loss models are employed without an understanding of this relationship. Rough bottoms such as rock and gravel present an especially difficult problem in this regard. The forward loss model yields very low loss because it neglects scattering due to roughness. Such effects are the province of the bistatic model, but the present version is not applicable to rough bottoms. The scattering model subsections (IV.C and IV.D) contain brief discussions of this issue.

## **A. MODEL INPUT PARAMETERS**

This section can be viewed as a "front end" designed to allow users to obtain reasonable estimates of the model input parameters given various sorts of information about the bottom. Some users may have only minimal information, e g., a sediment name such as "silty sand." Others may have a detailed geoacoustic characterization in terms of physical parameters such as sediment sound speed and density. To accommodate a wide range of such possibilities, this section is broken into a number of parts. Following is a brief outline of each part intended to guide users to the material essential to the application at hand.

1. **Comments on Geoacoustic Modeling**  
(This section is optional, but recommended, reading.)
2. **Definition of Model Input Parameters**  
(This is required reading for users intending to use the mathematical expressions that constitute the models).
3. **Table for Model Parameters in Terms of Sediment Name**  
(This is the least ambitious and least accurate approach to model input parameters. This section is self-contained.)



4. **Model Input Parameters Using Grain Size**  
(This provides a useful, but not always accurate parameterization in terms of a single, commonly encountered sediment parameter, grain size. This section is self-contained.)
5. **Model Input Parameters Using Geoacoustic Data**  
(This section depends on material in Section IV.A.4.)
6. **Refinement of Model Input Parameters Using Backscatter Data**  
(This supplements the methods discussed in Sections IV.A.3, IV.A.4, and IV.A.5.)
7. **Use of Bottom Roughness Data**  
(This supplements the methods discussed in Sections IV.A.3, IV.A.4, and IV.A.5.)

### **1. Comments on Geoacoustic Modeling**

Our modeling of the ocean bottom is confined to the top tens of centimeters because of the high attenuation of sound in sediments at high frequencies.<sup>2</sup> The upper few centimeters of sediment are more waterlike than the sediment in deeper layers, especially for soft sediments such as silts and clays. Unfortunately, quantitative geoacoustic data on this centimeters-thick transitional layer are almost nonexistent. With notable exceptions,<sup>3-8</sup> the layer is either ignored outright or destroyed during processing of the collected sediment. However, the data available strongly suggest the existence of significant gradients in porosity (hence density) along with generally weaker gradients in sound speed and attenuation. These gradients start at or near the interface and connect the more waterlike, unconsolidated sediments at the interface to the generally denser sediments that characterize the deeper layers. These gradients exist over several centimeters in depth. Preliminary theoretical calculations<sup>9</sup> show that these gradients can have important effects on the interaction of acoustic waves with sediment, by determining the effective impedance mismatch of the sediment/water interface. Long waves (relative to the average gradient in geoacoustical parameters) do not see the gradient—the effective impedance mismatch is determined by the bulk properties of the sediment. Short waves see only the surface values of the sediment's geoacoustical parameters.

TR 9407 IV-3

Our modeling efforts were constrained by the fact that there are not enough *simultaneous* acoustic and geoacoustic data with the necessary level of detail to construct a model of this interface that incorporates these effects in a realistic way. Our modeling efforts for both backscatter and forward loss are therefore based on the physical characteristics of the uppermost sediment, especially its density. Thus the sediments are modeled as a simple, semi-infinite fluid model which is assumed to be statistically homogeneous both in the horizontal and in the vertical. (Volume backscatter contributions are parameterized by an equivalent surface backscatter.) This avoids complicated models which would have included more detailed physics, at the cost of ill-defined bounds and poorly supported relationships for the appropriate parameters.

## 2. Definition of Model Input Parameters

Table 1 lists the geoacoustic parameters used as inputs for both the forward loss and backscattering models.

*Table 1. Bottom parameters used as model inputs.*

Symbol	Definition	Short Name
$\rho$	Ratio of sediment mass density to water mass density	Density ratio
$v$	Ratio of sediment sound speed to water sound speed	Sound speed ratio
$\delta$	Ratio of imaginary wavenumber to real wavenumber for the sediment	Loss parameter
$\sigma_2$	Ratio of sediment volume scattering cross section to sediment attenuation coefficient	Volume parameter
$\gamma$	Exponent of bottom relief spectrum	Spectral exponent
$w_2$	Strength of bottom relief spectrum ( $\text{cm}^4$ ) at wavenumber $2\pi/\lambda = 1 \text{ cm}^{-1}$	Spectral strength

The bottom backscattering model employs all six inputs from Table 1; the bottom forward loss model employs only the first three. The bistatic model uses all of the inputs from Table 1 except for  $\sigma_2$ , which is replaced by three new parameters. A default procedure is provided for obtaining these parameters in terms of  $\sigma_2$ . The working assumption is that the surficial characteristics of the sediment govern its acoustic properties. Therefore, one should have direct measurements of the first three geoacoustic parameters in Table 1 averaged over the upper few centimeters of the sediment, as well as direct measurements of the others. Unfortunately, many geoacoustic measurements consist of averages covering a depth of several tens of centimeters. Consequently a straightforward method of assigning values to the parameters and compensating for likely bias is essential for practical applications of the model.


The water sound speed immediately above the bottom,  $c_1$ , enters the backscatter and bistatic models through their dependence on the acoustic wavenumber,  $k = 2\pi f / c_1 = 2\pi / \text{wavelength}$ .

### 3. Table for Model Parameters in Terms of Sediment Name

Table 2 relates standard sediment types to model input parameters. The sediment name is assumed to be the name appropriate to the bulk of the sediment, rather than the surficial sediment. The user is cautioned that the density and sound speed ratios given in this table are surficial values derived from model fitting and tend to be smaller than the bulk values reported in the literature. The user is also cautioned that this table does *not* constitute the APL-LW bottom interaction model in any sense. These parameters are intended as defaults for use in the absence of physical data on bottom properties. In particular, for a given sediment name, there is considerable spread in observed scattering strength. Most of this spread can be ascribed to the parameters  $\sigma_2$  and  $w_2$ , as the output is particularly sensitive to these parameters. The range of variation of these parameters has been examined by fitting the model to unpublished survey data (K. Y. Moravan, personal communication). In these fits the parameters of Table 2 were used, except that  $\sigma_2$  and  $w_2$  were allowed to vary. One group of data was fit using the parameter for

TR 9407 IV-5

Table 2. Model inputs in terms of sediment name.



Sediment Name	Bulk Grain Size $M_z$ (φ)	Density Ratio $\rho$	Sound Speed Ratio $v$	Loss Parameter $\delta$	Volume Parameter $\sigma_2$	Spectral Exponent $\gamma$	Spectral Strength $w_2$ (cm <sup>-4</sup> )
Rough Rock	---	2.50	2.50	0.01374	0.002	3.25	0.00693
Rock	---	2.50	2.50	0.01374	0.002	3.25	0.01862
Cobble, Gravel, Pebble	---	2.50	1.80	0.01374	0.002	3.25	0.01600
Sandy Gravel	-1.0	2.492	1.3370	0.01705	0.002	3.25	0.01293
Very Coarse Sand	-0.5	2.401	1.3067	0.01667	0.002	3.25	0.010575
Muddy Sandy Gravel	0	2.314	1.2778	0.01630	0.002	3.25	0.008602
Coarse Sand, Gravelly Sand	0.5	2.231	1.2503	0.01638	0.002	3.25	0.006957
Gravelly Muddy Sand	1.0	2.151	1.2241	0.01645	0.002	3.25	0.005587
Medium Sand	1.5	1.845	1.1782	0.01624	0.002	3.25	0.004446
Muddy Gravel	2.0	1.615	1.1396	0.01610	0.002	3.25	0.003498
Fine Sand, Silty Sand	2.5	1.451	1.1073	0.01602	0.002	3.25	0.002715
Muddy Sand	3.0	1.339	1.0800	0.01728	0.002	3.25	0.002070
Very Fine Sand	3.5	1.268	1.0568	0.01875	0.002	3.25	0.001544
Clayey Sand	4.0	1.224	1.0364	0.02019	0.002	3.25	0.001119
Coarse Silt	4.5	1.195	1.0179	0.02158	0.002	3.25	0.000781
Sandy Silt, Gravelly Mud	5.0	1.169	0.9999	0.01261	0.002	3.25	0.000518
Medium Silt, Sand-Silt-Clay	5.5	1.149	0.9885	0.00676	0.001	3.25	0.000518
Sandy Mud	6.0	1.149	0.9873	0.00386	0.001	3.25	0.000518
Fine Silt, Clayey Silt	6.5	1.148	0.9861	0.00306	0.001	3.25	0.000518
Sandy Clay	7.0	1.147	0.9849	0.00242	0.001	3.25	0.000518
Very Fine Silt	7.5	1.147	0.9837	0.00194	0.001	3.25	0.000518
Silty Clay	8.0	1.146	0.9824	0.00163	0.001	3.25	0.000518
Clay (all grades)	9.0	1.145	0.9800	0.00148	0.001	3.25	0.000518

$M_z = 5.0$ , except that  $\sigma_2$  ranged from extremes of 0.0001 to 0.008 with about 80% of the data falling in the range 0.0003 to 0.004. Another group of data was fit using  $M_z = 2.0$  parameters; the extremes of  $w_2$  were 0.00052 to 0.016, and about 70% of the data fell in the range 0.0008 to 0.0086. In these fits,  $\sigma_2$  was also adjusted to improve the fit.

The sediment names are taken from the classification schemes of Wentworth,<sup>10</sup> Lane,<sup>11</sup> Inman,<sup>12</sup> Shepard,<sup>13</sup> and Folk.<sup>14</sup> The parameter  $M_z$  given in the second column of Table 2 is the mean grain size; it is included for completeness but is inessential for most applications of the table. Mean grain size is defined in Section IV.A.4. For the

Wentworth and Lane schemes, the  $M_z$  value given in Table 2 is the midpoint of the range defined by the sediment name. The Inman, Shepard, and Folk schemes base sediment name on the proportions of three component size classes, rather than the mean grain size. The  $M_z$  values given for these schemes in Table 2 are not identical to those of the original authors, but were chosen on the basis of consistency among all five schemes and with Section IV.A.4.

#### 4. Model Input Parameters Using Grain Size

A useful sediment descriptor is grain size. It is usually measured in logarithmic units and denoted  $M_z$ .

$$M_z = -\log_2 \frac{d}{d_0} = -3.32 \log_{10} \frac{d}{d_0} \quad (1)$$

where  $d$  is the mean grain size (or "diameter"),  $d_0$  is the reference length (1 mm), and the units of  $M_z$  are denoted  $\phi$ .

The foregoing comments about measuring the properties of the uppermost portion of the sediment apply to the grain size as well. Thus if the sediment consists of fine sand with a several-centimeter layer of broken shell, the grain size appropriate to the broken shell should be used for  $M_z$ . Similarly, if a gravel bottom has a patina of sand, the grain size of the sand is the relevant quantity, unless the layer is so thin as to permit acoustic penetration to the underlying gravel.

We offer parameterizations of the geoacoustic inputs in terms of the *bulk* grain size  $M_z$ . These parameterizations empirically relate  $M_z$  to the assumed geoacoustical characteristics of the upper few centimeters of the sediment. This provides the basis for assigning approximate parameter values in many cases of interest. Furthermore, sediment nomenclature is based on  $M_z$ , so one can estimate bulk grain size from the sediment name and then, via our parameterizations, the model inputs. However, this path of least resistance has its price: the uncertainty in the model predictions is greater than when accurate geoacoustic data are used to determine the inputs.

TR 9407 IV-7

The empirical relationships delineated below result in the best agreement between our acoustic models and measured reflection loss and backscatter data, while remaining consistent with the governing physics. In developing these relationships, data from three sites played a dominant role.<sup>9</sup> The development was also guided by published geoaoustic relationships<sup>2,15</sup> and our earlier APL-UW modeling work.<sup>16,17</sup> The relationships given below are defined only for  $-1 \leq M_z \leq 9$ .

$$\rho \equiv \frac{\rho_2}{\rho_1} \quad (2)$$

$$= 0.007797 M_z^2 - 0.17057 M_z + 2.3139, \quad -1 \leq M_z < 1$$

$$= -0.0165406 M_z^3 + 0.2290201 M_z^2 - 1.1069031 M_z + 3.0455, \quad 1 \leq M_z < 5.3$$

$$= -0.0012973 M_z + 1.1565, \quad 5.3 \leq M_z \leq 9$$

$$v \equiv \frac{c_2}{c_1} \quad (3)$$

$$= 0.002709 M_z^2 - 0.056452 M_z + 1.2778, \quad -1 \leq M_z < 1$$

$$= -0.0014881 M_z^3 + 0.0213937 M_z^2 - 0.1382798 M_z + 1.3425, \quad 1 \leq M_z < 5.3$$

$$= -0.0024224 M_z + 1.0019, \quad 5.3 \leq M_z \leq 9$$

(These parameterizations allow for four decimal places of accuracy.)

All subscripts 1 refer to water and all subscripts 2 refer to sediment. Parameters  $\rho$  and  $v$  are real quantities that are measures of the ratios of the densities and real (as opposed to complex) sound speeds of the two fluids. The density and sound speed ratios agree with those of Hamilton and Bachman<sup>15</sup> for  $-1 \leq M_z < 1$ , where for relatively coarse sediments we expect at best a negligible, tenuous layer. For  $M_z = 9$ , the sound speed ratio again agrees with that of Hamilton and Bachman, while the density ratio remains lower. For intermediate values of  $M_z$ , both  $\rho$  and  $v$  are smaller than the Hamilton and Bachman values.

The loss parameter  $\delta$  is a dimensionless quantity involving the complex sediment acoustic wavenumber  $k_2 = k_{2r} + ik_{2i}$ :

$$\delta \equiv \frac{k_{2i}}{k_{2r}} = \frac{\alpha_2 v c_1 \ln(10)}{f 40\pi} \quad (4)$$

This definition can be related to the quality factor,  $Q$ ,<sup>18</sup> through the simple expression  $2\delta = 1/Q$ . The loss parameter,  $\delta$ , contains the sediment sound attenuation coefficient,  $\alpha_2$ , which is usually expressed in units of decibels per meter (it is discussed by Hamilton<sup>2</sup>). Hamilton's parameterization of  $\alpha_2/f$  is reproduced below. Note that consistent units must be employed in Eq. 4. If  $\alpha_2/f$  is expressed in decibels per meter per kilohertz (as in Hamilton's parameterization),  $c_1$  must be expressed in meters per millisecond ( $c_1 = 1.528$  m/ms is used in determining  $\delta$  from Hamilton's expressions for  $\alpha_2/f$  and Eq. 4).

$$\frac{\alpha_2}{f} = 0.4556, \quad -1 \leq M_z < 0 \quad (5)$$

$$\frac{\alpha_2}{f} = 0.4556 + 0.0245 M_z, \quad 0 \leq M_z < 2.6$$

$$\frac{\alpha_2}{f} = 0.1978 + 0.1245 M_z, \quad 2.6 \leq M_z < 4.5$$

$$\frac{\alpha_2}{f} = 8.0399 - 2.5228 M_z + 0.20098 M_z^2, \quad 4.5 \leq M_z < 6.0$$

$$\frac{\alpha_2}{f} = 0.9431 - 0.2041 M_z + 0.0117 M_z^2, \quad 6.0 \leq M_z < 9.5$$

$$\frac{\alpha_2}{f} = 0.0601, \quad 9.5 \leq M_z$$

The sound speed ratio parameterization is based on measured sound speed ratios from three sites.<sup>9</sup> The measured values correlated well with apparent critical angle

TR 9407 IV-9

behavior in the data. Also, the gradients in vertical velocity were negligible in two cases. On the other hand, the measured density ratios from these sites were discarded because of the large scatter and vertical variations in porosity. Published bulk density measurements and standard parameterizations were considered, but were not used because of possible gradients which they do not incorporate. Rather, the acoustic models were fit to data in order to determine the relationship between grain size and density, while remaining consistent with the governing physics. However, it was found that the Hamilton<sup>2</sup> parameterization for absorption gave satisfactory results.

In the absence of information on sediment volume scattering, the volume parameter should be assigned the the following values:

$$\sigma_2 = 0.002 \quad , \quad -1.0 \leq M_z < 5.5 \quad (6)$$

$$\sigma_2 = 0.001 \quad , \quad 5.5 \leq M_z \leq 9.0 \quad .$$

The dimensionless volume parameter is defined in Table 1. It is a surface scattering parameterization of the volume scattering cross section when used in Eq. 66 (Section IV.C.2). There is considerable variation in the volume parameter, which sometimes takes on values differing by an order of magnitude from those given above (see Section IV.C.3).

The backscattering and bistatic models assume that the two-dimensional relief spectrum is isotropic and obeys a power law for wavenumbers comparable to the acoustic wavenumber:

$$W_2 (K) = (h_0 K)^{-\gamma} w_2 \quad . \quad (7)$$

In this expression,  $K$  is the wavenumber of bottom relief features;  $K = 2\pi/\Lambda$ , where  $\Lambda$  is the associated wavelength;  $h_0$  is a reference length, equal to 1 cm. Equation 7 requires two parameters, the spectral exponent  $\gamma$  and the spectral strength parameter  $w_2$ . Methods of determining  $\gamma$  and  $w_2$  from bottom roughness measurements are discussed in Section IV.A.7. Here, the parameterization of  $\gamma$  and  $w_2$  is considered in terms of grain size.



In the absence of measurements, the spectral exponent is assigned the fixed value

$$\gamma = 3.25 \quad (8)$$

for all grain sizes. An average of available data on spectral exponents<sup>19,20</sup> yields a value of 3.23 with a standard deviation of 0.44.

To parameterize the spectral strength, we start with a parameterization of the rms relief  $h$  of a 100-cm track, which is used to build  $w_2$ . The numbers in this parameterization were chosen by fitting the backscattering model to data.

$$\frac{h}{h_0} = \frac{2.03846 - 0.26923 M_z}{1.0 + 0.076923 M_z}, \quad -1.0 \leq M_z < 5.0, \quad (9)$$

$$\frac{h}{h_0} = 0.5, \quad 5.0 \leq M_z \leq 9.0.$$

With these functions, the spectral strength is related to  $h$  for  $\gamma = 3.25$  as follows<sup>17</sup>:

$$w_2 = 0.00207 h^2 h_0^2. \quad (10)$$

Note that  $w_2$  has units ( $\text{cm}^4$ ); it is the only model parameter that is not dimensionless. This is the least accurate of the parameterizations (not considering Eq. 6) as there is wide scatter in measured spectral strengths and weak correlation with grain size. Therefore, Eqs. 8–10 should be viewed as reasonable defaults, not as predictors of the roughness spectrum.

## 5. Model Input Parameters Using Geoacoustic Data

As noted earlier, measured sediment acoustic parameters often show appreciable gradients in the upper few centimeters. The most significant vertical variations are often confined to the density, while the sound speed and attenuation show smaller changes. Because of these vertical variations, the preferred method for determining  $\rho$ ,  $v$ , and  $\delta$  is

TR 9407 IV-11

direct measurement in the upper 10 cm using undisturbed core samples or in-situ probes with a resolution of at least 1 cm. This should be sufficient to resolve gradients to scales appropriate for use in modeling applications at 10–100 kHz. Sampling of the uppermost portion of the sediment is not as important for the loss parameter as it is for the sound speed and (especially) density ratios. This is partly because the loss parameter does not vary greatly with sediment type and partly because the models are not particularly sensitive to the loss parameter (save for the case of intromission; see below). However, the models are strongly dependent on  $v$ , especially near the critical angle,  $\theta_c$ , defined by  $\cos\theta_c \equiv 1/v$ , and on  $\rho$  near vertical incidence.

Some users may have access only to a single measured surficial geoaoustic quantity, such as mass density or sound speed. In such cases, Eq. 2 or 3 can be inverted to give a value for  $M_z$ . If measured values are available for both mass density and sound speed, inversion of the sound speed relation (Eq. 3) is the preferred means of determining  $M_z$ . Mean grain size can then be used to obtain the remaining input parameters using other expressions in Section IV.A.4. Surficial values of the absorption coefficient can be used to obtain a value for the loss parameter, but Eq. 5 should not be inverted to obtain a value for  $M_z$  in terms of the absorption coefficient because the uncertainty in this process is too great. If a surficial value is available for porosity (denoted  $n$  and given in percent),  $\rho$  can be obtained from

$$\rho = 2.66 - 0.0169n, \quad 35 < n < 85. \quad (11)$$

Equation 11 was derived by inverting a regression relation given by Hamilton and Bachman (p. 1903 of Ref. 15). With this value for  $\rho$ , Eq. 2 can be inverted for  $M_z$ , from which the other parameters can be obtained.

Some users may have access only to measured *bulk* geoaoustic quantities, rather than surficial values. If a measured value is available for  $M_z$ , it should be used in preference to the bulk geoaoustic quantities, following the procedures of Section IV.A.4. If  $M_z$  is not available, it can be inferred from the bulk geoaoustic quantities by using the

following inverted forms of the Hamilton-Bachman<sup>15</sup> regression relations.

If the bulk density ratio is known:

$$M_z = 10.937 - \sqrt{128.25\rho - 177.12} , \quad 1.22 < \rho < 2.05 . \quad (12)$$

If the bulk sound speed ratio is known:

$$M_z = 10.418 - \sqrt{369.09v - 363.09} , \quad 0.99 < v < 1.22 . \quad (13)$$

If the bulk porosity is known:

$$M_z = 12.6575 - \sqrt{220.5145 - 2.73972n} , \quad 35 < n < 85 . \quad (14)$$

## 6. Refinement of Input Parameters Using Backscattering Data

If backscattering strength data are available over at least a limited range of angles and frequencies, this information can be used to determine model parameters via fitting. This procedure is recommended only for determining those parameters whose variation causes large variations in predicted scattering strength. For soft sediments ( $M_z > 3.0$ ), such fitting provides a means of determining the sediment volume scattering parameter,  $\sigma_2$ . For harder sediments ( $M_z \leq 3.0$ ), this procedure can be used to determine the roughness spectral strength. Such acoustical determinations are preferred over estimates based on sediment name or grain size, which can introduce large errors.

In the fitting procedure defined here, it is assumed that the parameters  $\rho$ ,  $v$ ,  $\delta$ , and  $\gamma$  have already been fixed by the procedures given above. For soft sediments, ( $M_z > 3.0$ ), it is assumed that sediment volume scattering is dominant. Accordingly, the roughness spectral strength is temporarily set to zero and the volume parameter,  $\sigma_2$ , is set to any known value, e.g., 0.001. The resulting backscattering strength predicted by the model is then compared with data, and  $\sigma_2$  is adjusted to bring the model's results into agreement

TR 9407 IV-13

with the data. Since the backscattering cross section is proportional to  $\sigma_2$ , this adjustment is simple: e.g., if the data are 3 dB above the model,  $\sigma_2$  should be increased from 0.001 to 0.002. Once the volume parameter is determined, the spectral strength can be "turned on" (assigned a value determined by the procedures defined earlier.) After this new set of parameters is incorporated, the model should be checked for consistency by another comparison with data. If the roughness scattering component is negligible, as assumed in the fitting procedure, the model and data will agree. If not, the procedure outlined here fails and cannot be applied.

For harder sediments ( $M_z \leq 3.0$ ), the volume parameter,  $\sigma_2$ , is initially set to zero, and the spectral strength,  $w_2$ , is assigned an arbitrary value. It is subsequently adjusted to produce agreement with data in exactly the same manner as for the volume parameter. There is a slight nonlinearity in the dependence of scattering cross section on  $w_2$ , so some iteration may be required. Once a suitable value is found, the sediment volume scattering parameter is "turned on" and the consistency check is made as above.

## 7. Use of Bottom Roughness Data

As a general rule, the backscattering model is sensitive to both of the spectral parameters for coarser sediments ( $M_z < 3.5$ ) and becomes less sensitive for finer sediments.

From Eq. 7 it follows that  $w_2$  is the value of the spectrum for  $K = 1/h_0$ . The spectral exponent is limited in theory to the range  $2 < \gamma < 4$ , but practical considerations (Section IV.C.3) place the more stringent limits

$$2.4 \leq \gamma \leq 3.9 . \quad (15)$$

If the measured value of  $\gamma$  falls outside these limits, one should use  $\gamma = 2.4$  or  $3.9$ , whichever is closer to the measured value.

The normalization of the spectrum must be clearly defined if measured spectra are to be used as model inputs. It is important to distinguish between the formal power law

spectrum (Eq. 7), which is infinite at zero wavenumber, and the measured spectrum, which is necessarily finite. The measured spectrum must be normalized such that

$$\int_{-\infty}^{\infty} \int_{-\infty}^{\infty} W_2(K) dK_x dK_y = h^2, \quad (16)$$

where

$$K = (K_x^2 + K_y^2)^{1/2}, \quad (17)$$

and  $h$  is rms bottom relief. Note that the integral of Eq. 16 is undefined for the power law spectrum of Eq. 7. Still, Eq. 16 is useful because measured spectra are always finite. The rms bottom relief is actually a function of the length of the window used to estimate the spectrum. The same window length and taper must be used in estimating  $W_2(K)$  and  $h$ .

The preferred method for determining  $\gamma$  and  $w_2$  is to do a straight-line regression fit to the two-dimensional relief spectrum plotted in log-log fashion. The fit should be made at wavenumbers comparable to the acoustic wavenumber, which demands that the bottom profile be measured with a resolution of 1 cm or better.

Most such measurements to date have been published in the form of one-dimensional spectra rather than the two-dimensional spectra needed for the model. We now relate one-dimensional spectral measurements to the two-dimensional spectrum used in our model. The one-dimensional spectrum can be represented as follows:

$$W_1(K) = (h_0 K)^{-\gamma} w_1 \quad (18)$$

with normalization

$$\int_{-\infty}^{\infty} W_1(K) dK = h^2. \quad (19)$$

The conversion to two-dimensional parameters is as follows<sup>17</sup>:

$$\gamma = \gamma_1 + 1, \quad (20)$$

TR 9407 IV-15

$$w_2 = \frac{\Gamma\left(\frac{\gamma}{2}\right)}{\pi^{1/2} \Gamma\left(\frac{\gamma-1}{2}\right)} w_1 h_0 \quad (21)$$

where  $\Gamma(x)$  is the gamma function. Note that the factor  $h_0$  is present merely to balance units in this expression.

Some spectra are presented in terms of spatial frequency,  $f_s$ , rather than in terms of wavenumber,  $K$ . The relation between wavenumber and spatial frequency is

$$K = 2\pi f_s \quad (22)$$

When spatial frequency is used, the one-dimensional spectrum can be represented as

$$\Phi_1(f_s) = (h_0 f_s)^{-\gamma_1} \phi_1 \quad (23)$$

with normalization

$$\int_{-\infty}^{\infty} \Phi_1(f_s) df_s = h^2 \quad (24)$$

In this case, the conversion to two-dimensional parameters  $\gamma$  and  $w_2$  is as follows:

$$\gamma = \gamma_1 + 1 \quad (25)$$

$$w_2 = (2\pi)^{\gamma-2} \phi_1 h_0 \frac{\Gamma\left(\frac{\gamma}{2}\right)}{\pi^{1/2} \Gamma\left(\frac{\gamma-1}{2}\right)} \quad (26)$$

If the user does not have spectral data but has data on rms relief for scales comparable to the acoustic wavelength, the spectral exponent should be taken to be

$$\gamma = 3.25 \quad (27)$$

and the appropriate spectral strength is<sup>17</sup>

$$w_2 = h^2 h_0^\gamma \frac{2^{2\gamma} \gamma (\gamma-1) (\gamma-2) (4-\gamma) \Gamma(\frac{\gamma}{2})}{32 \pi \Gamma(3 - \frac{\gamma}{2}) L^{\gamma-2}} \quad (28)$$

where  $L$  is the window length used in estimating  $h$ , where the latter is defined in Eqs. 16, 19, and 24.

### 8. Limits on Model Parameters

The following limits are recommended for input parameters. These limits are extremes suggested by a combination of numerical and physical considerations. Published values of parameters fall within these limits, but the extreme values are unlikely to be encountered in practice and may yield suspect results.

- 1.0 ≤ Density Ratio ≤ 3.0
- 0.8 ≤ Sound Speed Ratio ≤ 3.0
- 0.0 < Loss Parameter ≤ 0.1
- 0.0 ≤ Volume Parameter ≤ 1.0
- 2.4 ≤ Spectral Exponent ≤ 3.9
- 0.0 < Spectral Strength (cm<sup>4</sup>) ≤ 1.0.

Other parameters should be limited as follows:

- 0.0 ≤ Grazing Angle (deg) ≤ 90.0
- 1400 ≤ Water Sound Speed (m/s) ≤ 1600
- 10.0 ≤ Frequency (kHz) ≤ 100.0.

TR 9407 IV-17

ADB199453

## B. FORWARD LOSS

The forward loss model is based on acoustic reflection rather than scattering concepts. This is because much of the forward scattering data used in building the model actually showed little pulse elongation, suggesting that the incident acoustic energy was reflected rather than scattered. Available data on small-scale bottom roughness<sup>19,20</sup> also support the modeling of forward scatter by forward reflection since they show that the bottom is often much smoother than the sea surface. In some applications, the angular spread of forward-scattered energy is important. The bistatic model (Section IV.D) provides estimates of this spreading.

### 1. Statement of the Forward Loss Model

The following simple model is adopted for forward reflection loss,  $r_0$ , with  $\theta$  being the grazing angle:

$$r_0 = -20 \log_{10} |R(\theta)| \quad (29)$$

$$R(\theta) = \frac{y - 1}{y + 1} \quad (30)$$

$$y = \frac{\rho \sin \theta}{P(\theta)} \quad (31)$$

$$P(\theta) = \sqrt{\kappa^2 - \cos^2 \theta} \quad (32)$$

$$\kappa = \frac{1}{v} (1 + i\delta) \quad (33)$$

The idea of a lossy Rayleigh coefficient was first published in an article by Mackenzie,<sup>21</sup> who quoted unpublished work by Morse. Note that  $R(\theta)$  (not the forward loss  $r_0$ ) is a complex quantity, as are the quantities  $y$ ,  $P(\theta)$ , and  $\kappa$ .

Because this model does not include gradients and layering, it has no explicit frequency dependence. The loss parameter,  $\delta$ , may be frequency dependent in general, but it has no such dependence in our parameterizations.



Figure 1 shows examples of forward loss for a variety of sediment types chosen as representative of the full spectrum of possible oceanic bottoms. The choices are taken from Table 2.

## 2. Model Accuracy

The forward loss model is based on a limited set of data from three sites, and comparisons of the model with these data are given by Mourad and Jackson.<sup>9</sup> The data are confined to the frequency range 20–30 kHz, and grazing angles are concentrated at small values, typically between 5° and 30°. In addition, a single data point is available for each site at vertical incidence (90°). High-quality geoaoustic data are available for all three sites. For the small angles, use of surficial geoaoustic parameters resulted in model errors that were about equal to the loss value. That is, for a soft, clayey bottom, the predicted loss at 5° was about 8 dB, and the data near this angle were within 6 dB of the

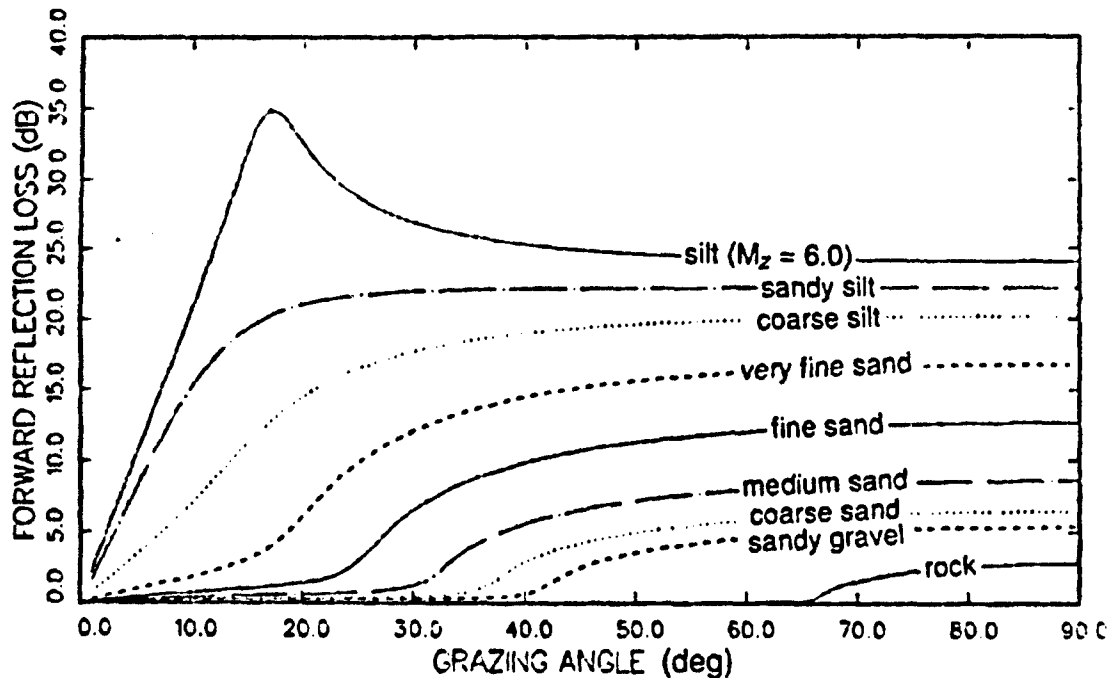


Figure 1. Curves predicted by the forward loss model for generic bottom types. The model input parameters are taken from Table 2. For a given set of input parameters, the loss model has no frequency dependence.

TR 9407 IV-19

ADB199453

model prediction. For a hard sandy bottom, the predicted loss at  $15^\circ$  was about 2 dB, and the measured values ranged from a fraction of 1 dB to 2 dB. Errors of the same magnitude occurred at  $90^\circ$ . These data were used in developing the relationship between grain size and model input parameters. As a result, use of grain size rather than measured geoaoustic data actually gave a better model fit for this small data set than use of high-quality geoaoustic data, but this is an artifact of the fitting process.

Because of the large fluctuations that can be found in forward scattering data, future work should incorporate the effects of horizontal spatial variations in input parameters, which may explain the large variation seen in measured forward loss.

In this model, bottom loss approaches zero as grazing angle approaches zero. This is a reasonable approximation, provided bottom roughness does not redirect acoustic energy substantially away from the specular direction. The experimental data support this assumption, as they tend to show low loss values as the grazing angle becomes small. It must be noted, however, that these data did not include angles smaller than  $3^\circ$ , and that they were gathered from single-bounce experiments. At longer ranges, multiple bottom and surface bounces will render the reflection loss approach invalid if the angular spread of the acoustic energy increases to a value exceeding the relevant system beamwidths. In such circumstances, a scattering approach is required, in principle. Such an approach could be based on the bistatic scattering model given in Section IV.D.

The error incurred by using the present model in multiple bounce situations will be greatest for relatively hard, rough bottoms such as sand, gravel, and rock. For softer bottoms, roughness scattering should be less important, and the error should be correspondingly smaller. For simulations that cannot employ a roughness scattering approach, it is necessary to introduce an effective loss that is greater than the loss given by the present model, and possibly nonzero in the limit of small grazing angles. Such an effective loss depends on system parameters and propagation conditions, including the angular spreading incurred by interaction with surface waves. That type of spreading will move a fraction of the acoustic energy to higher angles where it is more readily absorbed by the bottom (Marsh and Schulkin<sup>22</sup>). Quantitative prediction of these effects is difficult (Weston

and Ching<sup>23</sup>); nevertheless, a fixed effective loss-per-bounce is sometimes employed as a practical means of introducing scattering loss into acoustic simulations. For multiple bounce situations, a minimum loss-per-bounce of 1.5 dB is recommended by Hall and Watson.<sup>24</sup>

### 3. Numerical Considerations

Expressions 29–33 are all complex and are most simply evaluated by code that uses complex arithmetic and treats the variables  $R(\theta)$ ,  $y$ ,  $P(\theta)$ , and  $\kappa$  as complex numbers. The square root in Eq. 32 is defined as the complex number whose magnitude is the positive square root of the magnitude of the argument and whose phase is one-half the phase of the argument. This definition removes the ambiguity about the sign of the square root.

## C. BACKSCATTER

### 1. Introduction

The bottom backscattering strength model requires the six bottom parameters defined in Table 1 and the water sound speed as inputs. Users who need only estimates of bottom backscattering strength for generic bottom types may prefer to use Table 3 (computed using a water sound speed of 1528 m/s) or the curves of Figure 2 rather than the full model. Users that have physical data on bottom properties can obtain more accurate predictions using the full six-parameter model which was developed to encompass a wider range of bottom types. The equations defining the model are straightforward, but numerous. The model incorporates several submodels taken from the literature, suitably modified and combined to give a reasonably accurate description of the physical processes involved in bottom backscattering. Because the model is, in part, physically based, it can be used to study such topics as

- frequency dependence of scattering strength
- importance of scattering from sediment volume
- classification of bottom type from backscattering strength

TR 9407 IV-21

- extrapolation of measured data (in frequency, angle, and bottom properties)
- estimation of bottom loss from backscattering strength
- importance of various geoaoustic parameters.

The basis for this model is documented by Mourad and Jackson,<sup>9</sup> and comments on the model have been given by Jackson and Briggs.<sup>8</sup> The model is a generalization of the previous model,<sup>17,25</sup> which was a simplification of the work of Jackson et al.<sup>16</sup> Unlike its predecessor, the present model includes "slow" bottoms with a sound speed less than the overlying water, and it incorporates a wider class of roughness types. It improves on the work by Jackson et al.<sup>16</sup> in two ways: absorption is included in a more realistic fashion, and numerical integrations have been replaced by efficient analytic approximations. The present model assumes that the properties of the bottom material are statistically homogeneous vertically and horizontally. Thus, as with the reflection model, layering and vertical gradients are not included. McDaniel<sup>26</sup> has shown that layering can introduce substantial effects in high-frequency bottom backscattering.

## 2. Equations for Bottom Backscattering Strength

Bottom backscattering strength,  $S_b(\theta)$ , is a function of the six parameters defined in the introduction and also depends on acoustic frequency,  $f$ , and the grazing angle,  $\theta$ . As defined by Urick,<sup>27</sup>  $S_b(\theta)$  is the decibel equivalent of the scattering cross section, which is broken into two parts:

$$S_b(\theta) = 10 \log_{10} [ \sigma_r(\theta) + \sigma_v(\theta) ] , \quad (34)$$

where

$\sigma_r(\theta)$  = dimensionless backscattering cross section per unit solid angle per unit area due to interface roughness

$\sigma_v(\theta)$  = dimensionless backscattering cross section per unit solid angle per unit area due to volume scattering from below the interface.

Table 3. Scattering strengths for generic bottom types.

## Rough Rock

Ang.	10 kHz	15 kHz	20 kHz	25 kHz	30 kHz	40 kHz	60 kHz	80 kHz	100 kHz
1	-28.6	-26.4	-24.9	-23.8	-23.0	-21.7	-20.0	-18.9	-18.0
2	-24.2	-22.3	-21.1	-20.2	-19.4	-18.3	-16.9	-15.9	-15.2
3	-21.6	-19.9	-18.8	-18.0	-17.4	-16.4	-15.1	-14.2	-13.6
5	-18.4	-16.9	-16.0	-15.3	-14.8	-13.9	-12.8	-12.1	-11.5
7	-16.3	-15.0	-14.1	-13.5	-13.0	-12.3	-11.3	-10.7	-10.2
10	-14.0	-12.9	-12.2	-11.7	-11.3	-10.6	-9.8	-9.2	-8.8
20	-9.9	-9.1	-8.6	-8.2	-7.9	-7.5	-6.9	-6.5	-6.2
40	-6.8	-6.3	-5.9	-5.6	-5.4	-5.1	-4.7	-4.4	-4.2
60	-6.1	-5.7	-5.3	-5.1	-4.9	-4.6	-4.3	-4.0	-3.8
70	-6.1	-5.7	-5.4	-5.1	-5.0	-4.7	-4.3	-4.0	-3.9
80	-6.4	-5.9	-5.6	-5.4	-5.1	-4.8	-4.4	-4.2	-4.0
85	-6.5	-6.1	-5.7	-5.5	-5.3	-5.0	-4.6	-4.3	-4.1
88	-6.6	-6.2	-5.8	-5.6	-5.4	-5.1	-4.7	-4.4	-4.2
89	-6.6	-6.2	-5.9	-5.6	-5.4	-5.1	-4.7	-4.4	-4.2
90	-6.7	-6.2	-5.9	-5.6	-5.4	-5.1	-4.7	-4.4	-4.2

## Rock

Ang.	10 kHz	15 kHz	20 kHz	25 kHz	30 kHz	40 kHz	60 kHz	80 kHz	100 kHz
1	-52.0	-50.4	-47.7	-45.6	-44.0	-41.5	-38.3	-36.1	-34.5
2	-45.7	-42.8	-40.4	-38.7	-37.3	-35.2	-32.4	-30.6	-29.2
3	-41.5	-38.3	-36.2	-34.6	-33.3	-31.5	-29.0	-27.3	-26.1
5	-35.7	-32.7	-30.8	-29.5	-28.4	-26.8	-24.6	-23.2	-22.2
7	-31.8	-29.0	-27.3	-26.1	-25.2	-23.7	-21.8	-20.6	-19.7
10	-27.6	-25.1	-23.6	-22.6	-21.7	-20.5	-18.9	-17.8	-17.0
20	-19.8	-17.8	-16.8	-16.0	-15.4	-14.5	-13.4	-12.6	-12.0
40	-13.8	-12.3	-11.5	-11.0	-10.6	-10.0	-9.1	-8.6	-8.2
60	-11.8	-10.6	-9.9	-9.4	-9.1	-8.6	-8.0	-7.5	-7.2
70	-10.1	-9.2	-8.8	-8.5	-8.3	-8.0	-7.6	-7.4	-7.1
80	-6.0	-6.6	-6.9	-7.1	-7.3	-7.4	-7.5	-7.3	-7.2
85	-3.6	-5.1	-5.9	-6.4	-6.8	-7.2	-7.4	-7.4	-7.3
88	-2.8	-4.6	-5.6	-6.2	-6.6	-7.1	-7.4	-7.4	-7.3
89	-2.6	-4.5	-5.5	-6.2	-6.6	-7.1	-7.5	-7.5	-7.4
90	-2.6	-4.4	-5.5	-6.2	-6.6	-7.1	-7.5	-7.5	-7.4

## Cobble

Ang.	10 kHz	15 kHz	20 kHz	25 kHz	30 kHz	40 kHz	60 kHz	80 kHz	100 kHz
1	-49.4	-53.5	-51.9	-50.0	-48.5	-46.1	-43.0	-40.9	-39.4
2	-45.7	-46.7	-44.7	-43.0	-41.7	-39.6	-37.0	-35.2	-33.9
3	-43.1	-42.3	-40.4	-38.9	-37.6	-35.8	-33.4	-31.8	-30.7
5	-38.9	-36.6	-34.9	-33.6	-32.6	-31.0	-29.0	-27.6	-26.6
7	-35.5	-32.8	-31.3	-30.1	-29.2	-27.8	-26.0	-24.8	-24.0
10	-31.7	-28.8	-27.5	-26.5	-25.7	-24.5	-23.0	-22.0	-21.2
20	-24.2	-21.6	-20.6	-19.9	-19.3	-18.5	-17.4	-16.7	-16.2
40	-18.6	-16.6	-15.9	-15.3	-14.9	-14.3	-13.5	-13.0	-12.6
60	-15.5	-14.6	-13.9	-13.5	-13.1	-12.7	-12.2	-11.9	-11.7
70	-12.8	-12.2	-11.8	-11.6	-11.5	-11.5	-11.5	-11.5	-11.5
80	-6.6	-7.8	-8.3	-8.8	-9.2	-9.8	-10.6	-11.0	-11.3
85	-3.4	-5.6	-6.7	-7.6	-8.2	-9.2	-10.3	-10.9	-11.2
88	-2.3	-4.9	-6.2	-7.2	-7.9	-9.0	-10.2	-10.9	-11.3
89	-2.2	-4.7	-6.1	-7.1	-7.9	-9.0	-10.2	-10.9	-11.3
90	-2.1	-4.7	-6.1	-7.1	-7.8	-8.9	-10.2	-10.9	-11.3

Table 3 (cont.)

## Sandy Gravel

Ang.	10 kHz	15 kHz	20 kHz	25 kHz	30 kHz	40 kHz	60 kHz	80 kHz	100 kHz
1	-46.5	-48.3	-51.8	-51.4	-50.3	-48.5	-46.0	-44.3	-42.9
2	-43.4	-44.5	-46.3	-45.3	-44.2	-42.4	-40.1	-38.5	-37.3
3	-41.4	-41.9	-42.4	-41.3	-40.3	-38.6	-36.5	-35.1	-34.0
5	-38.2	-37.7	-37.1	-36.0	-35.1	-33.8	-31.9	-30.7	-29.8
7	-35.5	-34.4	-33.5	-32.5	-31.7	-30.5	-28.9	-27.9	-27.1
10	-32.2	-30.7	-29.6	-28.8	-28.1	-27.1	-25.8	-24.9	-24.2
20	-25.9	-24.1	-23.1	-22.5	-22.1	-21.4	-20.4	-19.7	-19.3
40	-21.2	-20.3	-19.7	-19.3	-18.9	-18.3	-17.6	-17.1	-16.8
60	-18.3	-17.7	-17.3	-16.8	-16.5	-16.1	-15.7	-15.5	-15.5
70	-14.7	-14.3	-14.0	-13.8	-13.7	-13.6	-13.9	-14.2	-14.5
80	-7.5	-8.3	-9.0	-9.5	-9.9	-10.7	-12.0	-12.9	-13.6
85	-3.2	-5.4	-6.7	-7.7	-8.4	-9.7	-11.3	-12.5	-13.3
88	-1.8	-4.4	-6.0	-7.1	-8.0	-9.3	-11.1	-12.3	-13.2
89	-1.7	-4.2	-5.9	-7.0	-7.9	-9.3	-11.1	-12.3	-13.2
90	-1.6	-4.2	-5.8	-6.9	-7.8	-9.2	-11.1	-12.3	-13.2

## Coarse Sand

Ang.	10 kHz	15 kHz	20 kHz	25 kHz	30 kHz	40 kHz	60 kHz	80 kHz	100 kHz
1	-54.2	-50.5	-48.1	-46.8	-47.1	-50.6	-50.5	-48.9	-47.7
2	-50.6	-47.2	-44.9	-43.6	-43.8	-46.0	-44.8	-43.1	-41.9
3	-47.8	-44.8	-42.8	-41.6	-41.5	-42.6	-41.0	-39.5	-38.3
5	-43.4	-41.1	-39.4	-38.3	-37.9	-37.6	-35.9	-34.6	-33.6
7	-39.8	-38.0	-36.6	-35.6	-34.9	-34.1	-32.5	-31.3	-30.5
10	-35.9	-34.4	-33.2	-32.3	-31.5	-30.3	-28.9	-27.9	-27.2
20	-29.0	-27.8	-26.8	-26.0	-25.1	-24.0	-23.0	-22.4	-21.8
40	-23.7	-22.9	-22.4	-21.9	-21.4	-20.8	-20.1	-19.6	-19.2
60	-21.1	-20.2	-19.6	-19.1	-18.8	-18.6	-17.8	-17.3	-17.1
70	-17.7	-16.4	-15.8	-15.5	-15.3	-15.1	-14.7	-14.6	-14.7
80	-9.6	-8.9	-8.6	-8.6	-8.9	-9.6	-10.5	-11.3	-12.0
85	-2.7	-3.2	-3.9	-4.7	-5.6	-7.2	-8.9	-10.1	-11.0
88	1.0	-0.8	-2.2	-3.4	-4.6	-6.3	-8.3	-9.7	-10.7
89	1.5	-0.6	-2.0	-3.3	-4.4	-6.1	-8.2	-9.6	-10.7
90	1.6	-0.5	-2.0	-3.2	-4.4	-6.1	-8.2	-9.6	-10.7

## Medium Sand

Ang.	10 kHz	15 kHz	20 kHz	25 kHz	30 kHz	40 kHz	60 kHz	80 kHz	100 kHz
1	-61.5	-57.7	-55.1	-53.0	-51.4	-49.1	-49.2	-50.8	-50.0
2	-56.8	-53.7	-51.4	-49.6	-48.1	-45.9	-45.5	-45.9	-44.9
3	-53.2	-50.7	-48.7	-47.1	-45.8	-43.8	-42.8	-42.5	-41.5
5	-47.6	-45.8	-44.4	-43.1	-42.1	-40.4	-38.6	-37.6	-36.6
7	-43.4	-42.0	-40.9	-39.9	-39.0	-37.6	-35.4	-34.2	-33.3
10	-38.8	-37.7	-36.8	-36.1	-35.4	-34.1	-31.7	-30.5	-29.8
20	-30.9	-30.1	-29.4	-28.8	-28.3	-27.4	-25.7	-24.8	-24.2
40	-24.4	-24.1	-23.9	-23.7	-23.5	-23.1	-22.4	-22.0	-21.7
60	-22.6	-22.2	-21.8	-21.5	-21.2	-20.6	-20.1	-19.8	-19.5
70	-20.4	-19.6	-18.9	-18.3	-17.7	-17.4	-16.9	-16.6	-16.4
80	-13.2	-12.0	-11.4	-11.0	-10.8	-10.6	-11.1	-11.7	-12.2
85	-5.0	-4.7	-4.9	-5.2	-5.5	-6.3	-8.2	-9.5	-10.4
88	1.2	-0.3	-1.5	-2.5	-3.4	-4.8	-7.2	-8.7	-9.8
89	2.3	0.3	-1.1	-2.2	-3.1	-4.7	-7.0	-8.6	-9.7
90	2.6	0.5	-1.0	-2.1	-3.1	-4.6	-7.0	-8.6	-9.7

Table 3 (cont.)  
Very Fine Sand

Ang.	10 kHz	15 kHz	20 kHz	25 kHz	30 kHz	40 kHz	60 kHz	80 kHz	100 kHz
1	-66.2	-64.0	-62.3	-60.9	-59.7	-57.8	-55.0	-52.9	-51.4
2	-58.8	-57.6	-56.5	-55.6	-54.7	-53.3	-51.0	-49.3	-47.9
3	-53.4	-52.7	-52.0	-51.3	-50.8	-49.7	-48.0	-46.6	-45.4
5	-45.9	-45.5	-45.2	-44.9	-44.6	-44.0	-43.0	-42.1	-41.3
7	-40.8	-40.6	-40.5	-40.3	-40.1	-39.8	-39.1	-38.5	-37.9
10	-35.6	-35.5	-35.4	-35.3	-35.2	-35.0	-34.7	-34.3	-34.0
20	-27.1	-27.1	-27.1	-27.1	-27.1	-27.1	-27.0	-27.0	-27.0
40	-25.0	-25.0	-24.9	-24.9	-24.9	-24.9	-24.9	-24.9	-24.8
60	-23.8	-23.8	-23.8	-23.7	-23.7	-23.7	-23.6	-23.5	-23.5
70	-23.4	-23.3	-23.2	-23.1	-23.1	-22.9	-22.7	-22.5	-22.3
80	-21.9	-21.4	-21.0	-20.6	-20.2	-19.5	-18.7	-18.3	-18.0
85	-16.9	-15.2	-14.1	-13.5	-13.1	-12.8	-12.5	-12.6	-12.9
88	-5.2	-5.0	-5.2	-5.5	-5.9	-6.8	-8.2	-9.4	-10.3
89	-0.2	-1.4	-2.5	-3.5	-4.3	-5.6	-7.5	-8.9	-10.0
90	1.8	-0.3	-1.7	-2.9	-3.8	-5.3	-7.4	-8.8	-10.0

Silt ( $\sigma_2 = 0.001$ )

Ang.	10 kHz	15 kHz	20 kHz	25 kHz	30 kHz	40 kHz	60 kHz	80 kHz	100 kHz
1	-60.7	-60.0	-59.3	-58.7	-58.2	-57.3	-55.8	-54.7	-53.8
2	-51.9	-51.7	-51.5	-51.3	-51.1	-50.8	-50.2	-49.6	-49.1
3	-46.9	-46.8	-46.8	-46.7	-46.6	-46.5	-46.2	-45.9	-45.7
5	-41.4	-41.3	-41.3	-41.3	-41.3	-41.3	-41.2	-41.2	-41.1
7	-38.4	-38.4	-38.3	-38.3	-38.3	-38.3	-38.3	-38.3	-38.3
10	-35.7	-35.7	-35.7	-35.7	-35.7	-35.7	-35.7	-35.7	-35.7
20	-31.8	-31.8	-31.8	-31.8	-31.8	-31.8	-31.8	-31.8	-31.8
40	-28.8	-28.8	-28.8	-28.8	-28.8	-28.8	-28.8	-28.7	-28.7
60	-27.4	-27.4	-27.4	-27.4	-27.4	-27.4	-27.4	-27.4	-27.4
70	-27.0	-27.0	-27.0	-27.0	-27.0	-27.0	-26.9	-26.9	-26.9
80	-26.6	-26.5	-26.4	-26.4	-26.3	-26.2	-26.0	-25.7	-25.5
85	-25.4	-25.0	-24.6	-24.2	-23.9	-23.2	-21.9	-20.9	-20.3
88	-18.0	-16.0	-14.6	-13.7	-13.1	-12.5	-12.1	-12.3	-12.6
89	-8.0	-7.0	-6.6	-6.6	-6.8	-7.3	-8.4	-9.5	-10.4
90	1.8	-0.1	-1.6	-2.7	-3.6	-5.1	-7.1	-8.6	-9.8

Silt ( $\sigma_2 = 0.0003$ )

Ang.	10 kHz	15 kHz	20 kHz	25 kHz	30 kHz	40 kHz	60 kHz	80 kHz	100 kHz
1	-66.0	-65.2	-64.5	-63.9	-63.4	-62.4	-61.0	-59.8	-58.9
2	-57.1	-56.9	-56.7	-56.5	-56.3	-56.0	-55.3	-54.8	-54.3
3	-52.1	-52.0	-52.0	-51.9	-51.8	-51.7	-51.4	-51.1	-50.8
5	-46.6	-46.6	-46.5	-46.5	-46.5	-46.5	-46.4	-46.3	-46.2
7	-43.6	-43.6	-43.6	-43.5	-43.5	-43.5	-43.5	-43.5	-43.4
10	-40.9	-40.9	-40.9	-40.9	-40.9	-40.9	-40.9	-40.9	-40.9
20	-37.0	-37.0	-37.0	-37.0	-37.0	-37.0	-37.0	-37.0	-37.0
30	-34.0	-34.0	-34.0	-34.0	-34.0	-34.0	-33.9	-33.9	-33.9
60	-32.6	-32.6	-32.6	-32.6	-32.6	-32.6	-32.5	-32.5	-32.5
70	-32.2	-32.1	-32.1	-32.1	-32.1	-32.0	-31.9	-31.8	-31.7
80	-31.3	-31.1	-30.9	-30.7	-30.5	-30.2	-29.6	-29.2	-28.7
85	-28.5	-27.6	-26.9	-26.3	-25.8	-24.8	-23.0	-21.7	-21.1
88	-18.4	-16.2	-14.8	-13.9	-13.3	-12.6	-12.3	-12.4	-12.7
89	-8.0	-7.0	-6.7	-6.7	-6.8	-7.3	-8.5	-9.5	-10.4
90	1.8	-0.2	-1.6	-2.7	-3.6	-5.1	-7.2	-8.7	-9.8

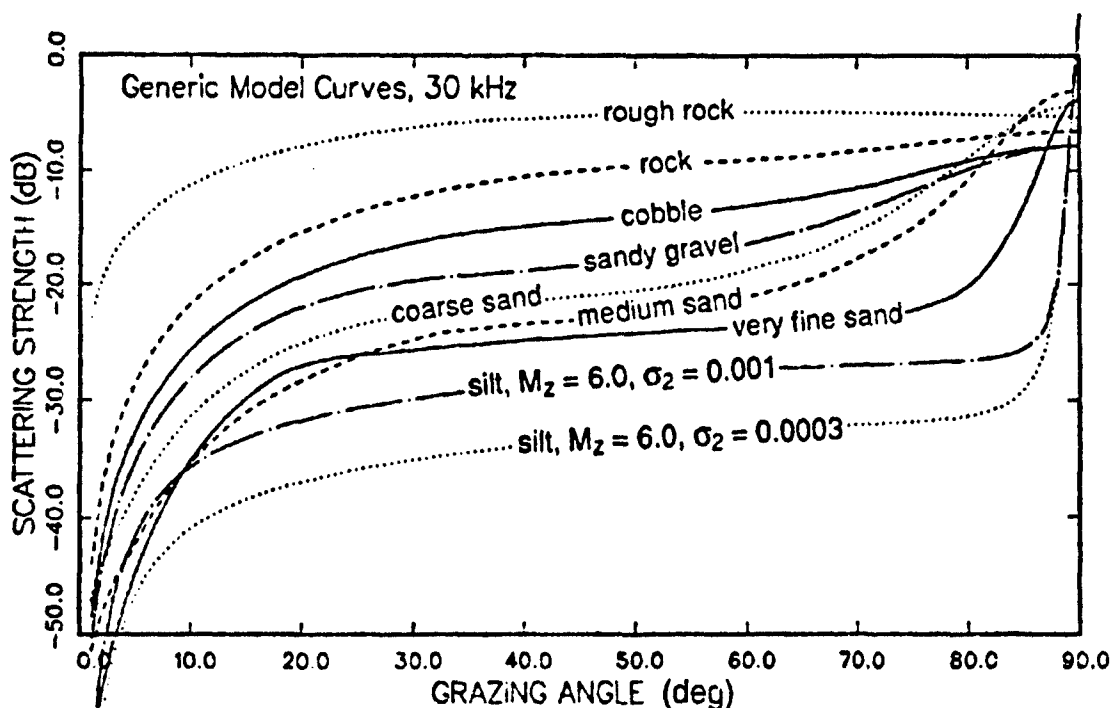


Figure 2. Model curves for backscattering strength at 30 kHz for generic bottom types. The model input parameters are taken from Table 2.

These two scattering cross sections are functions of the six parameters defined in Table 1. Evaluation of these cross sections involves numerous equations, which are developed in the following subsections, beginning with the roughness scattering cross section and ending with the sediment volume scattering cross section. No superfluous or intermediate equations are presented; *all* of the following equations must be included in code to evaluate the bottom backscattering strength.

**a. Roughness scattering cross section,  $\sigma_r(\theta)$**

Three different approximations are used for the roughness scattering cross section,  $\sigma_r(\theta)$ . For smooth and moderately rough bottoms (e.g., clay, silt, and sand), the roughness scattering cross section is computed using the Kirchhoff approximation for grazing angles near  $90^\circ$  and the composite roughness approximation for all other angles. For rough bottoms (e.g., gravel and rock), an empirical expression taken from the previous



version of this model is used.<sup>17,25</sup> The following discussion develops each of these approximations in turn, providing only those expressions needed for computation. The final result for  $\sigma_r(\theta)$  is given in Eq. 62, which is an interpolating expression that automatically shifts from one approximation to another.

#### *Kirchhoff Approximation*

In the Kirchhoff approximation, it is convenient to redefine the roughness parameters in terms of parameters  $\alpha$  and  $C_h^2$  of the so-called "structure function"<sup>28</sup>:

$$\alpha = \frac{\gamma}{2} - 1 \quad (35)$$

and<sup>16</sup>

$$C_h^2 = \frac{2\pi w_2 \Gamma(2-\alpha) 2^{-2\alpha}}{h_0^2 \alpha (1-\alpha) \Gamma(1+\alpha)} \quad (36)$$

Note that there is a physical constraint on  $\gamma$  equivalent to  $0 < \alpha < 1$ .

The Kirchhoff approximation yields an integral for the backscattering cross section (for example, see Ishimaru<sup>29</sup>) which must be integrated numerically or otherwise approximated. A simple approximation has been developed for this integral based on special cases for which exact analytical evaluation is possible.<sup>9</sup> The resulting approximation for the Kirchhoff backscattering cross section,  $\sigma_{kr}(\theta)$ , is

$$\sigma_{kr}(\theta) = \frac{b q_c |R(90^\circ)|^2}{8\pi [\cos^{4\alpha}(\theta) + a q_r^2 \sin^4(\theta)]^{\frac{1+\alpha}{2\alpha}}}, \quad \theta \geq 40^\circ \quad (37)$$

$$= 0, \quad \theta < 40^\circ.$$

TR 9407 IV-27

The Kirchhoff cross section is set to zero at angles less than  $40^\circ$ , where the composite roughness approximation is used. The abrupt jump at  $40^\circ$  will not be seen in the model output because a smooth interpolation is used at angles greater than  $40^\circ$ . Equation 37 contains the following parameters derived from the structure function parameters  $\alpha$  and  $C_h^2$ :

$$q_c = C_h^2 2^{1-2\alpha} k^{2(1-\alpha)} \quad (38)$$

$$a = \left[ \frac{8 \alpha^2 \Gamma(\frac{1}{2\alpha} + \frac{1}{2})}{\Gamma(\frac{1}{2}) \Gamma(\frac{1}{\alpha}) \Gamma(\frac{1}{2\alpha})} \right]^{2\alpha} \quad (39)$$

$$b = \frac{a^{\frac{1}{2}} + \frac{1}{2\alpha} \Gamma(\frac{1}{\alpha})}{2\alpha} \quad (40)$$

It also contains  $R(90^\circ)$ , the complex Rayleigh reflection coefficient (Eq. 30) evaluated at normal incidence.

#### *Composite Roughness Approximation*

In the composite roughness approximation, the small-roughness perturbation approximation is used with corrections for shadowing and large-scale rms bottom slope.<sup>30</sup> The large-scale rms slope,  $s$ , is defined as the positive square root of

$$s^2 = \frac{(2\pi w_z h_0^{-\gamma})^{\frac{1}{\alpha}}}{2(1-\alpha)} \left[ \frac{k^2}{\alpha} \right]^{\frac{1-\alpha}{\alpha}} \quad (41)$$

where  $k$  is the acoustic wavenumber. It is convenient to break the composite-roughness cross section into two factors:

$$\sigma_{cr}(\theta) = S(\theta, s) F(\theta, \sigma_{pr}, s) , \quad (42)$$

where  $S(\theta, s)$  is the shadowing correction and  $F(\theta, \sigma_{pr}, s)$  is a slope averaging integral, to be defined. Following Wagner,<sup>31</sup>

$$S(\theta, s) = \frac{1 - e^{-2Q}}{2Q} , \quad (43)$$

where

$$Q = \frac{\pi^{-1/2} e^{-t^2} - t [1 - \text{erf}(t)]}{4t} \quad (44)$$

and

$$t = \frac{\tan(\theta)}{s} . \quad (45)$$

In Eq. 44,  $\text{erf}(t)$  is the error function. In Eq. 42, the function  $F(\theta, \sigma_{pr}, s)$  is the small-roughness perturbation cross section averaged over bottom slope.

We approximate the slope averaging integral<sup>30</sup> by a three-point Gauss-Hermite quadrature<sup>32</sup>:

$$F(\theta, \sigma_{pr}, s) = \pi^{-1/2} \sum_{n=-1}^1 a_n \sigma_{pr}(\theta - \theta_n) , \quad (46)$$

$$a_{-1} = a_1 = 0.295410 , \quad a_0 = 1.181636 , \quad (47)$$

$$\theta_{-1} = -\theta_1 = 1.224745 \theta_s , \quad \theta_0 = 0.0 . \quad (48)$$

TR 9407 IV-29

The parameter  $\theta_s$  is the rms slope,  $s$ , converted to angular units as follows:

$$\theta_s = \frac{s \theta_\pi}{\pi} , \quad (49)$$

where the parameter  $\theta_\pi$  is simply an angle of  $180^\circ$ , defined to avoid confusion as to radians vs degrees. In Eq. 46, the argument of  $\sigma_{pr}$  sometimes falls outside the interval  $0^\circ$ – $90^\circ$  over which  $\sigma_{pr}$  is defined. If the argument is zero or negative, it should be set to  $0^\circ$ . This is equivalent to the composite roughness rule of setting the contribution to zero, as the cross section vanishes at  $0^\circ$ . If the argument is greater than  $90^\circ$ , it can be set to  $90^\circ$ . This choice is arbitrary; the composite roughness cross section at  $90^\circ$  will not contribute to our final result.

The function  $\sigma_{pr}(\theta)$  is the bottom backscattering cross section in the small-roughness perturbation approximation. We use a modified version of Kuo's expression for this function<sup>33</sup>:

$$\sigma_{pr}(\theta) = 4 k^4 \sin^4(\theta) |Y(\theta)|^2 W_2(K_\theta) . \quad (50)$$

In this expression,  $Y(\theta)$  is the complex function

$$Y(\theta) = \frac{(\rho - 1)^2 \cos^2(\theta) + \rho^2 - \kappa^2}{[\rho \sin(\theta) + P(\theta)]^2} , \quad (51)$$

where  $P(\theta)$  and  $\kappa$  are as defined in Eqs. 32 and 33.

The power spectrum,  $W_2$ , for random bottom relief appears in Eq. 50. It is evaluated at the wavenumber

$$K_\theta = [4 k^2 \cos^2(\theta) + (k/10)^2]^{1/2} . \quad (52)$$

The term involving  $k/10$  has been added to the usual expression for the argument of the spectrum. This is done to avoid the singularity in the power-law spectrum at zero

wavenumber (i.e., as  $\theta \rightarrow 90^\circ$ ); this somewhat arbitrary modification of the usual small-roughness expression only affects the cross section for grazing angles near  $90^\circ$ , and these angles are unimportant owing to the interpolation scheme used.

### *Large-Roughness Scattering Cross Section*

The observed scattering strengths for gravel and rock bottoms are relatively large and imply roughness parameters that fall outside the range of validity of the Kirchhoff and composite-roughness approximations. For these cases, an empirical fit taken from this model's predecessor<sup>17,25</sup> is used for the large-roughness cross section,  $\sigma_{lr}(\theta)$ .

$$\sigma_{lr}(\theta) = \sigma_1 \sin^m \left[ \frac{\theta_\pi}{1 + \frac{0.81 \theta_c^2}{\theta^2}} \right] + \frac{0.0260 |R(90^\circ)|^2}{s^2 \left[ 1 + \frac{(\theta - \frac{\theta_\pi}{2.0})^2}{2.6 \theta_s^2} \right]^{1.9} \left[ 1 + \frac{0.81 \theta_c^2}{\theta^2} \right]} \quad (53)$$

The sound speed ratio determines the critical angle,  $\theta_c$ , which is defined as

$$\theta_c = \cos^{-1}(1/v) \quad v \geq 1.001 \quad (54)$$

$$\theta_c = 2.5613^\circ \quad v < 1.001$$

For bottoms with  $v < 1.001$ , the critical angle is set to a fixed value, as in the predecessor model. This artifice led to problems when the earlier model was applied to sediments with low sound speeds. The interpolation used in the present model circumvents this problem because such sediments usually have small roughness, in which case the composite roughness model (which includes a physically correct treatment of low sediment sound speeds) is invoked. The parameter  $s$  is the large-scale slope defined in Eq. 41. Although this parameter is defined in the context of the composite roughness

TR 9407 IV-31

model, it is useful even when that model is invalid. The large-roughness cross section uses the following additional parameters:

$$m = 0.7263 (s)^{-1/3} \quad (55)$$

$$\sigma_l = \frac{0.04682 s^{1.25} v^{3.25} \left[ \left( 1 - \frac{2}{\rho} \right) v^{-2} + 1 \right]^2}{1 + \frac{3.54 \theta_s}{\theta_r}} \quad (56)$$

#### *Interpolation Between Approximations*

Interpolation of the various approximations employs the following function:

$$f(x) = \frac{1}{1 + e^x} \quad (57)$$

The first interpolation is between the Kirchhoff and composite roughness approximations. The interpolated cross section will be denoted  $\sigma_{mr}(\theta)$ , with the subscript signifying "medium roughness."

$$\sigma_{mr}(\theta) = f(x) \sigma_{kr}(\theta) + [1 - f(x)] \sigma_{cr}(\theta) \quad (58)$$

where

$$x = \frac{\cos(\theta) - \cos(\theta_{kDB})}{0.0125} \quad (59)$$

$$\cos(\theta_{kDB}) = \left[ \frac{1}{C_4} + 4 \right]^{-\frac{1}{4}} \quad (60)$$

$$C_4 = (1000)^{\frac{1}{1+\alpha}} (a q_c^2)^{\frac{1}{\alpha}} . \quad (61)$$

The interpolation shifts between the Kirchhoff approximation at grazing angles near  $90^\circ$  and the composite roughness approximation at smaller angles. The changeover occurs in the vicinity of  $\theta_{k,B}$ , which is approximately equal to the angle at which the Kirchhoff cross section has fallen 15 dB below its peak at  $90^\circ$ .

The Kirchhoff cross section,  $\sigma_{kr}(\theta)$ , accounts for the angular spread of energy that would be perfectly reflected if the interface were flat. The issue of double counting arises in modeling vertical-incidence or "fathometer" sonar echoes. If it is important to simulate the time and angle spread of this energy, the backscatter model can be used, but the forward loss model could be used if these spreads are deemed unimportant. It would be improper to combine the outputs of both approaches; this would be double counting.

The final interpolation, between the large roughness and medium roughness cross sections, gives the roughness scattering cross section appearing in Eq. 34.

$$\sigma_r(\theta) = f(y) \sigma_{mr}(\theta) + [1 - f(y)] \sigma_{kr}(\theta) . \quad (62)$$

The argument of the interpolating function is

$$y = \frac{(\tan^{-1} s - \theta_r)}{\Delta\theta} . \quad (63)$$

The parameters  $\theta_r$  and  $\Delta\theta$  are reference angles empirically set at the values

$$\theta_r = 7.0^\circ \quad \Delta\theta = 0.5^\circ . \quad (64)$$

#### b. Sediment volume scattering cross section, $\sigma_v(\theta)$

The term  $\sigma_v(\theta)$  in Eq. 34 describes volume scattering by the bottom material. An expression for sediment volume scattering including refraction and transmission loss at

TR 9407 IV-33

the sediment-water interface was published by Stockhausen.<sup>34</sup> This expression is generalized to allow for the effect of absorption on the transmission coefficient of the sediment/water interface and incorporate shadowing and bottom slope corrections analogous to Eq. 42:

$$\sigma_v(\theta) = S(\theta, s) F(\theta, \sigma_{pv}, s) \quad (65)$$

To evaluate  $F(\theta, \sigma_{pv}, s)$ , Eqs. 46–49 are used, with  $\sigma_{pv}$  replaced by

$$\sigma_{pv}(\theta) = \frac{5 \delta \sigma_2 |1 - R^2(\theta)|^2 \sin^2(\theta)}{v \ln 10 |P(\theta)|^2 \operatorname{Im}\{P(\theta)\}} \quad (66)$$

The function  $P(\theta)$  is given in Eq. 32. Equation 66 corrects a typographical error occurring in previous publications,<sup>1,9</sup> in which the exponent 2 of the reflection coefficient,  $R(\theta)$ , was omitted.

The volume scattering parameter,  $\sigma_2$ , is treated empirically. That is, it is not determined by measurement of sediment physical properties but rather is determined by comparing the model with backscattering data. The empirical approach to sediment volume scattering is in contrast to the treatment used for interface roughness scattering, where the roughness spectral parameters  $\gamma$  and  $w_2$  are measurable via stereophotography or other means. Analogous to this, there has been recent work on the physics of sediment volume scattering.<sup>35–37</sup> This work can be used to relate  $\sigma_2$  to measurable correlation functions or spectra describing sediment inhomogeneity. Such an approach is used, in fact, in the bistatic model presented in Section IV.D. Boyle and Chotiros<sup>38–39</sup> have argued that sediment volume scattering may often be due to the graininess of sediments or the presence of small gas bubbles. In such cases, sediment correlation functions may not provide a suitable characterization, but the parameter  $\sigma_2$  may be general enough to encompass such mechanisms.



### 3. Model Accuracy

The following comments on model accuracy are primarily derived from published reports on comparisons of this model with data from well characterized sites.<sup>8,9</sup> Because this model is similar to its predecessor,<sup>1</sup> earlier model-data comparisons<sup>5,6,17,40</sup> are also of value and are reflected in the discussion here.

Generally speaking, model accuracy improves as the quality of bottom characterization improves, and model predictions are most accurate when the grazing angle is not too small and the bottom roughness is not too large. The following estimates of model uncertainty are rough estimates based on engineering judgment rather than statistical analysis. Model "uncertainty" is defined as the largest difference expected between the model's prediction and measured data, neglecting errors in the data and discarding obvious outliers.

For rock and gravel bottoms, model uncertainty is approximately 10 dB for grazing angles greater than 15° and probably greater for smaller angles. Model uncertainty is approximately 3 dB for well-characterized sand and silt bottoms for grazing angles greater than 5°. For poorly characterized bottoms, uncertainties of approximately 5 dB and 10 dB can be expected for sand and silt bottoms, respectively.

Because the model incorporates many of the known mechanisms for bottom backscattering, it is reasonable to use the model to extrapolate measured scattering strength data to other frequencies, grazing angles, or bottom parameter values. Such extrapolations are expected to be most accurate for sand and silt bottoms.

For soft bottoms ( $M_2 > 3$ ), the model is most sensitive to the parameter  $\sigma_2$  describing sediment volume scattering. As noted earlier, this parameter is best determined by backscattering measurements, in which case the model becomes essentially a means of extrapolating in angle and frequency. As more and more data have accumulated, it has become clear that  $\sigma_2$  varies over a wide range. The largest reported values are about 0.1 and were obtained by direct measurement of sediment volume scattering.<sup>41</sup> A range of 15 dB is evident in the references cited here, and a range of 30 dB has been observed in

unpublished work by K.Y. Moravan on low-frequency bottom reverberation. These decibel values can be taken to be the range of scattering strengths observed for soft bottoms of nominally the same type.

For harder bottoms ( $M_s < 3$ ), the model is sensitive to the spectral parameters  $\gamma$  and  $w_2$ . The situation here is more favorable than for soft bottoms. Measurements of these parameters are available at some sites, and the range of variation in these parameters is not particularly great when translated into variation in scattering strength. Problems have arisen in applying the model to sites where the spectral exponent approaches the limits given in Eq. 15. The two known examples are a fine sand site,<sup>8</sup> where  $\gamma = 3.92$  was measured, and a coarse-shell bottom,<sup>6</sup> where  $\gamma = 2.47$  was measured.

The model is consistent with older data in the literature,<sup>42-44</sup> except for the fact that the model yields a more rapid falloff of backscattering strength with decreasing grazing angle than some of the earlier data. More recent data, such as those cited in the model/data comparisons above and those reported by Boehme et al.,<sup>45</sup> Boehme and Chotiros,<sup>46</sup> and Gensane,<sup>47</sup> confirm this more rapid falloff.

#### 4. Numerical Considerations

The gamma and error functions used in the model can be computed to sufficient accuracy using approximations found in Ref. 48. It should be noted that the argument of the gamma function sometimes falls outside the range 1-2, and this may require use of the relation  $\Gamma(x+1) = x \Gamma(x)$ . Numerical problems may be encountered if the exponential and error function arguments in Eqs. 43 and 44 become too large. To avoid such difficulties, the shadowing function can be set to unity if the parameter  $t$ , defined in Eq. 45, exceeds 2. Similarly, if the argument of the interpolating function, Eq. 57, is less than -40, set  $f(x) = 1$ ; if the argument is greater than 40, set  $f(x) = 0$ .

The scattering strength defined by Eq. 34 and subsequent equations approaches negative infinity as the grazing angle approaches zero. This presents problems in applications where a look-up table is used for scattering strength with entries at  $0^\circ$ ,  $1^\circ$ ,  $2^\circ$ , etc.

It is expected that angles of  $0.001^\circ$  and greater will present no numerical difficulty. For angles smaller than this, we recommend that the model output at  $0.001^\circ$  be used. The equations in this section have been written so as to be neutral with respect to the choice of angular units (radians or degrees). Complex expressions (Eqs. 51 and 66) are conveniently coded using complex arithmetic as noted in Section IV.B.3.

#### D. BISTATIC SCATTERING

The bottom bistatic scattering model is a generalization of the backscattering model presented in Section IV.C, and is documented in Ref. 49. Like the backscattering model, the bistatic model treats scattering from both interface roughness and sediment volume inhomogeneity. The input parameters for the bistatic model are identical to those for the backscattering model, with the exception of the volume scattering parameters. The single parameter,  $\sigma_2$ , used in the backscattering model is replaced by three parameters. Since most users will not have values for these parameters, a simple procedure is given so that  $\sigma_2$  can be used instead. The bistatic model employs three angular variables, defined in Figure 3.

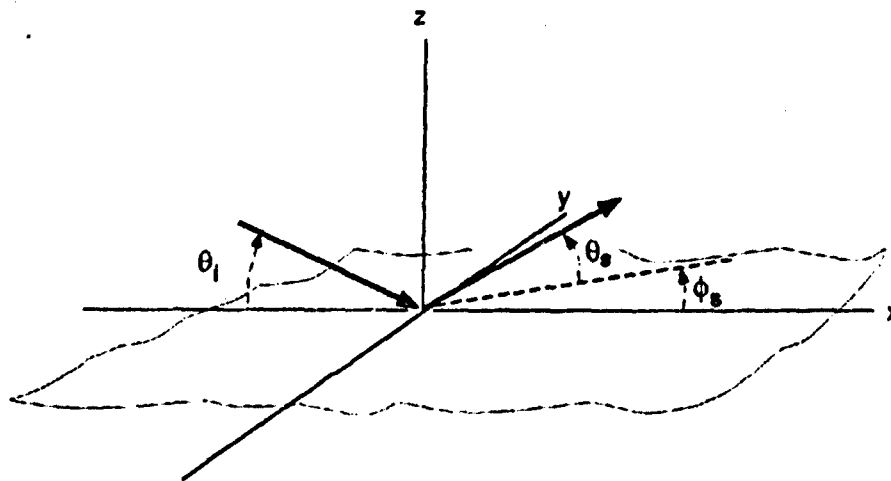


Figure 3. Bistatic scattering geometry. The angle  $\theta_i$  is the incident grazing angle,  $\theta_s$  is the scattered grazing angle, and  $\phi_s$  is the bistatic angle.

TR 9407 IV-37

The bistatic model has been compared with historical data, but these comparisons are not rigorous owing to lack of adequate physical data. Bistatic data and accompanying physical data suitable for model testing are currently being obtained under the Coastal Benthic Boundary Layer Program, managed by the Naval Research Laboratory.

The bistatic model embodies several features that are physically reasonable but untested experimentally. As illustrated in Figure 4, for hard (sandy) bottoms, interface scattering dominates sediment volume scattering away from the specular direction, while the opposite is true for soft (silt and clay) bottoms (Figure 5). The bistatic scattering strength exhibits a peak near the specular direction owing to interface scattering. This peak is broader in the vertical plane than in the horizontal plane (for example, compare Figures 4a and 4c and 5a and 5c); both widths decrease as the incident grazing angle decreases. In directions away from specular, the scattering strength is predicted to be a slowly varying function of the bistatic angle (the change in azimuth upon scattering). This can be seen in Figures 4c, 4d, 5c, and 5d.

The approximations used in this model fail for rough bottoms (e.g., gravel and rock). For the special case of backscattering, the model produces results similar to, but not identical to, the backscattering model and is consistent with available backscattering data for bottoms with small to moderate roughness (e.g., clay, silt, and sand).

### 1. Model Inputs

Table 4 lists the input parameters for the bistatic model. The parameters  $\gamma_3$ ,  $w_3$ , and  $\mu$  replace the volume scattering parameter,  $\sigma_2$ . Before defining these additional parameters, defaults will be provided for users who wish to employ only the backscattering model inputs of Table 1.

$$\gamma_3 = 3.0 \quad (67)$$

$$\mu = -1.0 \quad (68)$$

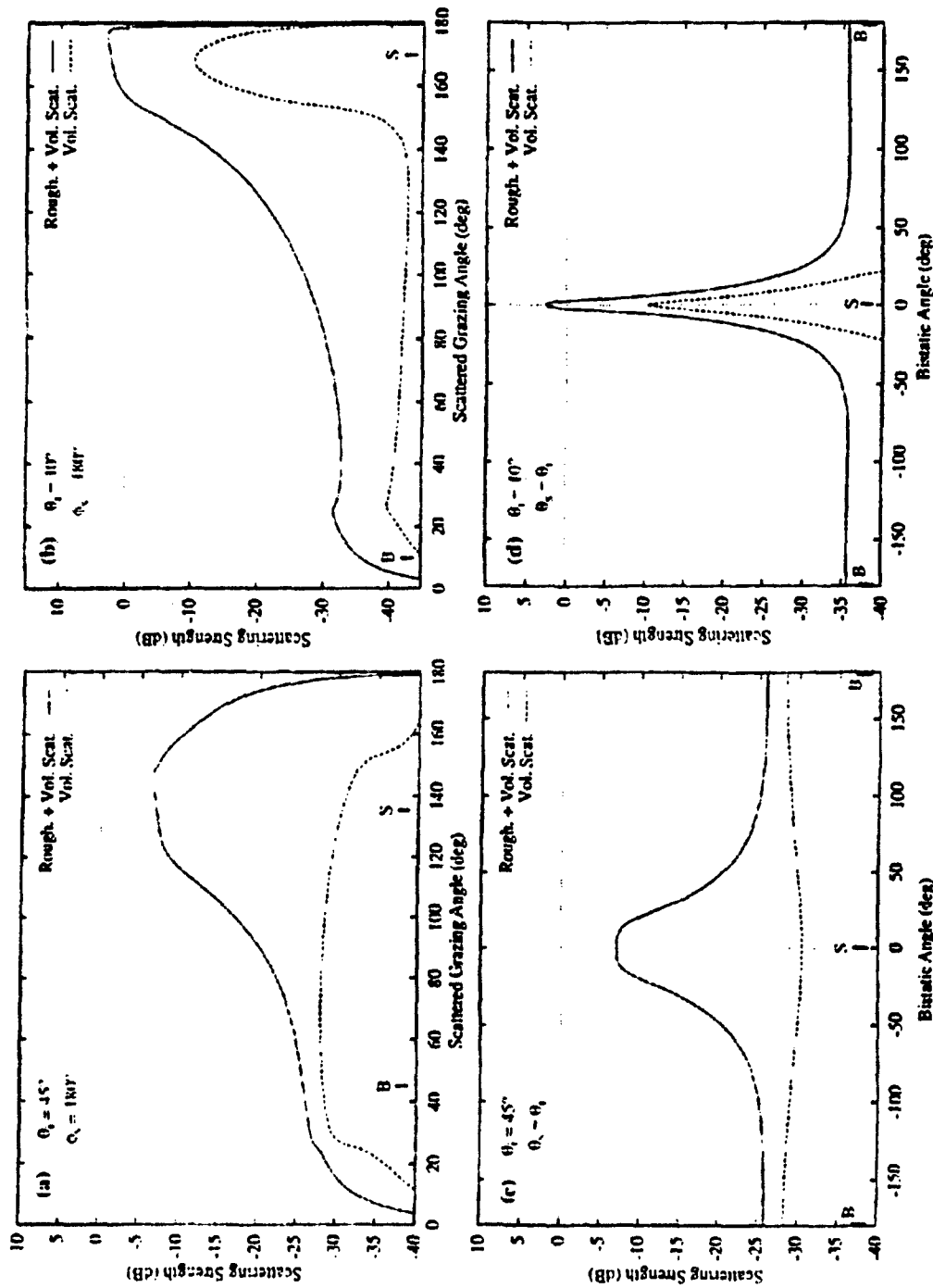


Figure 4. Model curves for bistatic scattering strength at 35 kHz for a sandy bottom. The sediment volume scattering component is shown as a dashed line while the total is shown as a solid line. (a) and (b) show the dependence on the scattered grazing angle,  $\theta_s$ , with the bistatic angle fixed ( $\theta_r = 180^\circ$ ). (c) and (d) show the dependence on bistatic angle with the scattered grazing angle fixed ( $\theta_s = \theta_r$ ). The specular and backscatterer directions are labeled "S" and "B". The model input parameters are  $v = 1.113$ ,  $\rho = 1.940$ ,  $\delta = 0.0115$ ,  $\gamma_1 = 3.0$ ,  $w_1 = 0.000127 \text{ cm}^3$ ,  $\mu = -1.0$ ,  $\gamma = 3.67$ ,  $w_2 = 0.00422 \text{ cm}^3$ ,  $c_1 = 1500 \text{ m/s}$ .

TR 9407 IV-39

ADB199453

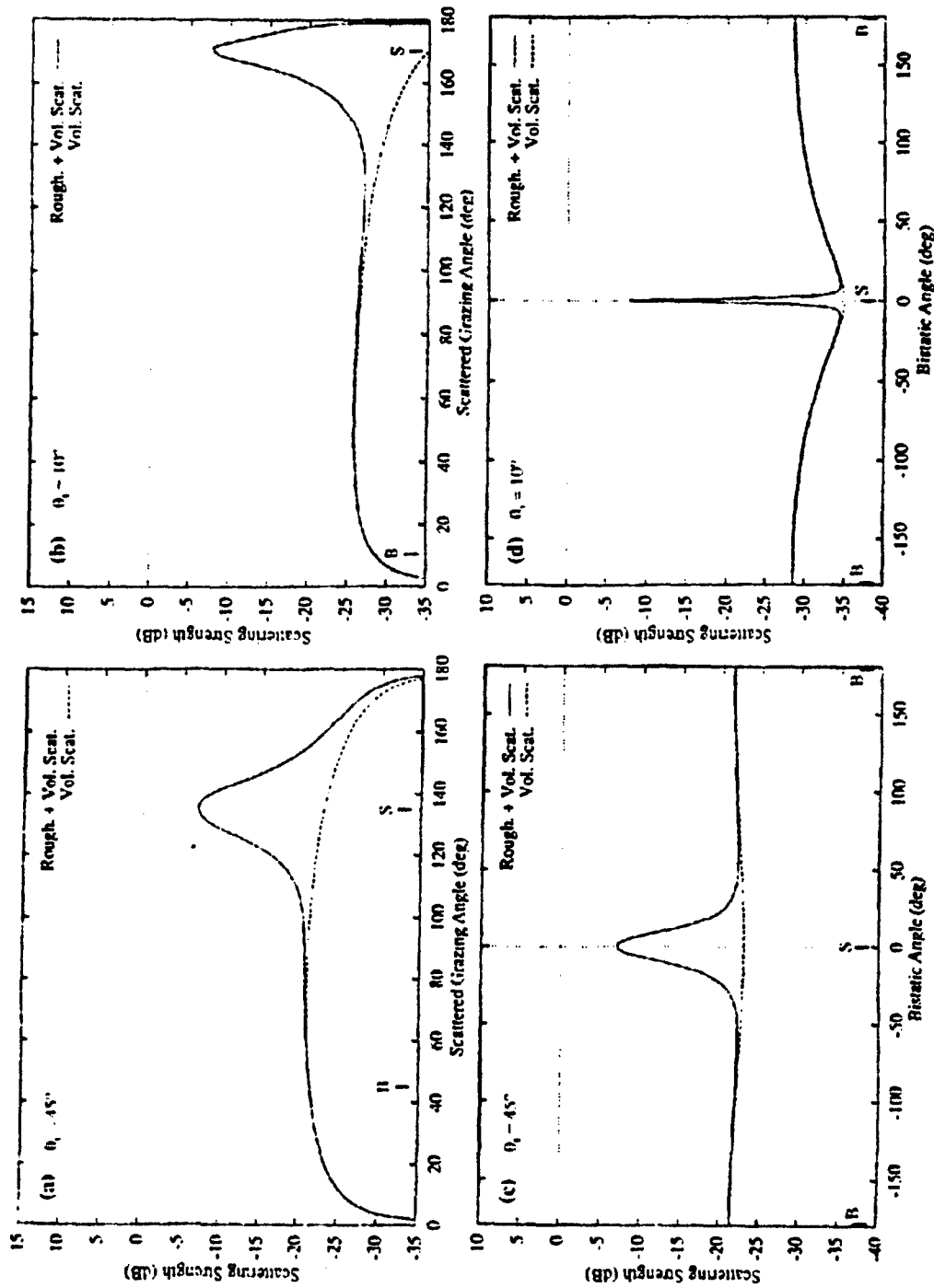


Figure 5. Model curves for bistatic scattering strength at 40 kHz for a silty bottom. The sediment volume scattering component is shown as a dashed line while the total is shown as a solid line. (a) and (b) show the dependence on the scattered grazing angle,  $\theta_s$ , with the bistatic angle fixed ( $\phi_s = 180^\circ$ ). (c) and (d) show the dependence on bistatic angle with the scattered grazing angle fixed ( $\theta_s = 0^\circ$ ). The specular and backscatter directions are labeled "S" and "B". The model input parameters are  $v = 0.988$ ,  $\rho = 1.390$ ,  $\delta = 0.00553$ ,  $\gamma_1 = 3.0$ ,  $w_3 = 0.000306 \text{ cm}^3$ ,  $\mu = -1.0$ ,  $\gamma = 3.18$ ,  $w_2 = 0.00318 \text{ cm}^4$ ,  $c_1 = 1528 \text{ m/s}$ .

Table 4. Bottom parameters used as inputs to the bistatic model.

Symbol	Definition	Short Name
$\rho$	Ratio of sediment mass density to water mass density	Density ratio
$v$	Ratio of sediment sound speed to water sound speed	Sound speed ratio
$\delta$	Ratio of imaginary wavenumber to real wavenumber for the sediment	Loss parameter
$\gamma_3$	Exponent of sediment inhomogeneity spectrum	Inhomogeneity exponent
$w_3$	Strength of sediment inhomogeneity spectrum ( $\text{cm}^3$ ) at wavenumber $2\pi/\lambda = 1 \text{ cm}^{-1}$	Inhomogeneity strength
$\mu$	Ratio of compressibility to density fluctuations in the sediment	Fluctuation ratio
$\gamma$	Exponent of bottom relief spectrum	Spectral exponent
$w_2$	Strength of bottom relief spectrum ( $\text{cm}^4$ ) at wavenumber $2\pi/\lambda = 1 \text{ cm}^{-1}$	Spectral strength

$$w_3 = \frac{40 \delta \sigma_2 (2h_0)^{\gamma_3}}{\pi \ln 10 \left( \frac{k}{v} \right)^{3-\gamma_3} (1 + \delta^2)^2 (\mu - 1)^2} \quad (69)$$

The expression for  $w_3$  is general and can be used with values of  $\gamma_3$  and  $\mu$  other than those given above. Ideally, the parameters  $\gamma_3$ ,  $w_3$ , and  $\mu$  should be assigned values based on measurements of sediment inhomogeneity. At present, such a characterization of sediments is in the realm of research.<sup>37,50</sup> There is no compilation of relevant inhomogeneity data. Consequently, these parameters will be defined, but detailed prescriptions for estimating these parameters in terms of grain size, etc., will not be given.

Sediment inhomogeneities are described in the model by three-dimensional spectra for compressibility and density fluctuations. These fluctuations are normalized by dividing by the mean values of compressibility and density; the normalized compressibility

TR 9407 IV-41

and density fluctuations are denoted  $\gamma_K(\mathbf{r})$  and  $\gamma_p(\mathbf{r})$ , respectively. It is assumed that the fluctuations in sediment compressibility and density are tied together by a simple proportionality relation,

$$\gamma_K(\mathbf{r}) = \mu \gamma_p(\mathbf{r}) . \quad (70)$$

The model parameter  $\mu$  is expected to have values in the neighborhood of  $-1$ , because density and compressibility tend to be anticorrelated. For example, if a loosening of the sediment produces a 10% *decrease* in density, then there will be a corresponding *increase* in compressibility of about 10%. The argument for this anticorrelation is based on the experimental fact that sediment sound speed is a rather slowly varying function of density.<sup>15</sup> That is, a 10% change in density is likely to produce a much smaller percentage change in sediment sound speed. Since sound speed depends on the product of compressibility and density, it follows that density and compressibility changes must be anticorrelated in order to produce the observed small change in sound speed. Note, however that  $\mu = -1$  is a default value and that the model allows *any* value for  $\mu$ .

We assume that the fluctuations in density and compressibility are spatially stationary, so that power spectra can be defined as Fourier transforms of the corresponding fluctuation covariances,

$$W_{\alpha\beta}(k_i) = \frac{1}{(2\pi)^3} \int e^{-i\mathbf{k} \cdot \mathbf{r}} \langle \gamma_\alpha(\mathbf{r}_0 + \mathbf{r}) \gamma_\beta(\mathbf{r}_0) \rangle d^3r , \quad (71)$$

where the dummy subscripts  $\alpha$  and  $\beta$  can be taken to be any combination of  $p$  and  $K$ .

We assume that the spectrum for density fluctuations obeys the following power law:

$$W_{pp}(k_i) = \frac{w_2}{(k_i h_0)^{\gamma_3}} , \quad 3.0 \leq \gamma_3 \leq 5.0 . \quad (72)$$



Equation 70 then forces the following expressions for the compressibility fluctuation spectrum  $W_{KK}(k_v)$  and the cross spectrum  $W_{\rho K}(k_v)$ :

$$W_{KK}(k_v) = \frac{w_3 \mu^2}{(k_v h_0)^{\gamma_1}} \quad (73)$$

and

$$W_{\rho K}(k_v) = \frac{w_3 \mu}{(k_v h_0)^{\gamma_1}} \quad (74)$$

For the sake of simplicity, three-dimensional isotropy is assumed for the sediment inhomogeneity. This is reflected in Eqs. 72–74 in that these spectra depend only on the *magnitude*,  $k_v$ , of the three-dimensional wavevector,  $\mathbf{k}_v$ . Layered sediments, by definition, do not possess three-dimensional isotropy. It is an open question whether a more complicated, anisotropic sediment model is needed at high frequencies.

Where grains and bubbles are the dominant causes of sediment volume scattering,<sup>38,39</sup> it may be possible to mimic the proper volume scattering behavior by adjusting  $\mu$ ,  $\gamma_1$ , and  $w_3$ , which then should be regarded as empirical, rather than physical, parameters.

As noted above, the inhomogeneity exponent,  $\gamma_1$ , is restricted to the range 3.0 to 5.0. The parameter  $\mu$  should be restricted to the range -10.0 to 10.0. The inhomogeneity strength,  $w_3$ , is restricted by the limits of 0.0 to 1.0 imposed on  $\sigma_2$ . Thus  $w_3$  must be in the range 0.0 to the value obtained by inserting  $\sigma_2 = 1.0$  in Eq. 69.

## 2. Equations for Bottom Bistatic Scattering Strength

The bistatic scattering strength will be defined in exactly the same fashion as the backscattering strength, the only difference being that more angular variables are required. The bottom bistatic scattering strength will be written in the form

TR 9407 IV-43

$$S_b(\theta_s, \phi_s, \theta_i) = 10 \log_{10} [\sigma_r(\theta_s, \phi_s, \theta_i) + \sigma_v(\theta_s, \phi_s, \theta_i)] . \quad (75)$$

As for backscattering, the bistatic scattering cross section is decomposed into two components—one,  $\sigma_r(\theta_s, \phi_s, \theta_i)$ , for scattering from the rough interface and one,  $\sigma_v(\theta_s, \phi_s, \theta_i)$ , for scattering from sediment volume inhomogeneities. In the following, all of the numbered equations are necessary for computation: no intermediate results are given except in the body of the text as unnumbered equations.

#### a. Definition of geometric parameters

The angles  $\theta_s, \phi_s, \theta_i$  appearing in Eq. 75, are defined in Figure 3. These are the same angles employed by Lang and Culver,<sup>51</sup> but our notation is slightly different. The "incident grazing angle" is denoted  $\theta_i$ , the "scattered grazing angle" is  $\theta_s$ , and  $\phi_s$  is the "bistatic angle," defined as the difference in azimuth between the scattered and incident directions. In general, one needs *four* angles, two grazing angles and two azimuths, but only the azimuthal difference is needed here because bottom statistics are assumed to be laterally isotropic.

It is useful to define some geometrical factors that will appear in later expressions for the roughness and volume scattering cross sections. In terms of the various angles, these geometric parameters are

$$\Delta = \frac{1}{\sqrt{2}} (1 + \sin \theta_i \sin \theta_s - \cos \theta_i \cos \theta_s \cos \phi_s)^{1/2} , \quad (76)$$

$$\Delta_z = \frac{1}{2} (\sin \theta_i + \sin \theta_s) , \quad (77)$$

and

$$\Delta_i = \frac{1}{2} (\cos^2 \theta_i - 2 \cos \theta_i \cos \theta_s \cos \phi_s + \cos^2 \theta_s)^{1/2} . \quad (78)$$

Note that  $\Delta = \sqrt{\Delta_i^2 + \Delta_s^2}$ . These parameters are related to the difference between wavevectors in the scattered and incident directions, normalized by dividing by  $2k$ . Equations 76, 77, and 78 represent, respectively, the magnitude, the normal component, and the transverse component of this normalized difference.

We will define the "specular direction" by  $\theta_s = \theta_i$ ,  $\phi_s = 0$ . This is the direction of mirror-like reflection from a flat, horizontal interface. In the specular direction,  $\Delta_t = 0$ . The correspondence between a given scattering direction and the angular variables is not unique. For example, the specular direction can also be specified as  $\theta_s = 180^\circ - \theta_i$ ,  $\phi_s = 180^\circ$ .

### b. Roughness scattering cross section

Two different approximations are used for the roughness scattering cross section,  $\sigma_r(\theta_s, \phi_s, \theta_i)$ . The Kirchhoff approximation is used for scattering near the specular direction, and the perturbation approximation is used for all other directions. This approach is somewhat different than that used in the backscattering model, where the perturbation approximation is "improved" by applying composite roughness averaging. This is a means of accounting for the large-scale random slope of the bottom, but is dropped in the bistatic case where such averaging becomes very cumbersome mathematically. An additional difference is that the empirical cross section used for very rough bottoms in the backscattering model is not used because it has no bistatic generalization.

#### *Kirchhoff Approximation*

Analogous to the monostatic expression of Eq. 37, the approximate bistatic Kirchhoff cross section can be expressed in the following form:

$$\sigma_{kr}(\theta_i, \phi_s, \theta_i) = \frac{|R(\theta_{is})|^2 \Delta^4}{8\pi} \frac{b q_c [1 + 100\Delta_i^4]}{[\Delta_i^{4\alpha} + a q_c^2 \Delta_s^4]^{\frac{1+\alpha}{2\alpha}}}, \quad (79)$$

TR 9407 IV-45

The numerator factor involving  $\Delta_i^4$  artificially increases the Kirchhoff contribution for directions far from specular (note the text following Eq. 84). Because the interpolation scheme favors the smaller of the Kirchhoff and perturbation cross sections, it suppresses the Kirchhoff contribution except near the specular direction. In Eq. 79,  $\alpha$  is as defined in Eq. 35, and  $q_i$ ,  $a$ , and  $b$  are as defined in Eqs. 38–40. The function  $R(\theta_{is})$  is the complex plane-wave reflection coefficient for a flat interface separating water and sediment (Eq. 30). This coefficient is *not* evaluated at normal incidence as in the backscattering model. Rather, in accordance with work by Thorsos (private communication), the local tilt of the interface is assumed to be such as to cause specular reflection in the scattered direction. This is the dominant process for scattered angles near the specular direction, and Thorsos finds that this approach gives improved accuracy in bistatic scattering. With this assumption, the reflection coefficient is to be evaluated at the grazing angle

$$\theta_{is} = \sin^{-1} \Delta \quad (80)$$

#### *Perturbation Approximation*

The bistatic form of the scattering cross section computed in the perturbation approximation<sup>8,9,16,33</sup> can be put in the following form convenient for computation:

$$\sigma_{pr}(\theta_i, \phi_s, \theta_s) = \frac{1}{4} k^4 [1 + R(\theta_i)]^2 [1 + R(\theta_s)]^2 |G|^2 W_2(\Delta K) \quad (81)$$

where

$$G = (1/\rho - 1) [1 - \sin^2 \theta_i \cos \theta_s \cos \phi_s - P(\theta_i)P(\theta_s)/\rho] + 1 - \frac{k^2}{\rho} \quad (82)$$

The parameter  $\Delta K$  in Eq. 81 is the "Bragg wavenumber," modified to avoid difficulty with the singularity at  $K = 0$  in the relief spectrum,  $W_2(K)$  (Eq. 7).

$$\Delta K = 2k(\Delta_i + 0.0001) \quad (83)$$

### Interpolation Between Approximations

The bistatic model uses an improved Kirchhoff-perturbation interpolation scheme in which the smaller of the cross sections takes precedence. This procedure is based on the fact that, for a power-law relief spectrum, the perturbation approximation overpredicts scattering near the specular direction owing to the singularity in the relief spectrum at zero wavenumber. In contrast, the Kirchhoff approximation tends to overpredict in other directions.<sup>52,53</sup> This overprediction is particularly bad for horizontal scattering, where the Kirchhoff approximation yields a finite cross section while energy conservation demands that the cross section vanish. The interpolation scheme used here is

$$\sigma_r(\theta_s, \phi_s, \theta_i) = [\sigma_{kr}^\eta(\theta_s, \phi_s, \theta_i) + \sigma_{pr}^\eta(\theta_s, \phi_s, \theta_i)]^{\frac{1}{\eta}} \quad (84)$$

The smaller cross section will dominate if the parameter  $\eta$  is negative. The value  $\eta = -2$  is recommended.

The issue of coherent vs incoherent scattering is not addressed by the present model. In fact, it is assumed that *all* scattered energy is incoherent. If the surface has very little roughness, the scattering strength will be sharply peaked in the specular direction, and the height and width of this peak will be such as to give approximately the same energy flux as the forward loss model in Section IV.B. If the forward loss model is used to account for energy scattered near the specular direction,  $\sigma_r$  should not be used for this purpose, as this would be double counting.

### c. Sediment volume scattering cross section

If composite roughness averaging is not used, the bistatic generalization of Eqs. 65 and 66 is

$$\sigma_i(\theta_s, \phi_s, \theta_i) = \frac{\sigma_{i,0} (1 + R(\theta_i))^2 (1 + R(\theta_s))^2}{2k\rho^2 \operatorname{Im} \left\{ P(\theta_i) + P(\theta_s) \right\}} \quad (85)$$

TR 9407 IV-47

where  $\sigma_{v,0}$  is the volume scattering cross section due to sediment inhomogeneities and  $\sigma_i$  is the resulting interface scattering strength to be inserted in Eq. 75. Following Hines,<sup>35</sup> Tang,<sup>36</sup> and Lyons and Anderson,<sup>37</sup> perturbation theory is used to obtain the volume scattering cross section,

$$\sigma_{v,0} = \frac{\pi}{2} k^4 \left[ \mu \kappa^2 + \cos \theta_i \cos \theta_s \cos \phi_s - P(\theta_i) P(\theta_s) \right]^2 W_{pp}(\Delta k) \quad (86)$$

The spectrum  $W_{pp}$ , is given by Eq. 72, and

$$\Delta k = k \left[ 4 \Delta_l^2 + \left( \operatorname{Re} \left[ P(\theta_i) + P(\theta_s) \right] \right)^2 \right]^{1/2} \quad (87)$$

is the Bragg wavenumber.

### 3. Model Accuracy

The bistatic model is compared with a limited set of historical data in Ref. 49. These comparisons qualitatively verify some of the features of the model but are not sufficient for a quantitative assessment of model accuracy because no physical data were available from which to estimate model inputs. The model predicts that scattering strength varies slowly with bistatic angle in the vicinity of the backscatter direction. This feature is supported by comparisons with historical data.<sup>54,55</sup> The bistatic model was found to be in reasonable agreement with the backscattering model in comparisons for two experimental sites having silty and sandy bottoms. Thus, for smooth and moderately rough bottoms (e.g., clay, silt, and sand), the accuracy of the bistatic model in directions near backscattering should be comparable to the accuracy of the backscattering model. The bistatic model is not expected to have useful accuracy for rough gravel and rock bottoms owing to failure of the scattering approximations used. Specifically, if the difference between the bistatic and backscattering models becomes significant ( $\sim 3$  dB or more) when using the same input parameters and equivalent angles, the bistatic model

should not be used. Near the specular direction, the bistatic model predicts essentially the same acoustic intensity as the forward loss model and so has similar accuracy in this respect. The model's prediction for the angular spread of near-specular energy has not been tested experimentally, however.

#### 4. Numerical Considerations

The expressions used in computing the perturbation approximations for roughness and volume scattering are conveniently coded using complex arithmetic in the fashion noted in Section IV.B.3. To avoid negative infinities in the scattering strength, values of  $\theta_i$  or  $\theta_r$  that are within  $0.001^\circ$  of either  $0^\circ$  or  $180^\circ$  should be replaced by  $0.001^\circ$  or  $179.999^\circ$ . To avoid underflow and overflow, the following quantities should be limited to be no smaller than  $10^{-15}$ :  $\sigma_{kr}$  (Eq. 79), the denominator of Eq. 79 (after exponentiation), and  $\sigma_{pr}$  (Eq. 81).

## REFERENCES — Section IV

1. APL-UW High-Frequency Ocean Environmental Acoustic Models (U), APL-UW 8907, November 1989. (Confidential)
2. E. L. Hamilton, "Compressional wave attenuation in marine sediments," *Geophysics*, 37, 620-646 (1972).
3. M. D. Richardson and D. K. Young, "Geoacoustic models and bioturbation," *Mar. Geol.*, 38, 205-218 (1980).
4. K. B. Briggs, M. D. Richardson, and D. K. Young, "Variability in geoacoustic and related properties of surface sediments from the Venezuela Basin, Caribbean Sea," *Mar. Geol.*, 68, 73-106 (1985).
5. S. Stanic, K. B. Briggs, P. Fleischer, R. I. Ray, and W. B. Sawyer, "Shallow-water high-frequency bottom scattering off Panama City, Florida," *J. Acoust. Soc. Am.*, 83, 2134-2144 (1988).
6. S. Stanic, K. B. Briggs, P. Fleischer, W. B. Sawyer, and R. I. Ray, "High-frequency acoustic backscattering from a coarse shell ocean bottom," *J. Acoust. Soc. Am.*, 85, 125-136 (1989).
7. K. B. Briggs, P. Fleischer, W. H. Jahn, R. I. Ray, W. B. Sawyer, and M. D. Richardson, Investigation of High-Frequency Acoustic Backscattering Model Parameters: Environmental Data from the Arafura Sea, NORDA Report 197, February 1989.
8. D. R. Jackson and K. B. Briggs, "High-frequency bottom backscattering: Roughness versus sediment volume scattering," *J. Acoust. Soc. Am.*, 92, 962-977 (1992).
9. P. D. Mourad and D. R. Jackson, "High frequency sonar equation models for bottom backscatter and forward loss," in *Proceedings of OCEANS '89* (Marine Technology Society and IEEE, 1989), 1168-1175.
10. C. K. Wentworth, "A scale of grade and class for clastic sediments," *J. Geology*, 30, 377-392 (1922).
11. E. W. Lane, "Report of the subcommittee on sedimentary terminology," *Trans. AGU*, 289, 936-938 (1947).
12. D. L. Inman, "Measure for describing the size distribution of sediments," *J. Sediment Petrol.*, 22, 125-145 (1952).
13. F. P. Shepard, "Nomenclature based on sand-silt-clay ratios," *J. Sediment Petrol.*, 24, 151-158 (1954).
14. R. L. Folk, "The distinction between grain size and mineral composition in sedimentary-rock nomenclature," *J. Geology*, 62, 344-359 (1954).



15. E.L. Hamilton and R.T. Bachmann, "Sound velocity and related properties of marine sediments," *J. Acoust. Soc. Am.*, 72, 1891-1904 (1982).
16. D.R. Jackson, D.P. Winebrenner, and A. Ishimaru "Application of the composite roughness model to high-frequency bottom backscattering," *J. Acoust. Soc. Am.*, 79, 1410-1422 (1986).
17. D.R. Jackson, Third Report o. TTCP Bottom Scattering Measurements: Model Development, APL-UW 8708. September 1987.
18. C.S. Clay and H. Medwin, *Acoustical Oceanography* (Wiley, New York, 1977), p. 491.
19. K.B. Briggs, "Microtopographical roughness of shallow-water continental shelves," *IEEE J. Oceanic Eng.*, 14, 360-367 (1989).
20. D.R. Jackson, A.M. Baird, J.J. Crisp, and P.A.G. Thomsom, "High-frequency bottom backscattering measurements in shallow water," *J. Acoust. Soc. Am.*, 80, 1188-1199 (1986).
21. K.V. Mackenzie, "Reflection of sound from coastal bottoms," *J. Acoust. Soc. Am.*, 32, 221-231 (1959).
22. H.W. Marsh and M. Schulkin, "Shallow-water transmission," *J. Acoust. Soc. Am.*, 34, 863-864(L) (1962).
23. D.E. Weston and P.A. Ching, "Wind effects in shallow-water acoustic transmission," *J. Acoust. Soc. Am.*, 86, 1530-1545 (1989).
24. H.R. Hall and W.H. Watson, An Empirical Bottom Reflection Loss Expression for Use in Sonar Range Prediction, NUC Tech. Note 10, Naval Ocean Systems Center, San Diego. July 1967.
25. APL-UW Ocean Environmental Acoustic Models, Revision 1 (U), APL-UW 8407, June 1984. (Confidential)
26. S.T. McDaniel, Effect of Variations of Sediment Properties on High-Frequency Sea Floor Reverberation, TM 88-23, Applied Research Laboratory, Pennsylvania State University, February 1988.
27. R.J. Urick, *Principles of Underwater Sound* (McGraw-Hill, New York, 1983).
28. A.M. Yaglom, *An Introduction to the Theory of Stationary Random Functions* (Prentice-Hall, Englewood Cliffs, New Jersey, 1962).
29. A. Ishimaru, *Wave Propagation and Scattering in Random Media, Volume 2, Multiple Scattering, Turbulence, Rough Surfaces, and Remote Sensing* (Academic Press, New York, 1978).

TR 9407 IV-51

30. S. T. McDaniel and A. D. Gorman, "Acoustic and radar sea surface backscatter," *J. Geophys. Res.*, **87**, 4127-4136 (1982).
31. R. J. Wagner, "Shadowing of randomly rough surfaces," *J. Acoust. Soc. Am.* **41**, 138-147 (1967).
32. B. Carnahan, H. A. Luther, and J. O. Wilkes, *Applied Numerical Methods* (Wiley, New York, 1969), p. 116.
33. E. Y. Kuo, "Wave scattering and transmission at irregular surfaces," *J. Acoust. Soc. Am.*, **36**, 2135-2142 (1964).
34. J. H. Stockhausen, Scattering from the Volume of an Inhomogeneous Half-Space, Report No. 63/9, Naval Research Establishment, Canada, 1963.
35. P. C. Hines, "Theoretical model of acoustic backscatter from a smooth seabed," *J. Acoust. Soc. Am.*, **88**, 324-334 (1990).
36. D. Tang, "Acoustic wave scattering from a random ocean bottom," Ph.D. thesis, Massachusetts Institute of Technology and Woods Hole Oceanographic Institution, June 1991.
37. A. P. Lyons and A. L. Anderson, "Acoustic scattering from the seafloor: Modeling and data comparison," *J. Acoust. Soc. Am.*, **95**, 2441-2451 (1994).
38. F. A. Boyle and N. P. Chotiros, Bottom Penetration at Shallow Grazing Angles II, ARL-TR-92-12, Applied Research Laboratories, The University of Texas at Austin, June 1992.
39. F. A. Boyle and N. P. Chotiros, Bottom Backscatter From Trapped Bubbles, ARL-TR-93-15, Applied Research Laboratories, The University of Texas at Austin, July 1993.
40. H. Boehme, N. P. Chotiros, and D. J. Churay, High Frequency Environmental Acoustics, Bottom Backscattering Results, ARL-TR-85-30, Applied Research Laboratories, The University of Texas at Austin, October 1985.
41. R. A. Stewart and N. P. Chotiros, "Estimation of sediment volume scattering cross section and absorption coefficient," *J. Acoust. Soc. Am.*, **91**, 3242-3247 (1992).
42. C. M. McKinney and C. D. Anderson, "Measurements of backscattering of sound from the ocean bottom," *J. Acoust. Soc. Am.*, **36**, 158-163 (1964).
43. H.-K. Wong and W. D. Chesterman, "Bottom backscattering near grazing incidence in shallow water," *J. Acoust. Soc. Am.*, **44**, 1713-1718 (1968).
44. A. V. Bunchuk and Yu. Yu. Zhitkovskii, "Sound scattering by the ocean bottom in shallow-water regions (review)," *Sov. Phys. Acoust.*, **26**, 363-370 (1980).

45. H. Boehme, N. P. Chotiros, L. D. Rolleigh, S. P. Pitt, A. L. Garcia, T. G. Goldsberry, and R. A. Lamb, "Acoustic backscattering at low grazing angles from the ocean bottom. Part I. Bottom backscattering strength," *J. Acoust. Soc. Am.*, **77**, 962-974 (1985).
46. H. Boehme and N. P. Chotiros, "Acoustic backscattering at low grazing angles from the ocean bottom," *J. Acoust. Soc. Am.*, **84**, 1018-1029 (1988).
47. M. Gensane, "A statistical study of acoustic signals backscattered from the sea bottom," *IEEE J. Oceanic Eng.*, **14**, 84-93 (1989).
48. M. Abramowitz and I. A. Stegun (editors), *Handbook of Mathematical Functions* (Dover Publications, New York, 1965).
49. D. R. Jackson, A Model for Bistatic Bottom Scattering in the Frequency Range 10-100 kHz, APL-UW 9305, August 1993.
50. T. Yamamoto, "Velocity fluctuations and other physical properties of marine sediments measured by crosswell acoustic tomography," *J. Acoust. Soc. Am.* (submitted, 1994).
51. D. C. Lang and R. L. Culver, A High Frequency Bistatic Ocean Surface Scattering Strength. Technical Memorandum 92-342, Applied Research Laboratory, Pennsylvania State University, December 1992.
52. E. I. Thorsos, "Exact numerical methods vs the Kirchhoff approximation for rough surface scattering," in *Computational Acoustics, Vol. II: Algorithms and Applications*, edited by D. Lee, R. L. Sternberg, and M. H. Schultz (North-Holland, Amsterdam, 1988), pp. 209-226.
53. E. I. Thorsos, "The validity of the Kirchhoff approximation for rough surface scattering using a Gaussian roughness spectrum," *J. Acoust. Soc. Am.*, **83**, 78-92 (1988).
54. R. J. Urick, "Side scattering of sound in shallow water," *J. Acoust. Soc. Am.*, **32**, 351-355 (1960).
55. S. Stanic, E. Kennedy and R. I. Ray, "Variability of shallow-water bistatic bottom backscattering," *J. Acoust. Soc. Am.*, **90**, 547-553 (1989).

TR 9407 IV-53

## **V. Arctic**

### *Introduction*

For arctic operations, a nonridged ice surface can be modeled similarly to the open sea surface. However, when ice is ridged, the under-ice keels act as discrete reflectors and must be treated differently. In modeling an ice keel, one can use either an "acoustic model" or an "ice block model," depending on the level of effort and the ice information available. An acoustic model that relates keel reflections to ridge dimensions and seasonal conditions is directly applicable and thus probably preferable. Modeling a keel as a pile of ice blocks requires an idealistic assumption as to keel structure and a detailed knowledge of the reflectivity of various ice surfaces. The greater effort may not necessarily provide a more accurate model. In this section, we provide parameters for either choice of model.

For many applications (e.g., measuring ice thickness from below), sound speed and absorption in the ice are important. Expressions for sound speed as a function of the salinity and temperature of the ice, average vertical sound speed as a function of thickness and air/ice interface temperature, and absorption as a function of temperature and frequency are given in Section V.A.

The ice cover, when formed in calm weather or in sheltered locations, is fairly flat and uniform. The backscattering and forward scattering from this ice are important to the modeler in two ways: (1) as an upper boundary to the medium in nonridged ice, and (2) as one surface of blocks in ice keels. In Section V.B we include a summary of forward scattering, near-normal "reflectivity," and low-angle backscattering from nonridged ice.

In Section V.C we discuss the formation of ice ridges and the statistical properties of the corresponding under-ice keels, which act as large false targets for acoustic systems. The target strength distributions for these false targets are provided in Section V.D. They can be used directly in acoustic modeling or as a verification of the results of ice keel modeling. There are not enough data to offer guidance about how to vary the distribution for seasonal or site-specific conditions, except for one curve that is applicable to sheltered areas. Distribution curves in both fall and spring were given in the previous version of this document (APL-UW TR 8907). They are not shown here because they are classified.

TR 9407 V-1

For more detailed modeling requirements (e.g., for a moving platform), we provide information on ice keel reflectors—their spacing in a keel and their angular response pattern. These can be used to compute such values as the number of pings from a moving torpedo that will detect a keel reflector and the variation in target strength from ping to ping.

Ice keel reflections depend on frequency and pulse length. Examples of the frequency dependence are given to help select optimum parameters. Also, the interference between reflectors depends on these parameters and may be a consideration in their selection. The results of some measurements and studies of this interference are given.

## A. SOUND SPEED AND ATTENUATION

### 1. Vertical Sound Speed as a Function of Salinity and Temperature

The density and porosity of the ice depend on the salinity and temperature. This dependence is summarized in equations of Biot<sup>1,2</sup> and Cox and Weeks<sup>1,3</sup>:

$$\rho = \beta \rho_f + (1 - \beta) \rho_s \quad (1a)$$

$$\beta = \frac{\rho_s S}{\rho_f S_f - \rho_f S + \rho_s S} \quad (1b)$$

$$\rho_s = 917.0 - 1.403 \times 10^{-1} T \quad (1c)$$

$$\rho_f = 1000.0 + 0.8 S_f(T) \quad (1d)$$

$$S_f = -3.9921 - 22.7T - 1.0015T^2 - 0.19956T^3, \quad (1e)$$

where  $\rho$  is the bulk density,  $\beta$  is the porosity,  $S$  is the bulk salinity,  $S_f$  is the brine salinity,  $\rho_f$  is the brine density,  $\rho_s$  is the ice frame density, and  $T$  is the temperature. The densities are in kilograms per cubic meter, the salinity in parts per thousand, and the temperature in degrees Celsius.

Ice supports both compressive and shear waves. Recent measurements of these speeds as a function of salinity and temperature<sup>1</sup> have been used to derive the following relations:

$$c_l = \sqrt{\left(K_{eff} + \frac{4\mu_{eff}}{3}\right)/\rho} , \quad \text{m/s} \quad (2a)$$

$$c_s = \sqrt{\mu_{eff}/\rho} , \quad \text{m/s} \quad (2b)$$

$$K_{eff} = 9.49 \times 10^6 (1 - 1.40\beta) \rho , \quad \text{N/m}^2 \quad (2c)$$

$$\mu_{eff} = 3.38 \times 10^6 (1 - 2.79\beta) \rho , \quad \text{N/m}^2 , \quad (2d)$$

where  $c_l$  is the longitudinal wave speed,  $c_s$  is the shear wave speed,  $K_{eff}$  is the bulk modulus,  $\mu_{eff}$  is the shear modulus, and  $\beta$  and  $\rho$  are determined from Eq. 1. It is important to note that the moduli  $K_{eff}$  and  $\mu_{eff}$  physically must be positive. Thus when the porosity becomes large enough that the moduli would be negative, a default value of zero should be used. Figure 1

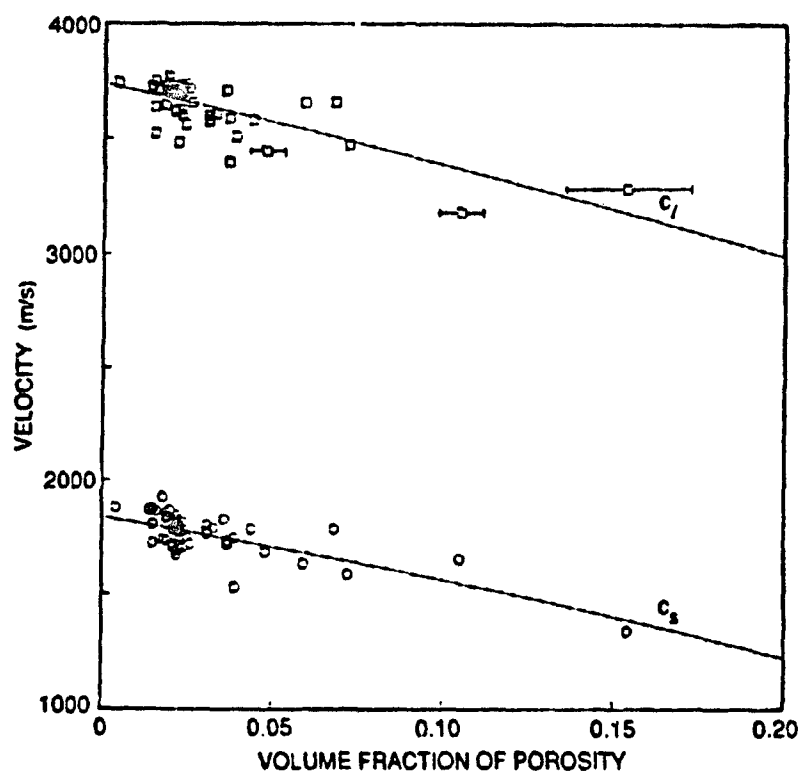


Figure 1. The longitudinal ( $c_l$ ) velocity data (shown as open squares) and shear ( $c_s$ ) velocity data (shown as open circles). Least-squares fit curves to the data are also shown. The largest errors come in determining porosities from the salinity and temperature of the samples. This uncertainty increases with porosity.

TR 9407 V-3

shows both the data from which these equations were derived and the model curves resulting from their implementation. In Ref. 1 the moduli are related to Biot parameters. In Ref. 4 they are used in a model for determining the reflection coefficient for sea ice as a function of  $S$ ,  $T$ , and frequency,  $f$ .

## 2. Average Longitudinal Sound Speed as a Function of Thickness and Air/Ice Interface Temperature

The average acoustic speeds through the ice canopy are of interest for low-frequency efforts and ice thickness measurements. By using a simple model for the salinity profile in first-year ice and assuming a linear temperature profile from the air/ice to the ice/water interface, one can determine vertical speed profiles and subsequently average speeds using the results of Eqs. 1 and 2.

The average speed of the longitudinal wave  $c_l$  in the vertical direction is of particular interest. For this reason polynomial fits were derived<sup>1</sup> for the average longitudinal wave speed as a function of thickness,  $d$ , in meters and air/ice interface temperature,  $T$ , in degrees Celsius.

$$c_l^{ave} = F_1(d) + F_2(d) T_{a/i} + F_3(d) T_{a/i}^2 + F_4(d) T_{a/i}^3 \quad \text{m/s}, \quad (3a)$$

$$F_1(d) = 2661.92 + 482.514 \times d - 191.152 \times d^2 + 28.1133 \times d^3 \quad (3b)$$

$$F_2(d) = -134.744 + 62.3017 \times d - 25.7015 \times d^2 + 3.82128 \times d^3 \quad (3c)$$

$$F_3(d) = -7.24730 + 3.34510 \times d - 1.38910 \times d^2 + 0.206891 \times d^3 \quad (3d)$$

$$F_4(d) = -0.129658 + 0.059669 \times d - 0.024812 \times d^2 + 0.003696 \times d^3. \quad (3e)$$

Figure 2 indicates the ice thickness and temperature regimes where the above fits are useful.



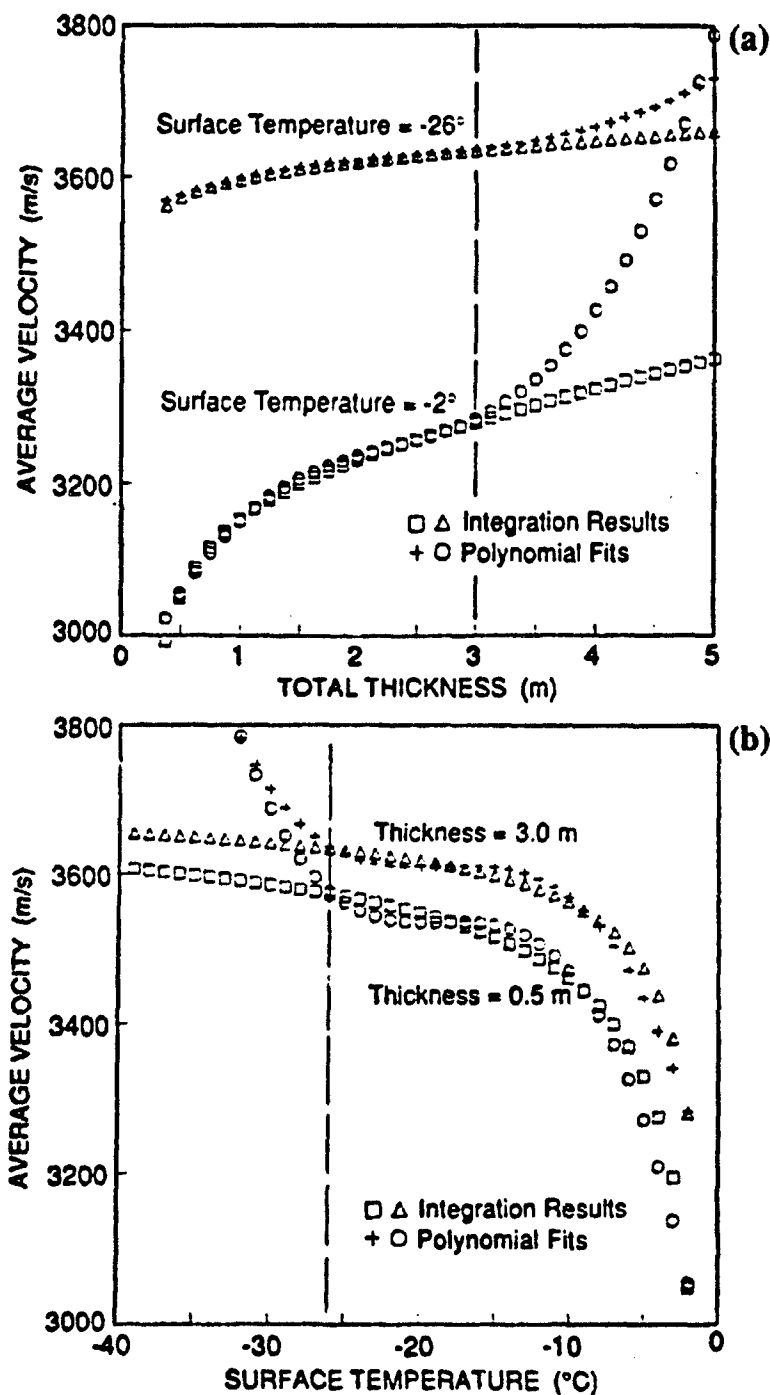


Figure 2. Part (a) shows the average longitudinal velocity as a function of thickness for two different air/ice surface temperatures. Part (b) shows the average longitudinal velocity as a function of air/ice surface temperature for two ice thicknesses. The figures show results of numerical integration of the velocity profiles and compare the polynomial fits in Eq. 3 with the integration results. They indicate the ice thickness and temperature regime where the polynomial fits are useful.

TR 9407 V-5

### 3. Attenuation as a Function of Temperature

McCammon and McDaniel suggested a form for attenuation<sup>5</sup> as a function of temperature and frequency which is based on the assumption that intergrain friction is the cause of absorption in ice. Their equation is

$$\alpha = kf(-6/T)^{2/3}, \quad (4)$$

where  $\alpha$  is absorption in decibels/meter,  $k$  is a constant,  $f$  is frequency in kilohertz, and  $T$  is temperature in degrees Celsius. Recent experiments<sup>6,7</sup> were aimed at determining whether Eq. 4 captures the correct dependences. The results indicate that, away from the 3–5 cm thick skeletal layer at the bottom of the ice, Eq. 4 can be used with  $0.18 \leq k \leq 0.3$ . Within the skeletal layer, Eq. 4 can be used as an approximation with  $k = 1.0$ .

## B. SCATTERING AND FORWARD ENERGY LOSS FROM UNRIDGED ICE

### 1. Forward Scattering

The rms roughness of unridged ice is typically much larger than an acoustic wavelength for frequencies greater than 10 kHz. Therefore, the interaction of high-frequency acoustic energy with unridged ice is most properly considered a scattering process. However, there are cases in forward scattering where only an estimate of the energy lost into the ice is needed, and the process can be treated by assigning an effective reflection coefficient. For this reason, this subsection starts with a discussion of energy losses given in terms of reflection coefficients. Subsequently, expressions are given in terms of scattering.

#### a. Energy loss

Unridged ice reflects sound so well that a surface-reflected signal will often overlap the direct-path signal and cause interference. Experimental results<sup>8</sup> are shown in Figure 3 for the reflection coefficient at 25 kHz as a function of angle for unridged ice. Results at 45 kHz

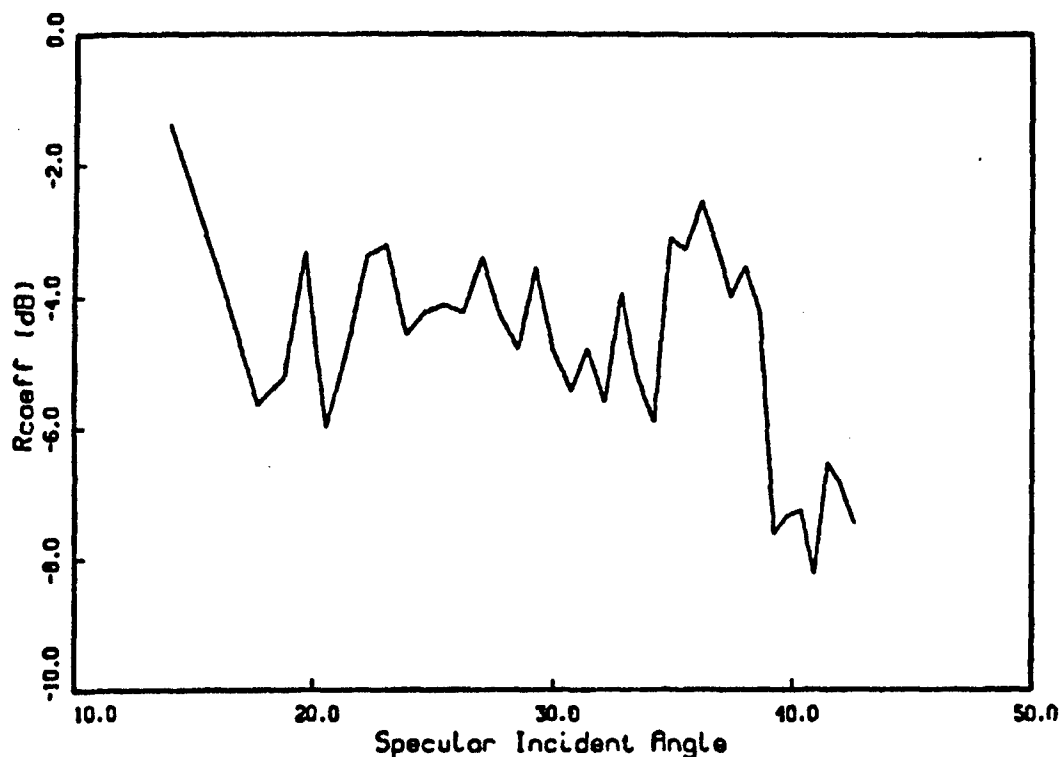


Figure 3. Average of reflection coefficient,  $R_{\text{coeff}}$ , vs grazing angle for data from Run: 31, 33, and 37 of Ref. 8.

for the same experimental geometries gave similar values; i.e., no obvious frequency dependence was observed. For grazing angles up to  $35^\circ$ , Figure 3 suggests using an average reflection coefficient loss in the range of 4–5 dB. Figure 3 and the modeling of Ref. 4 indicate that for higher grazing angles a larger loss is to be expected: the losses seen near normal incidence are given in Section V.B.2.a below.

The reflection loss quoted in the last paragraph is for growing spring ice. A monitoring of reflections<sup>9</sup> near the coast in the Beaufort Sea showed that the arrival of warm water from the Alaskan Coastal Current changed the character of the surface by melting out brine channels and making it more porous, with a resulting increase of about 10 dB in the reflection loss.

TR 9407 V-7

### b. Scattering coefficient

Similar to the facet scattering contribution to scattering from the ocean surface, the high-frequency approximation<sup>10</sup> can be used to arrive at the forward scattering cross section

$$\sigma(\gamma) = |R|^2 \frac{\sec^4 \gamma}{4\pi s^2} \times \exp \left( -\frac{\tan^2 \gamma}{s^2} \right), \quad (5)$$

where

$$\tan \gamma = \frac{\sqrt{\cos^2 \theta_i - 2 \cos \theta_i \cos \theta_s \cos \phi + \cos^2 \theta_s}}{\sin \theta_i + \sin \theta_s};$$

the angles  $\theta_s, \theta_i, \phi$  are measured relative to the mean surface as shown in Figure 4. The angle  $\gamma$  is the facet reflection angle.<sup>11</sup>  $|R|^2$  accounts for the energy loss into the ice, and  $s$  is the two-dimensional rms slope of the rough water/ice interface.

The results in Section V.B.1.a can be used to get an empirical estimate of the energy loss factor  $|R|^2$  (quoted there in decibels, but needed here in nondecibel form). Alternatively, a more theoretically based method of calculating the energy losses is given in Ref. 4

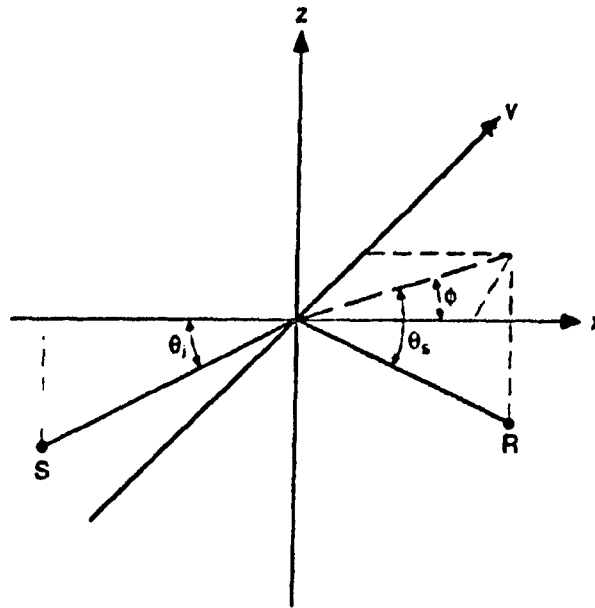


Figure 4. Measurement geometry.

where porous media theory and the results of Section IV.A are used to determine reflection coefficients.

An estimate of the rms slope,  $s$ , was determined in Ref. 12 based on the experimental results in Ref. 13. This estimate was based on a scattering strength expression equivalent to Eq. 5 and examination of the pulse elongation seen in 1-5 ms duration pulses forward scattered off the ice surface. The results indicate a slope range of

$$\tan(4.2^\circ) \leq s \leq \tan(6.4^\circ). \quad (6)$$

Equation 5 should not be used for grazing angles less than about twice  $6.4^\circ$ . For shallower grazing angles, the effects of shadowing are important. Reference 12 discusses one method of approximately incorporating shadowing effects.

#### c. Time-dependent intensity after forward scattering

The expressions for the time-dependent intensity, or "pulse elongation," given in Eq. 42 of Section II can be used for the Arctic if Eq. 6 is used for rms slope and the result is multiplied by the  $iRI^2$  of the last subsection, i.e.,

$$I_s(\tau) = \frac{|R|^2 I_o A_o}{(r_1 + r_2)^2} \begin{cases} 0 & \tau \leq 0 \\ \Phi(\sqrt{\tau/T}) & 0 \leq \tau \leq \tau_o \\ \Phi(\sqrt{\tau/T}) - \Phi(\sqrt{(\tau - \tau_o)/T}) & \tau \geq \tau_o \end{cases} \quad (7)$$

where the symbols are defined in association with Eq. 42 of Section II.

## 2. Near Normal Incidence

The discussion of ice keel reflections in Section V.D indicates that the larger reflections probably come from ice block faces that are nearly normal to the acoustic beam. The high angle reflection from the face of a block of arctic ice is therefore very important, and has motivated the APL measurements of normal-incidence reflections from expanses of unridged ice and from ice blocks cut from such a surface.

### a. Unridged ice amplitude "reflection" coefficient

The normal-incidence reflection and scattering from the under-ice surface are measured by placing a transducer beneath the ice and projecting sound upward. The return is used to determine an "effective" reflection coefficient that inherently includes contribution from both coherent reflection and incoherent scatter. The amplitude reflection coefficients measured in this way have been plotted in Figure 5. Some measurements by Stanton et al.<sup>14</sup> for a very thin (10 cm) ice sheet on an outdoor pond of salt water are added for comparison. A least squares fit to all the results (dashed line in Figure 5) is our recommendation for a simple "effective" reflection coefficient,  $R_a$ , at normal incidence:

$$R_a = 0.46 - 0.19 \log(f), \quad (8)$$

where  $f$  is the frequency in kilohertz. The relationship is limited to frequencies of 2–200 kHz and assumes beams at least a few degrees wide. Below 7 kHz, there are no data; the line provides a convenient transition to the maximum  $R_a$  of 0.4, which corresponds to that expected from the mismatch between water and ice. Above 200 kHz, we recommend using an  $R_a$  of 0.04, which is representative of limited experimental results obtained to date.

Equation 8 is a purely empirical expression. A semiempirical-based result for the effective reflection coefficient is shown as a solid curve in Figure 5. This result is based on a measured longitudinal sound speed profile<sup>6</sup> in the ice in conjunction with a theoretical expression<sup>15</sup> for the reflection coefficient as a function of frequency for a medium with a continually varying sound speed. This semiempirical reflection coefficient is given by

$$R_a = 2.34783 + \frac{3.9839}{[\log(f)]^2} - \frac{5.17682}{\log(f)} - 0.34449 \times \log(f). \quad (8a)$$

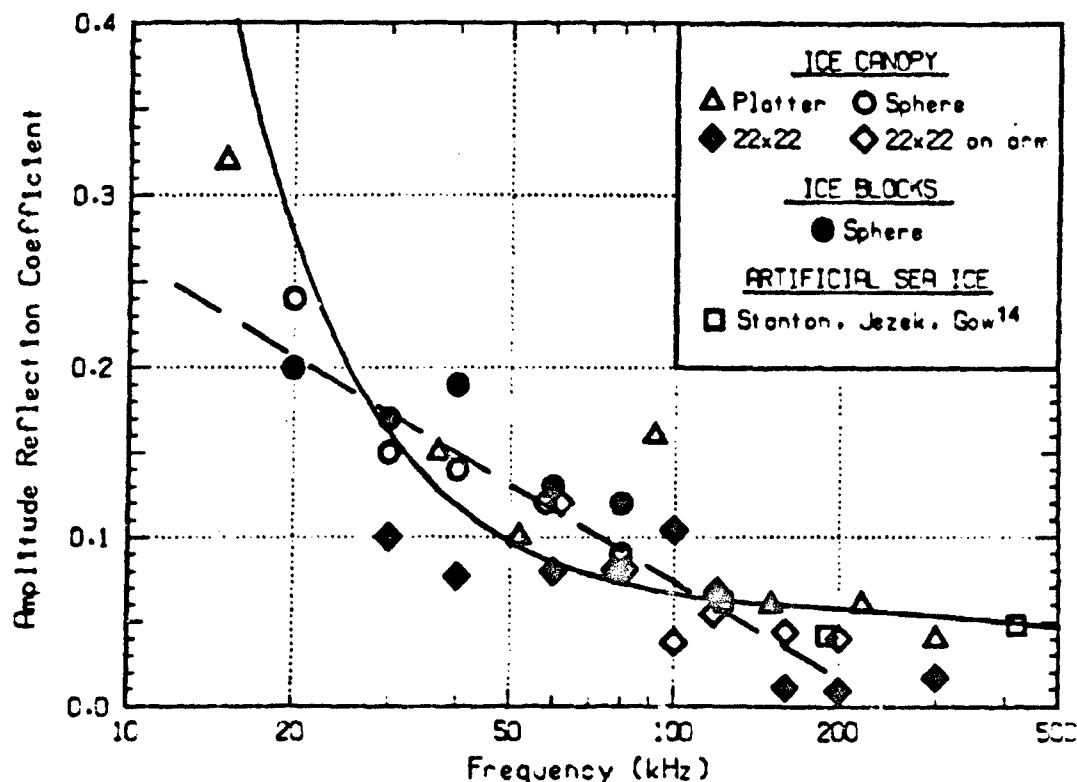


Figure 5. Measured reflection coefficients for the underside of the ice canopy. Data from an APL-UW ice block experiment and from Stanton et al.<sup>14</sup> are included for comparison. The dashed line is a least squares fit to all data below 200 kHz ( $R_a = 0.46 - 0.19 \log f$ ). The solid line is the theoretical result calculated using a typical sound speed profile within the ice (see text near Eq. 8a). All measurements were taken at 28-m range except for the 22 x 22 transducer on the arm, which was at 2 m.

Ice keels are made up of ice blocks, and large reflections come from block faces nearly normal to the acoustic beam. The reflection coefficients measured above can be used to predict the target strengths of these faces. One caveat is that some faces may not have a skeletal layer, in which case the reflection might be higher. Furthermore, sometimes these reflectors are so near the same range that interference occurs (see Section V.D).

#### b. Scattering from an ice block

In spring 1988, we measured normal-incidence reflections at 20–80 kHz from the end of a cylindrical ice block. In this experiment, blocks with diameters of 27, 38, 58, and 84 cm

TR 9407 V-11

were individually depressed below the surface so that when acoustic pulses were transmitted from beneath the fine the block's reflections were separable in time from the reflections off the underside of the ice canopy. A source/receiver placed 30 m below the block was moved horizontally to measure the angular response pattern. Precise calibration was obtained by replacing the block with an inverted pan of the same diameter, filled with air.

In the left-hand panel of Figure 6, returns from the air/water interface of the pan at three of the five frequencies are compared with the theory for a flat, rigid, circular plate (also good for a pressure relief surface). In this theory, the target strength,  $TS$ , for wavelength  $\lambda$  and incident angle  $\theta$  is given by<sup>16</sup>

$$TS = 10 \log \left[ |R_a| \left( \frac{\pi a^2}{\lambda} \right) \left( \frac{2J_1(\beta)}{\beta} \right) \cos \theta \right]^2 \quad (9)$$

where  $a$  is the radius of the plate,  $\beta = 2ka \sin \theta$ ,  $k$  is the wavenumber, and  $J_1$  is a Bessel function. The amplitude reflection coefficient,  $R_a$ , has been added to represent the reflection loss at the surface, which may be due to impedance change, roughness, or some other cause.

In the right-hand panel of Figure 6, the ice reflection measurements are plotted for comparison with theory. The returns are considerably lower than on the left, but still indicate the side lobes observed for the air surface. At the low frequencies the angular response pattern follows the flat plate theory, but at the higher frequencies roughness plays an important role, as indicated by the filling in of the nulls. After the block was removed, the bottom surface was measured and found to have a surface level standard deviation less than 0.3 cm.

### 3. Low Angle Backscatter

In areas of the Arctic where the ice has frozen with very little disturbance from wind or current, such as in narrow leads, the resulting surface is sufficiently flat and uniform that acoustic backscattering can be treated similarly to the backscattering from an open sea surface.

This backscattering, or surface reverberation, was measured at 20 and 60 kHz under refrozen leads at several ice camps in 1973-1975.<sup>17-19</sup> In 1982, measurements were made



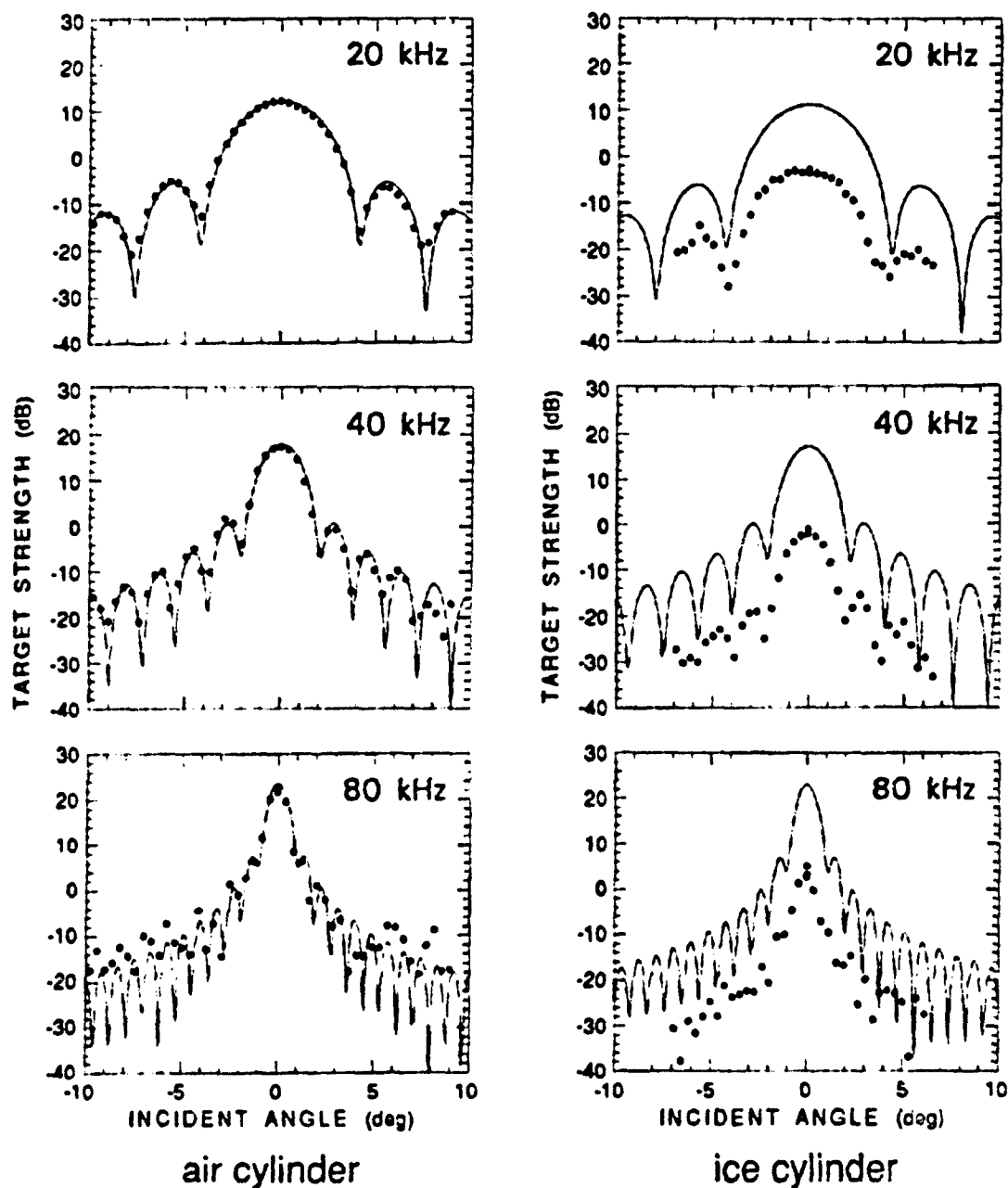


Figure 6. Measurements of the target strength of the end face of a 60 cm diameter cylinder of air and of a 58 cm diameter cylinder of ice. As the transducer was moved horizontally beneath the cylinder, the incident angle varied from  $10^\circ$  in one direction to  $10^\circ$  in the opposite direction.

TR 9407 V-13

at 100–300 kHz both in a laboratory tank<sup>20</sup> and in the field.<sup>21</sup> The backscattering strength was found to increase with frequency and with grazing angle. The measured results are shown in Figure 7. Three equations were derived for the modeling of backscattering at selected frequencies:

$$S_s = -35 + 19 \log \sin \theta \quad 20 \text{ kHz} \quad (10a)$$

$$S_s = -31 + 24 \log \sin \theta \quad 60 \text{ kHz} \quad (10b)$$

$$S_s = -72 + 25 \log f + 15 \log \sin \theta \quad 100\text{--}300 \text{ kHz}, \quad (10c)$$

where  $S_s$  is the backscattering strength in decibels,  $f$  is the frequency in kilohertz,  $\theta$  is the grazing angle (valid for  $6^\circ$ – $45^\circ$  only), and the logarithms are to base 10.

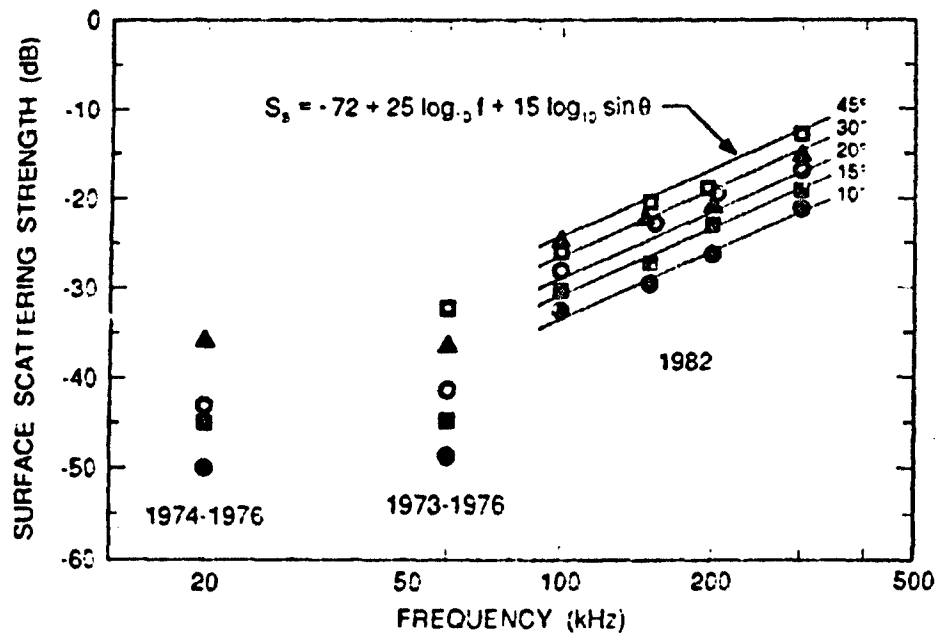


Figure 7. Surface reverberation measurements for flat sea ice, 1973–1976 and 1982. The 1982 data are a combination of laboratory tank measurements and arctic field measurements.

## C. ICE KEELS

### 1. Formation of Ridges

Arctic ice is subjected to various environmental forces and is continually undergoing some sort of transformation. In the summer, ablation on top and melting below reduce the quantity of ice. In the winter, freezing increases the thickness and coverage of ice. Variable winds and currents cause the ice floes to be forced together or spread apart. If floes of thin ice are forced together, one may overlap the other and rafting occurs. If two pieces of ice slide past each other while in contact, a shear ridge is produced. If the compressed ice floes are thick, pressure ridges are created, either at the point of contact or following cracking of the floe. These pressure ridges are generally larger, more spectacular, and, from our observations at many ice camps, more common than shear ridges. It should be noted, however, that the ridging process often involves both shear and pressure components. The ice in a shear ridge tends to be in small chunks with a ground up appearance, whereas that in a pressure ridge is composed of discrete blocks of many sizes.

For the ice blocks in a ridge, the relation between the long axis,  $L$ , and the thickness,  $t$ , has been found to be reasonably well represented by<sup>22</sup>

$$L = 2.04 t + 0.72 \quad (11)$$

where  $L$  and  $t$  are in meters.

### 2. Ridge Structure

The portion of the ridge above sea level is the sail, and the part below is the keel. Using a kinematic ridging model based on flexural failure as the ridging mechanism, Parmerter and Coon<sup>23</sup> found the sail height to be limited by the thickness of the constituent blocks. This was corroborated by the measurements of Tucker et al.<sup>22</sup> Empirically, the sail height has been found to depend on the square root of the average block thickness in a ridge.<sup>24</sup>

The ratio of keel draft to sail height of ridges has been shown to vary widely from 3 to 9. Kovacs<sup>25</sup> reported a ratio of 4 or 5 from measurements and sonar profiling of five ridge

structures in the Bering and Chukchi seas. Kovacs et al.<sup>26</sup> found a ratio of 3.3 for a multi-year ridge using coring and sonar profiling methods. Kozo and Diachok<sup>27</sup> gave a ratio of 5 for ridges in the Greenland Sea by comparing the distribution of sails obtained from airborne laser profiles with the distribution of keels obtained from submarine under-ice profiles. Francois<sup>28</sup> determined ratios of 4.4 to 9.3 for both first-year and multiyear ridges near Ice Island T-3 by comparing data obtained from topside surveying with data obtained from under-ice profiling with an unmanned submersible. Garrison et al.<sup>29</sup> showed a ratio of 7.5 using supposedly one-to-one correspondence between topside laser profiles and under-ice sonar profiles obtained in the Beaufort Sea. A theoretical value of about 8 was obtained by Parmerter and Coombs using model<sup>23</sup> based on calculations of limits on sail height and keel draft as a function of ice thickness.

Considering these results, we recommend using a draft-to-sail ratio of 6 for acoustic modeling, unless one of the above measurements seems more appropriate for the intended locale.

### 3. Keel Statistics

Ice keels are important not only because they are a hindrance to underwater navigation but because of their effect on acoustic propagation and backscattering. Statistical information on the properties of the keels is needed for analysis of both backscattering and forward scattering.

To compute a distribution function for ice keel drafts, a keel must first be defined. This is achieved using the analogous Rayleigh criterion in optics to define a keel as a downward protrusion of ice with a trough on one side of the maximum draft that is at least halfway toward the local level ice surface, which is arbitrarily defined as a draft of 2.5 m. Expressed mathematically, a feature with maximum draft,  $d$ , is a keel if the trough on one of the sides is less than  $(d + 2.5) / 2$  deep. This is an arbitrary definition of a keel, and for some keels with complex shape or odd size, it is not very satisfactory. It is used here, nevertheless, because of the lack of a better one, and because it has been used by several other investigators.<sup>30,31</sup> Having used the same definition of a keel, we can compare our probability density functions with theirs.

Straight-segment under-ice profiles have been obtained with a narrow-beam sonar by submarines during the SUBICEXs in which APL participated. The probability density function for ice keel drafts is shown in Figure 8. The figure shows best fits to the exponential  $N(h) = B \exp(-bh)$  for keels with a draft,  $h$ , between 5 and 19 m (where  $N(h)$  is the number of keels per kilometer with draft  $h$ ). For the fall, use  $B = 4.0$  keels per kilometer and  $b = 0.47$  per meter; for the spring, use  $B = 5.6$  and  $b = 0.38$ . These indicate fewer keels in the fall than in the spring, which is reasonable since in the fall freezing is just beginning and less ice is available for ridging. The spring distributions show fairly large differences between the years, probably a function of the local conditions during freezing. Overall, our data from the Beaufort Sea show fewer keels than data obtained in the central Arctic by other investigators.

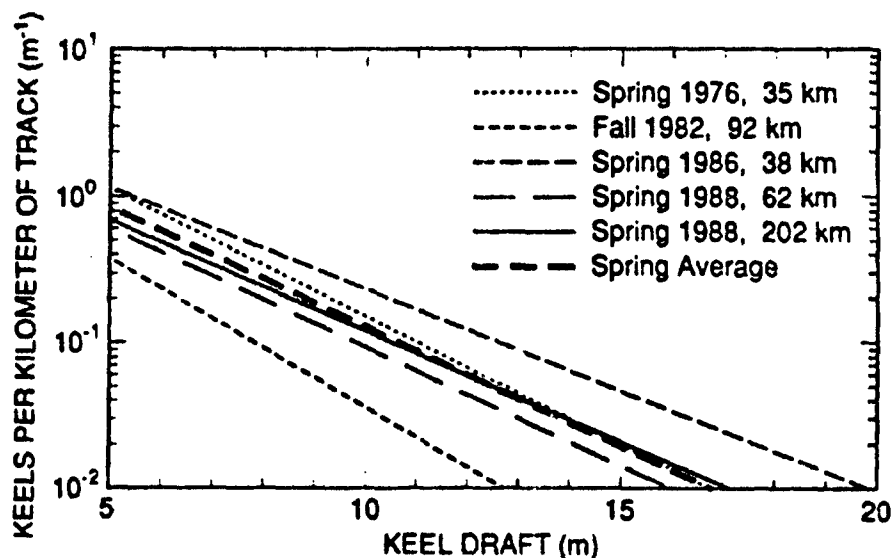


Figure 8. The distribution of maximum drafts of ice keels observed in the under-ice profiles obtained along given tracks of a submarine.

## D. ICE KEEL REFLECTIONS

In the Arctic, the returns from ice keels<sup>21,32-34</sup> dominate all other forms of acoustic backscatter. When short pulse lengths are used, the returns appear to be from discrete reflectors, which, at times, interfere. Some returns are certainly a combination of two reflectors, perhaps three or four at times, that appear at the same range. In this section, we summarize what we have learned about ice keels from an examination of some typical reflections. Some modeling is also included.

### 1. Point-Like Nature

When a weapon-frequency transducer is rotated to make a 360° scan of the ice, using a pulsed cw transmission, the return from individual point-like reflectors will rise and fall, replicating the beam pattern. Also, when a split-beam transducer is used, the left-right phase difference varies uniformly to show the changing direction as the transducer rotates.

If there are two reflectors spaced a few degrees apart in azimuth, the return will begin to rise as the first is approached; then, as the two echoes combine, the amplitude will depend on the relative phase of the two echoes. This relative phase depends on the range difference and could be any value by chance. Figure 9 shows the returns for pairs of reflections at the same range that overlap in azimuth. In the overlap region, the amplitude depends on the relative phase of the returns from the two reflectors. In (a) it follows the patterns well, but in (b) the two overlapping returns add constructively.

For the many reflectors that we have examined in this manner, about half have a good match to the transducer pattern and have well-behaved phase angles, while the other half show definite signs of interference. This ratio will hold true when implementing an ice keel reflection model with the reflector density recommended in the next paragraph.

### 2. Reflector Density

A detailed examination of ice scans at an ice camp in the fall of 1984<sup>35</sup> showed that there were 5.3 keels per square kilometer and that on the average each keel had 30 reflectors

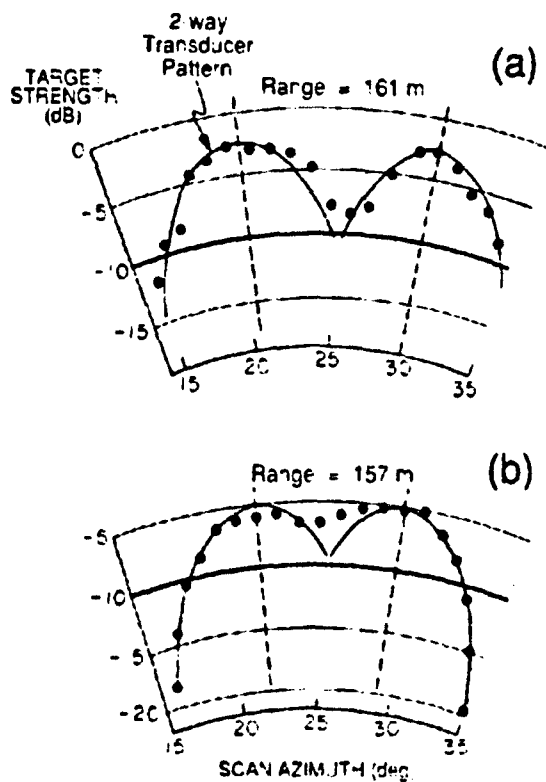


Figure 9. Scans past interfering ice keel reflectors. The measured target strength deviates from the transducer pattern when the reflections overlap.

and occupied an area with dimensions of 176 x 43 m. The actual shape of the keel may be less elongated because only one side of the keel is observed acoustically. Also, the keels often meander in plan view.

The average density given above corresponds to an average reflector spacing within the keel of 16 m, assuming that each reflector was an individual one. However, the overlapping of echoes from reflectors indicates that they are more closely spaced. A study of the interference between reflectors at different frequencies indicates a spacing of 3-4 m (see Section V.D.4 below). The density of reflectors is no doubt highly variable in nature. For modeling, we recommend using an average spacing of 6 m.

TR 9407 V-19

### 3. Response Pattern

An experiment in 1986 was designed to measure returns from a keel that formed after the ice camp was occupied. We measured bistatic reflections at 20 kHz using a receiving transducer at a range of 110 m and a portable omnidirectional transmitting transducer positioned 15 m from the keel. As the transmitter was lowered, some large echoes for successive pings showed a vertical response pattern with a  $3^\circ$  width (to  $-3$  dB reductions in target strength for an equivalent monostatic arrangement). This agrees well with the ice block response pattern at 20 kHz shown in Figure 6, possibly indicating that the keel reflectors had dimensions similar to the 58 cm diameter ice block. A similar experiment reported by McDaniel<sup>36</sup> showed somewhat narrower vertical response patterns. We have no horizontal response measurements, but since ice keel blocks tend to be larger horizontally than vertically, we assume that the horizontal pattern should be somewhat narrower.

### 4. Frequency Dependence

An example of some returns from ridged ice at ranges of 560–1050 m is shown in Figure 10.<sup>33</sup> The ordinate is target strength, so the general dropoff in amplitude from one graph to another indicates a decrease in keel reflectivity with increasing frequency. Some measurements for two selected keels (designated Keel A and Keel C) show the average amplitude (converted to target strength) decreasing at about  $0.5 \pm 0.1$  dB/kHz (Figure 11).

An experiment was performed in 1986 in which the frequency of successive pings was shifted by 2 kHz.<sup>33</sup> A close look at the returns in Figure 12 shows that the details in the return vary greatly with small changes in frequency. There is no continuous trend, but rather a variation that is thought to be due to the interference between overlapping returns from reflectors at nearly the same range.

A measure of this variation with frequency is shown by the cross correlation of amplitudes for two returns 2 kHz apart in frequency (see Figure 13).<sup>33</sup> The two 20 kHz pings were from successive sets; thus they span the others in time. Their high correlation shows that time changes were not an influence. A 2 kHz shift causes the correlation to drop below 0.80. A computer simulation<sup>33</sup> was run of the correlation of randomly spaced reflectors for



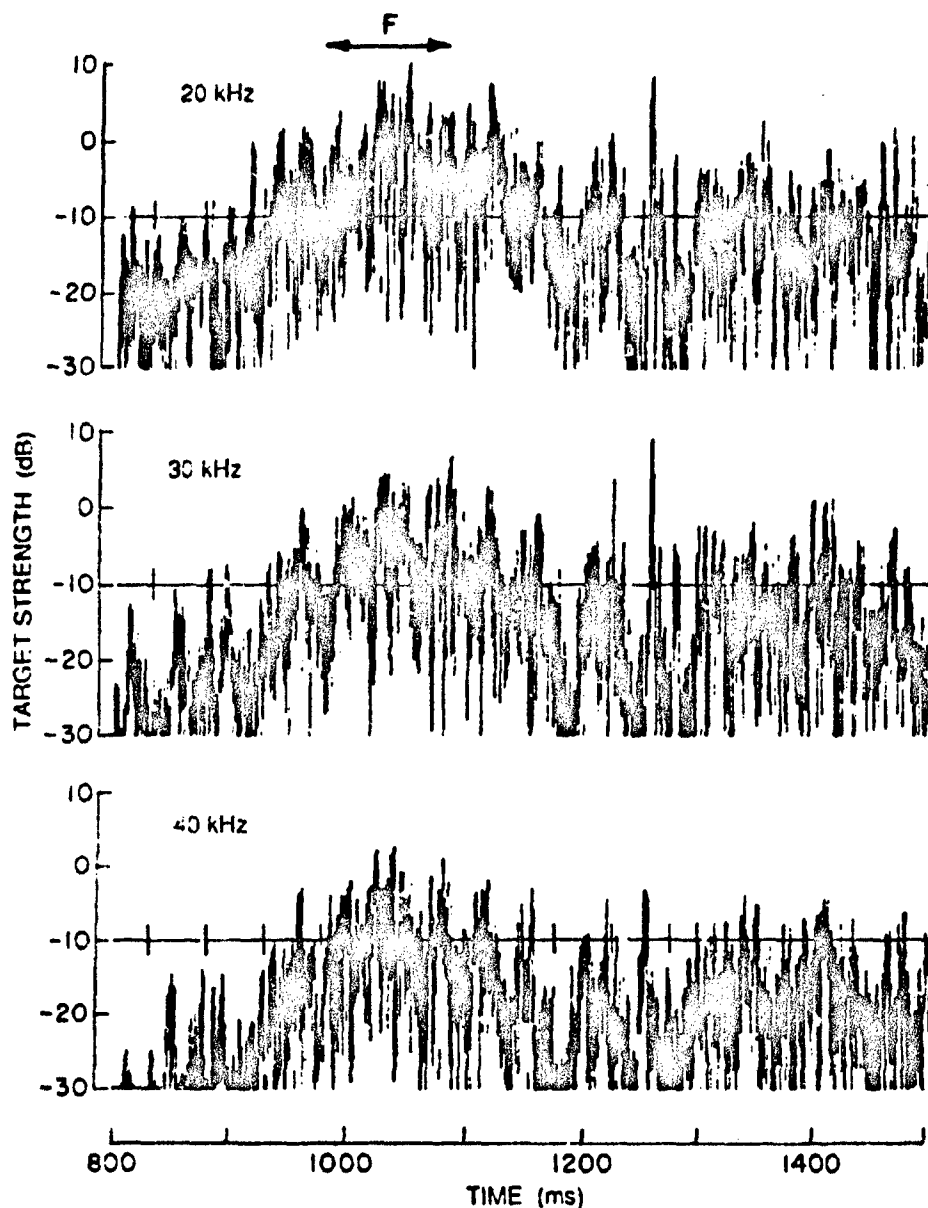


Figure 10. An example of the returns from the same ridged ice at three frequencies. Interval *F* is selected for expansion and treatment later. A general decrease in target strength with frequency is observed.

TR 9407 V-21

ADB199453

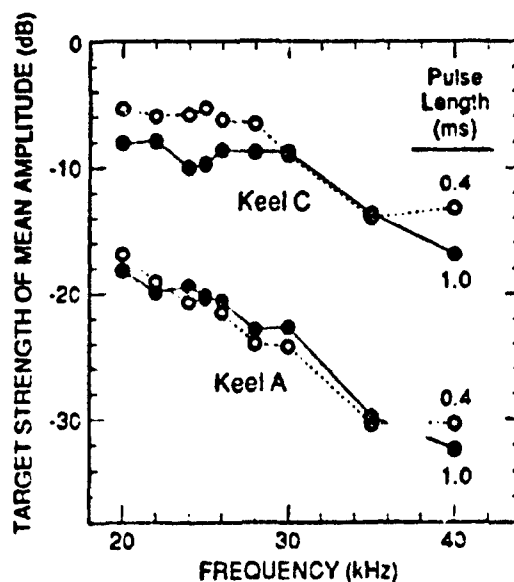


Figure 11. A decrease in target strength with increasing frequency is observed for two keels at range 500 m at the 1986 ice camp. Each target strength is calculated for the average amplitude of all reflectors in the keel.

a 0.4 ms pulse. According to the simulation, the measured correlations for Keel A would indicate more than 73 reflectors in a 12 ms interval (see Figure 14). Considering a transducer beam  $12^\circ$  wide (two-way) and a range of 440 m, this would correspond to a uniform reflector spacing of less than 3.3 m. For such a large number of reflectors, however, the cross correlation is only weakly dependent on the number of reflectors, and thus cross correlation does not give an accurate determination of their number.

### 5. Modeling of Ice Keels

A model of an ice keel was developed by Ellison<sup>37</sup> in which he built up a keel by stacking ice blocks of random size and orientation. He then summed the reflections from all block faces, using target strength response curves for a rigid surface.<sup>16</sup> With the adjustment of several parameters, his model gave a target strength distribution that was similar to our measured target strength distribution. This approach is a difficult one. Most ridges do not

V-22 TR 9407

ob 435

Fiche 2

06/24/95

08DB9AM453

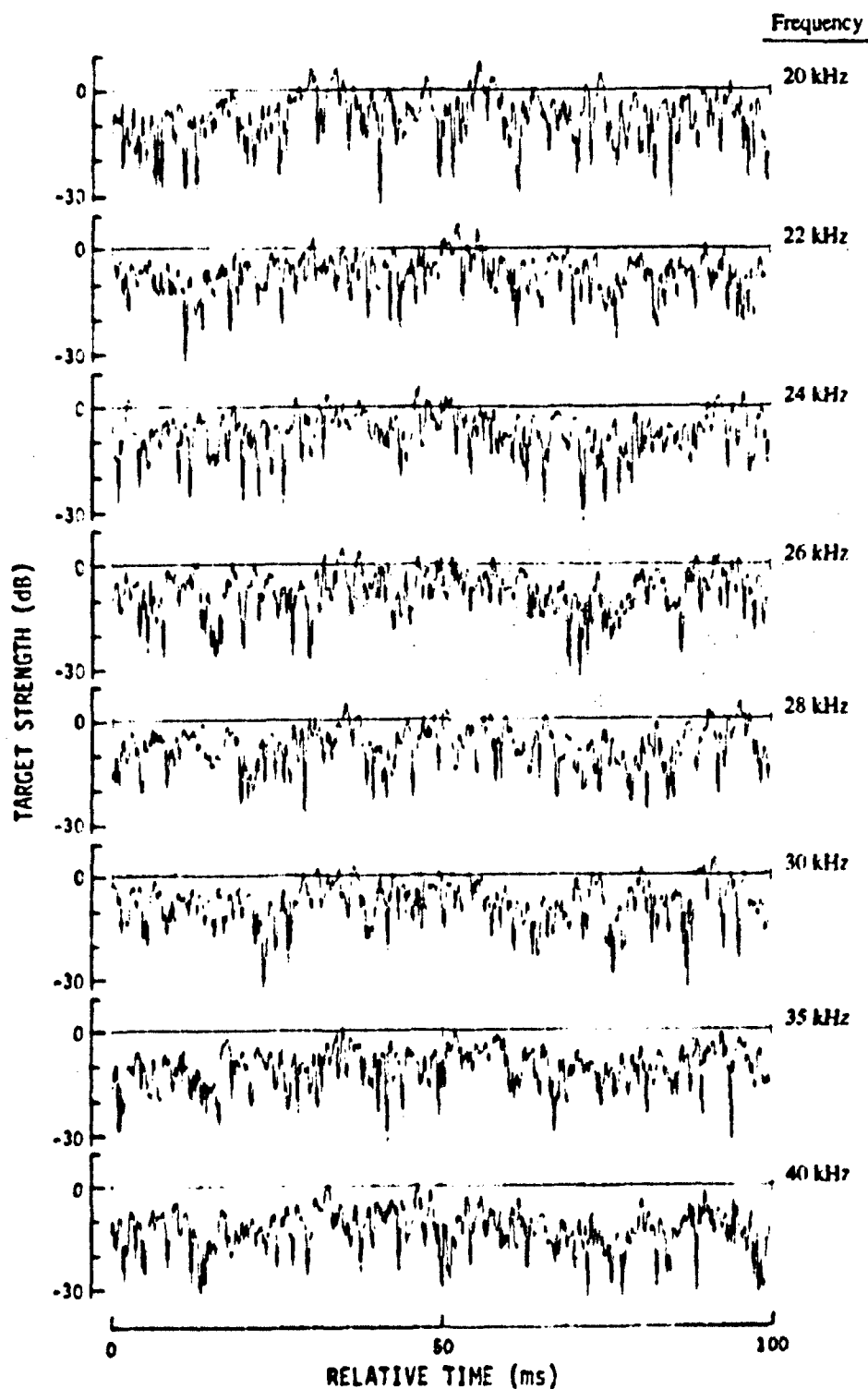


Figure 12. A comparison of returns at several frequencies for interval F in Figure 10. Pulse length is 1 ms. Individual peaks in the return are almost unrecognizable when the frequency changes by 2 kHz.

TR 9407 V- 23

ADB199453

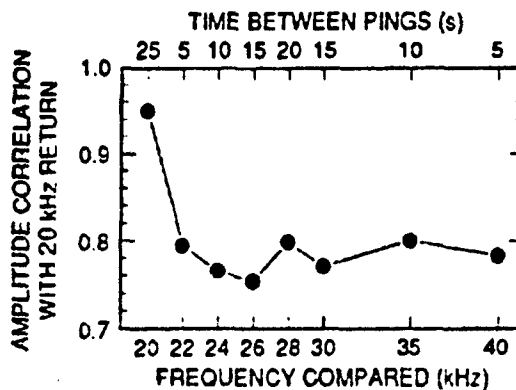


Figure 13. Amplitude correlation between the 100 ms samples of the closely spaced pings shown in Figure 12. Each is compared with the 20 kHz return. The time between returns varied from 5 to 25 s, as shown at the top of the graph. The correlation drops sharply for a change of 2 kHz in frequency.

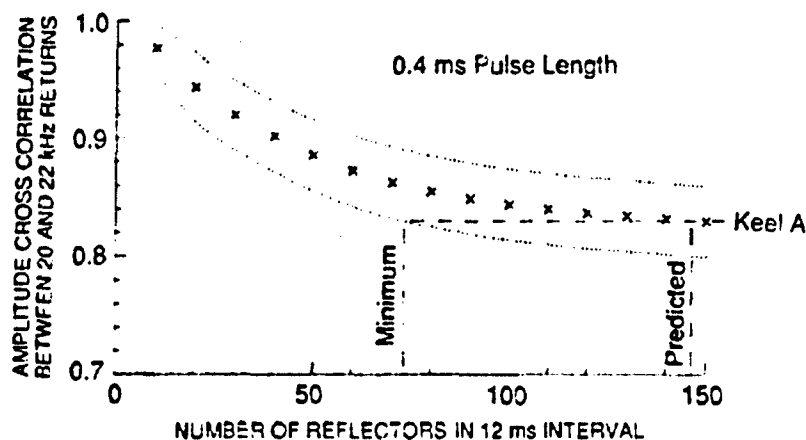


Figure 14. The modeled decrease in cross-frequency correlation as the number of reflectors increases. The results are an average for 50 random selections of reflector amplitude and range. The dotted lines indicate the standard deviation. Correlation measurements for returns from Keel A are shown by a dashed line. The intersection of the dashed line with the x-line gives a prediction of the number of reflectors in Keel A.

look like a pile of rectangular blocks, and the same could be said for the keels below. For confidence in the model, we need more checks along the way—e.g., a comparison between modeled and measured reflections for an actual keel of known overall dimensions.

The desired model is one that converts an observable feature of an ice field to keel target strengths. Satellite images, aerial photography, and laser profiling give information on ridge sails only, and the correspondence between sails and keels in older ice is not sufficiently known. The most likely usable observable feature, when an area of operation has been specified, is an under-ice profile obtained with a submarine.

Bishop et al.<sup>38</sup> took an under-ice profile obtained with a submarine and modeled ice keels to suit, using Ellison's ice keel model. They then predicted the acoustic return along the submarine's track and compared the average reverberation levels with the reverberation levels measured with a forward-looking acoustic transducer mounted on the submarine. Although the agreement for specific areas along the track was poor, the averages for a 1 km track agreed within a few decibels. The greatest source of error was the incompatibility between the narrow-beam profiler and the wide beam of the transducer used to measure the ice reflections; i.e., reflections were being included that came from keels too far off the profile track to be detected.

A less basic model than Ellison's, but one with more accuracy and immediate usefulness, would be an "acoustic" model. Such a model would use an empirically determined relationship between target strength distribution and the characteristics of the keels observed in the under-ice profile. The data needed to determine this relationship are not available.

TR 9407 V-25

## REFERENCES—Section V

1. K. L. Williams and R. E. Francois, "Sea ice elastic moduli: Determination of Biot parameters using in-field velocity measurements," *J. Acoust. Soc. Am.*, **91**, 2627–2636 (1992).
2. M. A. Biot, "Theory of propagation of elastic waves in a fluid-saturated porous solid. II. Higher frequency range," *J. Acoust. Soc. Am.*, **28**, 179–191 (1956).
3. G. F. N. Cox and W. F. Weeks, Equations for Determining the Gas and Brine Volumes in Sea Ice Samples, CRREL Report 82-30, Cold Regions Research and Engineering Laboratory, Hanover, NH, 1982.
4. G. S. Sammelmann, "Biot-Stoll model of the high-frequency reflection coefficient of sea ice," *J. Acoust. Soc. Am.*, **94**, 371–385 (1993).
5. D. A. McCammon and S. T. McDaniel, "The influence of the physical properties of ice on reflectivity," *J. Acoust. Soc. Am.*, **77**, 499–507 (1985).
6. K. L. Williams, G. R. Garrison, and P. D. Mourad, "Experimental examination of growing and newly submerged sea ice including acoustic probing of the skeletal layer," *J. Acoust. Soc. Am.*, **92**, 2075–2092 (1992).
7. G. R. Garrison, R. E. Francois, and T. Wen, "Acoustic reflections from arctic ice at 15–300 kHz," *J. Acoust. Soc. Am.*, **90**, 973–984 (1991).
8. K. L. Williams, R. E. Francois, R. Stein, and J. C. Luhy, Acoustic Forward Scattering Beneath the Arctic Canopy at 25 and 45 kHz: Experimental Procedure and Results, APL-UW TR 9118, September 1991.
9. R. E. Francois, G. R. Garrison, E. W. Early, T. Wen, and J. T. Shaw, Acoustic Measurements Under Shore-Fast Ice in Summer 1977 (U), APL-UW 7825, March 1981. (Confidential)
10. Tolystoy and C. S. Clay, *Ocean Acoustics* (American Institute of Physics, New York, 1987).
11. D. E. Barrick, "Rough surface scattering based on the specular point theory," *IEEE J. Trans. Antennas Propag.*, **AP-16**, 449–454 (1968).
12. G. S. Sammelmann, "High-frequency forward scattering in the Arctic," *J. Acoust. Soc. Am.*, **94**, 302–308 (1993).

13. K. L. Williams and D. E. Funk. "Acoustic Forward Scattering Beneath the Arctic Canopy at 25 and 45 kHz: Experiment and Specular Point Theory," APL-UW 9110, September 1991.
14. T. K. Stanton, K. C. Jezek, and A. J. Gow, "Acoustical reflection and scattering from the underside of laboratory grown sea ice: Measurements and predictions," *J. Acoust. Soc. Am.*, 80, 1486-1494 (1986).
15. D. Winebrenner. "Acoustical backscattering from sea ice at high frequencies," APL-UW TR 9017, January 1991.
16. R.J. Urick. *Principles of Underwater Sound* (McGraw-Hill, New York, 1983).
17. G.R. Garrison, E. A. Pence, and E.W. Early, Acoustic Studies from an Ice Floe Near Barrow, Alaska, in April 1974, APL-UW 7514, February 1976.
18. G.R. Garrison, R.E. Francois, and E.W. Early, Acoustic Studies from an Ice Floe in the Chukchi Sea in April 1975, APL-UW 7608, August 1976.
19. G.R. Garrison, E.A. Pence, E.W. Early, and H.R. Feldman. Studies in the Marginal Ice Zone of the Bering Sea: Analysis of 1973 Bering Sea Data (U), APL-UW 7410, September 1974. (Confidential)
20. R.E. Francois and T. Wen, Use of Acoustics in Localizing Under-Ice Oil Spills, APL-UW 8309, June 1983.
21. G.R. Garrison, R.E. Francois, and T. Wen, Acoustic Returns from Ice Keels, 1982 (U), APL-UW 8311, May 1984. (Confidential)
22. W.B. Tucker III, S.S. Devinder, and J.W. Govoni, "Structure of first-year pressure ridge sails in the Prudhoe Bay region," in *The Alaskan Beaufort Sea. Ecosystems and Environments* (Academic Press, Orlando, FL, 1984), pp. 115-135.
23. R.R. Parmerter and M.D. Coon, "Model of pressure ridge formation in sea ice," *J. Geophys. Res.*, 77, 6565-6575 (1972).
24. W.B. Tucker III and J.W. Govoni, "Morphological investigations of first-year sea ice pressure ridge sails," *Cold Regions Science and Technology*, 5, 1-12 (1981).
25. A. Kovacs, "On pressured sea ice," in *Proceedings of an International Conference in Reykjavik, Iceland, 1971* (National Research Council, Reykjavik, 1971).

TR 9407 V-27

26. A. Kovacs, W.F. Weeks, S. Ackley, and W.D. Hibler III, A study of a multiyear pressure ridge in the Beaufort Sea. AIDJEX Bull. 12, University of Washington, Seattle, 1972.
27. T.L. Kozo and O.I. Diachok, Spatial variability of topside and bottomside ice roughness and its relevance to underside acoustic reflection loss. AIDJEX Bull. 19, University of Washington, Seattle, 1973.
28. R.E. Francois, High Resolution Observations of Under-Ice Morphology. APL-UW 7712, March 1977.
29. G.R. Garrison, R.E. Francois, E.W. Early, and T. Wen, Comprehensive Studies of Arctic Pack Ice in April 1976. APL-UW 7724, May 1978.
30. P. Wadhams and R.J. Horne, An analysis of ice profiles obtained by submarine sonar in the Beaufort Sea, *J. Glaciol.*, 25, 401-424 (1980).
31. E. Williams, C. Swithinbank, and G. d Q. Robin, "A submarine sonar study of arctic pack ice," *J. Glaciol.*, 15, 349-362 (1975).
32. G.R. Garrison, R.E. Francois, and T. Wen, "Ice keels as false targets (U)," *Nav. J. Underwater Acoust.*, 30, 423-437 (1980). (Confidential)
33. G.R. Garrison, R.E. Francois, and T. Wen, Ice Keel Reflections Measured in Spring 1986 (U). APL-UW 8912, April 1989. (Confidential)
34. G.R. Garrison, R.E. Francois, T. Wen, and R.P. Stein, Acoustic Reflections from a Newly Formed Ice Keel (U). APL-UW 8507, September 1986. (Confidential)
35. Garrison, R.E. Francois, T. Wen, and R.P. Stein, Reflections from Ice Keels, 1984 (U). APL-UW 3-86, December 1987. (Confidential)
36. S.T. McDaniel, Vertical Spatial Coherence of Backscatter from Ice Keels (U), Tech. Note 86-172, Applied Research Laboratory, Pennsylvania State University, October 1986. (Confidential)
37. W.T. Ellison, Simulation Studies of Under-Ice Acoustic Scattering (U), Cambridge Acoustical Associates, Inc., 54 Rindge Ave. Extension, Cambridge, MA, October 1980. (Confidential)
38. G.C. Bishop, W.T. Ellison, and L.E. Mellberg, "A simulation model for high-frequency under-ice reverberation," *J. Acoust. Soc. Am.*, 82, 275-286, July 1987.



REPORT DOCUMENTATION PAGE			Form Approved OPM No. 0704-0188	
<small>Public reporting burden for this collection of information is estimated to average 1 hour per response, including the time for reviewing instructions, searching existing data sources, gathering and maintaining the data needed, and reviewing the collection of information. Send comments regarding this burden estimate or any other aspect of this collection of information, including suggestions for reducing this burden, to Washington Headquarters Services, Directorate for Information Operations and Reports, 1215 Jefferson Davis Highway, Suite 1204, Arlington, VA 22202-4302, and to the Office of Information and Regulatory Affairs, Office of Management and Budget, Washington, DC 20503.</small>				
1. AGENCY USE ONLY (Leave blank)		2. REPORT DATE October 1994		3. REPORT TYPE AND DATES COVERED Technical
4. TITLE AND SUBTITLE APL-UW High-Frequency Ocean Environmental Acoustic Models Handbook			5. FUNDING NUMBERS Contract N00039-91-C-0072	
6. AUTHOR(S)				
7. PERFORMING ORGANIZATION NAME(S) AND ADDRESS(ES) Applied Physics Laboratory University of Washington 1013 NE 40th Street Seattle, WA 98105-6698			8. PERFORMING ORGANIZATION REPORT NUMBER APL-UW TR 9407	
9. SPONSORING / MONITORING AGENCY NAME(S) AND ADDRESS(ES) AEAS Program Office of Naval Research Code 322TE 800 N. Quincy Street Arlington, VA 22217-5660			10. SPONSORING / MONITORING AGENCY REPORT NUMBER AEAS 9501	
11. SUPPLEMENTARY NOTES				
12a. DISTRIBUTION / AVAILABILITY STATEMENT Distribution authorized to Department of Defense and DoD contractors only; Software Documentation. Date of Determination: April 1995. Other requests shall be referred to the Chief of Naval Research, 800 North Quincy Street, Arlington, VA 22217-5660.			12b. DISTRIBUTION CODE	
13. ABSTRACT (Maximum 200 words)  This report updates several high-frequency acoustic models used in simulations and system design by Navy torpedo and mine countermeasure programs. The models presented augment and supersede those given previously in APL-UW technical note 7-79 (August 1979) and its successors, APL-UW technical reports 8407 and 8907. The report addresses the interaction of high-frequency acoustic energy with the ocean's volume, surface, bottom, and ice. It also addresses ambient noise generated by physical processes at the ocean surface and by biological organisms. The results are given in a form that can be exploited in simulations. The relevant fundamental experimental and theoretical research by APL and others upon which these models are based is available in the references.				
14. SUBJECT TERMS Speed of sound; absorption coefficient; surface reverberation, volume reverberation, bottom reverberation; surface forward scattering and reflection; bottom forward reflection; ambient noise; arctic acoustics; sea state; ocean high-frequency acoustic models; ocean environmental models			15. NUMBER OF PAGES 195	
			16. PRICE CODE	
17. SECURITY CLASSIFICATION OF REPORT Unclassified	18. SECURITY CLASSIFICATION OF THIS PAGE Unclassified	19. SECURITY CLASSIFICATION OF ABSTRACT Unclassified	20. LIMITATION OF ABSTRACT SAR	

NSN 7540-01-280-5500

Standard Form 298 (Rev. 2-89)  
Prescribed by ANSI Std. Z39-18  
299-11

ADB199453

**Distribution List For  
APL-UW TR 9407, AEAS 9501  
"APL-UW High-Frequency Ocean  
Environmental Acoustic Models Handbook"**

**NAVY AGENCIES**

**Center for Naval Analyses**  
4401 Ford Avenue  
P.O. Box 16268  
Alexandria, VA 22302-0268

Attn: Technical Information Center - CNA Standard Naval  
Distribution List Code: Part II List C4EE  
Joe Molitoris, Room 528

**Commander**  
**Mine Warfare Command**  
325 Fifth Street Southeast  
Corpus Christi, TX 78419-5032

Attn: Code NO2X (Charles Wicke, Science Advisor)

**Commanding Officer**  
**Naval Ice Center**  
Federal Office Bldg. 4  
4251 Suitland Road  
Washington, DC 20395

Attn: Eric Long

**Director**  
**Office of Naval Intelligence**  
4251 Suitland Road  
Washington, DC 20395-5720

Attn: Lee Edmonds

**Commander**  
**Naval Meteorology & Oceanography Command**  
1020 Balch Boulevard  
Stennis Space Center, MS 39529-5000

Attn: Robert Martin  
Code N53 (CDR Chris Hill)  
N534 (Bruce Northridge)

**Commander**  
**Naval Sea Systems Command**  
Washington, DC 20362-5101

Attn: Code 91  
PMO-401 (George Tsuchida)  
PMO-407 (MIW) (J. D. [Jim] Grembi)  
PEO (MIW) (Dale G. Uhler)  
PEO (USW) (Timothy E. Douglass)  
PEO (USWT) (James N. Thompson)

**Office of the Oceanographer of the Navy**  
U.S. Naval Observatory  
3450 Massachusetts Avenue, N.W.  
Washington, DC 20392-5421

Attn: Code NO96T (Edward Whitman)

**Office of Naval Research**  
Ballston Towers 1  
800 North Quincy Street  
Arlington, VA 22217-5660

Attn: Code 01 (Fred E. Saalfeld)  
03 (Arthur E. Bisson)  
32 (James J. DeCorpo)  
321 (Steven Ramberg)  
321N (James Andrews)  
321OA (Edward Chaika)  
321OA (Edward Estalote)  
321OA (Jeffrey Simmen)  
321OE (David Small)  
321SR (Frank Herr)  
321SS (Kenneth G. Dial)  
321TS (Wallace Ching)  
321TS (Randall Jacobson)  
321US (Richard Doolittle)  
321US (B. N. [Bobby] Wheatley)  
322 (Tommy Goldsberry)  
322GG (Joseph Kravitz)  
322OM (John Bergin)  
322OM (Manuel Fiadeiro)  
322PO (Louis Goodman)  
322TE (Barry P. Blumenthal)  
333 (Dale C. Houser)  
334 (Kam Ng)

**Commander**  
**Submarine Development Squadron TWELVE**  
Box 70  
Naval Submarine Base-New London  
Groton, CT 06349-5200

Attn: Code N714 (LCDR Jessie Carmen, Oceanographer)

**Commander**  
**Submarine Group NINE**  
Bangor, WA 98315

Attn: Code N73 (LCDR Jim Hill, Staff Oceanographer)

Superintendent  
U.S. Naval Postgraduate School  
Monterey, CA 93943

**NAVY LABORATORIES**

Commander  
Naval Air Warfare Center--Aircraft Division (NAWCAD)  
Patuxent, MD 20670-5304

Attn: Claude Martin, MS-29, Bldg. 3169 (Staff)

Commander  
Naval Air Warfare Center--Aircraft Division  
Warminster, PA 18974-5020

Attn: Library  
Code 4.5.5.3.6 (Arthur W. Horbach, Bldg. 2)

Commanding Officer  
Naval Command, Control & Ocean Surveillance Center  
RDT&E Division  
53560 Hull Street  
San Diego, CA 92152-5000

Attn: Code 0274 Technical Library (Cathy Wright,  
Librarian)  
02211 (Patricia A. Marsh)  
532 (Robert W. Floyd)  
78 (Paul M. Reeves)  
782 (Bob Dukelow)  
783 (Robert J. Vent)  
807 (Jack T. Avery)

Commanding Officer  
Naval Oceanographic Office  
1002 Balch Boulevard  
Stennis Space Center, MS 39522-5001

Attn: Technical Library  
Code N333 (Thomas A. Best - Database)  
N333 (Richard H. Simmens)  
N341 (Robert F. Joyce - Product)

Commanding Officer  
Naval Research Laboratory  
4555 Overlook Avenue, S.W.  
Washington, DC 20375-5000

Attn: Code 5200 Library  
7100 (Edward R. Franchi - Head,  
Acoustics)  
7120 (Marshall H. Orr)  
7142 (Fred T. Erskine)

Commanding Officer  
Naval Research Laboratory  
Detachment Stennis Space Center  
Stennis Space Center, MS 39529-5004

Attn: Code 7170 (Roger W. Merideth)  
7170 (Joe Posey)  
7170 (Dan J. Ramsdale)

7170 (J. S. [Steve] Stanic)  
7174 (Robert W. Farwell)  
7174 (Richard H. Love)  
7180 (Paul J. Bucca)  
7180 (George A. Kerr)  
7181 (Stanley A. Chin-Bing)  
7330 (Ming-Yang Su)  
7333 (Kevin G. Briggs)  
7430 (Samuel G. Tooma)  
7431 (Michael D. Richardson)

Commander  
Naval Surface Warfare Center  
Carderock Division  
Bethesda, MD 20084-5000

Attn: Library

Director  
Naval Surface Warfare Center  
Detachment Puget Sound  
530 Farragut Avenue  
Bremerton, WA 98314-5215

Attn: Code 704 (C. P. Henson)  
712 (Mike Schlut)

Commanding Officer  
Naval Surface Warfare Center  
Coastal Systems Station  
6703 West Highway 98  
Panama City, FL 32407-7001

Attn: Code E29 Technical Library  
10M (Elan Moritz)  
130B (Raymond Lim)  
130B (Joseph L. Lopes)  
130B (Gary S. Sammelman)  
130B (Cynthia C. Weilert)  
3110 (Kerry W. Commander)  
3110 (Robert V. Croft)  
3110 (William C. Littlejohn)

Commander  
Naval Surface Warfare Center  
Dahlgren Division, Detachment White Oak  
10901 New Hampshire Avenue  
Silver Spring, MD 20903-5000

Attn: Library  
Code A10 (Charles F. McClure)  
R02 (Bernard F. DeSavage, Jr.)

Officer in Charge  
Naval Undersea Warfare Center  
Arctic Submarine Laboratory  
49250 Fleming Road  
San Diego, CA 92152-7210

Attn: Code 906 (Robert M. Anderson)

TR 9407 Initial Distribution List  
May 3, 1995

Commanding Officer  
Naval Undersea Warfare Center  
Division Keyport  
Keyport, WA 98345-5000

Attn: Code 50 (Ernest E. Varnum - Weapons  
Systems Test Group)  
5540 (Glen A. Anunson)  
57 (Alan L. Lindstrom)  
70C1 (Robert Helton)

Commander  
Naval Undersea Warfare Center  
Division Newport  
1176 Howell Street  
Newport, RI 02841-1708

Attn: Code 0262 Technical Library  
22101 (Anthony F. Bessacini)  
2211 (Asa S. Davis, Jr.)  
821 (James G. Kelly)  
8212 (Robert N. Carpenter)  
8212 (Adam Mirkin)  
8219 (Carl J. Albanese)  
823 (David Goodrich)  
842 (Frank E. Aidala, Jr.)  
8423 (Carlos M. Godoy)  
8423 (John R. Ventura)

Officer in Charge  
Naval Undersea Warfare Center  
New London Detachment  
New London, CT 06320-5594

Attn: Library  
Code 101 (Robert F. Laplante)  
2122 (Albert Dugas, Jr.)  
3112 (Raymond J. Christian)  
3122 (Henry Weinberg)  
3122 (Thomas H. Wheeler)  
3123 (Rudolph E. Croteau, Jr.)  
33A (Joseph M. Monti)  
3314 (Roger J. Tremblay)  
3421 (David S. Cwalina)  
61 (Charles J. Batts)  
6291 (Gary N. Leticcq)

#### DEPARTMENT OF DEFENSE

Commander  
Advanced Research Projects Agency  
3701 North Fairfax Drive  
Arlington, VA 22203-1714

Attn: William Carey  
CAPT Bruce Dyer  
Charles Stewart

Defense Technological Information Center  
Cameron Station, Bldg. 5  
Alexandria, VA 22304-6145

#### UNIVERSITY LABORATORIES

The Johns Hopkins University  
Applied Physics Laboratory  
Johns Hopkins Road  
Laurel, MD 20723-6099

Attn: Lee Danzler

The Pennsylvania State University  
Applied Research Laboratory  
P.O. Box 30  
State College, PA 16804-0030

Attn: Library  
Carter L. Ackerman  
Lee Culver  
Ralph Goodman  
Edward G. Liszka  
Francis R. Menotti  
Harvey S. Piper, Jr.  
Dennis W. Ricker  
Frank W. Symons, Jr.

University of California, San Diego  
Scripps Institution of Oceanography  
P. O. Box 6049  
San Diego, CA 92166-6049

Attn: M. Buckingham  
C. DeMoustiev

University of California, San Diego  
Scripps Institution of Oceanography  
Marine Physical Laboratory, 0701  
P.O. Box 6049  
San Diego, CA 92166-6049

Attn: William Kuperman, Director  
William S. Hodgkiss

University of Texas at Austin  
Applied Research Laboratory  
P.O. Box 8029  
Austin, TX 78713-8029

Attn: Nicholas P. Chotiros  
H. Boehme  
J. Wellman  
Tom Muir

#### INDUSTRY AND CONSULTING AGENCIES

Alliant Techsystems Inc.  
600 Second Street Northeast  
Hopkins, MN 55343

Attn: Paul Greenblat (MN11-2881)  
John Reeves (MS-2865)

TR 9407 Initial Distribution List  
May 3, 1995

**Alliant Techsystems Inc.**  
**Marine Systems Division**  
6500 Harbour Heights Parkway  
Mukilteo, WA 98275-4844  
Attn: Ken Caproni (MS-4D16)

**Analysis & Technology Inc.**  
2341 Jefferson Davis Highway, Suite 1250  
Arlington, VA 22202  
Attn: Eleanor Holmes

**Areté Associates**  
P.O. Box 8050  
La Jolla, CA 92038  
Attn: Don W. Miklovic

**Hughes Aircraft Co.**  
**Aerospace Defense Section Surface Systems**  
Ground Systems Group  
P. O. Box 3310  
Fullerton, CA 92634-3310

**Planning Systems Inc.**  
115 Christian Lane  
Slidell, LA 70458  
Attn: Marshall R. Bradley

**Planning Systems Inc.**  
7923 Jones Branch Drive  
McLean, VA 22102  
Attn: Charles W. Holland

**Raytheon Electronics Systems Division**  
528 Boston Post Road  
Sudbury, MA 01776  
Attn: Stanley Chamberlain

**Science Applications International Corporation (SAIC)**  
P. O. Box 1303  
McLean, VA 22102  
Attn: Anthony I. Eller

**Science Applications International Corporation (SAIC)**  
P. O. Box 658  
Mashpee, MA 02649  
Attn: Ruth Keenan

**Tracor Applied Sciences, Inc.**  
35 Thomas Griffin Road  
New London, CT 06320-6498  
Attn: Sean M. Reilly



DEPARTMENT OF THE NAVY  
OFFICE OF NAVAL RESEARCH  
800 NORTH QUINCY STREET  
ARLINGTON, VA 22217-5660

IN REPLY REFER TO  
5510/6  
Ser 93/170  
19 Feb 97

From: Chief of Naval Research  
To: Administrator  
Defense Technical Information Center (ATTN: RSR)  
8725 John J. Kingman Road  
Ft. Belvoir, VA 22060-6218

Subj: CHANGE IN DISTRIBUTION STATEMENT

Encl: (1) Copy of Report Cover  
(2) Copy of SF 298

AD-B199 453

1. It is requested that the distribution statement for APL-UW TR 9407 report be changed to "A"  
- Approved for Public Release; Distribution Unlimited.
2. Since I do not know the AD number, enclosures (1) and (2) are provided for your information.
3. Questions may be directed to the undersigned on (703) 696-4619.

A handwritten signature in cursive script, reading "Peggy Lambert", is positioned above the typed name.

PEGGY LAMBERT  
By direction